# Development of enriched gadolinium target for cross section measurement and future production of terbium for nuclear medicine

Yizheng Wang

DOCTORAT MATIERE BRETAGNE MOLECULES LOIRE ET MATERIAUX

Nantes Université

# THESE DE DOCTORAT DE

NANTES UNIVERSITE

ECOLE DOCTORALE N° 596
*Matière, Molécules, Matériaux*
Spécialité : « *Chimie Physique, chimie théorique»*

Par
**Yizheng WANG**

# Development of Enriched Gadolinium Target for Cross Section Measurement and Future Production of Terbium for Nuclear Medicine

**Thèse présentée et soutenue à Nantes, le 6 décembre 2022**
**Unité de recherche : SUBATECH, UMR 6457**

**Rapporteurs avant soutenance** :

Ondřej Lebeda Nuclear Physics Institute of the CAS, Prague, République tchèque
Saverio Braccini Laboratory for High Energy Physics (LHEP), Berne, Suisse

**Composition du Jury :**

| | | |
|---|---|---|
| Président : | Saverio Braccini | Professeur associé, LHEP, Université de Berne, Suisse |
| Examinateurs : | Christelle Stodel | Chargée de recherche, CNRS, GANIL |
| | Ondřej Lebeda | Professeur, Nuclear Physics Institute of the CAS, République tchèque |
| Dir. de thèse : | Férid Haddad | Directeur de GIP ARRONAX, professeur de Nantes Université |
| Encadr. de thèse : | Thomas Sounalet | Chargé de recherche, CNRS, SUBATECH |
| | Nathalie Michel | Ingénieur de recherche, SUBATECH |

# Acknowledgement

This Ph.D. project was conducted in the Prisma group at SUBATECH laboratory under the direction of Prof. Dr. Férid Haddad, Dr. Thomas Sounalet, and Dr. Nathalie Michel. And I have been working at GIP ARRONAX for most of these three years. At the end of this Ph.D. project, I would like to express my deepest gratitude to all those people, without whom I would never able to complete this thesis.

I would like to extend my sincere gratitude to all my jury members who have kindly devoted their time to my thesis. I would like to thank Prof. Dr. Ondřej Lebeda and Prof. Dr. Saverio Braccini for accepting to be my rapporteurs, and I show my gratitude to Dr. Christelle Stodel for accepting to be my reviewer.

I wish to show my appreciation to my dear supervisors, Férid, Thomas, and Nathalie, for their professionalism and their scientific advice, their patient guidance, and their encouragement. Based on his vast experience, Férid always gives me fresh ideas and sharp advice for my work. This deepened my understanding of this project and radioisotope production. As a chemist, Thomas taught me electrochemistry almost from scratch. He not only guided me and inspired me through each step of the process, but also helped me integrate into the French work environment and taught me many ways to interact with people. Nathalie is my role model as a professional woman, she has given me a lot of guidance in both chemistry and engineering, whether the target fabrication or thermal calculations.

I would like to acknowledge Dr. Arnaud Gurtin and Dr. Etienne Nigron, for their efforts and contributions to the cross section measurement and data acquisition. All irradiation experiments were carried out with their help. They are also coauthors of my first articles, and their professional feedback helps me a lot.

I would also express my gratitude to Robin Bellamy from the GAMO group of ARRONAX and Arnaud Cadiou from the Mechanics group of SUBATECH for their design and fabrication of experimental equipment.

I am also deeply indebted to my colleagues in SUBATECH and GIP ARRONAX for their scientific and technical support. Many thanks to Prof. Dr. Vincent Métivier for all the support he has given me as leader of the Prisma group. I would like to thank Prof. Dr. Tomo Suzuki-Muresan for her help with the use of DRX devices and her guidance on DRX result analysis. I express my gratitude to Nadia Audouin for her help with the use of ICP-OES and SEM devices. I would also like to thank the company Capacité for their measurement of the thermal conductivity of $Gd_2O_3$ pellet.

I also owe a special debt of gratitude to my two CSI members Prof. Dr. Gilles Montavon and Dr. Gaia Pupillo for their follow-up of thesis work.

In addition, I would particularly like to acknowledge other master or Ph.D. students and post-doc researchers in the laboratory: Alexandre, Dingbang, Emeline, Haohan, Keerthana, Manon, Marie, Maxence, Teddy, Vincent, Yangjing, and Yihua. The support and encouragement of these people made me feel the friendship in a foreign country. Without these wonderful friends, my doctoral career would have lacked a lot of joy.

Finally, my thanks would go to my beloved family. Affected by covid, I haven't seen my parents for three years. However, the distance of 14,000 kilometers has never stopped us from missing, supporting and loving each other. At the same time, special thanks to the most important person in my life, my dear Honglu, for his company and unconditional support.

## Abstract

Radionuclides of terbium have attracted much attention for their potential applications in nuclear medicine. However, the short supply of terbium isotopes has limited their applications. This work proposes to use enriched gadolinium targets to produce terbium radioisotopes in biomedical cyclotrons via light-particle-induced reactions. The Auger and gamma emitter $^{155}$Tb is taken as a study case, the involved production reaction is $^{155}$Gd(d,2n)$^{155}$Tb.

To estimate the production yield of $^{155}$Tb, thin Gd-containing targets have been first developed to measure the reaction cross sections. To this end, the electrochemical co-deposition method has been chosen to manufacture Ni-$Gd_2O_3$ composite targets. Several process parameters that have an impact on the deposit quality have been investigated to increase the incorporation of Gd mass (up to 3 mg). The cross section measurement of the reaction $^{nat}$Gd(d,x)Tb, as proof-of-conception experiment, has been carried out at GIP ARRONAX using natural Ni-$^{nat}Gd_2O_3$ targets. The obtained results are consistent with existing data. Then the cross section of $^{155}$Gd(d,x)Tb has been measured using enriched Ni-$^{155}Gd_2O_3$ composite targets with a beam energy ranging from 8 MeV to 30 MeV. The production yield and the purity of $^{155}$Tb have been estimated using these measured results.

Meanwhile, thick targets have been developed via pelletizing method for mass production. The optimal experimental conditions and the physical and thermal properties of the pellets under these conditions were investigated. A manufactured enriched $^{155}Gd_2O_3$ target is irradiated with an incident energy of 15 MeV. The production yield of $^{155}$Tb is found to be 10.2 MBq/µAh and the purity is found to be 89%, which are in good agreement with the estimation obtained using the measured cross sections.

The coproduction of other Tb isotopes and the recycle of Gd are also parts of this thesis.



**Keywords:** terbium production, cross-section measurement, production yield, deuteron irradiation, theranostics radioisotope, cyclotron-produced radionuclide



## Résumé

Les radionucléides du terbium ont attiré beaucoup d'attention pour leurs applications potentielles en médecine nucléaire. Cependant, leur pénurie a limité leurs applications. Ce travail propose d'utiliser des cibles de gadolinium enrichies pour produire du terbium dans des cyclotrons biomédicaux. Le radionucléide $^{155}$Tb est pris comme cas d'étude et la réaction de production impliquée est $^{155}$Gd(d,2n)$^{155}$Tb.

Pour estimer le rendement de production, des cibles minces contenant du Gd sont développées pour mesurer les sections efficaces de production. La méthode de co-électrodéposition est choisie pour fabriquer ces cibles composées de Ni-$Gd_2O_3$. Plusieurs paramètres sont étudiés pour augmenter la masse de Gd incorporée dans la cible (jusqu'à 3 mg). Les sections efficaces de la réaction de $^{155}$Gd(d,x)Tb est mesurées au cyclotron du GIP ARRONAX dans une gamme d'énergie de 8 MeV à 30 MeV. Le rendement de production et la pureté de $^{155}$Tb sont estimé à partir de ces nouveaux résultats.

Pour la production de masse, des cibles épaisses sont développées via la méthode de pastillage. La condition expérimentale optimale et les propriétés physiques et thermiques des pastilles sous cette condition sont étudiées. Une cible de $Gd_2O_3$ enrichie en $^{155}Gd$ est irradiée avec une énergie incidente de 15 MeV. Le rendement de production de $^{155}Tb$ obtenu est de 10.2 MBq/µAh et la pureté est de 89 %. Ces résultats sont en bon accord avec les estimations obtenues par la mesure de sections efficaces.
La coproduction d'autres isotopes de Tb et le recyclage de Gd sont également présentés dans cette thèse.

**Mots clés** : production de terbium, mesure de sections efficaces, rendement de production, irradiation avec des deutérons, théranostique, cyclotron

# CONTENTS

**RESUME** ..... I

**LIST OF FIGURES** ..... VI

**LIST OF TABLES** ..... X

**LIST OF ABBREVIATIONS** ..... XI

**1. APPLICATIONS OF RADIONUCLIDES IN NUCLEAR MEDICINE** ..... 2

1.1. NUCLEAR MEDICINE ..... 2
*1.1.1. Physical principles* ..... *2*
1.1.1.1. Radioactivity and decay modes ..... 2
1.1.1.2. Nuclear reaction and cross section ..... 4
*1.1.2. Radionuclide imaging* ..... *5*
1.1.2.1. The Single-Photon Emission Computed Tomography (SPECT) ..... 6
1.1.2.2. The Positron Emission Tomography (PET) ..... 6
1.1.2.3. Hybrid imaging: PET/CT and SPECT/CT ..... 7
*1.1.3. Radiation therapy* ..... *8*
1.1.3.1. External radiation therapy ..... 8
1.1.3.2. Radionuclides therapy ..... 8
*1.1.4. Theranostics* ..... *9*
1.2. RADIONUCLIDE PRODUCTION IN NUCLEAR MEDICINE ..... 10
*1.2.1. Various radionuclide production routes* ..... *10*
1.2.1.1. Reactor production ..... 10
1.2.1.2. Accelerator production: Cyclotron ..... 11
1.2.1.3. Accelerator production: spallation reactions ..... 13
1.2.1.4. Radionuclide generator ..... 14
*1.2.2. Targetry system* ..... *16*
1.2.2.1. Solid targets ..... 16
1.2.2.2. Liquid targets ..... 17
1.2.2.3. Gas targets ..... 18
1.2.2.4. Encapsulation design ..... 18
1.3. THE TERBIUM FAMILY AND HOW TO MAKE THEM AVAILABLE ..... 19
*1.3.1. Radionuclides of interest: terbium radionuclides* ..... *19*
1.3.1.1. Production of $^{161}$Tb by nuclear reactors ..... 20
1.3.1.2. Production of $^{149,152,155}$Tb by spallation reaction ..... 20
1.3.1.3. Production of $^{149,152}$Tb by heavy-ion-induced reactions ..... 22
1.3.1.4. Production of $^{149,152,155}$Tb by light-charged-particle-induced reactions ..... 23
1.3.1.5. Comparison of Tb production routes ..... 26
*1.3.2. Objectives of this work* ..... *26*
1.3.2.1. Choice of production route ..... 27
1.3.2.2. Targetry strategy ..... 27
1.3.2.3. Irradiation strategy ..... 28

**2. MANUFACTURE OF THIN TARGETS THROUGH CO-ELECTRODEPOSITION METHOD** ..... 31

2.1. METHOD AND MATERIALS ..... 31
*1.3.3. Principle of the co-electrodeposition technique* ..... *31*
*1.3.4. The choice of experimental materials* ..... *33*
1.3.4.1. Selection of electrodeposited metals ..... 33
1.3.4.2. Selection of electrolytes ..... 36
1.3.4.3. Selection of substrates ..... 38
1.3.4.4. Co-electrodeposition cell structure ..... 38
*1.3.5. Tools for the manufacturing and the characterization of deposits* ..... *39*
1.3.5.1. Deposit manufacturing equipment ..... 39
1.3.5.2. Scanning Electron Microscopy (SEM) with Energy Dispersive X-Ray Analysis (EDX) ..... 40
1.3.5.3. Inductively Coupled Plasma - Atomic Emission Spectrometry (ICP-AES) ..... 41
2.2. CO-ELECTRODEPOSITION OF NI AND $Gd_2O_3$ ..... 41
*1.4.1. Optimization of co-electrodeposition parameters of Ni-$Gd_2O_3$* ..... *41*
1.4.1.1. Substrate roughness effects ..... 41

1.4.1.2. Applied potential effects ... 43
1.4.1.3. $Gd_2O_3$ loading quantity effects ... 49
1.4.1.4. Stirring speed effects ... 50
1.4.1.5. Temperature effects ... 53
1.4.1.6. Deposit homogeneity under optimal experimental conditions ... 53
*1.4.2. Multilayer deposit ... 56*
2.3. CO-ELECTRODEPOSITION OF ZN AND $GD_2O_3$ ... 57
*1.5.1. Optimization of co-electrodeposition parameters of Zn-$Gd_2O_3$ ... 57*
1.5.1.1. Applied potential effects ... 57
1.5.1.2. $Gd_2O_3$ loading quantity effects ... 60
1.5.1.3. Stirring speed effects ... 63
*1.5.2. Comparison of Ni-$Gd_2O_3$ and Zn-$Gd_2O_3$ deposits ... 64*
2.4. REUSE OF $GD_2O_3$ LOADING ... 64
2.5. CONCLUSION OF THIS CHAPTER ... 66

**3. MANUFACTURE OF THICK TARGETS THROUGH THE PELLETIZING METHOD ... 69**

3.1. METHOD AND MATERIALS ... 69
*3.1.1. Principle of the pelletizing method ... 69*
*3.1.2. Materials for the pelletizing ... 69*
3.1.2.1. Hydraulic press and pellet die ... 69
3.1.2.2. Candidate pelleting powders ... 71
*3.1.3. Materials for the characterization of pellets ... 71*
3.1.3.1. Mass and thickness measurement ... 71
3.1.3.2. X-ray diffraction (XRD) ... 71
3.1.3.3. Thermal conductivity measurement ... 71
3.1.3.4. Temperature estimation during irradiation ... 72
3.2. PELLETIZING OF NO-ENRICHED GD-CONTAINING POWDER ... 74
*3.2.1. Optimization of pelletizing parameters ... 74*
3.2.1.1. Selection of pelleting powder ... 74
3.2.1.2. Pressure effects ... 78
3.2.1.3. Pelleting time effects ... 79
*3.2.2. Characterization of $Gd_2O_3$ pellet ... 80*
3.2.2.1. Pellet densification ... 80
3.2.2.2. Morphology and crystal structure study ... 81
3.2.2.3. The temperature effects on the pellets ... 84
*3.2.3. Pellet dissolution and recycling of $Gd_2O_3$ powders ... 88*
3.3. THE ENRICHED $^{155}GD_2O_3$ PELLET PREPARED FOR IRRADIATION ... 89
3.4. CONCLUSION OF THE CHAPTER ... 91

**4. IRRADIATION OF TARGETS FOR THE PRODUCTION OF TB RADIONUCLIDES ... 94**

4.1. CROSS SECTION MEASUREMENT WITH THIN TARGETS ... 94
*4.1.1. Materials and methods ... 94*
4.1.1.1. The cross section calculation ... 94
4.1.1.2. The stacked foils technique ... 95
4.1.1.3. The energy calculation for each foil ... 97
4.1.1.4. Activity measurements ... 98
4.1.1.5. Activity data processing ... 102
4.1.1.6. Thickness measurement ... 103
4.1.1.7. Irradiation experimental set-up ... 103
*4.1.2. Activation cross sections of deuteron-induced reactions on natural Gd ... 105*
4.1.2.1. Theoretical analysis of the production $^{nat}$Gd(d,x)Tb ... 105
4.1.2.2. Characterization of Tb radionuclides ... 107
4.1.2.3. Irradiation conditions ... 109
4.1.2.4. The cross section of $^{nat}$Gd(d,x)$^{155}$Tb ... 109
4.1.2.5. Cross sections of impurities produced by deuteron irradiation on $^{nat}Gd_2O_3$ targets ... 111
4.1.2.6. Comparison with TENDL simulation ... 116
4.1.2.7. Summary of this section ... 118
*4.1.3. Production cross sections of deuteron-induced reactions on enriched 155Gd ... 119*
4.1.3.1. Theoretical analysis of the production Tb through enriched Gd ... 119
4.1.3.2. Irradiation conditions ... 121
4.1.3.3. The cross section of $^{155}$Gd(d,2n)$^{155}$Tb ... 122

4.1.3.4. Cross section of impurities with enriched $^{*}Gd_2O_3$ targets ..... 125
4.1.3.5. Comparison with proton induced reaction of enriched $^{155}Tb$ ..... 128
4.1.3.6. Summary of this section ..... 129
4.2. THICK TARGET PRODUCTION OF $^{155}TB$ ..... 129
*4.2.1. Theoretical analysis ..... 129*
4.2.1.1. The production yield and the thick target yield (TTY) ..... 129
4.2.1.2. Production yield simulated by RYC ..... 130
4.2.1.3. Optimal target thickness and energy window ..... 133
*4.2.2. Experimental production of $^{155}Tb$ ..... 133*
4.2.2.1. Capsule conception and irradiation condition ..... 134
4.2.2.2. Experimental production yield and purity of $^{155}Tb$ ..... 135
4.2.2.3. Future target material ..... 137
4.2.2.4. Future capsule conception ..... 139
4.3. CONCLUSION OF THE CHAPTER ..... 140

**5. SUMMARY AND CONCLUSION OF THIS THESIS ..... 142**

APPENDIX 2.1: DISSOLUTION OF $Gd_2O_3$ IN ACID SOLUTIONS ..... 145
APPENDIX 2.2: COMPONENT OF ENRICHED $Gd_2O_3$ ..... 146
APPENDIX 2.3: SEM IMAGES FOR MULTILAYER DEPOSIT ..... 147
APPENDIX 2.4: EDX ANALYSIS OF NI-$Gd_2O_3$ DEPOSIT UNDER -1.30 V/NHE ..... 148
APPENDIX 3.1: EXPERIMENTAL PROCEDURES TO PRODUCE $GdCl_3$ AND $GdF_3$ ..... 150
APPENDIX 3.2: HEAT TRANSFER CALCULATION IN THE TARGET ..... 152
APPENDIX 4.1 TI AND NI MONITOR REACTIONS ..... 155
APPENDIX 4.2 ENERGY AND EFFICIENCY CALIBRATION OF GAMMA DETECTOR ..... 158
APPENDIX 4.3 ACTIVITIES OF RADIONUCLIDES IN A DECAY CHAIN ..... 162

**REFERENCE ..... 165**
**Résumé de thèse ..... A**

# List of figures


Fig. 1.1 Comparison of action positions and ranges of different particles[22] ..... 9
Fig. 1.2 The fission yield of thermal neutron fission of $^{235}U$ as a function of product mass number. Image presented by Hasan and Prelas[32]. ..... 10
Fig. 1.3 Distribution of research reactors less than 40 years and used for isotope production[31], The numbers in the figure represent the number of reactors. ..... 11
Fig. 1.4 The distribution of cyclotrons for medical radionuclide production in the world in 2022[38]. ..... 12
Fig. 1.5 Schematic diagram of the internuclear cascade. ..... 14
Fig. 1.6 Possible produced nuclides through the proton-induced spallation reaction on $^{238}U$. The figure was down by Armbruster et al.[48]. ..... 14
Fig. 1.7 Equilibrium between mother and daughter radionuclides: (1a) transient equilibrium between $^{99}Mo$ and $^{99m}Tc$; (1b) relative activity of $^{99}Mo$ and $^{99m}Tc$ after each elution; (2a) secular equilibrium between $^{81}Rb$ and $^{81m}Kr$; (2b) relative activity of $^{81}Rb$ and $^{81m}Kr$ after each elution. Figures modified based on figures from IAEA[54]. ..... 15
Fig. 1.8 Production route of $^{161}Tb$ in nuclear reactors. ..... 20
Fig. 1.9 Theoretical cross section values of Tb isotopes of proton induced reactions on $^{152}Gd$ [96]. ..... 24
Fig. 1.10 Theoretical cross section values of Tb isotopes of proton induced reactions on $^{155}Gd$ [96]. ..... 25
Fig. 1.11 Schematic structure of the ARRONAX cyclotron and 6 particle beams. Picture based on the picture in the official website of ARRONAX. ..... 28
Fig. 2.1 Pourbaix diagram of Gd in water at 25°C[107]. ..... 32
Fig. 2.2 the processes involved in the incorporation of $Gd_2O_3$ into a growing metal matrix. ..... 33
Fig. 2.3 Dominance diagram of nickel in the solution in different pH values at the presence of $NH_3/NH_4^+$. ..... 37
Fig. 2.4 Dominance diagram of zinc in the solution in different pH values. ..... 38
Fig. 2.5 Schematic diagram (left) and photo (right) of the cell structure and the electrodes positions used in our experiments. The cell contains 35 mL electrolyte. During the process, a magnetic stirring, a sealing film and a stainless steel plate are also used. Suspended $Gd_2O_3$ particles (black dots) were evenly distributed in the electrolyte thanks to the stirring. The schematic diagram is not drawn according to the actual scale. ..... 39
Fig. 2.6 The overall experimental assembly of co-electrodeposition. ..... 40
Fig. 2.7 Photo of a deposit with rough gold plate substrate (left) and its surface image under SEM (right). The applied potential was -1.20 V/NHE, the stirring speed was 300 rpm, the $Gd_2O_3$ loading was 6.5 g, and the temperature was 30°C. ..... 42
Fig. 2.8 photo of deposit on a gold foil polished with 80-grit sandpaper (left) and its surface morphology under SEM (right). The applied potential was -1.20 V/NHE, the stirring speed was 300 rpm, the $Gd_2O_3$ loading was 6.5 g, and the temperature was 30°C. ..... 42
Fig. 2.9 Voltammetry curves of Ni with or without $Gd_2O_3$ loading (0.8 g $Gd_2O_3$ for (a) and 6.5 g $Gd_2O_3$ for (b)). Sweep from -0.1 V/NHE to -1.5 V/NHE for 5 cycles with a scanning speed of 0.05 V/s. The curves presented are the curves of the fifth cycle (all curves). The temperature of the electrolyte was 30°C and the pH was 9.8. .. 44
Fig. 2.10 EDX analysis of the chemical composition of the deposits. Applied potential was -1.20 V/NHE, stirring speed was 300 rpm, $Gd_2O_3$ loading was 6.5g, $Ni^{2+}$ concentration was 0.14 mol/L, pH = 9.8. ..... 46
Fig. 2.11 Microscopic images of surface morphology and $Gd_2O_3$ distribution of the deposits, as areas with high concentration of Gd are the brighter areas. Loaded $Gd_2O_3$ was 6.5 g, stirring speed was 300 rpm, applied potential was -1.04 V/NHE (a, b), -1.16 V/NHE (c, d), -1.20 V/NHE (e, f), -1.30 V/NHE (g, h). ..... 47
Fig. 2.12 Microscopic images of surface morphology and $Gd_2O_3$ particle size of the same deposit in Fig. 2.11 (c,d), the surface was magnified 10000 times. ..... 48
Fig. 2.13 Effects of $Gd_2O_3$ loading on the quantity of Gd trapped in Ni-$Gd_2O_3$ deposits. (a) mass of Gd in deposits. (b) Percentage of trapped Gd relative to the mass of $Gd_2O_3$ incorporated. The stirring speed was 300 rpm, the applied potential was -1.20 V/NHE. ..... 50
Fig. 2.14 Photo of several deposits with different stirring speeds. The applied potential was -1.20 V/NHE, the $Gd_2O_3$ loading was 6.5 g, and the temperature was 30°C. ..... 51
Fig. 2.15 Microscopic images of surface morphology and Gd2O3 distribution of the matte part (1) and bright part (2) at a magnification of 100×. The stirring speed of the deposit was 800 rpm,the applied potential was -1.2 V/NHE, the $Gd_2O_3$ loading was 6.5 g, and the temperature was 30°C. ..... 52
Fig. 2.16 Effects of stirring speed on the Gd content of Ni- $Gd_2O_3$ deposits. The applied potential was -1.2 V/NHE, the $Gd_2O_3$ loading was 6.5 g, and the temperature was 30°C. ..... 52

FIG. 2.17 SEM ANALYSIS OF THE SURFACE OF DEPOSITS BEFORE (A) AND AFTER (B) THE DISSOLUTION OF CONCENTRATED $H_2SO_4$. DEPOSIT WAS MADE BY OPTIMAL CONDITIONS: THE APPLIED POTENTIAL WAS -1.2 V/NHE, THE STIRRING SPEED WAS 300 RPM, THE $Gd_2O_3$ LOADING WAS 6.5 G, AND THE TEMPERATURE WAS 30°C. ..... 54
FIG. 2.18 SEM ANALYSIS OF THE SURFACE MORPHOLOGY OF (A) A DEPOSIT WITH A PURE NI LAYER ON GOLD SUBSTRATE AND A NI-$Gd_2O_3$ LAYER ON NI LAYER, AND (B) A DEPOSIT WITH SIMPLE NI-$Gd_2O_3$ LAYER ON GOLD SUBSTRATE. THE APPLIED POTENTIAL WAS -1.2 V/NHE, THE STIRRING SPEED WAS 300 RPM, THE $Gd_2O_3$ LOADING WAS 6.5 G, AND THE TEMPERATURE WAS 30°C. ..... 55
FIG. 2.19 SEM IMAGES OF THE SURFACE OF THE SAME DEPOSIT AT 2.3 μM (A) AND AT 13.5 μM (B). ..... 56
FIG. 2.20 SCHEMA OF MULTILAYER DEPOSITS WITH 7 LAYERS. THE SCHEMA IS NOT DRAWN TO ACTUAL SCALE. ..... 56
FIG. 2.21 VOLTAMMETRY CURVES ASSOCIATED WITH THE FIFTH CYCLE IN ZN ELECTROLYTE WITHOUT $Gd_2O_3$ LOADING (BLACK CURVE) AND WITH 1.0 G $Gd_2O_3$ LOADING (RED CURVE) AT 30°C. THE STIRRING SPEED WAS 800 RPM WITH A MAGNET. ..... 58
FIG. 2.22 MICROSCOPIC IMAGES OF THE MORPHOLOGY OF ZN DEPOSITS IN DIFFERENT APPLIED POTENTIAL: (A) -1.52 V/NHE, (B) -1.54 V/NHE, (C) -1.56 V/NHE, (D) -1.58 V/NHE, (E) -1.60 V/NHE AND (F) -1.62 V/NHE. THE STIRRING SPEED WAS 800 RPM AND THE TEMPERATURE WAS 30°C ..... 60
FIG. 2.23 PHOTO OF DEPOSITS (A) WITHOUT $Gd_2O_3$, (B) WITH 1.0 G $Gd_2O_3$, AND (C) WITH 6.5 G $Gd_2O_3$. THE APPLIED POTENTIAL WAS -1.52 V/NHE, THE SIRRING SPEED WAS 800 RPM, THE TEMPERATURE WAS 30°C, AND THE DURATION OF CO-ELECTRODEPOSITION WAS 60 MIN ..... 61
FIG. 2.24 MORPHOLOGY STUDIES OF ZN DEPOSIT (A) AND ZN-$Gd_2O_3$ CO-DEPOSIT (B) BY SEM. THE APPLIED POTENTIAL WAS -1.52 V/HNE, THE STIRRING SPEED WAS 800 RPM, THE TEMPERATURE WAS 30°C, AND EXPERIMENT LASTED 60 MIN. FOR (B), 6.5G $Gd_2O_3$ WAS ADDED. ..... 62
FIG. 2.25 EDX ANALYSIS OF THE CHEMICAL COMPOSITION OF THE DEPOSITS IN NO-DENDRITES AREA. APPLIED POTENTIAL WAS -1.52 V/NHE, STIRRING SPEED WAS 800 RPM, $Gd_2O_3$ LOADING WAS 6.5G. ..... 62
FIG. 2.26 PHOTO AND SEM IMAGE OF A ZN-$Gd_2O_3$ DEPOSIT STIRRED AT 400 RPM. THE APPLIED POTENTIAL WAS -1.52 V/NHE, THE $Gd_2O_3$ LOADING WAS 6.5 G, THE TEMPERATURE WAS 30°C, AND CO-ELECTRODEPOSITION DURATION WAS 60 MIN. ..... 63
FIG. 2.27 THE CHANGE OF TRAPPED GD MASS WITH THE DEPOSITION TIMES. THE GD2O3 LOADING WAS 1.0 G AND 0.5 G, THE APPLIED POTENTIAL WAS -1.2 V/NHE, THE STIRRING SPEED WAS 300 RPM, AND THE TEMPERATURE WAS 30°C. ..... 66
FIG. 3.1 HYDRAULIC PRESS USED IN THIS WORK, THE MAXIMUM CAPACITY IS 950 MPA FOR A 20-MM-DIAMETER-PELLET. ..... 70
FIG. 3.2 THE 20-MM-DIAMETER PELLET DIE USED IN THIS WORK. LEFT SIDE: PHOTO OF THE PLUNGER, TWO REPLACEMENT PELLET, AN ITEM FOR DEMOLDING, THE DIE BODY AND THE EVACUABLE DIE BASE. RIGHT SIDE: THE SCHEMATIC DIAGRAM OF THE PELLETING APPARATUS. ..... 70
FIG. 3.3 SCHEMATIC DIAGRAM OF THE HEAT TRANSFER OF THE ENCAPSULATED PELLET WITH TWO-SIDE WATER-COOLING. $X_i$ (I=0,1,2,…,5) REPRESENTS THE BOUNDARY OF EACH COMPONENT OF THE ENCAPSULATED PELLET IN THE LATERAL DIRECTION, $T_i$ (I=0,1,2,…,5) IS THE TEMPERATURE OF THE $X_i$. THICKNESS OF LAYEY-I IS NOTED AS $E_i$ (I=1,2,…,5). THE DIRECTION OF HEAT FLUX IS FROM $X_0$ TO $X_5$, AND THERE IS A CONSTANT FLOW OF WATER ON $X_0$ AND $X_5$. THE SCALE SHOWN DOES NOT REPRESENT THE ACTUAL SCALE. ..... 74
FIG. 3.4 EDX SPECTRA OF OBTAINED $GdCl_3$ (ABOVE) AND $GdF_3$ (BELOW) POWDERS. THE TENSION WAS 15 KEV, THE MAGNIFICATION FACTOR WAS 5000. ..... 75
FIG. 3.5 XRD SPECTRA OF OBTAINED $GdCl_3$ (ABOVE) AND $GdF_3$ (BELOW) POWDERS. THE RED VERTICAL LINES IN EACH SPECTRUM REPRESENT THE PEAKS CORRESPONDING TO STANDARD $GdCl_3$ (OR $GdF_3$) CRYSTALS. ..... 76
FIG. 3.6 MASS CHANGE OF 50.17 G OF EXPOSED $GdCl_3$ POWDER WITH TIME AT 20°C. ..... 77
FIG. 3.7 PHOTO OF GDCL3 PELLET BEFORE HEATING (LEFT) AND AFTER HEATING AT 300 °C FOR 30 MINUTE (RIGHT). THE MASS OF THE PELLET IS 0.50 G, THE DIAMETER IS 20 MM. ..... 77
FIG. 3.8 PHOTOS OF A DAMAGED PELLET (LEFT) AND A COMPLETE PELLET (RIGHT) DURING THE RECOVERY PROCESS. ..... 78
FIG. 3.9 THE THICKNESS OF THE PELLET WITH DIFFERENT COMPRESSION TIME. THE APPLIED PRESSURE WAS 600 BARS, THE MASS OF THE POWDER WAS 1.50 G. BLACK DOTS REPRESENT THE AVERAGE THICKNESS OF PELLETS, RED DOTTED LINE PRESENT THE AVERAGE VALUE OF ALL PELLETS. ..... 80
FIG. 3.10 THE THICKNESS OF THE PELLETS WITH DIFFERENT MASS OF $Gd_2O_3$ POWDER UNDER 600 BAR OF PRESSURE AND 60 S OF COMPRESSION DURATION. ..... 81
FIG. 3.11 SEM IMAGES OF THE SURFACE OF FOUR PELLETS, IMAGES 1A, 2A, 3A, AND 4A REPRESENT THE PELLET WITH A THICKNESS OF 0.36 MM, 0.54 MM, 0.85MM AND 1.14 MM AFTER MAGNIFICATION OF 1000 TIMES RESPECTIVELY. WHEREAS IMAGES 1B, 2B, 3B, AND 4B REPRESENT THE SAME PELLETS AFTER MAGNIFICATION OF 100 TIMES RESPECTIVELY. THE APPLIED PRESSURE WAS 600 BAR AND THE COMPRESSION TIME WAS 60 S. ..... 83
FIG. 3.12 RYC SIMULATION ABOUT THE OPTIMAL THICKNESS FOR THE REACTION $^{155}Gd(d,2n)^{155}Tb$ WITH THE ENRICHED $Gd_2O_3$ USED IN THIS WORK. THE CROSS SECTION DATA REFERS TO THE DATABASE TENDL-2019. ..... 84
FIG. 3.13 THE EVOLUTION OF THE THERMAL CONDUCTIVITY OF $Gd_2O_3$ AT 24°C, 100°C, 200°C, 300 °C, AND 400°C. ..... 85

FIG. 3.14 SEM IMAGES OF FOUR PELLETS BEFORE AND AFTER HEATING. THE IMAGES A, B, C AND D REPRESENT THE IMAGE OF 4 PELLETS BEFORE THE HEATING; AND THE IMAGES A, B, C AND D REPRESENT THE IMAGE OF THE SAME PELLETS AFTER 100°C, 200°C, 400°C AND 600°C OF HEATING RESPECTIVELY. ..... 87
FIG. 3.15 XRD PATTERN OF THE $Gd_2O_3$ PELLET BEFORE (BLACK) AND AFTER (RED) HEATING AT 600°C. ..... 88
FIG. 3.16 XRD SPECTRA OF OBTAINED POWDER (BLACK) AND $Gd_2O_3$ POWDER SUPPLIED BY SIGMAALDRICH (RED). ..... 89
FIG. 3.17 THE PRECIPITATION OF THE $Gd_2O_3$ POWDER IN A BOTTLE AND IN THE CO-ELECTRODEPOSITION CELL. LEFT SIDE: THE LAYERING OF THE NI ELECTROLYTE AND THE POWDER; RIGHT SIDE: THE POWDER LEFT IN THE BOTTOM OF THE CELL AFTER REMOVING THE NI ELECTROLYTE WITH A PIPETTE. ..... 90
FIG. 3.18 PHOTO OF THE PELLET MADE OF ENRICHED $^{155}Gd_2O_3$. ..... 90
FIG. 3.19 PACKAGING PROCESS OF THE ENRICHED PELLET: (A) THE ENRICHED PELLET MADE BY THE PRESS; (B) THE HAND WRAPPED PELLET BY TWO ALUMINUM FOILS; (C) THE WRAPPED PELLET IN THE PRESS DIE; (D) THE TIGHTLY WRAPPED PELLET AFTER THE COMPRESSION. ..... 91
FIG. 4.1 SCHEMATIC DIAGRAM OF THE STACK COMPOSITION USED FOR A TYPICAL EXPERIMENT WHERE WE IRRADIATED TWO TARGETS SIMULTANEOUSLY. THE SIZE AND THICKNESS OF THE FOILS ARE NOT DRAWN ACCORDING TO THE ACTUAL SCALE. ..... 96
FIG. 4.2 LINEAR ATTENUATION COEFFICIENT OF THE PHOTOELECTRIC INTERACTION, COMPTON INTERACTION AND PAIR-PRODUCTION INTERACTION FOR GERMANIUM, FIGURE MADE BY LEE ET AL[187]. ..... 98
FIG. 4.3 SCHEMATIC REPRESENTATION OF THE PHOTOELECTRIC EFFECT. ..... 98
FIG. 4.4 SCHEMATIC REPRESENTATION OF THE COMPTON EFFECT. ..... 99
FIG. 4.5 SCHEMATIC REPRESENTATION OF THE PAIR PRODUCTION EFFECT. ..... 99
FIG. 4.6 CANBERRA HPGE DETECTOR USED IN THIS WORK: (1) CRYOSTAT AND COOLING SYSTEM WITH LIQUID NITROGEN, (2) GE CRYSTAL COVERED WITH ALUMINUM ENDCAP, (3) HIGH POSITION (19 CM) ABOVE THE DETECTOR, SURROUNDED BY LEAD SHIELD. ..... 100
FIG. 4.7 PHOTO OF THE BEAM LINE USED AT GIP ARRONAX FACILITY. 1: THE END OF BOMBARDMENT (EOB), 2: THE POSITION OF THE STACK, 3: ALUMINUM BEAM STOPPER FOR STOPPING PARTICLES. ..... 104
FIG. 4.8 THE STAINLESS STEEL RING CAPSULE (A) AND THE LEAD POT FOR COLLECTING THE ENCAPSULATION (B). ..... 104
FIG. 4.9 SIMULATED PRODUCTION CROSS SECTION OF TB ISOTOPES BY DEUTERON INDUCED REACTIONS ON NATURAL GD TARGET. . 106
FIG. 4.10 EXPERIMENTAL CROSS SECTION OF $^{nat}Gd(d,x)^{155}Tb$ REACTIONS MEASURED IN THIS WORK (RED POINTS) AND OTHER EXISTING DATA IN THE LITERATURE [91–93]. ..... 110
FIG. 4.11 EXPERIMENTAL CROSS SECTION OF $^{nat}Gd(d,x)^{153}Tb$ REACTIONS MEASURED IN THIS WORK (RED POINTS) AND OTHER EXISTING DATA IN THE LITERATURE[91,92] ..... 113
FIG. 4.12 EXPERIMENTAL CROSS SECTION OF $^{nat}Gd(d,x)^{154m2}Tb$ REACTIONS MEASURED IN THIS WORK (RED POINTS) AND OTHER EXISTING DATA IN THE LITERATURE[91,92] ..... 114
FIG. 4.13 EXPERIMENTAL CROSS SECTION OF $^{nat}Gd(d,x)^{154m1}Tb$ REACTIONS MEASURED IN THIS WORK (RED POINTS) AND OTHER EXISTING DATA IN THE LITERATURE[91,92] ..... 114
FIG. 4.14 EXPERIMENTAL CROSS SECTION OF $^{nat}Gd(d,x)^{154g(cum)}Tb$ REACTIONS MEASURED IN THIS WORK (RED POINTS) AND OTHER EXISTING DATA IN THE LITERATURE[91]. ..... 115
FIG. 4.15 EXPERIMENTAL CROSS SECTION OF $^{nat}Gd(d,x)^{156}(cum)Tb$ REACTIONS MEASURED IN THIS WORK (RED POINTS) AND OTHER EXISTING DATA IN THE LITERATURE[91,92] ..... 115
FIG. 4.16 EXPERIMENTAL CROSS SECTION OF $^{nat}Gd(d,x)^{160}Tb$ REACTIONS MEASURED IN THIS WORK (RED POINTS) AND OTHER EXISTING DATA IN THE LITERATURE[91,92] ..... 116
FIG. 4.17 COMPARISON OF MEASURED AND TENDL SIMULATED VALUES OF $^{155}Tb$ AND $^{156}Tb$ CROSS SECTIONS. ..... 117
FIG. 4.18 COMPARISON OF MEASURED AND TENDL SIMULATED VALUES OF $^{153}Tb$, $^{154g,m1,m2}Tb$ AND $^{160}Tb$ CROSS SECTIONS. ..... 117
FIG. 4.19 DOMINANT RADIONUCLIDES AT DIFFERENT ENERGIES ACCORDING TO THE MEASURED CROSS SECTIONS. ..... 118
FIG. 4.20 SIMULATED PRODUCTION CROSS SECTION OF TB ISOTOPES BY DEUTERON INDUCED REACTIONS ON ENRICHED *GD. ..... 120
FIG. 4.21 CONTRIBUTION OF THE PRODUCTION OF 155TB BY GD ISOTOPES. ..... 121
FIG. 4.22 COMPARISON OF MEASURED CROSS SECTIONS AND SIMULATED VALUES OF THE REACTION $^{*}Gd(d,x)^{155}Tb$. RED CURVE: SIMULATED VALUES USING EQ.4.20; BLACK POINTS: MEASURED VALUES USING ENRICHED $^{*}Gd_2O_3$ TARGETS; ORANGE POINTS: MODIFIED MEASURED VALUES USING NATUREL $Gd_2O_3$ TARGETS ACCORDING TO EQ.4.23. ..... 124
FIG. 4.23 COMPARISON OF MEASURED CROSS SECTIONS AND SIMULATED VALUES OF THE REACTION $^{*}Gd(d,x)^{153}Tb$. BLUE CURVE: SIMULATED TENDL-2019 VALUES; BLACK POINTS: MEASURED VALUES USING ENRICHED $^{*}Gd_2O_3$ TARGETS. ..... 126
FIG. 4.24 COMPARISON OF MEASURED CROSS SECTIONS AND SIMULATED VALUES OF THE REACTION $^{*}Gd(d,x)^{154g,m1,m2}Tb$. GREEN, YELLOW AND BLUE CURVES REPRENSENT THE SIMULATED TENDL-2019 VALUES OF $^{154g}Tb$, $^{154m1}Tb$ AND $^{154m2}Tb$, RESPECTIVELY; GREEN, YELLOW AND BLUE POINTS REPRESENT MEASURED VALUES OF $^{154g}Tb$, $^{154m1}Tb$ AND $^{154m2}Tb$, RESPECTIVELY. ..... 126
FIG. 4.25 COMPARISON OF MEASURED CROSS SECTIONS AND SIMULATED VALUES OF THE REACTION $^{*}Gd(d,x)^{156g}Tb$. GRAY CURVE: SIMULATED TENDL-2019 VALUES USING EQ.4.16; BLACK POINTS: MEASURED VALUES USING ENRICHED $^{*}Gd_2O_3$ TARGETS 127
FIG. 4.26 MEASURED CROSS SECTION VALUES OF $^{155}Tb$ AND $^{156}Tb$. ..... 128

Fig. 4.27 Comparison of $^{155}$Tb cross sections produced by proton induced and deuteron induced reactions of enriched $^{155}$Gd. ..... 129
Fig. 4.28 Fitted excitation function of $^{155}$Tb and $^{156}$Tb with Experimentally Modified Gaussian (EMG) distribution fitting function. A1: inputs of cross sections of $^{155}$Tb measured in this work;B1: inputs of cross sections of $^{156}$Tb measured in this work. ..... 131
Fig. 4.29 RYC simulation of production yield of $^{155}$Tb and $^{156}$Tb using measured data. ..... 132
Fig. 4.30 The ratio of the production yield of $^{155}$Tb and $^{156}$Tb as a function of energy using the data simulated by RYC. ..... 132
Fig. 4.31 The capsule and the assembly of the target. a: empty capsule; b: assembly of enriched targets fixed by Al balls and natural target; c: closed capsule. ..... 134
Fig. 4.32 Schematic diagram of the assembly of Ti foil and pellets in the capsule. ..... 134
Fig. 4.33 Spectrum of a diluted sample which is counted 9 days after EOB. ..... 135
Fig. 4.34 Activation cross section data of the $^{nat}$Ti(d, x)$^{46}$Sc reaction with estimated uncertainties according to data of IAEA. ..... 136
Fig. 4.35 Purity change of $^{155}$Tb as a function of time after irradiation. ..... 137
Fig. 4.36 Cross sections of Tb radionuclides of proton induced (on top) or deuteron induced (on bottom) reactions on pure $^{155}$Gd target. Data calculated by TENDL-2019. ..... 138
Fig. 4.37 The ratio of the $^{155}$Tb yield to the $^{156}$Tb yield as a function of energy. ..... 139
Fig. 4.38 Welded Nb capsule (A) and opened capsule (B). ..... 139
Fig. 4.39 Shuttle used for placing the encapsulated targets. The shuttle has two holes as inlet and outlet of cooling water. ..... 140

# List of tables


Table 1.1 Decay information of several SPECT radionuclides[8]. ..... 6
Table 1.2 Decay information of several PET radionuclides[8]. ..... 7
Table 1.3 Cyclotron produced radionuclides and production information. ..... 12
Table 1.4 Information of radionuclides produced or to be produced at CERN-MEDICIS [46]. ..... 13
Table 1.5 Principles and remarks of several target manufacture methods. ..... 17
Table 1.6 Thermal conductivity and nuclear activation of several encapsulation materials[37]. ..... 19
Table 1.7 Maximum cross sections of $^{nat}$Ta(p,x)Tb and corresponding energies at maximum cross sections. ..... 21
Table 1.8 Collection activity and separation efficiencies of terbium radioisotopes[46] ..... 21
Table 1.9 Impurities produced in the spallation production route[83]. ..... 22
Table 1.10 Comparison of reactor production route and accelerator production route of $^{161}$Tb [81]. ..... 25
Table 1.11 Advantages and disadvantages of different radionuclide production routes. ..... 26
Table 2.1 List of well-studied metals and their standard electrode potentials (E°)[102]. ..... 34
Table 2.2 Decay characteristic of radionuclides produced by Zn[123] ..... 35
Table 2.3 Decay characteristic of radionuclides produced by Ni[124]. ..... 35
Table 2.4 Cumulative formation constants for $Ni^{2+}$ and $NH_3$ complexes[102] ..... 36
Table 2.5 Cumulative formation constant for the complexation of zinc and hydroxide[102]. ..... 37
Table 2.6 Applied potential effects on average current density, deposit areal density, deposited Gd mass, and Gd content in Ni-$Gd_2O_3$ composites deposits. ..... 45
Table 2.7 Deposits information under different temperatures. ..... 53
Table 2.8 Comparison of deposit on a nickel substrate and deposit on a gold substrate ..... 55
Table 2.9 Comparison of multilayer deposit and monolayer deposit. ..... 57
Table 2.10 Applied potential effects on average current density, deposit areal density, deposited Gd mass and Gd content in Zn-$Gd_2O_3$ composites deposits. ..... 59
Table 2.11 Comparison of deposit quality with different stirring speed. ..... 63
Table 3.1 Mean thickness and success rate under different pressures. ..... 79
Table 3.2 Thermal properties of different solid targets in room temperature (20-25°C) and their productions. ..... 86
Table 3.3 Mass change of the pellets before and after heating. ..... 86
Table 4.1 Composition of natural gadolinium and abundance of each isotope. ..... 105
Table 4.2 Decay information and reaction information of terbium radionuclides[8,113,198].The $E_{THRESOLD}$ corresponds to the threshold energy for producing ground state radionuclides. ..... 107
Table 4.3 Target information and beam parameters of cross section measurement on $^{nat}$Gd. ..... 109
Table 4.4 Measured cross section values of the reaction $^{nat}$Gd(d,x)$^{155}$Tb. ..... 110
Table 4.5 Measured deuteron-induced reactions cross section values of $^{153}$Tb, $^{154g,m1,m3}$Tb, $^{156(cum)}$Tb, and $^{160}$Tb on natural Gd targets. ..... 111
Table 4.6 Isotopic composition of enriched $Gd_2O_3$. ..... 119
Table 4.7 Target information of the irradiation for enriched targets. ..... 122
Table 4.8 Measured cross section values of the reaction *Gd(d,x)$^{155}$Tb. ..... 123
Table 4.9 Cross section of the reaction $^{155}$Gd(d,2n)$^{155}$Tb converted from measured values of $^{*}$Gd(n,x)$^{155}$Tb. ..... 123
Table 4.10 The original measured cross section and the modified cross section using natural $Gd_2O_3$ targets. ..... 125
Table 4.11 Measured deuteron-induced reactions cross section values of $^{153}$Tb, $^{154}$Tb, and $^{156}$Tb on enriched *Gd targets. ..... 125
Table 4.12 Comparison of different production routes of $^{155}$Tb ..... 137

# List of abbreviations

| | |
|---|---|
| AE | Auxiliary Electrode |
| BR | Branching Ratio |
| CT | Computed Tomography |
| DSC | Differential Scanning Calorimetry |
| EC | Electron Capture |
| EDX | Dispersive X-Ray Analysis |
| EMG | Experimentally Modified Gaussian |
| EOB | End Of Bombardment |
| ERT | External Radiation Therapy |
| HER | Hydrogen Evolution Reaction |
| HIVIPP | High Energy Vibrational Powder Plating |
| HPGe | High Purity Germanium |
| HTDS | Hi-Tech Detection Systems |
| IAEA | International Atomic Energy Agency |
| ICP-AES | Inductively Coupled Plasma - Atomic Emission Spectrometry |
| iso | International Organization Ofr Standardization |
| ISOL | Isotope Separation Online |
| LET | Linear Energy Transfer |
| MRI | Magnetic Resonance Imaging |
| MS | Magnetron Sputtering |
| NHE | Normal Hydrogen Electrode |
| PEEK | Polyetheretherketone |
| PET | Positron Emission Tomography |
| RBE | Relative Biological Effectiveness |
| RE | Reference Electrode |
| RYC | Radionuclide Yield Calculator |
| SEM | Scanning Electron Microscopy |
| SHE | Standard Hydrogen Electrode |
| SPECT | Sighe-Photon Emission Computerized Tomography |
| SRIM | Stopping And Range Of Ions In Matter |
| TTY | Thick Target Yield |
| WE | Working Electrode |
| XRD | X-Ray Diffraction |

# Chapter 1:
# Applications of radionuclides in nuclear medicine

# 1. Applications of radionuclides in nuclear medicine

## 1.1.Nuclear medicine

Nuclear medicine is a branch of medicine that uses the nuclear properties of substances for diagnosis or treatment. This section begins with a short introduction of physical principles applied in nuclear medicine, and then follows with the introductions of radionuclides for imaging and radiation therapies. In addition, an emerging paradigm, theranostics, will be introduced with its relevant radionuclides.

### 1.1.1. Physical principles

#### 1.1.1.1. Radioactivity and decay modes

An atom is formed by positive charged protons, neutral neutrons, and negative charged electrons. The core region consisting of protons and neutrons is called the nucleus of the atom, and the protons and neutrons are also known as nucleons.

A nuclide is a classification of atoms that have specific proton and neutron numbers and energy state. The notion ${}^{A}_{Z}X$ is used to summarize the composition of a nuclide, where *X* is the chemical symbol of the element, *A* is the mass number or the nucleons number, and *Z* is the proton number. Nuclides that have the same proton number but different neutron number are called isotopes.

The nuclide can be stable or unstable. Most of the natural existed atoms are stable. An unstable nuclide is called a radionuclide, it has a spontaneous process to emit its excess internal energy and transform it to a more stable nuclide. This process is known as radioactive decay, or radioactivity.

Most radionuclides do not decay directly into stable states, but go through a series of decay reactions until they finally reach stable nuclide. The series of the decay products formed in a chain during the radioactive decay, it is called a decay chain.

The modes of decay can be classified as α decay, $\beta^-$ decay, $\beta^+$ decay, electron capture, γ decay and internal conversion, and spontaneous fission decay for very heavy isotopes.

The α decay occurs when the unstable nucleus emits an α particle (${}^{4}_{2}He$ ), this occurs more often in heavy nuclides (eg. $^{222}$Rn, $^{225}$Ac, $^{226}$Ra). The process can be expressed in *eq.1.1*:

$$ {}^{A}_{Z}X \rightarrow {}^{A-4}_{Z-2}Y + {}^{4}_{2}He \qquad (eq.1.1) $$

The $\beta^-$ decay occurs to radionuclide who decays by emitting an electron ($e^-$) and an electronic antineutrino ($\bar{\nu}_e$). This decay mode often occurs on nuclides who has excess neutron number, such as $^{67}$Cu and $^{177}$Lu. The reaction equation of $\beta^-$ decay is presented in *eq.1.2*:

$$ {}^{A}_{Z}X \rightarrow {}^{A}_{Z+1}Y + e^- + \bar{\nu}_e \qquad (eq.1.2) $$

The $\beta^+$ decay occurs to proton-rich atoms, for example $^{18}$F and $^{82}$Rb. The parent nucleus transfers to the daughter nucleus by emitting a positron ($e^+$) and an electronic neutrino ($\nu_e$). This process is explained in *eq.1.3*:

$$ {}^{A}_{Z}X \rightarrow {}^{A}_{Z-1}Y + e^+ + \nu_e \qquad (eq.1.3) $$

Electron capture (EC) is a process in which an electron in an inner orbital of the atom is captured by a proton (converting a proton into a neutron) and simultaneously emits a neutrino. This decay mode is in competition with $\beta^+$ decay. The process of electron capture is shown in *eq.1.4*:

$$ {}^{A}_{Z}X + e^{-} \rightarrow {}^{A}_{Z-1}Y + \nu_e \qquad (eq.1.4) $$

The γ decay and internal conversion occur when the daughter nuclides produced by α decay or β decay are in an excited state (the energy of the nuclide was not all carried away). To reach the ground state, unstable nucleons either emit the excitation energy by emitting one or several photons (γ decay) or transfer the excess energy directly to one of their own orbiting electrons and emit the electron from the atom (internal conversion). The process of γ decay and internal conversion are respectively presented in *eq.1.5* and *eq.1.6* [1]:

$$ {}^{A}_{Z}X^{*} \rightarrow {}^{A}_{Z}X + \gamma \qquad (eq.1.5) $$

$$ {}^{A}_{Z}X^{*} \rightarrow {}^{A}_{Z}X^{+} + e^{-} \rightarrow {}^{A}_{Z}X \qquad (eq.1.6) $$

Where ${}^{A}_{Z}X^{*}$ and ${}^{A}_{Z}X^{+}$ are the excited state and singly ionized stage of the nucleus ${}^{A}_{Z}X$, respectively.

Except for particles and photons, the emission of X rays and Auger electrons are also frequent for radionuclides who decay by electron capture and internal conversion coming from the rearrangement of the electron cloud, for example $^{99m}$Tc, and $^{123}$I.

For very heavy nuclides that have a high neutron-proton ratio, the spontaneous fission is also a decay mode for them. In this decay mode, the nucleus splits into two parts with different atomic numbers and atomic masses.

In some cases, the radionuclide does not have only one decay mode. In this case, we use the "branching ratio" to express the fraction of nuclei that decay in a single decay mode relative to the total number of decaying nuclei. For example, $^{149}$Tb (ground state) decays by α and electron capture, the branching ratios are 16.7% and 83.3% respectively.

For the radioactive element, the decay possibility for each nucleus is the same. Therefore, during the unit time, the decayed nuclei are proportional to the total number of nuclei. The law of radioactive decay can be expressed as *eq.1.7*:

$$ \frac{\mathrm{dN}}{\mathrm{dt}} = -\lambda \mathrm{N} \qquad (eq.1.7) $$

where N is the total nuclei number, t (s) is the decay time and λ ($s^{-1}$) is the decay constant of the radioactive element.

From *eq.1.7*, the number of the nuclei at time t, N(t), can be expressed as *eq.1.8*, which is also the radioactive decay law:

$$ \mathrm{N(t)} = \mathrm{N_0 e^{-\lambda t}} \qquad (eq.1.8) $$

where $N_0$ is the initial nuclei number.

To measure the decay rate, the "activity" of a radionuclide is defined, it is noted as Act. The relation of the activity and the nuclei number at any time "t" can be expressed as *eq.1.9*:

$$Act(t) = \lambda \mathrm{N(t)} \qquad (\mathrm{eq.}\ 1.9)$$

The unit of the activity is Becquerel (Bq) or Curie (Ci), and 1 Ci = $3.7 \times 10^{10}$ Bq.

The time required for half of the nuclei of a radionuclide to decay is called the half-life, note as "$T_{1/2}$". The relation between the half-life and the decay constant is shown in *eq.1.10*:

$$T_{\frac{1}{2}} = \frac{\ln 2}{\lambda} \qquad (eq.\ 1.10)$$

#### 1.1.1.2. Nuclear reaction and cross section

The nuclear reaction refers to a process that two nuclei or one nuclei and an external subatomic collide and produce one or more nuclides. A nuclear reaction can be expressed as *A(a,b)B*, where *A* is the target, *a* is the projectile, *b* is the ejectile and *B* is the produced nuclide. The amount of the energy released from the collision is called Q value. It is calculated as the *eq.1.11*:

$$\mathrm{Q} = (\mathrm{m_A} + \mathrm{m_a} - \mathrm{m_b} - \mathrm{m_B})\,\mathrm{c}^2 \qquad (eq.\ 1.11)$$

where $\mathrm{m_A}, \mathrm{m_a}, \mathrm{m_b}, \mathrm{m_B}$ (g) are respectively the mass of the target A, the projectile a, the emission b and the product B, and c (m/s) is the light speed. When the rest energy of the final state is lower than that of the initial state, the Q value is positive, and the nuclear reaction is an exothermic reaction. Spontaneous reactions have a positive Q value. On the contrary, the reaction is endothermic when Q value is negative and the reaction can only occur by adding energy, mostly in the form of the kinetic energy of the projectile. The minimal required energy is called the threshold energy.

To measure the probability of the occurrence of a given nuclear reaction, the reaction cross section is defined. It is expressed as a surface and is measured in $\mathrm{cm}^2$, the unit is barn (b), 1 b = $1\times10^{-24}$ $\mathrm{cm}^2$.

The cross section can be expressed as a function of the produced nuclei, the target nuclei and the ions of the beam. The formula is presented in *eq.1.12*:

$$\sigma\,(E) = \frac{N_{produced}}{N_{target} \times D} \qquad (eq.\ 1.12)$$

where $N_{produced}$ is the produced nuclei which can be estimated by measuring the activity, $N_{target}$ is the target nuclei which can be calculated by measuring the target density, and *D* is the ions of the beam which is proportional to the beam intensity.

The activity of the produced radionuclide is proportional to the cross section, it can be expressed as a function of the cross section σ(E). The formula is shown in *eq.1.13*:

$$\mathrm{Act} = \mathrm{I} \cdot \chi \cdot \frac{N_A . \rho}{A} \cdot \left(1 - e^{-\lambda t}\right) \int_{E_e}^{E_i} \frac{\sigma\,(E)}{\frac{dE}{dx}} dE \qquad (eq.\ 1.13)$$

Where:

$Act$ is the activity of nuclei produced (Bq), $I$ is the number of the projectiles per second hitting the target ($s^{-1}$), $\chi$ is the purity of the target (%), $N_A$ is the Avogadro number ($at \cdot mol^{-1}$), $\rho$ is the target material bulk density ($g \cdot cm^{-3}$), $A$ is the molar mass of the target nuclei ($g \cdot mol^{-1}$), $\lambda$ is the decay constant of produced nuclei ($s^{-1}$), $t$ is the irradiation time (s), $\sigma(E)$ is the cross section at the energy E ($cm^2$), $\frac{dE}{dx}$ is the linear energy transfer (LET) of the injected particle in the target ($MeV \cdot cm^{-1}$), $E_i$ and $E_e$ are respectively the incident and exit energies of particles passing through the target (MeV).

More details of the cross section calculation will be introduced in Chapter 4.

The production yield of a nuclear reaction reflects the amount of radioactive isotopes produced, it is usually expressed in terms of the radioactivity produced per integrated time beam current. The number of the produced nuclei $Y(t)$ by the nuclear reaction during an irradiation $t$ can be expressed as *eq.1.14* [2]:

$$Y(t) = tI_0 \int_{E_1}^{E_0} dE \left(\frac{1}{\rho}\frac{dE}{dx}\right)^{-1} \sigma(E)/(Ze) \qquad (eq.1.14)$$

where $I_0$ is the number of projectiles per second hitting the target ($s^{-1}$), $E_0$ is the incident beam energy impinging the target (MeV); $E_1$ is the beam energy after crossing the target (MeV), $E_1$ is zero while the charged particles remains in the target; $\rho$ is the density of the target ($g/cm^3$); $\frac{dE}{dx}$ is the linear energy transfer ($MeV \cdot cm^{-1}$); $\sigma(E)$ is the reaction cross section at energy E ($cm^{-2}$); $Z$ is the charged state of the accelerated ion; and $e$ is the elementary charge.

The produced nuclei $Y(t)$ can also be defined as:

$$Y(t) = tI_0 y \qquad (eq.1.15)$$

With $y$ the production yield. For a target with an enrichment $x$ ($0 < x < 1$), $y$ can be expressed as:

$$y = x \int_{E_1}^{E_0} dE \left(-\frac{1}{\rho}\frac{dE}{dx}\right)^{-1} \sigma(E)/(Ze) \qquad (eq.1.16)$$

The unit of the production yield is MBq/μAh.

### 1.1.2. Radionuclide imaging

Nuclear medicine imaging includes several techniques that use radionuclides to examine organ structure and function body for diagnostic and monitoring purposes. Typical imaging techniques are the Single-photon Emission Computed Tomography (SPECT), the Positron Emission Tomography (PET), and the hybrid of the former two with the Computed Tomography (CT) to benefit from complementary information. In opposite to other imaging technique which gives mainly morphologic information, such as CT or Magnetic Resonance Imaging (MRI), nuclear medicine imaging gives functional information. For example, the PET imaging can track biochemical changes and metabolic function in a patient; it can therefore be useful for studying bodily functions, determining how far a disease is spreading, and even detecting diseases before symptoms[3]. Radionuclides used for imaging are associated to gamma emission that are highly penetrating radiation that can be detected outside the body. These gamma rays are produced either directly during the radionuclide's decay or indirectly through the electron-positron conversion into a pair of 511 keV gamma ray. In most cases, these radionuclides are attached to a vector molecule to form a radiopharmaceutical that targets

cancer cells. In some specific cases, radionuclides can be used alone, for example, iodine in case of thyroid. The radionuclides used in radiopharmaceuticals should be nontoxic, carrier free, low cost and have a short half-life[4].

#### 1.1.2.1. The Single-Photon Emission Computed Tomography (SPECT)

The Single-photon Emission Computed Tomography (SPECT) is an imaging technique that uses γ rays to generate a 2D or 3D image of cross-sectional information of the body. The γ ray energy range for all radionuclides for SPECT imaging must be between 80 keV and 250 keV with an optimal value at 140 keV.

The SPECT imaging requires the patient to be injected with a radiopharmaceutical, and the labelled radionuclide should emit a γ ray. These γ rays will be detected and converted into light signals thanks to scintillators and photon transducers, and then transferred into electrical signals by semiconductors[5], the output is a projection of the tomography. To obtain a 3D SPECT image, a gamma camera should rotate 360° around the patient.

The main radionuclides used for SPECT imaging are $^{99m}$Tc (the most widely used in the world), $^{123}$I , $^{111}$In, , $^{67}$Ga and $^{201}$Tl[6]. Recently, $^{155}$Tb ($T_{1/2}$ = 5.32 d) has attracted attention for its suitable energy (Eγ = 87 keV (32%), 105 keV (25%)) [7]. The decay information of these radionuclides are shown in Table 1.1.

Table 1.1 Decay information of several SPECT radionuclides[8].

| Isotope | Half-life | Main γ energy (keV) | Intensity (%) |
|---|---|---|---|
| $^{67}$Ga | 3.3 d | 93.3 | 38.8 |
| | | 184.6 | 21.4 |
| $^{99m}$Tc | 6.0 h | 140.5 | 89 |
| $^{111}$In | 2.8 d | 171.3 | 90.7 |
| | | 245.4 | 94.1 |
| $^{123}$I | 13.2 h | 159.0 | 83.6 |
| $^{201}$Tl | 3.0 d | 167.4 | 10.0 |
| $^{155}$Tb | 5.3 d | 86.6 | 32.0 |
| | | 105.3 | 25.1 |
| | | 108.1 | 7.5 |

#### 1.1.2.2. The Positron Emission Tomography (PET)

The Positron Emission Tomography (PET) is a 3D imaging technique that uses radiotracers based on positron emitters to visualize and monitor organ function, metabolic process, and absorption process in 3D.

The emitted positron will slow down by interacting with the body and when almost at rest will interact with an electron in the organism. These electron/positron pair annihilates producing a pair of 511keV photons emitted in almost back-to-back directions[9]. Thanks to a ring of scintillation detectors, these photons are detected by the two opposite detectors and at the same time they will be recorded (coincidence detection)[10]. Each recorded pair allows defining a line of response. Using complex algorithms, it is then possible to reconstruct the original distribution of the radiopharmaceuticals in the patient's body[11].

The most used PET radionuclide is $^{18}F$ [12]. Meanwhile, several metal radionuclides have also been studied as PET isotopes, such as $^{64}Cu$, $^{68}Ga$, $^{82}Rb$, and $^{89}Zr$ [9]. In addition, the $^{152}Tb$, as a positron emitter, is considered as an interesting candidate for PET and a first study has already been conducted in mice[13]. The conventional radionuclides, $^{11}C$, $^{13}N$, $^{15}O$, and $^{18}F$, have a branching ratio close to 100%; on the contrary, other radionuclides, especially for $^{64}Cu$, $^{89}Zr$, and $^{152}Tb$, have smaller branching ratios (less than 25%). The branching ratio indicates the proportion of nucleus of the radionuclide emitting positron, so for radionuclides having lower branching ratio, the injection dose needs to be increased to collect enough photons. Radionuclides such as $^{11}C$, $^{18}F$, $^{64}Cu$ and $^{89}Zr$, their mean positron energies are relatively small (smaller than 0.4 MeV); on the contrary, $^{82}Rb$ and $^{152}Tb$ have bigger mean positron energy. Experiments show that the increase of mean positron energy can induce the decrease in image accuracy[14]. The decay information of these radionuclides is shown in Table 1.2. The half-lives of these radioisotopes are usually short to minimize exposure to the patient, but long enough to allow the drug to find its target.

Table 1.2 Decay information of several PET radionuclides[8].

| Isotope | Half-life | $\beta^+$ decay branching ratio (%) | Mean $\beta^+$ energy (MeV) |
|---|---|---|---|
| $^{11}C$ | 20.4 min | 99.8 | 0.39 |
| $^{13}N$ | 10.0 min | 99.8 | 0.49 |
| $^{15}O$ | 122.2 s | 99.9 | 0.74 |
| $^{18}F$ | 109.8 min | 96.7 | 0.25 |
| $^{64}Cu$ | 12.7 h | 17.5 | 0.28 |
| $^{68}Ga$ | 67.7 min | 88.9 | 0.74 |
| $^{82}Rb$ | 1.3 min | 95.4 | 1.41 |
| $^{89}Zr$ | 78.4 h | 22.7 | 0.39 |
| $^{152}Tb$ | 17.5 h | 20.3 | 1.14 |

#### 1.1.2.3. Hybrid imaging: PET/CT and SPECT/CT

Although SPECT and PET have significant advantages in imaging, they also have certain limitations, such as the lack of anatomic details. Therefore, hybrid imaging, a combination of several imaging techniques, has been developed in the past twenty years[15]. Nowadays, PET and SPECT have been more and more combined with CT imaging. CT is another imaging technique that uses X-rays taken from different angles and then generates a cross-sectional body image by a computer. CT images give accurate morphologic images allowing to detailed size, shape, and location of concerning structure.

The SPECT/CT hybrid imaging was first developed in 1991, the first commercial system was launched in 2000, and it has been widely established in clinical practice in the past decade[15]. This hybrid has improved the correction of attenuation of SPECT and the accuracy in identifying anatomical structures[16].

The PET/CT hybrid imaging emerged in the early 2000s, it is firstly proposed by Beyer et al.[17]. The combination of PET/CT ensures both the identification of normal or abnormal uptake of radiotracer (PET) and the accuracy of anatomic details (CT).

### 1.1.3. Radiation therapy

Radiation therapy is one of the cancer treatments that use ionizing radiation to destroy tumors. It is usually used in combination with surgery and/or chemotherapy to treat patients. High-energy radiation can damage the DNA of cells and prevent their ability to divide and proliferate further. Although radiation damages normal and cancer cells, the goal of radiation therapy is to maximize the radiation dose to abnormal cancer cells while minimizing that on normal cells. There are two main types of radiation therapy, external radiation therapy (teletherapy or radiotherapy) and internal radiation therapy (radionuclides therapy). In external radiation therapy, radiation are generated outside the patients (thanks to accelerators or radioactive sources) and are sent to the tumor site, while in radionuclides therapy, a systemic injection of a radionuclide labeled to a vector is performed to bring the radiation source as close as possible to the cells to destroy.

#### 1.1.3.1. External radiation therapy

External radiation therapy (ERT) uses a direct radiation beam outside the body to destroy the tumor in specific places. The most used irradiation beams in ERT are X-rays photons obtained by Bremsstrahlung from electron beams. Few facilities are devoted to protons (only 3 proton-therapy centers in France[18]) or carbon ions (only 1 carbon-therapy center in France being built at the moment). Some sealed sources can also be used to provide γ rays, such as $^{60}$Co that is used in the gamma knife, or $^{137}$Cs which is still in used in developing countries. The advantage of external radiation therapy is that it is non-invasive and works well; nonetheless, the biggest limitation is that the radiation beam interact with normal tissues before reaching the target[19] and it is not adapted to treat disseminated disease.

#### 1.1.3.2. Radionuclides therapy

Applications of non-sealed radionuclides for internal therapy have been developed for decades. Radionuclides therapy is a targeted therapy that uses chemical properties or biological properties to guide radionuclides to a place of interest (tumors), and then deliver a great amount of energy through the decay of the radionuclides that can destroy tumors.

Radiations used in radionuclides therapy must strongly interact with matter to deliver as much energy as possible over a short distance. This is why charged particles, such as α particles, β particles, Auger electrons or conversion electron[20], are used. Each of these particles has a different range and linear energy transfer (LET) value leading to various relative biological effectiveness (RBE)[21]. The LET corresponds to the rate of energy transfer per unit length of track (keV/µm); it decreases as particle energies increases.

The range of the various type of particles is presented in Fig. 1.1 along with its translation of the size of biological objects[22]. Auger emitters (such as $^{111}$In and $^{123}$I) have low energy (10 eV-10 keV), the radiation can be highly localized in a small volume (nucleus size) and kill cells by damaging the cell membrane[23]. The range of α particles emitted by decay can be up to 100 µm for an energy range of 4-8 MeV. This corresponds to high LET values and a maximum distance of action of several cell diameter. Radionuclides emitting $\beta^-$ particles have a longer range (more than 1 mm) and lower energy (less than 1 MeV in most caces) leading to low LET values. In this case, cross-fire technique is used to bring enough energy to kill cancer cells.

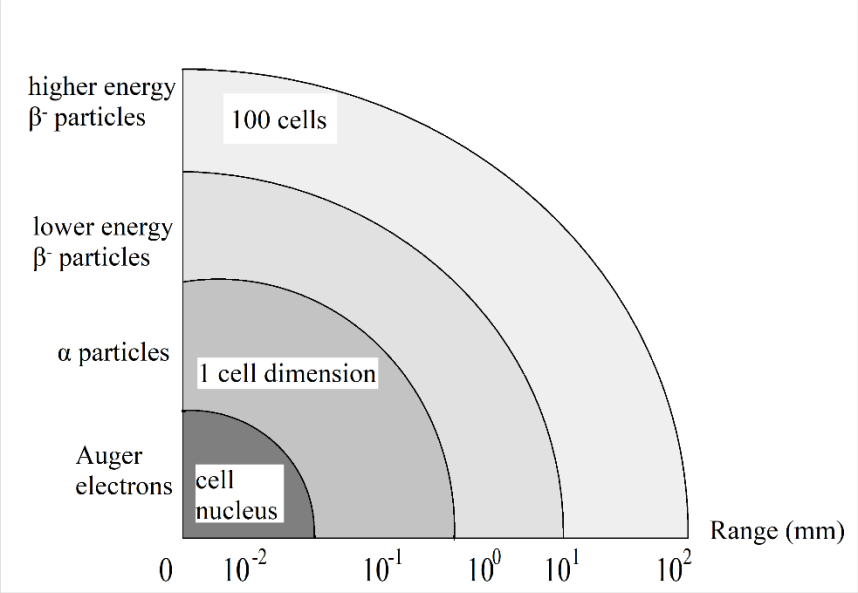


Fig. 1.1 Comparison of action positions and ranges of different particles[22]

The choice of the radionuclide depends on its decay properties[22] and half-life. Generally, the half-lives of these radionuclides should not be too long (hours or days), and their daughters should be stable or have a very short half-life.

### 1.1.4. Theranostics

The term theranostics is defined as the combination of a diagnostic test with a therapeutic process. In nuclear medicine, the theranostics approach is quite straightforward as it can be obtained by just changing the radionuclide that is used, keeping the same vector[24]. The main idea behind the theranostics is to determine patient's response to a specific drug, to track the initial results of treatment, and finally personalize and adapt the treatment for the patient. For this purpose, a radionuclides pair from the same element or from element having similar chemical properties can be applied: the first one being used for imaging (PET or SPECT) the second one for therapy (α, $\beta^-$, Auger or conversion electron).

This concept was first proposed in 1990s by Herzog et al.[25] using the $^{86}Y/^{90}Y$ pair. The $\beta^+$ emitting radionuclide $^{86}Y$ was chosen to combine the $\beta^-$ emitting radionuclide $^{90}Y$ for the treatment of breast cancer. Since then, several radionuclide combinations of the same element have been considered as good candidates for theranostics, such as $^{44g}Sc/^{47}Sc$, $^{64}Cu/^{67}Cu$, $^{83}Sr/^{89}Sr$, $^{124}I/^{131}I$, and $^{152}Tb/^{161}Tb$[26]. These combinations are characterized by the fact that the first radioisotope is $\beta^+$ emitters and the second radioisotope is $\beta^-$ emitters. The advantage of this combination is that chemical properties of the radionuclide pair are the same, which facilitates subsequent pharmacological studies. However, these radionuclides are not all available, several isotopes, such as $^{47}Sc$, $^{83}Sr$ and $^{152}Tb$, are not commercially available yet[26].

Thus, the concept of theranostics has been extended in recent years to use chemically similar isotope pairs to replace unavailable isotope pairs. A typical example is the combination of the $\beta^+$ emitter $^{68}Ga$ and the $\beta^-$ emitter $^{177}Lu$ [27–29]. The $^{68}Ga$ is mainly produced by the $^{68}Ge/^{68}Ga$ generator or by cyclotrons while the $^{177}Lu$ ($T_{1/2}$ = 6.647 d) is mainly produced by nuclear reactors through the production route $^{176}Lu(n,\gamma)^{177}Lu$ or $^{176}Yu(n,\gamma)^{177}Yb \rightarrow ^{177}Lu$ [30]. Studies have shown the benefit of this $^{68}Ga/^{177}Lu$ combination on prostate cancer[24,27,28] treatment.

In summary, the theranostics paradigm allows to move to a more personalized medicine that should provide a better treatment to patient.

## 1.2. Radionuclide production in nuclear medicine

As the first step in nuclear medicine treatment, the production and supply of radionuclides play a decisive role in the development of a radiopharmaceuticals and the selection of treatment options. Most of the radionuclides are produced through a nuclear reaction between a stable isotope (the target) and a projectile that can be either a neutron or a charged particle (eg: protons, deuterons, α particles). In the first part of this section, the various radionuclide production routes will be presented. Then, principles of targetry and different types of targets will be introduced.

### 1.2.1. Various radionuclide production routes

#### 1.2.1.1. Reactor production

The use of nuclear reactors to produce radioisotopes has been developed since the WW2. According to IAEA, there are 223 operational nuclear research reactors in 2022, and 82 of them are used for regular isotope production[31] making them essential for the availability of medical radionuclides.

Two types of nuclear reactions are involved for radionuclides production: nuclear fission and neutron capture.

Nuclear fission is a process in which a heavy nucleus splits into smaller nuclei fragments along with the release of energy. Few nuclei can encounter spontaneous nuclear fission, but in most cases, neutrons are used to induce nuclear fission. The most commonly used heavy nucleus in which nuclear fission is induced is $^{235}U$. $^{235}U$ targets are irradiated on research nuclear reactor to produce $^{99}Mo$, the mother nucleus of $^{99m}Tc$ that is widely used in SPECT imaging, $^{131}I$ that is used to treat thyroid cancers, and other radionuclides such as $^{133}Xe$ and $^{137}Cs$. The fission yield as a function of fission product number is shown in Fig. 1.2 according to the work of Hasan and Prelas[32].

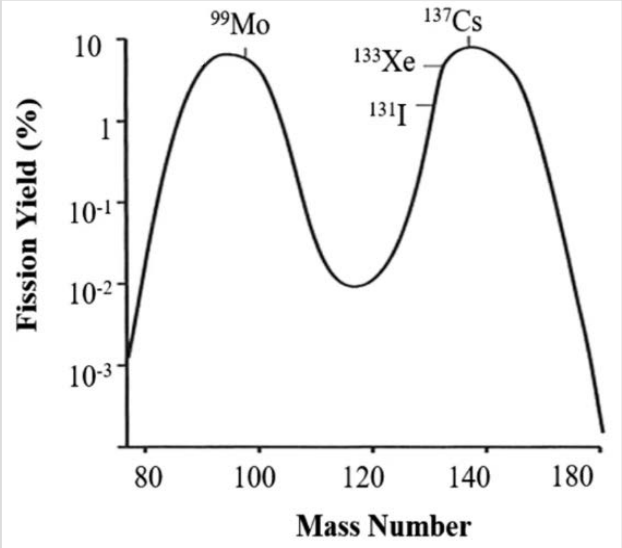


Fig. 1.2 The fission yield of thermal neutron fission of $^{235}U$ as a function of product mass number. Image presented by Hasan and Prelas[32].

More than 90% of the reactor produced $^{99}Mo$ is produced by the fission of the highly enriched uranium, but some $^{99}Mo$ can also be produced by accelerators[33].

Neutron capture is another production route in nuclear reactor. It refers to the reaction where a nucleus captures a neutron to generate an isotope of the same element and emits γ photon, or to generate an isotope of different element and emits proton or alpha particles. The energy to release these nucleons comes from a part of the kinetic energy of the projectile and a part of binding energy of the target and the residue. Examples of the production routes are $^{98}Mo(n,\gamma)^{99}Mo$, $^{50}Cr(n,\gamma)^{51}Cr$, $^{14}N(n,p)^{14}C$, and $^{67}Zn(n,p)^{67}Cu$ [34].

Although nuclear reactors are currently the mainstream of radionuclide production, their shortcomings are also obvious. On the one hand, this production route creates some long-lived radioactive wastes, such as $^{99}Tc$. On the other hand, target materials are firstly sealed and placed in the core of the reactor for irradiation and then transported to the radioisotope processing laboratories[35]. Constrained by the limited distribution of reactors, transportation may last for several days, and the activity of short-period radionuclides will be greatly reduced by decay. In addition, most of the reactors are the product of the last century, and although the total number of reactors in the world to date exceeds 800, there are as many as 513 reactors currently in decommissioning or have been decommissioned[31]. The distribution of young reactors (less than 40 years) used for isotope production is shown in Fig. 1.3[31], it can be seen that there are only 24 reactors in the world and only one in Western Europe (FRM II in Germany).The reduction in reactors can also create a shortage of some radioisotope supplies. However, Nuclear reactors produce neutron-rich nuclei that are not accessible by other means of production. They are therefore essential and complementary to the accelerators.


Fig. 1.3 Distribution of research reactors less than 40 years and used for isotope production[31], The numbers in the figure represent the number of reactors.

### 1.2.1.2. Accelerator production: Cyclotron

A cyclotron is a kind of accelerator that uses a static magnetic field to spin charged particles and an alternating electric field to accelerate them. For medical radionuclide production, the projectile energy is relatively low (normally < 100 MeV). This techniques has been invented in

1934 in the USA[36] and developed rapidly over the past few decades. According to IAEA, there were more than 700 cyclotron facilities in 2006[37] and this number has doubled in 2021[38]. The distribution of cyclotrons for medical radionuclide production in the world in 2022 is shown in Fig. 1.4. The cyclotron facilities are distributed to all over the world. The popularity and the rapid growth of cyclotrons have boosted the development of the radionuclide production. Nowadays, from 10% to 12% of radiopharmaceuticals in the world are produced in cyclotrons[39].

Fig. 1.4 The distribution of cyclotrons for medical radionuclide production in the world in 2022[38].

The principle of cyclotron route is to accelerate charged particles to a certain energy, and use the interaction of the target nucleus and the accelerated particles to produce radionuclides[40]. Examples of cyclotron produced radionuclides and their production information are listed in Table 1.3 [41–43]. According to the table, the energy required for the production is only a few mega-electronvolts (MeV) or tens of mega-electronvolts, these energies are accessible for many biomedical cyclotrons.

Table 1.3 Cycltron produced radionuclides and production information.

| Radionuclide | Half-life | Production route | Energy range (MeV) |
|---|---|---|---|
| $^{44}$Sc | 3.9 h | $^{44}$Ca(p,n) | 8-13 |
| $^{64}$Cu | 12.7 h | $^{64}$Ni(p,n) | 9-14 |
| $^{68}$Ga | 67.7 min | $^{66}$Zn(p,n) | 8-13 |
| $^{86}$Y | 14.7 h | $^{86}$Sr(p,n) | 10-14 |
| $^{89}$Zr | 78.4 h | $^{89}$Y(p,n) | 10-14 |
| $^{124}$I | 4.2 d | $^{124}$Te(p,n) | 8-12 |

An advantage of cyclotron production route is that, in general, the target nucleus and the produced radionuclide are different chemical element, which makes it easier to separate them by chemical or physical properties leading to non-carrier added form. In addition, it is possible to reduce the coproduction of impurities by selecting the proper projectile and/or the energy window[38]. Another advantage of the cyclotron is that many biomedical cyclotrons are located

near the medical center; the transport time can be much reduced. However, highly enriched targets are often required for the production, many of them are expensive, this is a shortcoming for cyclotron production route.

#### 1.2.1.3. Accelerator production: spallation reactions

At low energy, the wavelength of the projectile is of the order of the nucleus size, as the energy increases, the wavelength decreases and can reach to the size of a nucleon. When such high-energy (more than 100 MeV) particles bombard heavy nuclei, the projectile sees the nucleus as an independent set of nucleons. The interaction leads some of the nucleons to be "stripped," or bombarded out, this process is called spallation. The bombarded atoms heat up, break up into lighter nuclei, and release large numbers of neutrons. Spallation production route uses highly accelerated particles to produce radionuclide of interest.

Currently, isotopes are produced mainly by bombarding thick natural targets with high-energy protons, generating a beam of low-energy secondary ions and subsequent electromagnetic mass separation[44]. This production technique is called Isotope Separation On-Line (ISOL). The operating are mainly located in Europe and North America, such as CERN-ISOLDE, GANIL-SPIRAL (France) and TRIUMF-ISAC (Canada)[45]. Among them, CERN-ISOLDE (Switzerland) is the most productive facility, and it has an associated facility specifically devoted for the production of radionuclides for medical applications, the CERN-MEDICIS facility. Natural or enriched targets are irradiated by high-energy particles at CERN, the material of the target can be $^{nat}$Ti, $^{nat}$Ta and uranium carbide ($UC_x$). Then the irradiated targets are heated to high temperatures (700-2000°C) and ionized, different atoms will be separated by a mass separator, and the radionuclides of interest will be then collected and sent to the radiochemistry separation process[46,47]. As a specialized facility, the CERN-MEDICIS also allows to mass separate targets irradiated at other facilities, such as ILL ($^{169}$Er and $^{174}$Yb) or ARRONAX ($^{155}$Tb). The information of several radionuclides produced or to be produced is listed in Table 1.4[46]. For $^{155}$Tb and $^{225}$Ac, their targets use natural materials, which are much cheaper than targets used in other production routes (eg. cyclotron production route needs enriched targets).

Table 1.4 Information of radionuclides produced or to be produced at CERN-MEDICIS [46].

| Radionuclide | Half-life | Target material | Ion source |
|---|---|---|---|
| $^{155}$Tb | 5.3 d | $^{nat}$Ta/$^{nat}$Gd | W/Re/MELISSA |
| $^{225}$Ac | 9.9 d | $UC_x$ | Re |
| $^{165}$Tm | 30.1 h | $^{nat}$Ta | Re |
| $^{169}$Er | 9.4 d | $^{168}Er_2O_3$ | W/Re/MELISSA |
| $^{175}$Yb | 4.2 d | $^{174}Yb_2O_3$ | W/Re/MELISSA |

The advantage of the spallation route is that it produces many non-conventional radionuclides with a very high production level (up to GBq), such as the production of $^{149}$Tb (estimated about 10 GBq)[44]. However, this production route has many problems. First, the intranuclear cascade occurs because of the high energy of the incident particles and the secondary nucleons generated by the primary collisions have high energy, and will collide with the remaining nucleons to generate second-generation nucleons, and so on (Fig. 1.5). As a result, many residual nuclides

can be found as impurities. As an example, Fig. 1.6 shows the possible produced nuclides through the spallation reaction of $^{238}U$ and 1 GeV of proton. The nuclides in red color represent nuclides that are more possible to be produced. So for the production of $^{225}Ac$, since the target is $UC_x$, many impurities are produced due to intranuclear cascade in uranium and it makes it difficult to separate the radionuclide of interest. This is especially true for isotopic impurities. An example of the production of Tb isotopes will be presented in section 1.3.1.2.. In addition, this production route is limited by the very few number of facilities.

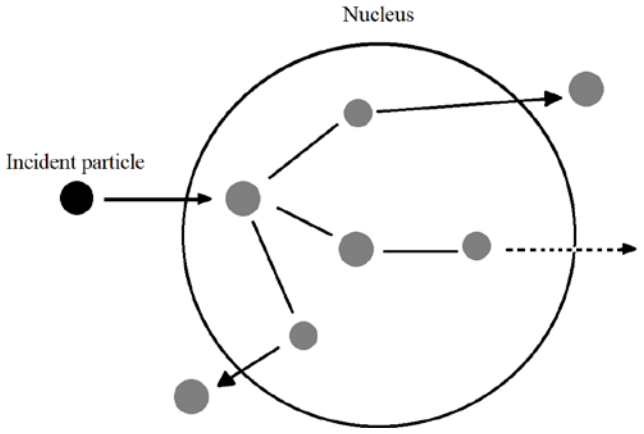


**Fig. 1.5 Schematic diagram of the internuclear cascade.**

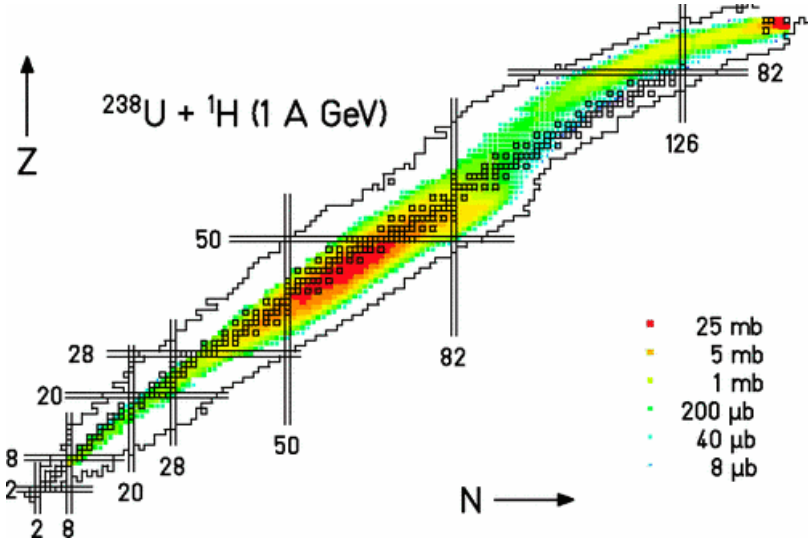


Fig. 1.6 Possible produced nuclides through the proton-induced spallation reaction on $^{238}U$. The figure was down by Armbruster et al.[48].

### 1.2.1.4. Radionuclide generator

A radionuclide generator system is made of a long-lived mother radionuclide that decays to a daughter radionuclide having a much shorter half-life. The mother radionuclide can be created from uranium fission products ($^{99}Mo/^{99m}Tc$ [49]) or decay products ($^{225}Ac/^{213}Bi$ [50]) or from cyclotron ($^{68}Ge/^{68}Ga$, $^{82}Sr/^{82}Rb$, and $^{62}Zn/^{62}Cu$ [51–53] ). A radionuclide generator is a self-contained device that holds the mother/daughter radionuclides' mixture in equilibrium. Depending on the half-life of the mother radionuclide, two kinds of equilibriums can be established between the mother and the daughter radionuclide: transient equilibrium and secular equilibrium. The mother radionuclide decays significantly during transient equilibrium while essentially not during secular equilibrium. Fig. 1.7 shows an example of transient equilibrium

of $^{99}Mo/^{99m}Tc$ (Fig. 1.7 (1a)) and an example of secular equilibrium of $^{81}Rb/^{81m}Kr$ (Fig. 1.7 (2a)) [54].

The mother radionuclide is adsorbed on a support that do not adsorb the daughter created from the decay. The process of removing the daughter radionuclide is called elution. One method to elute the generator system is to use the column chromatographic, for example for $^{99}Mo/^{99m}Tc$ generator, the $^{99}MoO_4^{2-}$ is absorbed on alumina to form molybdate, and the generated $^{99m}TcO_4^-$ can be washed off since it is difficult to be bound by the alumina[55]. Except for the column chromatographic method, other methods can also be used to separate the parent radionuclide and the daughter radionuclide according to their chemical properties. For example, pyrogallol-formaldehyde resins can be used to separate $^{68}Ge$ and $^{68}Ga$ since it has a strong adsorption capacity for Ge [56]. Other method such as precipitation, solvent extraction and electrodeposition can also be used to separate radionuclides with different solubility, hydrophobicity and electrochemical potential, respectively[55]. Once the daughter radionuclide is recovered, its activity will accumulate and increase again until reach a new equilibrium. Fig. 1.7 shows the relative activity of mother/daughter after each elution for generators under transient equilibrium (Fig. 1.7 (1b)) or under secular equilibrium (Fig. 1.7 (2b)).

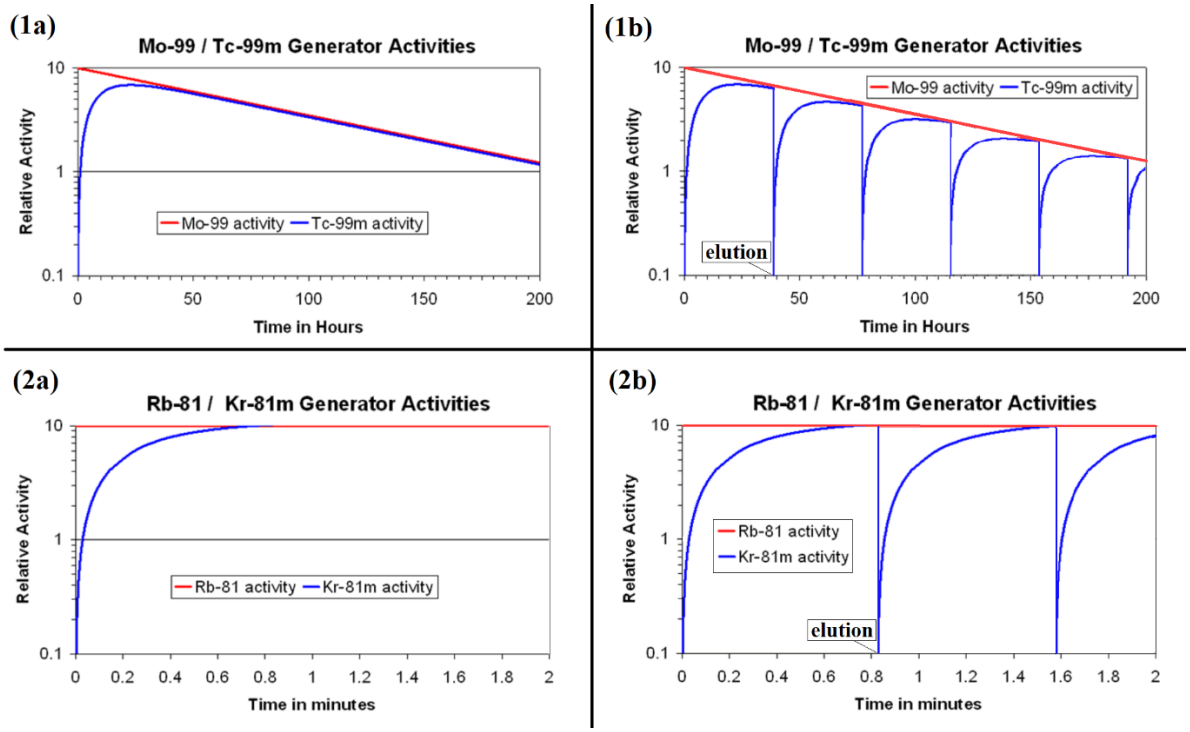


Fig. 1.7 Equilibrium between mother and daughter radionuclides: (1a) transient equilibrium between $^{99}Mo$ and $^{99m}Tc$; (1b) relative activity of $^{99}Mo$ and $^{99m}Tc$ after each elution; (2a) secular equilibrium between $^{81}Rb$ and $^{81m}Kr$; (2b) relative activity of $^{81}Rb$ and $^{81m}Kr$ after each elution. Figures modified based on figures from IAEA[54].

One big advantage of the generator is that it solves the transportation issue of short-period radionuclides. Meanwhile, limited supply of parent radionuclides is a shortcoming of this production route. In addition, the service life of generator is limited by the activity and purity of daughter radionuclide. The shelf life for $^{99}Mo/^{99m}Tc$ generator is less than 2 weeks while that for $^{82}Sr/^{82}Rb$ generator is from 6-8 weeks[57].

### 1.2.2. Targetry system

From the formula of the production yield (eq.1.16), it can be seen that the nuclear reaction (projectile and cross section) and the target material affect the production. Therefore, to improve the production yield, in addition to the production route, the study the targetry system is also important. The physical form of the target material, the encapsulation material and the method of encapsulation are all aspects of targetry system. The main goal of the targetry is not only to introduce the target materials to the beam and maintain them during the irradiation process, but also to collect easily the produced radionuclide[35].

This subsection will introduce three types of target forms and the encapsulation design.

#### 1.2.2.1. Solid targets

Solid target is a commonly used target form for the production of radioisotopes, especially for heavier atoms. Solid targets can not only be used for the measurement of reaction cross sections, but also for the mass production of radioisotopes.

A good solid target should meet at least the following requirements[58]:

- Under irradiation, the temperature of the target will increase because of the interaction of radiation with matter. This temperature should be at least several tens of degrees below its melting point.
- The target should be homogeneous, smooth, dense and stress free to keep the energy loss uniform in the surface and to improve the production yield.
- If the target materials are deposited or sputtered on a substrate, it should have good adherence to prevent shedding during irradiation, cooling or post-processing.
- The production efficiency of the target needs to meet the economic conditions, that is, lower production costs and higher production yield.

To meet these requirements, many manufacturing methods have been developed linked to the properties of the target element and the conditions required for irradiation. These methods can be classified as 3 types[59]:

- Mechanical method: mechanically reshape or reassemble target material, such as pelletizing method[60], cold rolling method[59], and the High energy Vibrational Powder Plating (HIVIPP) method[61];
- Physical method: using the phase transition of materials to make targets, such as levitation heating and melting[59], magnetron sputtering (MS)[62], and evaporation under vacuum [63];
- Chemical method: using chemical reactions to change the state of target materials, such as electrodeposition method[64].

Principles and remarks on several manufacturing methods are listed in

Table 1.5. For thin target preparation, the HIVIPP, the electrodeposition, and the MS methods can be applied; while for thick target, the magnetron sputtering and the pelletizing methods are more suitable. Thin target can be used for cross section measurement and thick target can be used for mass production.

Table 1.5 Principles and remarks of several target manufacture methods.

| Method | Principle | Remarks |
|---|---|---|
| Electrodeposition | Applying an electric field to deposit target ions in the electrolyte to the electrode. | Raw materials should be conductive;<br>Normally thin thickness (<20μm)[64] but the thickness can reach to 1 mm.<br>High efficiency: 80 – 90% |
| HIVIPP | Applying a voltage causes the particles to move to an electrode. | Metallic raw materials;<br>Thin thickness (<20 μm)[65];<br>Long time (several hours)[65].<br>High efficiency: > 95% |
| MS | Hit the target atoms with high-energy particles to knock them off the surface. | Large thickness variable range (0.1 μm- 1 mm)[62];<br>Low efficiency: 20-30%[59]. |
| Pelletizing | Pressing the target powder to form a pellet. | Thick thickness (> 100 μm);<br>Excluded for very hard materials.<br>High efficiency: > 90% |

Solid targets are much denser than liquid and gas targets, resulting in higher production yields. Meanwhile, additional steps after radiation, such as the dissolution of the irradiated target, and the recovery and recycling of enriched materials, may result in high costs and complex operating procedures[66].

#### 1.2.2.2. Liquid targets

Liquid and gas targets are usually used for low atomic weight target elements, as these elements naturally exist in liquid or gas form. A typical example for liquid target is the enriched $^{18}O$ water for the production of $^{18}F$ radionuclide[37] through the reaction $^{18}O(p,n)^{18}F$.

However, heavier element can also under liquid or gas form. In recent years, the use of liquid targets to produce metal radionuclides has emerged[67–69]. Typically, these liquid targets are a salt solution containing the target metal elements or liquid metals, such as enriched $^{68}ZnCl_2$ solution for the production of $^{68}Ga$ [68], yttrium nitrate salts for the production of $^{89}Zr$ [70], and liquid rubidium for the production of $^{82}Sr$ [71].

Compared with solid targets, liquid targets do not need to be dissolved after irradiation, and liquid targets can be irradiated multiple times[66]. Even though the production yield is smaller with liquid targets, the design of liquid or gas targets allows reuse of many existing accelerators that do not possess solid target station. However, the radiolysis of water in liquid targets needs to be considered because it may generate $H_2$ gas or $H_2O_2$ strong oxide[67,69]. Therefore, the beam current is often limited during irradiation. In addition, liquid targets have stricter requirements

for sealing[37]. Since the boiling temperature for water is 100°C at air condition, high pressure is necessary to avoid the boiling.

#### 1.2.2.3. Gas targets

The gas target is mainly composed of a gas container, an entrance window and the gas material in it. In general, a cooling system is also necessary.

Examples for this type of gas targets are listed as follows[37]:

- $^{14}N$ or $^{15}N$ gas: for the production of $^{15}O$ with deuterons or protons, respectively;
- $^{18}O$ or $^{20}Ne$ gas: for the production of $^{18}F$ with protons or deuterons, respectively.

Some noble gases can also be used as targets, examples are listed as follows[37]:

- $^{82}Kr$ gas: for the production of $^{81}Rb$ with protons[72];
- $^{124}Xe$ gas: for the production of $^{123}I$ with protons[73].

Similar to liquid targets, gas targets also have strict air tightness requirements[37,74].

#### 1.2.2.4. Encapsulation design

Normally, solid targets are installed in a "rabbit" system (transfer shuttle) and gas or liquid targets uses capillaries to move material between hot cells and the irradiation vault. All targets need to be cooled down during the irradiation.

For gas and liquid target, it is necessary to have a container to limit the target materials, so the encapsulation process is mandatory. Meanwhile, for solid target, the encapsulation is also important. On the one hand, because the target has a risk of melting under irradiation, on the other hand, because most targets are cooled by being immersed on all sides in the cooling water (except for a solid target deposited on a substrate which is only cooled at the back), encapsulation can ensure that the target is not contaminated by cooling water.

The material of the encapsulation needs to meet the following properties[37]:

- Good thermal conductivity;
- Stable chemical reactivity during irradiation;
- Not too active after irradiation, or the production of radionuclide is limited in case of direct transportation in capsule ;
- Ease of manufacture/fabrication;
- Good mechanical strength;
- Low price.
- Easy to open in order to recover the target material after irradiation

Examples for several common used materials and their properties are listed in Table 1.6. The table is referred to the IAEA "radioisotopes and radiopharmaceuticals series" publication[37].

- Most of these materials have a high melting point, especially for Nb (2410°C) and Ti (1725°C). Higher melting point ensures that the material can resist higher beam intensities.
- The "thermal conductivity" measures the ability of the material to transfer heat. High thermal conductivity materials, such as silver, copper, and aluminum, are more likely to dissipate heat from the target.
- The "produced radionuclides" shows possible radionuclides produced by the material under irradiation of proton or deuteron beam. Only proton and deuteron are considered because these are the most common particles in medical cyclotrons (even if alpha

particles are used for the production of $^{211}$At and $^{97}$Ru). Of all the radionuclides produced in encapsulation material, most have short half-lives (<100 d), except for $^{109}$Cd (461.4 d), $^{65}$Zn (243.9d), $^{22}$Na (2.6 y), $^{93}$Mo (4000 y), and $^{57}$Co (271.7 d)[8] produced by silver, copper, aluminum, niobium and stainless steel, respectively.

- The "tensile strength" is the maximum stress that a material can withstand before breaking when it is allowed to stretch or pull. Materials with high tensile strength are not prone to breakage, such as stainless steel.

Table 1.6 Thermal conductivity and nuclear activation of several encapsulation materials[37].

| Material | Melting Point (°C) | Thermal conductivity ($W \cdot m^{-1} \cdot K^{-1}$) | Produced radionuclides | Tensile strength (MPa) |
|---|---|---|---|---|
| Silver | 961 | 429 | $^{107,109}$Cd | 140 |
| Copper | 1085 | 398 | $^{62,65}$Zn, $^{56,58}$Co | 220 |
| Aluminum | 660 | 237 | $^{22,24}$Na | 90 |
| Nickel | 1455 | 98 | $^{56,58}$Co, $^{64}$Cu | 45 |
| Niobium | 2469 | 54 | $^{93}$Mo | 275 |
| Titanium | 1668 | 17 | $^{46}$Sc, $^{48}$V | 240 |
| Stainless steel | 1400-1530 | 15 | $^{55,56,57}$Co | 621 |

The encapsulation techniques are different for targets; the design depends not only on their physical forms, but also on their chemical properties. It is also strongly linked to the target station and the cooling system available at the cyclotron facility.

For many solid targets, the encapsulation consists mainly to wrap the sheet-shaped target in the packaging material by welding. The main techniques are cold indentation welding, electron beam welding and laser welding[75]. These techniques mainly use high pressure, electron beam or laser to plastically deform the wrapping material for welding.

For liquid and gas targets, the target station can be divided into at least 3 parts: the entrance window (usually in Havar foils), the target chamber, and the cooling system (one side or several sides).

## 1.3. The Terbium family and how to make them available

### 1.3.1. Radionuclides of interest: terbium radionuclides

As mentioned before, several radionuclides of the terbium family are considered as competitive candidates in nuclear medicine.

For therapy, the $^{149}$Tb, with a relatively short half-life ($T_{1/2}$ = 4.1 h) and low alpha energy (Eα = 3.97 MeV), has been proposed as a candidate for targeted alpha therapy[76]. The radionuclide $^{161}$Tb, as a low-energy $\beta^-$ and Auger electron emitter with a relatively short half-life (6.95 days[77]), has been studied as an alternative to $^{177}$Lu because of their similar chemical behavior and decay characteristics. In fact, theoretical simulations and recent clinical studies prove that $^{161}$Tb is very suitable to be applied in β-therapy[78,79].

For diagnostic, the $^{152}$Tb, as a $\beta^+$ emitter, can be used in PET imaging because of two end-point $\beta^+$ energies 2620 keV (5.9%) and 2970 keV (8%). Moreover, as explained in subsection 1.1.4, the $^{155}$Tb can be used for SPECT imaging and Auger therapy because it is a γ and Auger emitter.

Therefore, the pair $^{152}$Tb/$^{161}$Tb, $^{152}$Tb/$^{149}$Tb, $^{155}$Tb/$^{161}$Tb, $^{155}$Tb/$^{149}$Tb and even the single $^{155}$Tb have a great application potential in theranostics.

Terbium is like a Swiss knife in theranostics, however, applications of Tb radionuclides are limited nowadays because of their low availabilities. Several existing and envisioned production routes will be introduced and compared in this subsection.

#### 1.3.1.1. Production of $^{161}$Tb by nuclear reactors

Nuclear reactors are considered as the tool to produce $^{161}$Tb. The relative reaction is $^{160}$Gd (n, γ)$^{161}$Gd → $^{161}$Tb (Fig. 1.8). This route is feasible because the half-life of $^{161}$Gd is only 3.66 min while the half-life of $^{161}$Tb is 6.89 d.

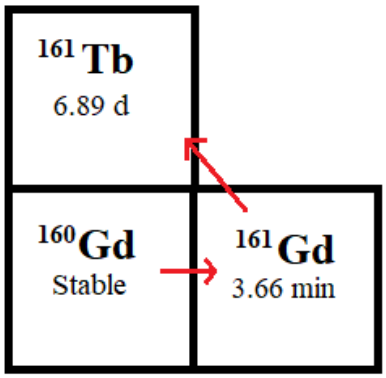


Fig. 1.8 Production route of $^{161}$Tb in nuclear reactors.

According to the work of Lehenberger et al[80], highly enriched (98.2%) $^{160}$Gd targets were irradiated by a thermal neutron flux ($10^{14}$-$10^{15}$ neutrons cm$^{-2}$ s$^{-1}$) during several days (14 days). After 5 days of cooling, the $Gd^{3+}$ and $Tb^{3+}$ are separated by column chromatography. The production of $^{161}$Tb can reach to 2.1 TBq/mg after 24 days of cooling and transport. Despite an indirect production route, the production yield of $^{161}$Tb is considerable. The cross section of the reaction $^{160}$Gd (n, γ)$^{161}$Gd is 1500 mb[81], with 7-33 mg of highly enriched $^{160}Gd_2O_3$ target, the production of $^{161}$Tb can reach up to 20 GBq[82]. High production yield is the main advantage of this production route.

This route is only used for the production of $^{161}$Tb thanks to the good decay property of $^{161}$Gd. For other radionuclides, this route is not suitable: the half life of $^{149}$Gd is too long (9.28 d) to produce $^{149}$Tb efficiently; the $^{152}$Gd and $^{155}$Gd are stable, they cannot decay to $^{152}$Tb and $^{155}$Tb, respectively.

#### 1.3.1.2. Production of $^{149,152,155}$Tb by spallation reaction

Nowadays, other terbium radionuclides, like $^{149}$Tb, $^{152}$Tb, and $^{155}$Tb, are generally produced by spallation reaction on natural tantalum target through the reaction $^{nat}$Ta(p,x)$^{149,152,155}$Tb. The maximum cross sections and the corresponding energies are shown in Table 1.7. The maximum cross sections for $^{149}$Tb, $^{152}$Tb, and $^{155}$Tb are respectively 15 mb, 40 mb, and 45 mb. To reach maximum values, the corresponding energy should be larger than 900 MeV.

Table 1.7 Maximum cross sections of $^{nat}$Ta(p,x)Tb and corresponding energies at maximum cross sections.

| Radionuclide of interest | Maximum σ (mb) | Energy (MeV) |
|---|---|---|
| $^{149}$Tb | 15 | 1100 |
| $^{152}$Tb | 40 | 1000 |
| $^{155}$Tb | 45 | 900 |

After irradiation, these radionuclides are firstly released from the Ta target by heating and ionized by surface ionization in a source at 2000°C and finally separated by an electromagnetic online mass separator[7]. The CERN-MEDICIS produced successfully $^{149}$Tb, $^{152}$Tb and $^{155}$Tb since 2018, the collected activities and separation efficiencies in 2018 are listed in Table 1.8. The collection activity of $^{149}$Tb and $^{152}$Tb, 8 MBq and 1 MBq respectively, is relative low compared with the production of $^{161}$Tb by nuclear reactor (20 GBq). For $^{155}$Tb, the collection activity is higher, 71 MBq, but the separation yield is very low, less than 6% [46].

Table 1.8 Collection activity and separation efficiencies of terbium radioisotopes[46]

| Radionuclide of interest | Collection activity (MBq) | Separation efficiencies (%) |
|---|---|---|
| $^{149}$Tb | 8 | - |
| $^{152}$Tb | 1 | - |
| $^{155}$Tb | 71 | 6% |

This production route has many disadvantages. On the one hand, as explained in section 1.2, only three facilities can produce Tb radionuclides through spallation reactions nowadays, the lack of facilities greatly limits the total production of Tb radionuclides. Secondly, as shown in Table 1.8, the production is limited in the CERN-MEDICIS facility. On the other hand, the separation yield is very low (6%) and many isobaric impurities are produced. Examples of generated impurities are listed in Table 1.9 according to the work of Webster[83]. In this table, many isobar nuclides can be produced during the spallation reaction, such as $^{149}$Gd for $^{149}$Tb, $^{152}$Dy for $^{152}$Tb, and $^{155}$Dy for $^{155}$Tb. Meanwhile, there are some nuclides who are not isobar for radionuclides of interest, but their oxide form have the same mass, such as $^{133}$Ba$^{16}$O for $^{149}$Tb, $^{136}$Ce$^{16}$O for $^{152}$Tb and $^{139}$Ce$^{16}$O for $^{155}$Tb. These impurities cannot be separated by mass, so additional radiochemical separation processes are necessary. Even if the chemical separation efficiency is much higher than the mass separation, this process still reduces the recovery of relevant radionuclides and increase processing time.

Overall, although spallation reaction coupled with an isotope separator makes it possible to produce terbium radionuclides for research, it is not suitable for mass production because of its high cost and low yield.

Table 1.9 Impurities produced in the spallation production route[83].

| Impurity type | $^{149}$Tb | $^{152}$Tb | $^{155}$Tb |
|---|---|---|---|
| Isobar nuclide | $^{149}$Gd, $^{149}$Eu, $^{149}$Sm, $^{149}$Pm | $^{152}$Dy, $^{152}$Gd, $^{152}$Eu, $^{152}$Sm | $^{155}$Dy, $^{155}$Gd, $^{155}$Eu |
| Same mass in oxide form | $^{133}$Ba, $^{133}$Cs | $^{136}$Ce, $^{136}$Cs, $^{136}$Ba | $^{139}$Ce, $^{139}$La, $^{139}$Pr |
| Daughter products | $^{145}$Eu, $^{145}$Sm, $^{145}$Pm, $^{145}$Nd | $^{152}$Gd | $^{155}$Gd |

### 1.3.1.3. Production of $^{149,152}$Tb by heavy-ion-induced reactions

Tb radionuclides can also be produced by heavy-ion induced reactions. Several ions were studied theoretically or experimentally, such as $^{12}$C and $^{14}$N [84–88].

The $^{149}$Tb can be produced directly by the reaction $^{141}$Pr($^{12}$C,4n)$^{149}$Tb. Maiti et al[84] have measured the cross section of the reaction using $Pr_6O_{11}$ target. The maximum cross section of $^{nat}$Pt($^{12}$C,x)$^{149}$Tb is about 30 mb at 62 MeV. However, there is no experiment for mass production through this production route.

Allen et al[85] used natural Nd target to produce $^{149}$Tb and $^{152}$Tb through the indirect routes: $^{nat}$Nd($^{12}$C, x)$^{149}$Dy→ $^{149}$Tb and $^{nat}$Nd($^{12}$C, x)$^{152}$Dy→ $^{152}$Tb, respectively. The half-life of $^{149}$Dy and $^{152}$Dy are 4.20 min and 2.378 h, while the half-life of $^{149}$Tb and $^{152}$Tb is 4.118 h and 17.5 h, respectively. The production of $^{149}$Tb is dominant when the irradiation time is limited to 6 h while $^{152}$Tb becomes dominant when the irradiation is longer than 20 h[85]. After 15 h of irradiation, the activity of $^{152}$Dy can reach up to 100 MBq. However, authors did not give information on the activity of $^{149}$Tb or $^{152}$Tb. Zaitseva et al[86] used the same production route with 120 MeV of $^{12}$C to produce $^{149}$Tb, the activity is 15-30 GBq with a beam current of 50-100 µA and 10 h of irradiation, so the production yield is 30 MBq/µAh. Meanwhile, the co-production of impurities remain unknown in these two works.

The indirect route $^{142}$Ce($^{16}$O,6n) $^{152}$Dy→ $^{152}$Tb was also studied to produce $^{152}$Tb. In the work of Lahiri et al.[87], natural $CeO_2$ was irradiated by ions of $^{16}$O with an energy of 80 MeV to produced $^{151,152,153}$Dy. $^{151,152,153}$Tb were therefore produced as daughter products of $^{151,152,153}$Dy. To eliminate impurities, authors used liquid cation exchanger, but they stated neither the separation efficiency nor the final yield of $^{152}$Tb.

In addition, Nayak et al.[88] studied the production route $^{139}$La($^{16}$O,3n)$^{152}$Tb. Natural $La_2O_3$ target was irradiated by $^{16}O^{6+}$ with an energy of 85 MeV for 9 h, the average beam current was 50-60 nA. The production yield of $^{151}$Tb and $^{152}$Tb are 82 kBq/µAh and 33 kBq/µAh, respectively. Additional radiochemical separation process were executed, more than 70% of Tb can be extracted from La, but authors did not separate $^{151}$Tb and $^{152}$Tb.

In conclusion, various production routes for the production of Tb radionuclides using heavy ions have been investigated, the most important of which is the production of $^{152}$Tb. However, most of these studies were from two decades ago, the authors mostly did not consider impurities and purification issues, and the yield of $^{152}$Tb was relatively small. Furthermore, the limited number of heavy ion accelerator facilities is also a disadvantage of this production route: only

13 facilities provide $^{12}C$ for clinical use, and these facilities are located only in Europe and Asia[89].

#### 1.3.1.4. Production of $^{149,152,155}Tb$ by light-charged-particle-induced reactions

The use of light-charged-particle-induced reaction is also an alternative to produce Tb radionuclides.

Natural Gd target was first used for Tb isotope production in the recent years. Formento-Cavaier et al.[90] (2020) measured the cross section of $^{nat}Gd(d,x)^{149,150,151,152,153,154,155,156}Tb$ at 58-70 MeV. Using measured cross section values, authors estimated the production yield of $^{149}Tb$ in the energy window 69.8 MeV and 58.2 MeV, the thick target yield is 40 MBq/µAh. Similar work with deuteron induced reactions has been done by Tarkanyi et al.[91] (2014) and by Duchemin et al[92] (2016) at 5-50 MeV and 10-34 MeV, respectively. However, the two measurements are not fully consistent and differences exist for $^{154}Tb$ and $^{160}Tb$ production. New measurements must be done to solve this problem. Meanwhile, the two works did not measure the thick target yield. The excitation function of $^{nat}Gd(d,x)^{155}Tb$ and $^{nat}Gd(d,x)^{161}Tb$ have been re-measured by Szelecsenyi et al.[93] (2016) at 4-30 MeV later. However, authors did not measure the thick target yield either.

The disadvantages of natural target are not only the lower cross section values but also the co-production of other Tb isotopes $^{148,150,151,153,154,156,160}Tb$. Theses radionuclides have the same chemical properties as the radionuclides of interest ($^{149,152,155,161}Tb$), so they are difficult to separate even if electromagnetic isotope separation method has been proposed by many researchers[94]. Therefore, enriched gadolinium or europium targets are taken into account to increase the supply of Tb radionuclides and their final purities.

For the production of $^{149}Tb$, Steyn et al.[94] firstly measured the cross sections of $^{152}Gd(p,4n)^{149}Tb$, the maximum cross sections is 250 mb at 42 MeV. According to authors' estimation, the theoretical production yield of $^{149}Tb$ can reach up to 2556 MBq/µAh. The main problem of this production route is the low enrichment rate of $^{152}Gd$, only 30.6%, and the target materials contain other Gd isotopes $^{154,155,156,157,158,160}Gd$. The presence of these Gd isotopes leads to the co-production of Tb impurities. Moiseeva et al[95] therefore used high enriched $^{151}Eu$ to produce $^{149}Tb$ by the reaction $^{151}Eu(^{3}He,5n)^{149}Tb$. In the energy window from 70 to 12 MeV, the production yield of $^{149}Tb$ is 39 MBq/µAh, and the saturation yield can reach up to 230 MBq/µA. The co-production of $^{148}Tb$ and $^{150}Tb$ were reported in the work.

For $^{152}Tb$, Steyn et al.[94] measured the cross section of $^{155}Gd(p,4n)^{152}Tb$ at 30-66 MeV, the biggest cross section is 900 mb at 39 MeV. The production yield is 1924 MBq/µAh by authors' estimation. Meanwhile, Guray et al. used the route $^{152}Gd(p,n)^{152}Tb$ and measured the cross section at 4.9-8.0 MeV. The cross section reaches up to 100 mb at 8 MeV. In fact, the production route $^{152}Gd(p,n)^{152}Tb$ has a huge advantage because co-produced impurities can be limited by choosing good energy window. The threshold energy for the reaction $^{152}Gd(p,3n)^{150}Tb$, $^{152}Gd(p,2n)^{151}Tb$ and $^{152}Gd(p,\gamma)^{152}Tb$ are 20.7 MeV, 12.0 MeV, and 0 MeV, respectively. It is clear that only $^{153}Tb$ will be co-produced through (p,x) when energy is below 12.0 MeV. Fig. 1.9 shows the theoretical cross section of Tb radionuclides produced by proton induced $^{152}Gd$ target using Tendl-2019 [96]. It can be seen from the figure that the cross section of $^{153}Tb$ is negligible compared to the cross section of $^{152}Tb$.

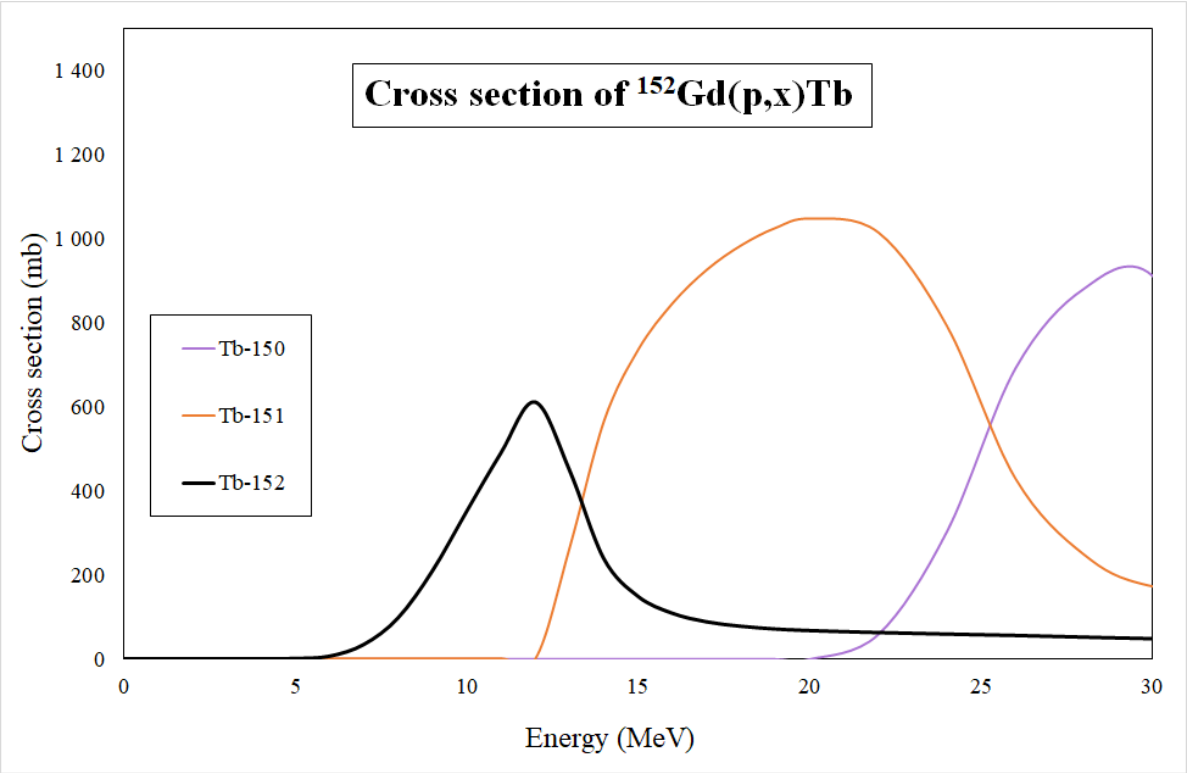


Fig. 1.9 Theoretical cross section values of Tb isotopes of proton induced reactions on $^{152}$Gd [96].

For the production of $^{155}$Tb, the production route $^{155}$Gd(p,n)$^{155}$Tb was considered. The theoretical cross sections of $^{153,154,155,156}$Tb are shown in Fig. 1.10. The maximum cross section of $^{155}$Tb is about 440 mb at 11 MeV. This production route has the same advantage as that of the route $^{152}$Gd(p,n)$^{152}$Tb: the co-production of the impurities $^{153}$Tb and $^{154}$Tb can be limited by choosing the good energy window (less than 10.83 MeV, threshold energy of $^{154}$Tb), and the production of $^{156}$Tb through $^{155}$Gd(p,γ)$^{156}$Tb is small compared to that of $^{155}$Tb. Therefore, $^{155}$Tb can be produced with high purity in cyclotron with low energy. Favaretto and al.[97] have used 40 mg of enriched solid $^{155}Gd_2O_3$ targets to produce $^{155}$Tb at a medical cyclotron, the production yield is about 3.1 MBq/µAh. Similar work has been done by Dellepiane et al.[98] with 91.9% enriched $^{155}Gd_2O_3$, the production yield is about 3.5 MBq/µAh and the purity of $^{155}$Tb is 93.5%. The results represent an important step forward the quantitative production of $^{155}$Tb in nuclear medicine.

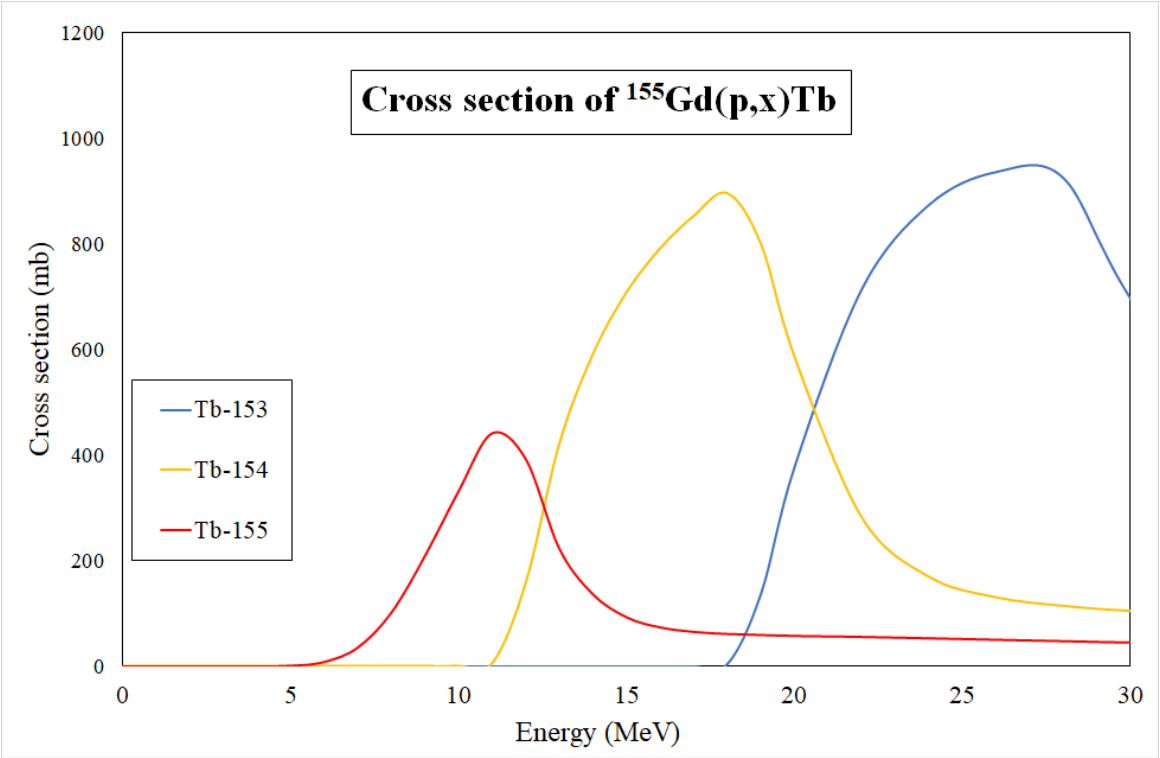


Fig. 1.10 Theoretical cross section values of Tb isotopes of proton induced reactions on $^{155}$Gd [96].

For $^{161}$Tb, it can also be produced by cyclotron through $^{160}$Gd(d,γ)$^{161}$Tb. Tarkanyi et al.[81] measured the cross section and estimated the thick target yield. Authors also reported the co-production of $^{160}$Tb and compared the production route with reactor route. It is proven by theoretical calculation that accelerator production of $^{161}$Tb is not competitive with the reactor production[81]. Details of the comparison can be found in Table 1.10[81].

Table 1.10 Comparison of reactor production route and accelerator production route of $^{161}$Tb [81].

| Equipment | Reactor | Accelerator |
|---|---|---|
| Reaction | $^{160}$Gd (n, γ) $^{161}$Gd → $^{161}$Tb | $^{160}$Gd (d,x) $^{161}$Tb |
| Energy | Thermal | 5-30 MeV |
| Average cross section (mb) | 1500 | 125 |
| Irradiation | Single-channel | Single channel |
| Disturbing reaction | - | $^{160}$Gd (n, γ) $^{160}$Tb |

In conclusion, light-charged-particle-induced reactions on enriched Gd or Eu targets can be an alternative route to increase $^{149,152,155}$Tb supply. Firstly, the energy of these reactions are relatively low (5-40 MeV), especially for $^{152}$Tb and $^{155}$Tb (5-12 MeV); this energy is reachable for many biomedical cyclotrons. Secondly, compared with the production with heavy ion-induced production route, the production yields are larger with light charged particles. In addition, since the number of cyclotrons is gradually increasing to meet the needs of nuclear medicine, the production of Tb radionuclides using cyclotrons will therefore become

increasingly available to medical institutions, thereby alleviating shortages problem of Tb radionuclides.

#### 1.3.1.5. Comparison of Tb production routes

To compare different production routes, a summary of their advantages and disadvantages is presented in Table 1.11.

Table 1.11 Advantages and disadvantages of different radionuclide production routes.

| **Production routes** | **Advantages** | **Disadvantages** |
|---|---|---|
| Nuclear reactor | High production yield for $^{161}$Tb | Not suitable for other Tb isotopes<br>Expensive enriched targets |
| Spallation reaction | Possible route for $^{149,152,155}$Tb<br>Very high production yield<br>Cheaper target materials | Too many impurities<br>Low separation yield<br>Very limited facilities |
| Heavy ions | Possible route for $^{152}$Tb | Limited facilities<br>Low production yield<br>Impurities of $^{151}$Tb and $^{153}$Tb<br>Expensive enriched targets |
| Light charged particles and enriched Gd targets | Possible route for $^{149,152,155}$Tb<br>Huge number of facilities<br>Higher production yield<br>Less or even no impurities by limiting energy | Expensive enriched targets<br>Not efficient to produce $^{161}$Tb |

According to the table, the nuclear reactor is the optimal production route for the production $^{161}$Tb because of the high yield. For other Tb isotopes $^{149,152,155}$Tb however, light charged particle-induced reactions on enriched Gd target are the most suitable production route. In these cases, the production yield is relatively high, the co-produced impurities are very limited by choosing good energy window, and since many cyclotrons are located in medical center, it takes less time for transport too. However, even though this production route has many advantages, the current research on mass production of Tb radionuclides is still in the initial stage.

### 1.3.2. Objectives of this work

Objectives of this work are firstly to develop solid enriched Gd targets for the use of cross section measurement and thick target production, and secondly to optimize Tb production routes to improve its availability. To prove the concept of thin target, the cross section with natural Gd targets were measured and compared with existing data. Then, enriched target were manufactured and used for cross section measurements. These measurements are used not only to select energy windows and to estimate production yields but also to complete existing data.

#### 1.3.2.1. Choice of production route

As proven in the previous subsection, enriched targets has great advantages compared with natural targets. So far, the enrichment of $^{152}$Gd, $^{154}$Gd and $^{155}$Gd are 30-34%, 64-67% and 90-92% respectively (supplied by *Tracesciences international*[99]). High enrichment $^{155}$Gd was therefore chosen in this work.

As mentioned above, the use of enriched $^{155}$Gd target for the production of $^{155}$Tb has been studied by several researchers[97,98]. However, only proton was involved in the production route. Experimental study of deuteron-initiated production route has not yet been conducted.

The biggest advantage for $^{155}$Gd(p,n)$^{155}$Tb is the high purity of $^{155}$Tb at low energy (Fig. 1.10). However, except for $^{155}$Gd, other Gd isotopes, such as $^{156,157,158,160}$Gd, are also mixed in the enriched target, especially for $^{156}$Gd, the proportion is about 5%[98]. The presence of $^{156}$Gd results in the presence of $^{156}$Tb impurities due to the reaction $^{156}$Gd(p,n)$^{156}$Tb. The threshold energy for this reaction is only 3.2 MeV. In addition, the half-life of $^{156}$Tb (5.35 d) is very close to that of $^{155}$Tb (5.32 d). Therefore, the $^{156}$Tb impurities will always exist during the production of $^{155}$Tb. Dellepiane et al[98] used a proton beam of 18.2 MeV, and they detected the generation of $^{153}$Tb, $^{154}$Tb and $^{156}$Tb impurities in their 91.9% enriched $^{155}$Gd targets. The purity of $^{155}$Tb is only about 47% at EOB and 93% after 96 h of the decay.

Theoretical analysis shows that the production route $^{155}$Gd(d,2n)$^{155}$Tb has similar purity level (around 90%) but the reaction cross section is much higher compared with that of $^{155}$Gd(p,n)$^{155}$Tb (details will be explained in Chapter 4).

To experimentally verify the results of the theoretical analysis, deuteron was chosen for this work to study the reaction $^{155}$Gd(d,2n)$^{155}$Tb. The use of deuterons can provide the first experimental cross section values of $^{155}$Gd(d,2n)$^{155}$Tb. Moreover, if the experimental results agree with the theoretical results, the production yield of $^{155}$Tb will at least be doubled.

#### 1.3.2.2. Targetry strategy

In order to maximize the production yield while maintaining the purity of $^{155}$Tb, the choice of the energy window is crucial. Therefore, the reaction cross section and the excitation function need to be investigated first. Thin targets were used for cross section measurements.

Many techniques have been developed to fabricate thin targets, such as the HIVIPP, the MS and the electrodeposition (introduced in subsection 1.2.2.1). However, the HIVIPP needs a set-up under vacuum and takes considerable time, and it is only suitable for metal materials. Meanwhile, the MS requires control of air pressure and temperature, and the high material consumption rates are not economical for enrichment targets. The electrodeposition method requires simple installation and low cost, but one primary problem is that Gd has an extremely large negative equilibrium potential (details will be presented in Chapter 2). These three common techniques are therefore not suitable for this work. In this case, an alternative method, the co-electrodepostion method was used to produce Gd-containing thin target. Principles of this method, influential factors, and characterization of obtained targets will be presented in **Chapter 2**.

Then, thicker targets were developed for mass production. The pelletizing technique was used in this work. Methodology and materials of the technique, the choice of materials, the characterization of obtained pellets, and the encapsulation will be described in **Chapter 3**.

### 1.3.2.3. Irradiation strategy

The irradiation experiments for cross section measurement and for mass production were carried out at ARRONAX facility at Saint-Herblain, France.

Supported by eight institutions including universities, medical institutions, and government agencies, the ARRONAX facility is a scientific cyclotron facility for multi-disciplinary usage[100]. It hosted a high energy accelerator, the ARRONAX cyclotron, that can accelerate proton, deuteron, and α particles with the maximum energy of 70 MeV, 35 MeV and 68 MeV[101] and the maximum intensity of 375 µA, 50 µA and 70 µA, respectively. Positive ions, $H^{++}$ and $He^{++}$, are extracted through an electromagnetic septum, while negative ions, $H^-$ and $D^-$, are extracted using the stripper foil technique[101]. The cyclotron is located in a center hall and is equipped with six beam lines extending into six separated experimental vaults (P1, P2, P3, A1, A2, AX). The proton and deuteron beams are available in all of the experimental vaults while α particle beams are only available in A1, A2 and AX[101].

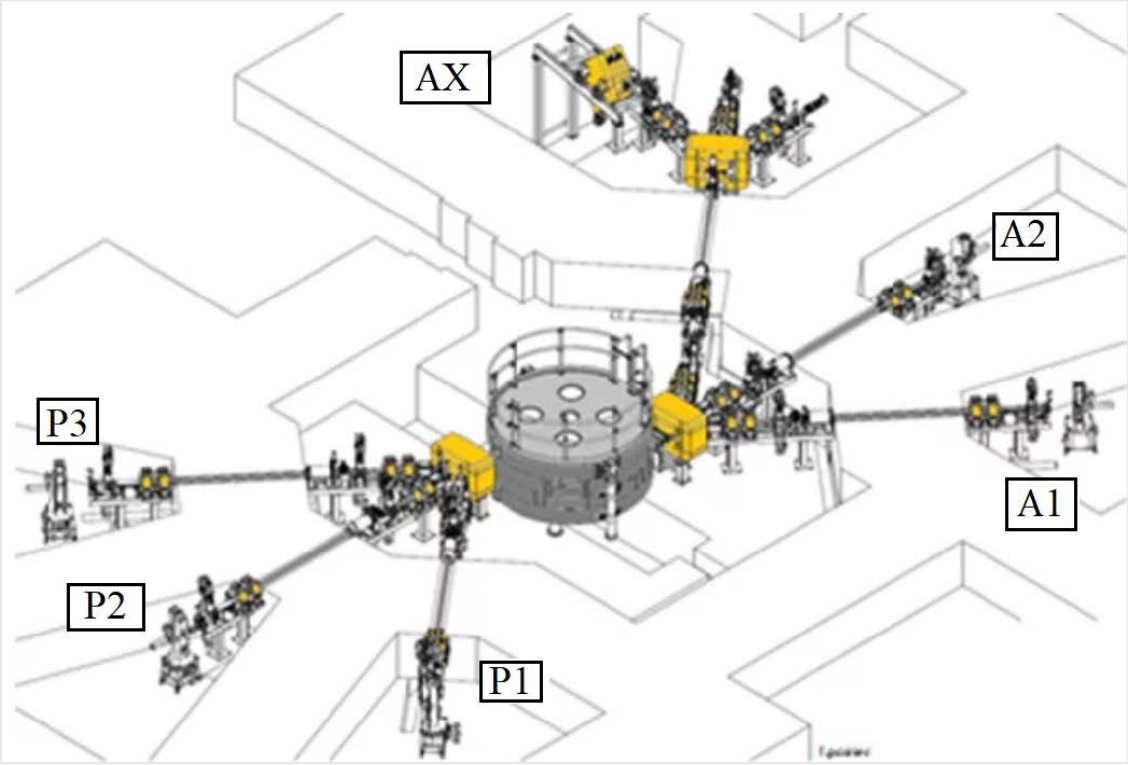


Fig. 1.11 Schematic structure of the ARRONAX cyclotron and 6 particle beams. Picture based on the picture in the official website of ARRONAX.

In this work, cross section measurements were carried out at AX experimental vaults with the help of the stacked-foils technique. The deuteron beam energy on target varied from 8 to 30 MeV, and the beam intensity was between 50-100 nA. After measuring cross sections and estimating the production yield, one test was carried out for the mass production in the same experimental vaults, with a beam intensity of 500 nA and a thick target. This low intensity test aims to check whether the experimental thick target yield value is consistent with the value estimated from measured cross sections. Principles of stacked-foils techniques, materials for data acquisition, calculation method, experimental device and target transport systime, as well as results of all the irradiation experiments will be presented in **Chapter 4**.

In summary, this thesis will demonstrate the whole process of the $^{155}$Tb production: from the production and encapsulation of uniform thin or thick solid targets, to the measurement of reaction cross sections, estimation of yield and to the experimental measurement of yield and purity in mass production. In addition, as a part of the production chain, the recycling of $^{155}$Gd target after irradiation will also be discussed in this thesis.

# Chapter 2 :
# Manufacture of thin targets through co-electrodeposition method

# 2. Manufacture of thin targets through co-electrodeposition method

As explained in Chapter 1, to measure the reaction cross section, thin and uniform Gd targets must first be fabricated. This chapter will be divided into two parts, the first part is the introduction of the experimental methods and associated materials, and the second part is the experimental results and related discussions.

For the first part (section 1), the method used to make thin targets, namely co-electrodeposition, will be presented in details, including the principle of this method and the choice of experimental materials (electrolyte, electrodes, and the design of electrodeposition cells). In addition, several tools for quantifying the deposit quality will also be introduced, including the Scanning Electron Microscopy (SEM) coupled with Energy Dispersive X-Ray Analysis (EDX) and the Inductively Coupled Plasma - Atomic Emission Spectroscopy (ICP-AES).

For the second part (section 2.2 and section 2.3), two types of thin deposits, Ni-$Gd_2O_3$ and Zn-$Gd_2O_3$ deposits, will be presented including the influences of process parameters (applied potential, $Gd_2O_3$ loading quantity, stirring speed, temperature, and roughness of substrate) and different co-deposition modes. The two deposits will be compared to select the best target for measuring reaction cross sections. Finally, the chapter will be concluded in section 2.4.

## 2.1. Method and materials

This section will introduce the method and materials used for thin Gd targets. $Gd_2O_3$ is used for target preparation since the enriched $^{155}Gd$ is supplied in this form. In addition, because of the high price of enriched $Gd_2O_3$, in this chapter, all studies used natural $Gd_2O_3$ for research.

### 1.3.3. Principle of the co-electrodeposition technique

The co-electrodeposition technique is based on the electrodeposition technique. The classical electrodeposition technique uses the principle of electrolysis to reduce metal cations ($X^{n+}$) to a thin layer of the metal (X) with the help of an electrical current. This process can be written as *eq.2.1*:

$$X^{n+} + n\,e^- \rightarrow X \qquad (eq.\,2.1)$$

However, if the redox potential of the metal is too negative, which is the case of $Gd^{3+}$/Gd in this work, a low potential has to be applied to allow reduction of the metal. In this case, as the $H^+$ in the electrolyte is easier to reduce, the process becomes as *eq.2.2*:

$$2\,H^+ + 2\,e^- \rightarrow H_2 \qquad (eq.\,2.2)$$

This process is called the Hydrogen Evolution Reaction (HER).

The Pourbaix diagram of $Gd^{3+}$ in water at 25°C is shown in Fig. 2.1. The main species of gadolinium is $Gd^{3+}$ (in acid condition), $Gd(OH)_3$ (in alkaline condition), and Gd (more negative potential), there are also other species less stable according to pH and Eh, such as $GdOH^{2+}$, $GdO^+$, and $GdO^{2-}$. The redox potential of $Gd^{3+}$/Gd is more negative than -2.4 V/SHE[102] in acid conditions and even more negative in alkaline solutions. This value is too much lower than the reduction potential of water (dotted line “a”), which means that there is a strong competition with water decomposition at all pH values. Under HER, the deposit will be oxidized quickly and do not adhere to the substrate. Therefore, the electrodeposition method is not suitable to

fabricate Gd deposits in an aqueous solution. To overcome such a problem, several Gd deposits tests were carried out in organic mediums [103–105], however, they resulted either with too small area (<1.1 cm²) or too fine (<1 µm). In addition, these experiments have strict restrictions on moisture content, which makes them complicated to master. Molten salt mediums were also studied[106], but this experiment had also many constraints (high temperature, pure argon environment…).

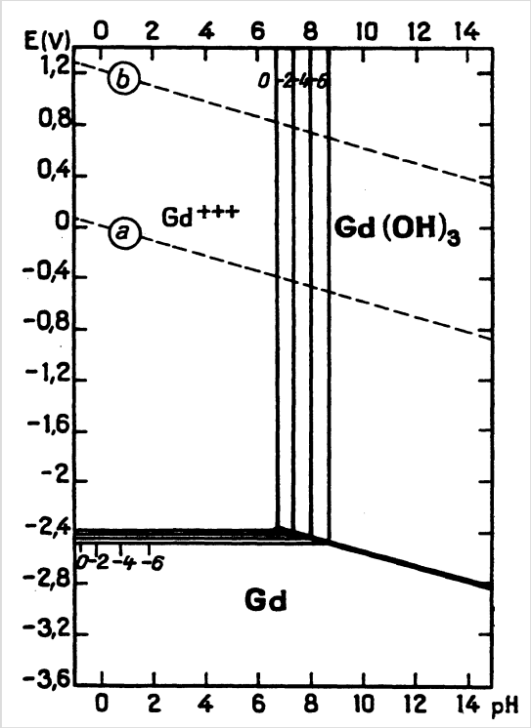


Fig. 2.1 Pourbaix diagram of Gd in water at 25°C[107].

Therefore, the co-electrodeposition technique was adopted as an alternative technique in this work to prepare thin targets. Based on the principle of electrolysis, the co-electrodeposition technique mixes insoluble solid particles into the electrolyte. While the metal is electrodeposited, the solid particles are mechanically transported and physically trapped and finally embedded in the growing metal matrix[108]. The obtained composite deposit is often called as X-M composite deposit, where X is the metal matrix obtained by electrodeposition while M are the solid particles. For this work, X refers to Ni or Zn atoms, and the solid particle M refers to $Gd_2O_3$.

For the co-electrodeposition method, the process of metal deposition remains unchanged, the process is as shown in *eq.2.1*. Meanwhile, the globally neutral $Gd_2O_3$ solid particles are surrounded by charged cations $X^{n+}$ and move to the cathode.

The mechanism of the co-electrodeposition remains still unclear, but the most recently accepted theory[109] divides this process into five stages:

- The $Gd_2O_3$ particles mixed into the bulk electrolyte will firstly be surrounded by metal cations $X^{n+}$ to form charged ionic clouds.

- The charged clouds will then physically pass through the convection layer[110]. In this layer, particles move towards the cathode due to the convection of the electrolyte, such as the magnetic stirring in this work.
- The charged clouds are transported through the diffusion layer. In this layer, the concentration of particles are not homogeneous, particles move from high concentration zone (near the bulk electrolyte) to low concentration zone (near the cathode).
- Then the particles pass the electrical double layer. This layer has two parallel charge layers surrounding the substrate. The first layer (closer to the substrate) consists of cations that are attracted to the substrate due to chemical interaction. The second layer consists of ions attracted by the Coulomb force of the surface charge[111].
- The $Gd_2O_3$ particles can be physically incorporated into the growing electrodeposition metal layer by losing their ionic clouds[108,112].

The stages involved are summarized in Fig. 2.2, referring to the conclusion of Walsh et al.[108].

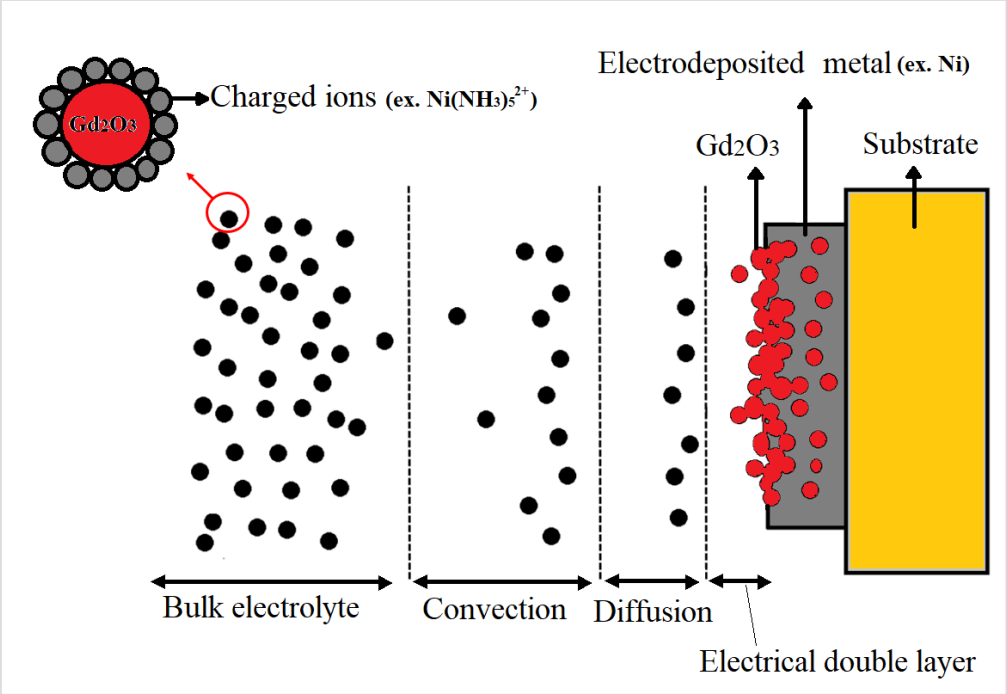


Fig. 2.2 the processes involved in the incorporation of $Gd_2O_3$ into a growing metal matrix.

### 1.3.4. The choice of experimental materials

#### 1.3.4.1. Selection of electrodeposited metals

For the metal used for co-electrodeposition, there are at least three constraints that should be met:

- the standard potential of the metal cannot be too low to avoid the strong HER;
- radionuclides produced by the metal under irradiation must have short half-lives and do not interfere with measurements of terbium radionuclides,
- the metal need to be deposited in alkaline solution.

For the first constraint, several well-studied metals were listed as candidates, the list of these metals and their standard reduction potentials[102] are presented in Table 2.1. From the table, gold has the biggest standard electrode potential (1.69 V/SHE) while zinc has the smallest (-0.76 V/SHE). It is clear that all these metals satisfy the first constraint.

Table 2.1 List of well-studied metals and their standard electrode potentials (E°)[102].

| Metal | Reaction | E° (V/SHE) |
|---|---|---|
| Gold | $Au^{+} + e^{-} \rightarrow Au$ | 1.69 |
| Copper | $Cu^{2+} + 2\ e^{-} \rightarrow Cu$ | 0.34 |
| Nickel | $Ni^{2+} + 2\ e^{-} \rightarrow Ni$ | -0.24 |
| Cobalt | $Co^{2+} + 2\ e^{-} \rightarrow Co$ | -0.28 |
| Zinc | $Zn^{2+} + 2\ e^{-} \rightarrow Zn$ | -0.76 |

For the second constraint, the gold can produce $^{198m}Au$ ($T_{1/2}$ = 2.272 d, E = 180.31 keV, $I_\gamma$ = 50 %)[113] that will interfere with the detection of $^{155}Tb$ ($T_{1/2}$ = 5.32 d, E = 180.103 keV, $I_\gamma$ = 7.45 %), so it should be excluded. The cobalt should also be excluded because of the production of $^{60}Co$ ($T_{1/2}$ = 1925.28 d), which will cause problems for nuclear waste management.

Among the remaining three metals (Cu, Ni, and Zn), the electrodeposition of Cu is mainly studied in acid solution[114] and there have many difficulties to electrodeposit Cu in alkaline solution[115]. Meanwhile, the electrodeposition of Ni and Zn were widely studied[116–120] in both acid and alkaline solution. This work needs to study in alkaline condition to keep $Gd_2O_3$ inert, so Ni and Zn have more advantage. In addition, the excitation functions of Ni and Zn were also well studied[121], they were finally selected as the metals for co-electrodeposition in this work.

As composite deposits, either Ni or Zn will be irradiated when measuring cross section, so the radionuclides produced by their irradiation have to be considered. Excessive production of radionuclides not only makes radiation protection difficult but also affects the counting process by increasing the dead time. Given that cross sections were measured at energies between 5-30 MeV (see section 4.1.2 and section 4.1.3), the following comparisons of radioisotopes produced by Ni and Zn also focus on this energy range.

Induced by deuterons, several radionuclides produced by natural Zn at low energy (5-30 MeV) are listed in Table 2.2[122]. Only radionuclides with a half-life longer than 1 h has been listed, because the data acquisition of the deposit begins at least 12 h after the EOB, shorter lived radionuclides will decay to undetectable level. Among them, the half-life of $^{65}Zn$ is more than 100 days, unlike other radionuclides with very short half-lives, they need extra attention as short-lived wastes according to the French classification of radioactive waste. The cross section of $^{nat}Zn(d, x)^{65}Zn$ is between 80 to 350 mb when deuteron energy is limited to 5-30 MeV, especially, its cross section reaches a maximum (350 mb) at 11 MeV[123], which is in the studying energy range of cross section measurement.

Meanwhile, for Ni, radionuclides produced by Ni at low energy (5-30 MeV) are listed in Table 2.3[124], only radionuclides with a half-life longer than 1 h has been listed. The main radionuclides who have a half-life of more than 100 days are $^{57}Co$ ($T_{1/2}$ = 271.79 d), $^{60}Co$ ($T_{1/2}$ = 5.27 y) and $^{54}Mn$ ($T_{1/2}$ = 312.2 d)[124,125]. However, for $^{60}Co$ and $^{54}Mn$, even if their half-lives are relatively

long, their cross sections are very small, so these impurities have little effect. For $^{57}$Co, the cross section increase from 5 mb to 400 mb when energy increase from 10 MeV to 30MeV.

Table 2.2 Decay characteristic of radionuclides produced by Zn[123].

| Nuclide | Half-life | Energy at the maximum cross section (MeV) | Cross section at 5-30 MeV (mb) |
|---|---|---|---|
| $^{66}$Ga | 9.49 h | 18 | 55-110 |
| $^{67}$Ga | 3.2612 d | 10 | 70-100 |
| $^{62}$Zn | 9.186 d | 50 | 0-1 |
| $^{65}$Zn | 244.26 d | 11 | 80-350 |
| $^{69m}$Zn | 13.76 h | 10 | 5-10 |
| $^{61}$Cu | 3.333 h | 22 | 25-45 |
| $^{64}$Cu | 12.7 h | 50 | 20-50 |
| $^{67}$Cu | 61.83 h | 50 | 0-2 |
| $^{58}$Co | 70.86 d | 50 | 3-5 |

Table 2.3 Decay characteristic of radionuclides produced by Ni[124].

| Nuclide | Half-life | Energy at the maximum cross section (MeV) | Cross section at 5-30 MeV (mb) |
|---|---|---|---|
| $^{61}$Cu | 3.333 h | 5 | 15-65 |
| $^{56}$Ni | 6.075 d | 46 | 0-5 |
| $^{57}$Ni | 35.6 h | 50 | 3-50 |
| $^{55}$Co | 17.53 h | 25 | 1-20 |
| $^{56}$Co | 77.24 d | 50 | 2-35 |
| $^{57}$Co | 271.79 d | 34 | 0-400 |
| $^{58}$Co | 70.86 d | 20 | 10-250 |
| $^{60}$Co | 5.27 y | 36 | 0-20 |
| $^{52}$Mn | 5.59 d | 30 | 0-2 |
| $^{54}$Mn | 312.2 d | 39 | 0-18 |
| $^{51}$Cr | 27.7 d | 41 | 0-1 |

In general, by comparison, both Zn and Ni produce nuclides with a half-life of more than 100 days, all these radionuclides will increase the dead time of counting. From the perspective of radiation protection and radioactive waste treatment, it is difficult to define which one is better. That is why this work uses both of the two metals making targets for the first stage of research.

#### 1.3.4.2. Selection of electrolytes

For the co-electrodeposition of $Gd_2O_3$ and other metals, it is necessary that $Gd_2O_3$ remains inert in the electrolyte. The dissolution of $Gd_2O_3$ was firstly studied to find the pH range of the electrolyte. It was proven that $Gd_2O_3$ is soluble in acid solution, especially in the presence of nickel or zinc ions (*Appendix 2.1*). However, the insolubility of $Gd_2O_3$ has been validated in basic mediums. This is the reason why alkaline solutions were chosen for the co-electrodeposition

For the nickel electrolyte, to keep the pH of the solution, the $NH_3/HN_4^+$ pair was used as a buffer. The following electrolyte was prepared: 0.5 mol/L $(NH_4)_2SO_4$ + 0.5 mol/L $NH_4Cl$ + 0.14 mol/L $NiSO_4 \cdot 6H_2O$ + 1 mol/L $NH_3$. These compositions and concentration settings referred to the work of Skital et al.[116].

In order to study the main forms of nickel at different pH under this solution composition, the dominance diagram was simulated via Phreeqc[126] by considering the complexations of $NH_3$ and $Ni^{2+}$. The cumulative formation constants for nickel complexes with $NH_3$ are shown in Table 2.4.

Table 2.4 Cumulative formation constants for $Ni^{2+}$ and $NH_3$ complexes[102].

| Species | $Ni(NH_3)^{2+}$ | $Ni(NH_3)_2^{2+}$ | $Ni(NH_3)_3^{2+}$ | $Ni(NH_3)_4^{2+}$ | $Ni(NH_3)_5^{2+}$ | $Ni(NH_3)_6^{2+}$ |
|---|---|---|---|---|---|---|
| Log K | 2.80 | 5.04 | 6.77 | 7.96 | 8.71 | 8.74 |

According to these values, the predominance diagram of Ni species is presented in Fig. 2.3. In more acidic solutions (pH less than 6), nickel mainly exists in the form of $Ni^{2+}$. However, the presence of $Ni^{2+}$ decreases progressively and it completely disappears after pH higher than 8. With the increase of pH, nickel ions tend to be complexed with ammonium ions, and the higher the pH, the more $NH_3$ is complexed. Between pH 6 and 8, new complexes are formed reaching their maximum values at each pH step of 1, the maximum proportion of $Ni(NH_3)^{2+}$, $Ni(NH_3)_2^{2+}$, and $Ni(NH_3)_3^{2+}$ can reach up to 45%, 40% and 45%, respectively. $Ni(NH_3)_4^{2+}$ appears at pH 7 and disappears at pH 10, with a maximum proportion of 10% at pH 8.5. At pH 10, there are only two forms $Ni(NH_3)_5^{2+}$ and $Ni(NH_3)_6^{2+}$ left, each counting around 50%. The final pH of the electrolyte was therefore fixed at 9.8, adjusted by 5 mol/L of NaOH.

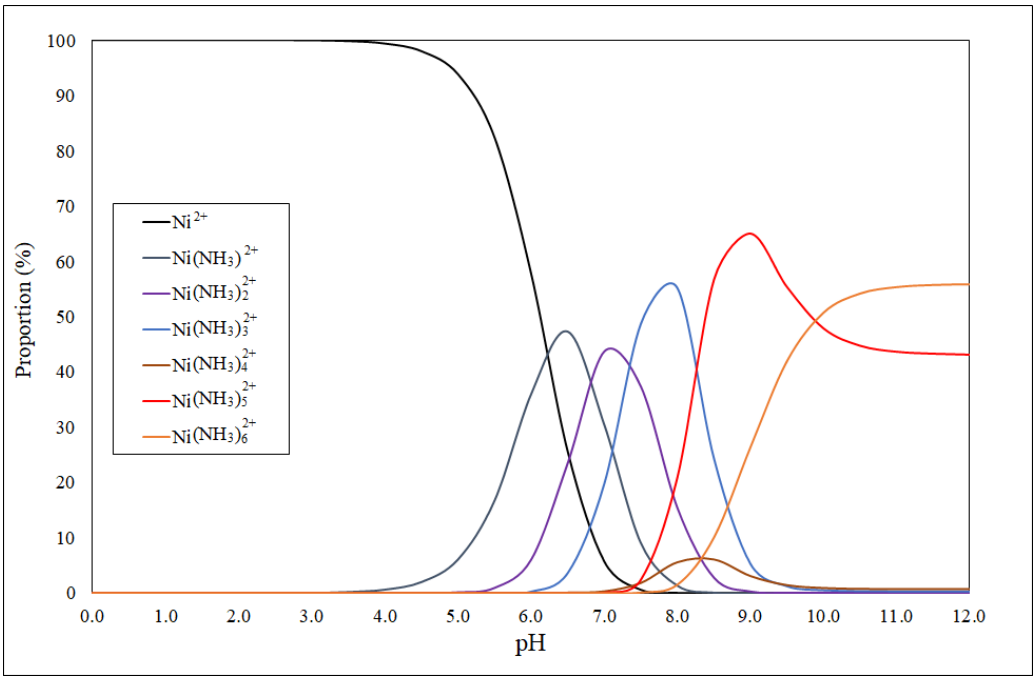


Fig. 2.3 Dominance diagram of nickel in the solution in different pH values at the presence of $NH_3/NH_4^+$.

For the zinc electrolyte, it was prepared as: 0.14 mol/L ZnO + 3.75 mol/L NaOH. The compositions and concentration settings referred to the work of Yuan et al.[117].
Similarly, the cumulative formation constant for complexation of zinc and hydroxide is listed in Table 2.5.

Table 2.5 Cumulative formation constant for the complexation of zinc and hydroxide[102].

| Species | $Zn(OH)^+$ | $Zn(OH)_2$ | $Zn(OH)_3^-$ | $Zn(OH)_4^{2-}$ |
|---|---|---|---|---|
| Log K | 4.40 | 11.30 | 14.14 | 17.66 |

The predominance diagram of zinc in the solution is shown in Fig. 2.4. It can be seen that zinc ions are in form of $Zn^{2+}$ in acid solution but it decreases when pH is greater than 7 and it disappears after pH 10. The complexation of zinc and hydroxide begins at pH 7, the formation of $Zn(OH)^+$ begins at pH 7 reaches the maximum value at pH 8.5 (10%), and it disappears when pH is greater than 10. When pH is between 9 and 11, $Zn(OH)_2$ precipitation dominates the solution, the proportion can reach to 95%. At pH 11, $Zn(OH)_2$ precipitate and $Zn(OH)_3^-$ complex are present in the same proportion in solution with small amount of $Zn(OH)_4^{2-}$. Then, the proportion of $Zn(OH)_3^-$ and $Zn(OH)_4^{2-}$ tends to increase as the pH continues to increase. Due to the limitations of *Phreeqc*, Fig. 2.4 only simulates the proportion of each specie in the solution between pH 0 and pH 12. Another predominance diagram studied by Reichle et al.[127] shows that $Zn(OH)_3^-$ disappears at pH 14. Therefore, when the pH is greater than 14, the zinc ion in the solution exists only in the form of $Zn(OH)_4^{2-}$. So in our electrolyte, zinc is in form of $Zn(OH)_4^{2-}$.

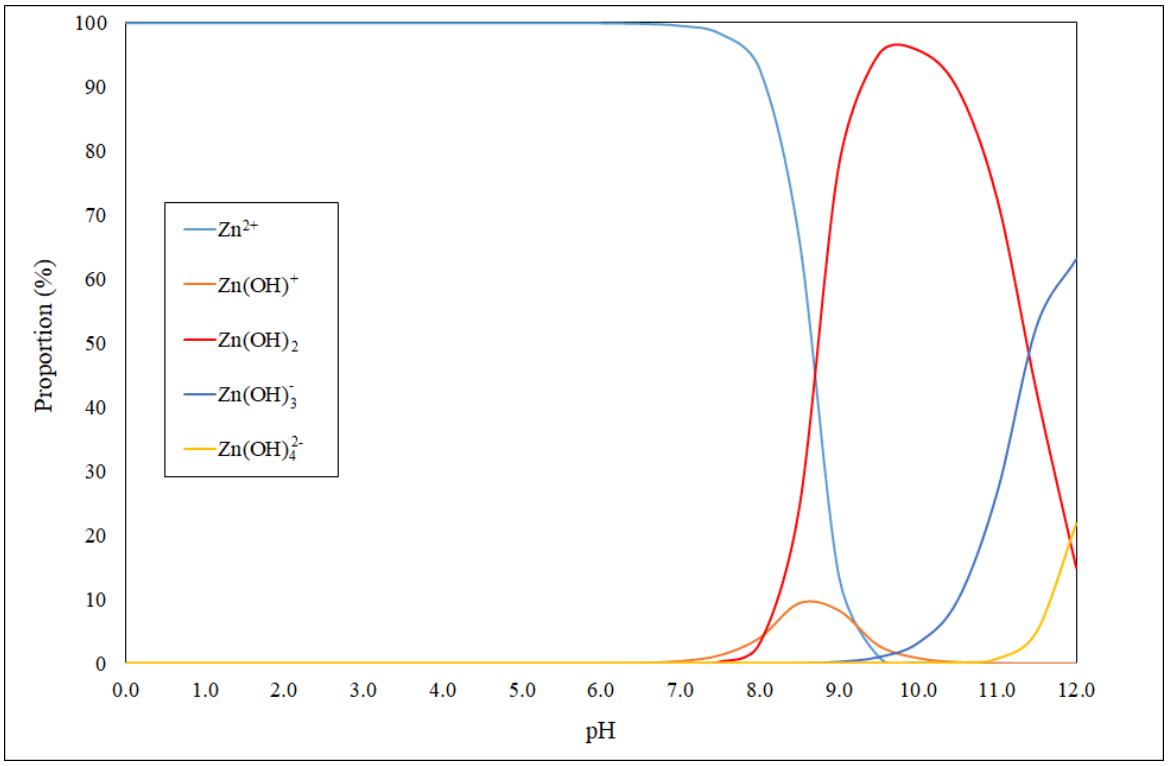


Fig. 2.4 Dominance diagram of zinc in the solution in different pH values.

For both electrolytes, the concentration of metal ions ($Ni^{2+}$ and $Zn^{2+}$) has been chosen about 9 g/L. In the subsequent co-electrodeposition experiments, the loading of $Gd_2O_3$ ranged from 0.5 g (14 g/L) to 6.5 g (185 g/L), that is, the loading particle concentration was 1.5 to 20 times the metal ion concentration.

All chemicals mentioned above are supplied by *Sigma-Aldrich*[128], including natural $Gd_2O_3$ powders (less than 230 mesh). For the ten deposits fabricated with enriched $Gd_2O_3$ powders for cross section measurements (section 4.1.3), the enriched $Gd_2O_3$ powders are supplied by *Tracescience*[129]. The compositions of the enriched powder are shown in *Appendix 2.2*.

#### 1.3.4.3. Selection of substrates

As a substrate for co-electrodeposition, it needs to meet the following conditions: on the one hand, it needs to have good thermal conductivity to better evacuate the heat and avoid to melt the deposit during irradiation; on the other hand, it should be inert enough to avoid being dissolved during the dissolution of deposits by HCl.

Gold was chosen for its high thermal conductivity (318 $W \cdot m^{-1} \cdot K^{-1}$ at 273°K[130]) and its stable chemical properties (Gold will not be corroded by HCl).

#### 1.3.4.4. Co-electrodeposition cell structure

The co-deposition was carried out in a homemade PEEK (Polyetheretherketone) cylinder cell containing 35 mL of the electrolyte (Fig. 2.5). The cell made by PEEK has exceptional chemical resistance, very low moisture absorption, good mechanical strength and good creep resistance[131], which is suitable for this work. A hole with a diameter of 20 mm was on the side of the cylinder to place the working electrode. The thickness of the cylinder wall near the substrate side is about 1 mm, this thickness is intended to minimize boundary effects. A Kapton film with a hole was glued on the substrate to limit the deposit surface; the diameter of the hole

(i.e. the diameter of the deposit) was 15 mm. A sealing film and a stainless steel plate were used to ensure the tightness of the cell and electric connection. A stirring magnet with a length of 20 mm was used to stir the solution at the bottom of the cell.
For the co-deposition study, the working electrode (WE) was a 2.5 cm × 2.5 cm gold foil with a thickness of 50 µm provided by *Goodfellow*[132] (99.95 % purity). The auxiliary electrode (AE) was made of a platinum rod having a diameter of 1 mm. A silver chloride (Ag/AgCl/sat KCl), as the reference electrode (RE), was also used during the process. The distance between the WE and the AE was set at (1.0 ± 0.1) cm.

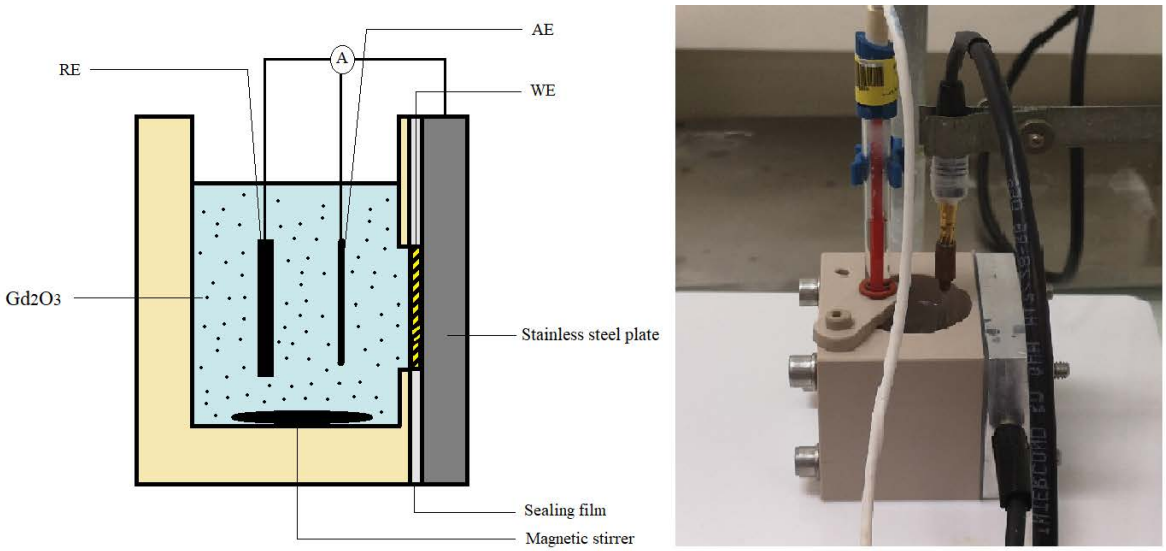


Fig. 2.5 Schematic diagram (left) and photo (right) of the cell structure and the electrodes positions used in our experiments. The cell contains 35 mL electrolyte. During the process, a magnetic stirring, a sealing film and a stainless steel plate are also used. Suspended $Gd_2O_3$ particles (black dots) were evenly distributed in the electrolyte thanks to the stirring. The schematic diagram is not drawn according to the actual scale.

### 1.3.5. Tools for the manufacturing and the characterization of deposits

#### 1.3.5.1. Deposit manufacturing equipment

During the manufacturing of deposits, chronopotentiometry and voltammetry were carried out using a *PGP201 Voltalab* Potentiostat/galvanostat with a *VWR Professional hotplate* to heat and stir the solution. The overall experimental assembly of co-electrodeposition is shown in Fig. 2.6. The cell was placed in the center of the hotplate; the three electrodes were connected with the potentiostat/galvanostat with wires.


Fig. 2.6 The overall experimental assembly of co-electrodeposition.

#### 1.3.5.2. Scanning Electron Microscopy (SEM) with Energy Dispersive X-Ray Analysis (EDX)

The scanning electron microscopy (SEM) coupled with the energy Dispersive X-Ray Analysis (EDX) is an instrument used to study the surface of a sample. SEM provides detailed images of sample surface by scanning a focused electron beam across a surface and detecting secondary or backscattered electron signals. EDX provides elemental identification and quantitative compositional information of samples by interaction of emitting electrons with matter and X-rays detection[133]. The emitted electrons may excite an electron in an inner shell of the sample atom and eject it from the shell; this process creates an electron hole, which will be filled by an electron from an higher energy shell. Then the difference in energy between the higher energy shell and the lower energy shell may be released in the form of an X-ray. Since the energy of the X-ray comes from the energy difference of the two shells and is specific to each atom, EDX is allowed to identify the sample atoms and measure the speciation of the sample.

In this work, the *JEOL JSM 71OOF* was used. For the characterization of surface morphology through SEM, the accelerating voltage used was 15 kV. At this high voltage, the distinction between non-metallic $Gd_2O_3$ particles and Ni metal particles is more obvious[134]. For each sample, five measurements were carried out with a magnification of 100×, 1000× and 5000× at 5 positions of the surface (top, bottom, left, right, and center positions). For EDX measurements, the region dimension of the analysis was about 1.1 mm × 0.8 mm at a magnification of 100×. The measuring time was 60 s. The uncertainties are determined by calculating the standard deviations on these values. Since the surface of the deposit was not perfectly flat, and the X-rays scattered by the sample can be absorbed, quantitative measurements were impossible, the results of EDX were only used to have a first idea of the composition of the investigated position. The proportion of each component in the deposit was characterized by the Inductively Coupled Plasma - Atomic Emission Spectrometry (ICP-AES) after the dissolution of the deposit.

#### 1.3.5.3. Inductively Coupled Plasma - Atomic Emission Spectrometry (ICP-AES)

The Inductively Coupled Plasma - Atomic Emission Spectrometry (ICP-AES) is a technique used to measure the composition and concentration of elements in a sample. ICP uses plasma to excite sample atoms and then detect the wavelength emitted by excited atoms. Since the wavelength is highly selective for a specific element, and its intensity is proportional to the amount of that element in the sample, ICP-AES can therefore identify and quantify elements in samples[135]. This technique is complementary to EDX: EDX can only give qualitative local elemental composition, while ICP can analyze the total quantification value of the whole deposit.

In this work, the *Thermo Scientific iCAP 6000 Series ICP-AES* was used to investigate the concentration of Gd in the deposit. Gd, Ni and Zn standards from *SCP Science*[136] were used to perform calibration in the range from 10 ppb to 200 ppb for Gd and 50 ppb to 2000 ppb for Zn and Ni. All deposits were dissolved in 10 mL of concentrated HCl (37%) for 2 h to separate deposits and gold substrates. The concentrated HCl was provided by *Sigma-Aldrich*. The dissolved solution was diluted 1000 times with 1% $HNO_3$ (67% $HNO_3$ supplied by *Sigma-Aldrich* diluted in ultra pure water) and then analyzed by ICP. Each sample was measured three times, and the uncertainty was determined by the variance of the three measurements. The detection limit was less than 1 ppb[137].

## 2.2. Co-electrodeposition of Ni and $Gd_2O_3$

### 1.4.1. Optimization of co-electrodeposition parameters of Ni-$Gd_2O_3$

To evaluate the optimal condition for Ni-$Gd_2O_3$ composite deposit, several studies of the influences of process parameters were carried out.

#### 1.4.1.1. Substrate roughness effects

Many researches show that substrate roughness can affect the deposit quality[138–140]. To evaluate effects of roughness substrate on deposit quality, a rough gold plate with a thickness of 1000 µm and a gold foil with a thickness of 50 µm polished with 80-grit sandpaper were used as substrates.

The photo of a deposit on a rough gold plate and its surface morphology under SEM are shown in Fig. 2.7. It can be seen that, affected by the roughness of the substrate surface, the entire deposit is very uneven, with obvious protrusions and depressions. In addition, $Gd_2O_3$ particles are rarely observed in the depression parts. This inhomogeneity of the distribution may be due to changes in the diffusion layer due to surface roughness. When the substrate is smooth, the diffusion layer is evenly distributed on the base surface, the concentration gradient of Ni ions and $Gd_2O_3$ particles between the bulk solution and the substrate-solution interface is therefore linear thanks to homogenous diffusion[138,141]. However, when the substrate is rough, the diffusion layer is concentrated to protrusion parts, which contributes to the nucleation in protrusions[138,141]. Thereby, more $Gd_2O_3$ particles can be incorporated into this process.

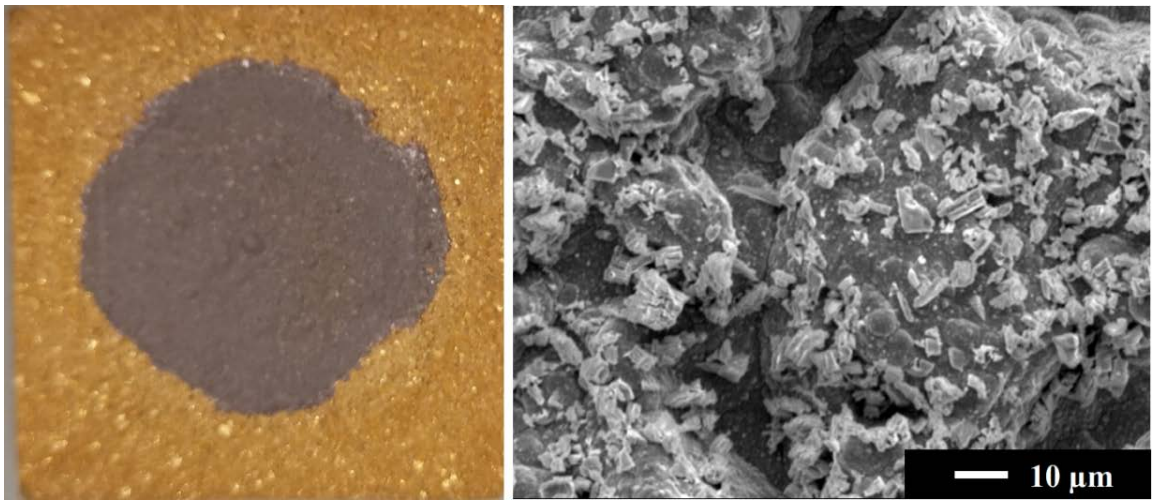


Fig. 2.7 Photo of a deposit with rough gold plate substrate (left) and its surface image under SEM (right). The applied potential was -1.20 V/NHE, the stirring speed was 300 rpm, the $Gd_2O_3$ loading was 6.5 g, and the temperature was 30°C.

The photo of a deposit on a gold foil polished with 80-grit sandpaper and its surface morphology under SEM are shown in Fig. 2.8. Compared with Fig. 2.7, the distribution of $Gd_2O_3$ is similar to that of Fig. 2.7 but the roughness of the substrate is reduced. However, since nickel is more likely to nucleate at the protrusions, the grinding marks are still obvious on the surface.

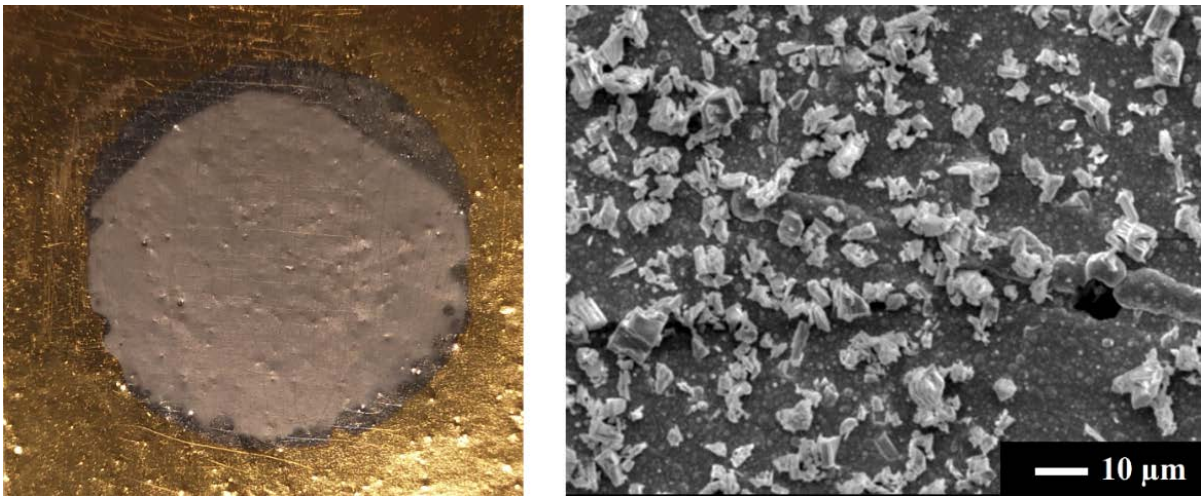


Fig. 2.8 photo of deposit on a gold foil polished with 80-grit sandpaper (left) and its surface morphology under SEM (right). The applied potential was -1.20 V/NHE, the stirring speed was 300 rpm, the $Gd_2O_3$ loading was 6.5 g, and the temperature was 30°C.

The influence of the rough substrate on the deposit is mainly on the distribution of particles, and this inhomogeneity will cause a variety of computational difficulties during the measurement of cross sections. Therefore, smooth gold foil was chosen as substrate in this work.

All deposits manufactured in sections from 1.4.1.1 to 1.4.1.5 were deposited on smooth gold foils with a thickness of 50 µm.

#### 1.4.1.2. Applied potential effects

To choose the potential ranges for a good Ni deposit, voltammetry curves with 5 cycles were performed. Since the potential range of interest is in the negative interval (to reduce Ni ions), the scanning potential varied from -0.1 V/NHE (Normal Hydrogen Electrode) to -1.5 V/NHE for 5 cycles, the scanning speed was 0.05 V/s. All curves of each cycle have the same behavior. Fig. 2.9 shows the voltammetry curves associated with the fifth cycle in Ni electrolyte (9 g/L) at pH 9.8, with $Gd_2O_3$ loading (0.8 g or 6.5 g) or without $Gd_2O_3$ loading. The temperature of the electrolyte was fixed at 30°C. The solution was stirred by a magnet rod at 300 rpm. It can be seen from the figure that the reduction process happens when the potential is less than -0.7 V/NHE while the oxidation process happens when the potential is bigger than -0.5 V/NHE. For the voltammetry curves without $Gd_2O_3$ loading (red dotted curves in both (a) and (b) of Fig. 2.9), an oxidation peak can be observed between -0.4 V/NHE and -0.5 V/NHE, which may be explained by the formation of $Ni(OH)_2$ on the surface of the electrode according to Milosev et al.[142]. In the range -1.1 V/NHE to -1.3 V/NHE, the current density is between -10 mA/cm² and -25 mA/cm². The reduction process has also a peak near -1.1 V/NHE, which is probably due to the reduction from $Ni(OH)_2$ to Ni [142]. When the voltage is more negative than -1.3 V/NHE, small fluctuations appear on the curve. This may be due to the enhanced reduction of hydrogen, which may explain the formation of dendritic structures and holes on the deposits in this voltage range (Fig. 2.11, pictures g and h).

It should be noted that when only 0.8 g of $Gd_2O_3$ was loaded, the voltammetry curves (figure (a) of Fig. 2.9) is very similar to that without $Gd_2O_3$ loading, while the difference became more obvious when 6.5 g of $Gd_2O_3$ was loaded (figure (b) of Fig. 2.9). From -1.1 V/NHE to -1.5 V/NHE, the difference of the current density between 0.8 g loading and no loading is only 3.7 %, while this difference increases to 12.2 % with 6.5 g of loading. The influences of $Gd_2O_3$ loading will be explained in the next subsection.

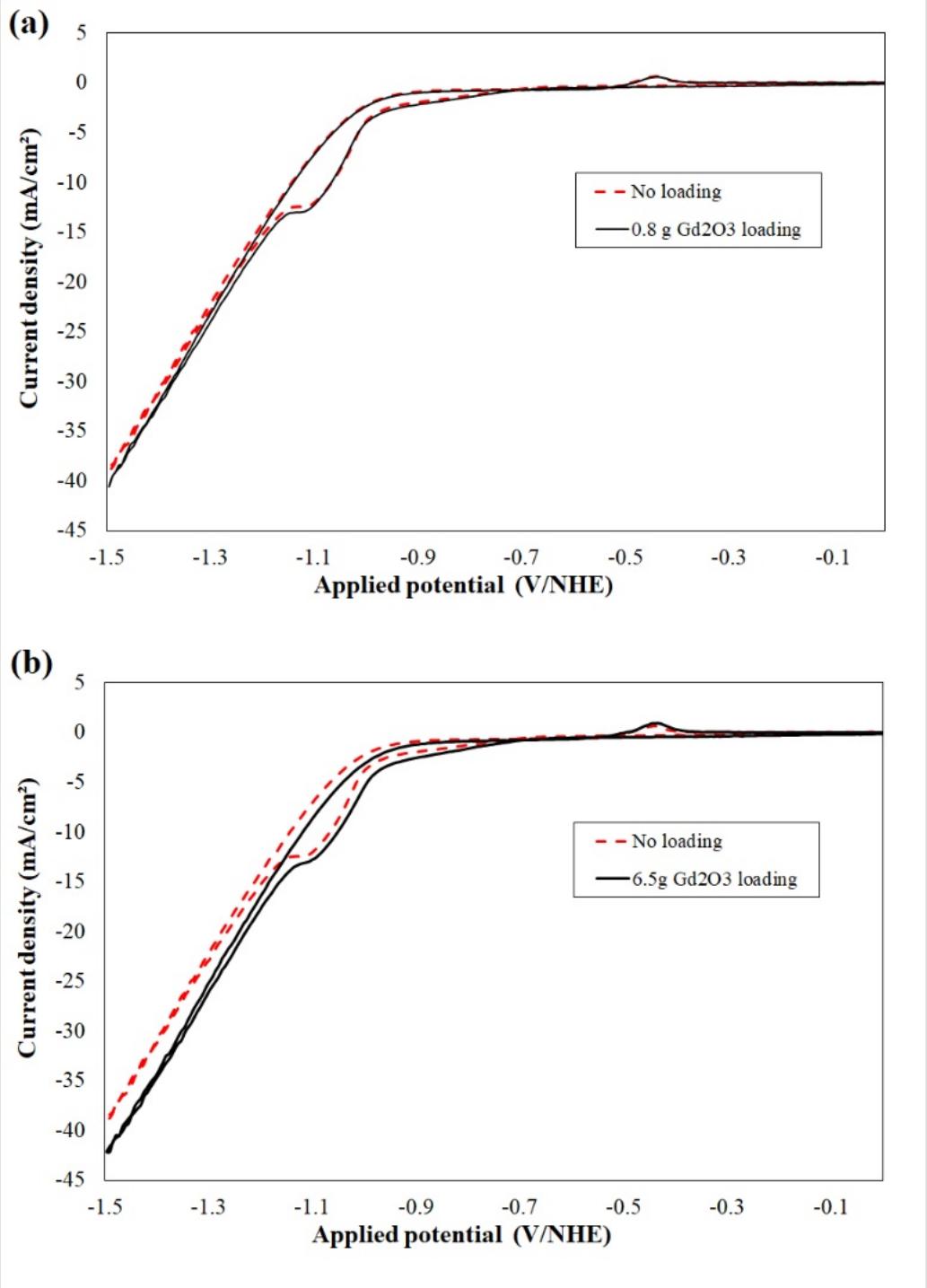


Fig. 2.9 Voltammetry curves of Ni with or without $Gd_2O_3$ loading (0.8 g $Gd_2O_3$ for (a) and 6.5 g $Gd_2O_3$ for (b)). Sweep from -0.1 V/NHE to -1.5 V/NHE for 5 cycles with a scanning speed of 0.05 V/s. The curves presented are the curves of the fifth cycle (all curves). The temperature of the electrolyte was 30°C and the pH was 9.8.

Several deposits were performed to investigate the effects of applied potential on deposit quality. Four applied potential values were -1.04, -1.16, -1.20 and -1.30 V/NHE. These values were chosen because they are evenly distributed in the reduction potential range. Effects on the average current density, the areal density, the Gd quantity and the Gd ratio are summarized in Table 2.6. The areal density is calculated after measuring the mass and the surface (counting

pixels) of the deposit. The Gd quantity is measured by ICP-OES. The "Gd ratio in the deposit" represents the Gd content fraction, it is the ratio of the atomic weight of Gd to the total atomic weight in the deposit. Each of the co-electrodeposition processes lasted 1 hour at 30°C, with a stirring speed of 300 rpm, and a loading of $Gd_2O_3$ of 6.5 g. Table 2.6 shows that when the applied potential is low enough (-1.04 V/NHE), the Gd ratio in the deposit is the highest (8.5 at.%). However, due to the lower current density (-1.9 mA/cm²), the areal density of the deposit is limited ($0.28 \times 10^{18}$ at/cm²), as a result, the total Gd content is limited (only 1.2 mg of Gd were trapped in the deposit in these conditions). As the applied potential becomes more and more negative, the deposit kinetics increases, although the Gd ratio in the deposit remains relatively low (around 4%). In this case, the total Gd quantity trapped in the deposit increases as the increase of deposit thickness.

Table 2.6 Applied potential effects on average current density, deposit areal density, deposited Gd mass, and Gd content in Ni-$Gd_2O_3$ composites deposits.

| Applied potential (V/NHE) | Average current density (mA/cm²) | Areal density ($10^{18}$ at/cm²) | Gd quantity (mg) | Gd ratio in the deposit (%) |
|---|---|---|---|---|
| -1.04 | -1.9 ± 0.4 | 0.28 ± 0.04 | 1.2 ± 0.3 | 8.5 ± 0.6 |
| -1.16 | -9.3 ± 0.6 | 1.11± 0.05 | 1.8 ± 0.1 | 3.6 ± 0.1 |
| -1.20 | -10.2 ± 0.6 | 1.31 ± 0.06 | 3.0 ± 0.4 | 4.3 ± 0.3 |
| -1.30 | -17.3 ± 0.9 | 2.42 ± 0.16 | 8.6 ± 0.6 | 4.5 ± 0.6 |

EDX analysis coupled with SEM were also performed to see deposits morphology. Two kinds of particles with different brightness appear on the surface, the contrasts can be seen easily in Fig. 2.11. The EDX analysis at a magnification of 100x was carried out in different area of the deposit to analyze the composition of the deposit and identify particles with different brightness, one spectrum is shown in Fig. 2.10. From the spectrum, several KLM lines of Ni, Gd or O atoms were detected, which proves the presences of Ni and $Gd_2O_3$ in the deposit. The expression and differences of the KLM lines are presented in *Appendix 2.4*. To further identify the Ni and $Gd_2O_3$ areas, the darker particles and the brighter areas were focused and magnified 5000 times, EDX results showed that the proportion of Gd increased a lot (*Appendix 2.4*) when the brighter areas were focused and vice versa. Therefore, the darker particles were identified as Ni while the brighter particles were identified as $Gd_2O_3$ structures.

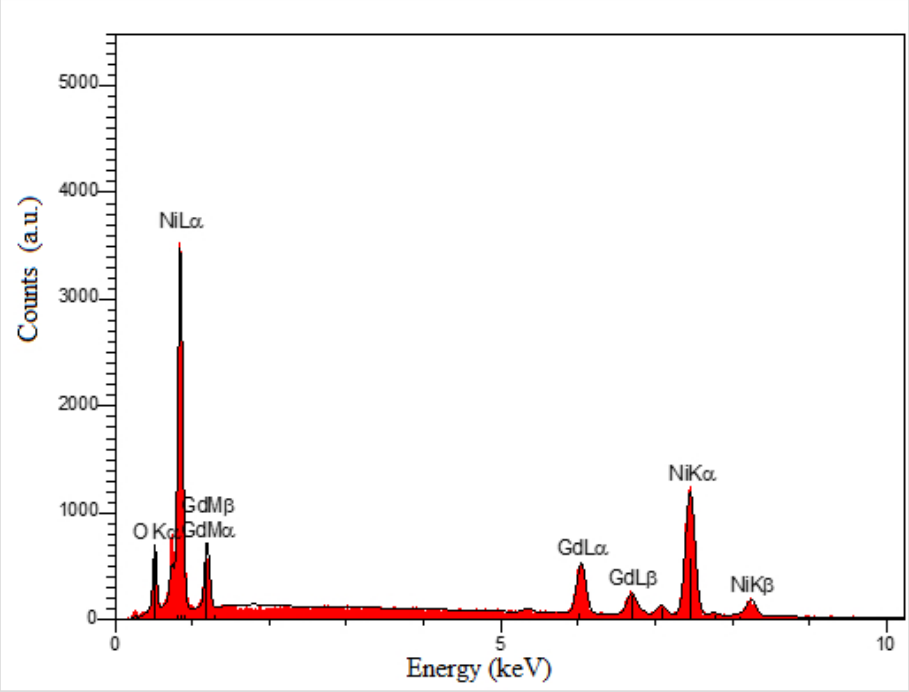


Fig. 2.10 EDX analysis of the chemical composition of the deposits. Applied potential was -1.20 V/NHE, stirring speed was 300 rpm, $Gd_2O_3$ loading was 6.5g, $Ni^{2+}$ concentration was 0.14 mol/L, pH = 9.8.

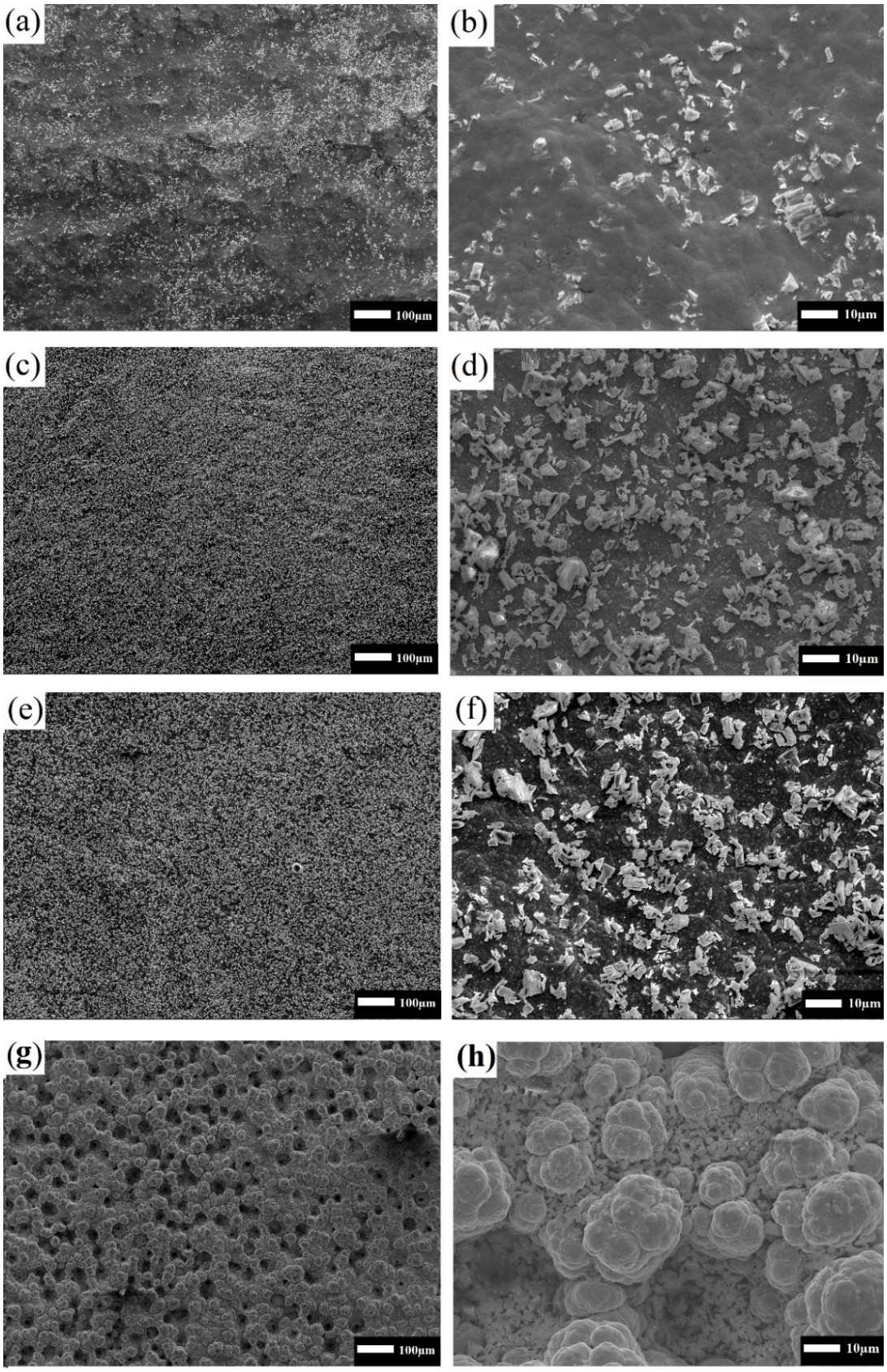


Fig. 2.11 Microscopic images of surface morphology and $Gd_2O_3$ distribution of the deposits, as areas with high concentration of Gd are the brighter areas. Loaded $Gd_2O_3$ was 6.5 g, stirring speed was 300 rpm, applied potential was -1.04 V/NHE (a, b), -1.16 V/NHE (c, d), -1.20 V/NHE (e, f), -1.30 V/NHE (g, h).

Fig. 2.11 presents general morphology studies of four deposits under different potentials (from -1.04 V/NHE to -1.30 V/NHE). As can be seen in (a) and (b) of Fig. 2.11, with a potential of -1.04 V/NHE, the deposit surface was uneven and some Ni matrix was not covered by $Gd_2O_3$. This may be because the thickness of the deposit is too thin to smooth enough the rough surface of the substrate. In addition, under this applied potential condition, the distribution of $Gd_2O_3$ particles was not uniform on a microscopic scale (10 µm). When the potential value was set between -1.16 V/NHE and -1.20 V/NHE (c, d, e and f on Fig. 2.11), the microscopic surface structures of deposits were very similar. Their surfaces were smoother with more uniform $Gd_2O_3$ trapped in the Ni matrix as compared to the previous conditions. However, when the applied potential was too negative (-1.30 V/NHE), cauliflower-like structures and craters of Ni form on the deposit surface leading to a honeycomb-like overall deposit structure. This morphology is similar to morphologies of Ni or Cu co-electrodeposition in very negative potential[143–145]. Crater structures may be caused by the formation of water due to hydrogen reduction reaction[145]. There was very little quantity of $Gd_2O_3$ on the larger cauliflower particles, $Gd_2O_3$ particles were gathered in the craters. However, because the surface was too rough, we cannot see bright areas as $Gd_2O_3$ particles deposited in the crater did not show a bright color (Fig. 2.11 h). The EDX analysis of craters after 5000x magnification can be seen in *Appendix 2.4*. With the formation of dendritic patterns, these deposits exhibit low adhesion and poor uniformity of $Gd_2O_3$, which makes them unsuitable as a target.

The $Gd_2O_3$ composite size were mesured with the help of SEM, and Fig. 2.12 shows the SEM image of the same deposit in Fig. 2.11 (c,d) by magnifing 10000 times. It can be seen from the image that $Gd_2O_3$ particle size is between 0.5-3 µm, and most particles are clustered together.

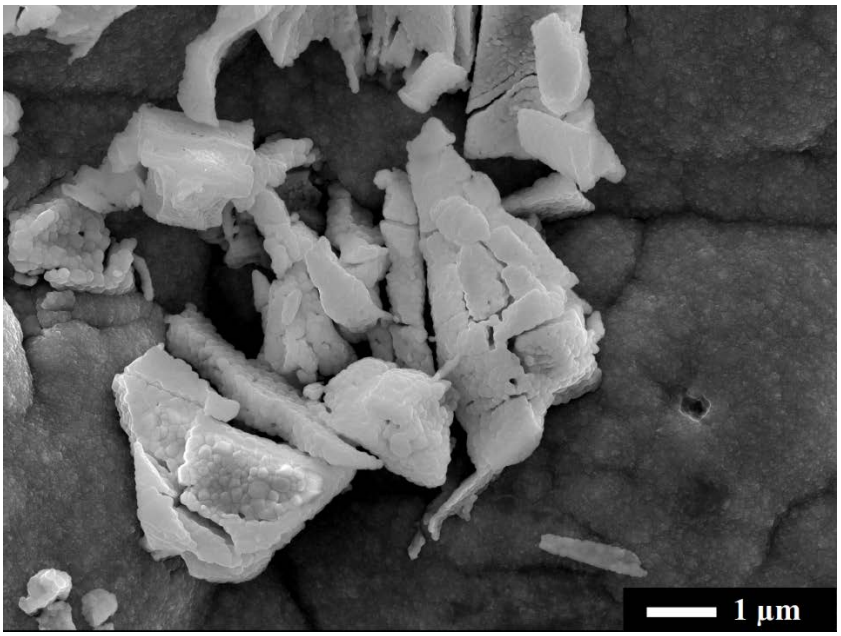


Fig. 2.12 Microscopic images of surface morphology and $Gd_2O_3$ particle size of the same deposit in Fig. 2.11 (c,d), the surface was magnified 10000 times.

Considering both the total Gd quantity obtained in the composite target and the quality of the deposit, -1.20 V/NHE was selected as the best-applied potential to prepare the composite target for irradiation experiments.

#### 1.4.1.3. $Gd_2O_3$ loading quantity effects

Voltammetry curves (Fig. 2.9) show a deviation of current density at the same potential. The comparison between no loading curves and $Gd_2O_3$ loading curves shows that with the addition of $Gd_2O_3$, the current density slightly decreases for the reduction of $Ni^{2+}$, which means the reduction of $Ni^{2+}/Ni$ becomes easier with $Gd_2O_3$. This may be because the absorption of $Gd_2O_3$ increases the surface area of the cathode, which in turn provides more nucleation sites for nickel ions[146]. Meanwhile, the slope of the reduction curve remains unchanged with or without $Gd_2O_3$, which indicates that the reaction mechanism does not be affected. Through the comparison between curves (a) and (b) of Fig. 2.9, it can be found that under the same potential, current density decrease is more obvious with more $Gd_2O_3$ loaded, which also means that more deposits can be obtained. Therefore, it can be speculated that $Gd_2O_3$ is a catalyst that can promote the reduction of $Ni^{2+}$ without affecting the electrochemical behavior of the solution.

To investigate the effect of $Gd_2O_3$ loading, deposit Gd content was analyzed by ICP-AES. From Fig. 2.13, $Gd_2O_3$ loading varies from 0.1 g to 6.5 g with 6 measuring points: 0.1 g, 0.5 g, 1.0 g, 2.0 g, 4.0 g and 6.5 g, the associated concentrations are 2.9 g/L, 14.3 g/L, 28.6 g/L, 57.1 g/L, 114.3 g/L and 185.7 g/L. The mass was measured by a balance, and the error was 0.001g. The stirring speed was 300 rpm, the applied potential was -1.20 V/NHE, and the temperature was 30°C for all these deposits. Experiments were repeated 3 times for each $Gd_2O_3$ loading, Fig. 2.13 shows the change of the Gd quantity trapped in the deposit as the addition of $Gd_2O_3$ increased. Data present mean values and standard deviations associated with each $Gd_2O_3$ content were measured by ICP-AES. Lines in Fig. 2.13 are not adjustments, they were only used to connect the points.

The total amount of $Gd_2O_3$ trapped in the deposit is positively correlated with the amount of $Gd_2O_3$ in the solution (Fig. 2.13 (a)). About 0.4 mg Gd is trapped in the deposit for 0.1 g of $Gd_2O_3$ loading that corresponds to 0.04 % of the initial amount, while for 6.5 g of $Gd_2O_3$ loading, the deposit contains 3.0 mg Gd which is 0.05% of the initial amount. The effect of $Gd_2O_3$ loading is more obvious when the amount is smaller: when the loading mass increases from 0.1 g to 2.0 g, the trapped mass increases from 0.4 mg to 2.5 mg, corresponds to 0.04% and 0.13% of the initial amount. The effect of $Gd_2O_3$ loading is weakened when its quantity is more than 2.0 g.

The change in utilization rate of Gd with the $Gd_2O_3$ loading is reported in Fig. 2.13 (b). For one deposit, if $Gd_2O_3$ remaining after deposition cannot be collected, a high incorporation rate is beneficial for cost saving when using enriched gadolinium oxide. So, a balance must be found to use as little as possible $Gd_2O_3$ while ensuring that sufficient Gd is trapped in the deposit. However, if these powders can be collected and recycled for the next deposition, the large amount of powder initially added will not be all wasted (section 2.4). This utilization rate can be important to estimate how many deposits can be obtained with initial $Gd_2O_3$ loading.

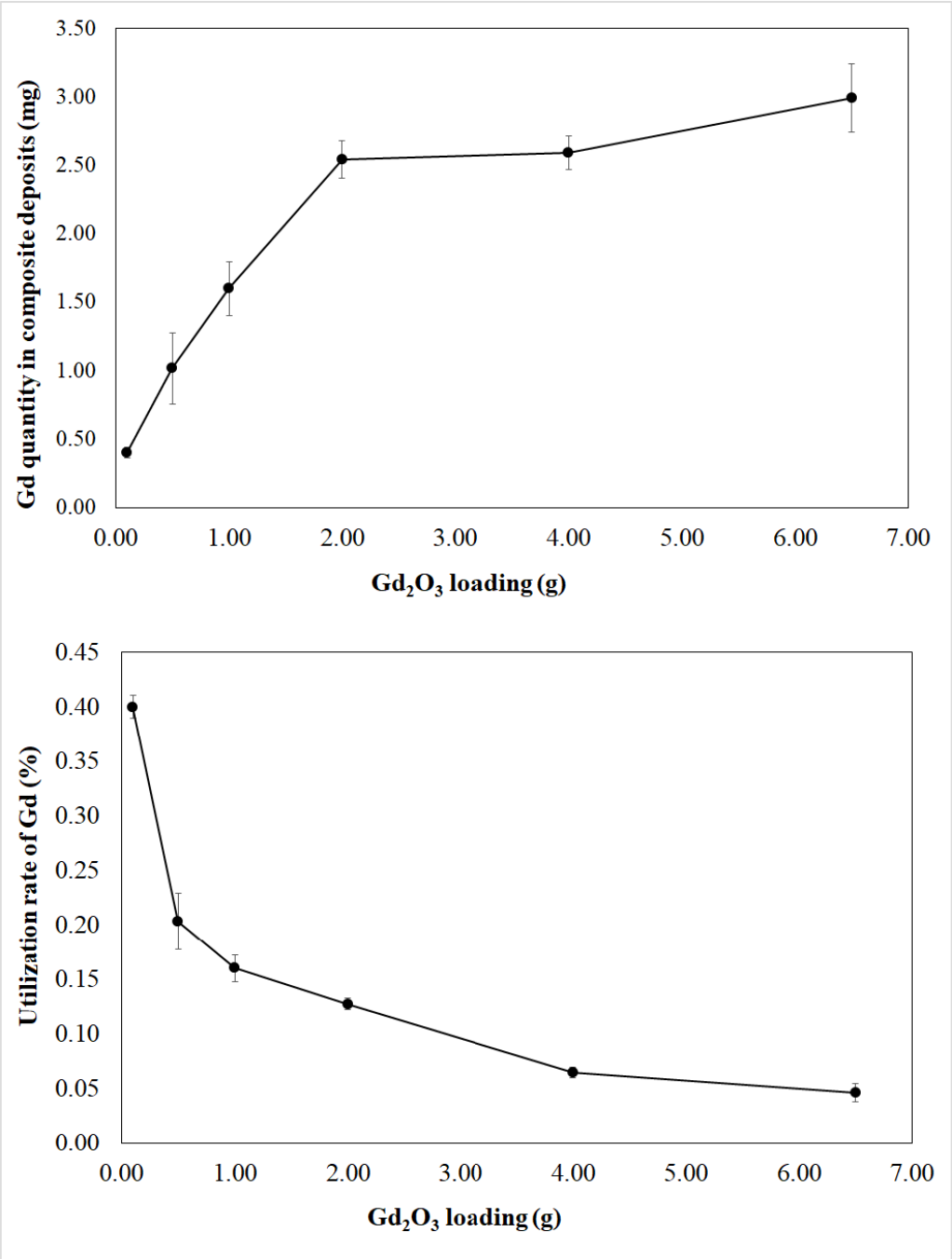


Fig. 2.13 Effects of $Gd_2O_3$ loading on the quantity of Gd trapped in Ni-$Gd_2O_3$ deposits. (a) mass of Gd in deposits. (b) Percentage of trapped Gd relative to the mass of $Gd_2O_3$ incorporated. The stirring speed was 300 rpm, the applied potential was -1.20 V/NHE.

#### 1.4.1.4. Stirring speed effects

In the process of co-electrodeposition, the capture of $Gd_2O_3$ particles is a mechanical process where charged $Ni(NH_3)_6^{2+}$ and $Ni(NH_3)_5^{2+}$ ions formed by the complexation of $NH_3$ and $Ni^{2+}$ (see 2.1.1) could wrap around $Gd_2O_3$ particles to form clusters. To achieve this, $Gd_2O_3$ clusters that are in suspension in the electrolyte need to pass through the convection layer, diffusion layer and electrical double layer to finally reach the deposited layer[146] (see section 1.3.3). The effect of stirring is not only to distribute the clusters as evenly as possible in the electrolyte but

also to change the flow rate of the fluid (turbulent, laminar, etc.), which will affect the transport of clusters in the convection layer.

To evaluate the effects of stirring speed, different deposits were fabricated with a stirring speed varied from 100, 300, 400, 600, to 800 rpm. Applied potential was fixed at -1.20 V/NHE, the $Gd_2O_3$ loading was 6.5 g, and the temperature was 30°C. Photos of some of the deposits are shown in Fig. 2.14. It can be seen that when the stirring speed is too high (400 rpm, 600 rpm or 800 rpm), the deposit appears in two parts, bright and matte. Fig. 2.15 shows SEM analysis of a deposit at 800 rpm in matte part (1) and bright part (2). Many $Gd_2O_3$ amount were observed in the matte part of the deposit while only a few $Gd_2O_3$ amount were trapped in the bright part. So the bright part can almost be seen as only Ni crystals. The same phenomenon was observed on different deposits. Therefore, when the stirring speed is too high, the distribution of $Gd_2O_3$ is completely inhomogeneous, and such deposits cannot be used for the measurement of cross-sections.

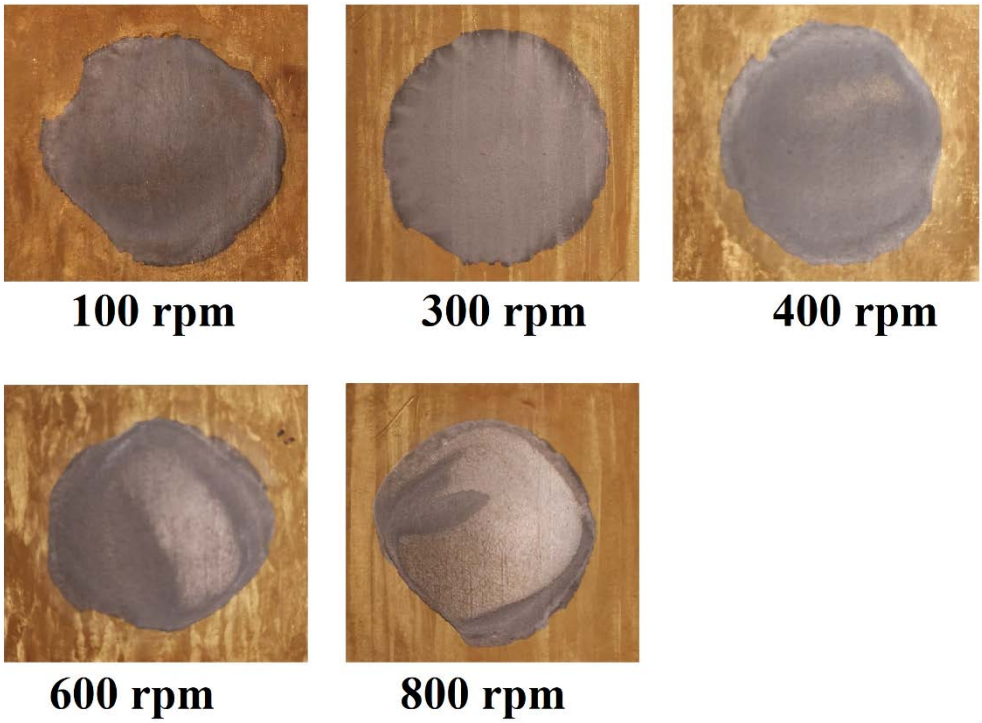


Fig. 2.14 Photo of several deposits with different stirring speeds. The applied potential was -1.20 V/NHE, the $Gd_2O_3$ loading was 6.5 g, and the temperature was 30°C.

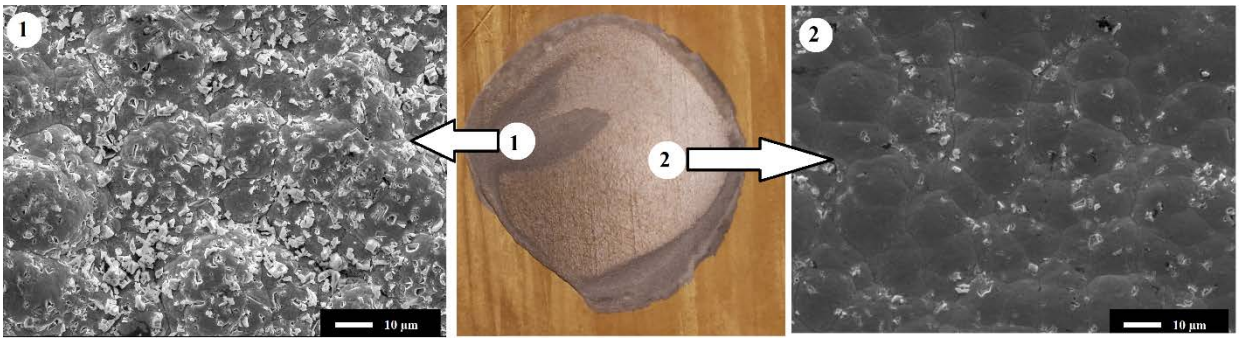


Fig. 2.15 Microscopic images of surface morphology and Gd2O3 distribution of the matte part (1) and bright part (2) at a magnification of 100×. The stirring speed of the deposit was 800 rpm,the applied potential was -1.2 V/NHE, the $Gd_2O_3$ loading was 6.5 g, and the temperature was 30°C.

The effects of stirring speed on the Gd content of Ni-$Gd_2O_3$ deposits can be seen in Fig. 2.16. Each point in the figure is the average of three repeated experiments, and the error corresponds to the standard deviation. The line is not adjustment; it is just used for connecting all the points. It can be seen that the Gd content increases when the stirring speed increases from 100 rpm to 300 rpm (from 1.4 mg to 3.0 mg), but it decreases when the stirring speed increases further, from 300 rpm to 800 rpm (from 3.0 mg to 1.8 mg). The low Gd content at lower stirring speed may be explained as a cluster distribution problem: when the stirring speed is too low (100 rpm), the distribution of clusters is not homogeneous, more clusters gather at the bottom of the cell. The low Gd content at high stirring speed may be related to the convection process: when the stirring speed is too high (800 rpm), the electrolyte is in a turbulent state, and the strong hydrodynamic force takes away part of the $Gd_2O_3$ particles so that they cannot diffuse into the deposited layer. According to Guglielmi[147], the incorporation of inert particles takes two steps, particles are firstly loosely adsorbed and then irreversibly adsorbed. Excessive stirring may disrupt the loose absorption process. This could also explain why the higher the stirring speed, the bigger the bright part in the deposits (Fig. 2.14).

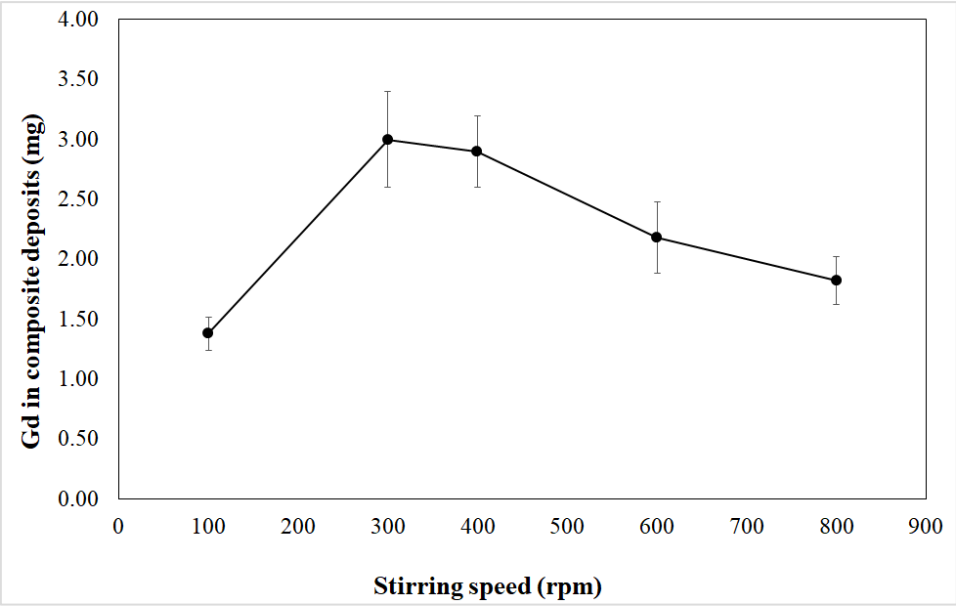


Fig. 2.16 Effects of stirring speed on the Gd content of Ni- $Gd_2O_3$ deposits. The applied potential was -1.2 V/NHE, the $Gd_2O_3$ loading was 6.5 g, and the temperature was 30°C.

From these results, the stirring speed was fixed at 300 rpm for the composite target making.

#### 1.4.1.5. Temperature effects

To evaluate temperature effects of co-electrodeposition, several deposits were made at different temperatures (25°C, 30°C, 35°C, and 40°C). Initial pH of electrolyte was 9.8, the applied potential was -1.20 V/NHE, $Gd_2O_3$ loading quantity was 6.5 g, stirring speed was 300 rpm, and deposition duration was 35 min. Experiments were repeated twice for each experiment temperature. The final pH of electrolyte, the areal density, the Gd quantity and the Gd content per unit thickness were shown in Table 2.7.

Table 2.7 Deposits information under different temperatures.

| Temperature (°C) | Final pH | Areal density ($10^{18}$ at/cm²) | Gd quantity (mg) | Gd content per unit thickness (µg/µm) |
|---|---|---|---|---|
| 25 | 9.8 ± 0.1 | 0.79 ± 0.13 | 1.8 ± 0.2 | 207 ± 40 |
| 30 | 9.5 ± 0.0 | 0.87 ± 0.01 | 1.8 ± 0.3 | 189 ± 32 |
| 35 | 9.4 ± 0.0 | 1.84 ± 0.23 | 2.9 ± 0.3 | 144 ± 23 |
| 40 | 9.3 ± 0.1 | 1.66 ± 0.03 | 2.7 ± 0.3 | 148 ± 17 |

According to Table 2.7, the decrease of electrolyte pH occurred in every sample and the higher the temperature, the greater the pH dropped. This decrease may be explained by the generation of $H^+$ during the reduction of $Ni^{2+}$ and the evaporation of $NH_3$ during the experiments. With final pH results, it can be supposed that when the temperature was higher, from 25°C to 35°C, the reduction process may be promoted. This can also be confirmed by the change of areal density and Gd incorporation quantity of deposits: at 35°C, the areal density is more than twice thicker that at 25°C, and the Gd quantity at 35°C is 2.9 mg while it is only 1.8 mg at 25°C. Meanwhile, when the temperature increased from 35°C to 40°C, thickness and Gd incorporation quantity decreased. Heating promotes electrodeposition but further heating has the opposite effect, this phenomena has also be confirmed in several works of Ni electrodeposition[118,148]. It may be because high temperature enhanced hydrogen evolution[118], which hindered the reduction of $Ni^{2+}$.

Although the Gd incorporation quantity is maximum at 35°C, if we compare Gd content per unit thickness, it can be seen that the maximum value is obtained at 25°C (207 µg/µm) followed by 30°C (189 µg/µm), and the minimum value is at 35°C (144 µg/µm). It is possible to prolong the deposition time to increase the thickness and get more Gd content at low temperatures (25°C and 30°C). In this case, a high Gd content per unit thickness is an advantage, which means low temperatures (25°C and 30°C ) are more suitable in this work. However, the deposition rate at 25°C is too low and the deposition homogeneity is poor (large areal density error). Therefore, considering all the factors, the selected temperature for this experiment is 30°C.

#### 1.4.1.6. Deposit homogeneity under optimal experimental conditions

Although we have studied the surface morphology of the deposits, we still do not know the distribution of $Gd_2O_3$ particles along the growth direction. To verify the distribution of $Gd_2O_3$

particles in our deposits, deposits made in the optimal conditions were immersed in 10 mL of concentrated sulfuric acid (98.3 wt.%) for 30 min at room temperature. $Gd_2O_3$ particles on the surface dissolve under the action of concentrated sulfuric acid, however, nickel is preserved due to the passivation[149] and protects inside $Gd_2O_3$ particles from being dissolved. SEM analysis of the surface of one deposit before and after the dissolution of concentrated $H_2SO_4$ is shown in Fig. 2.17. Apparently, after dissolution, $Gd_2O_3$ particles on the surface of the deposit all disappeared and left vacancies. All dissolved deposits show similar phenomena. These deposits, without $Gd_2O_3$ particles on the surface, were further dissolved with 10 mL of 12 mol/L of HCl at room temperature. The dissolved solution was used for ICP-AES analysis, which showed that the concentration of Gd was only 25% ± 2% of that in deposits not treated by $H_2SO_4$. This verifies that the distribution of $Gd_2O_3$ in the deposit is not uniform; $Gd_2O_3$ is more distributed on the surface of the deposit and less distributed inside the deposit. This gradient distribution of incorporated particles has been observed in many Ni co-electrodeposition studies[143,146,150]. Gradient distribution means that we may get less Gd compared to a uniformly distributed deposit with the same thickness. Therefore, it is necessary to find reasons for the gradient distribution and increase the Gd content inside the deposit.

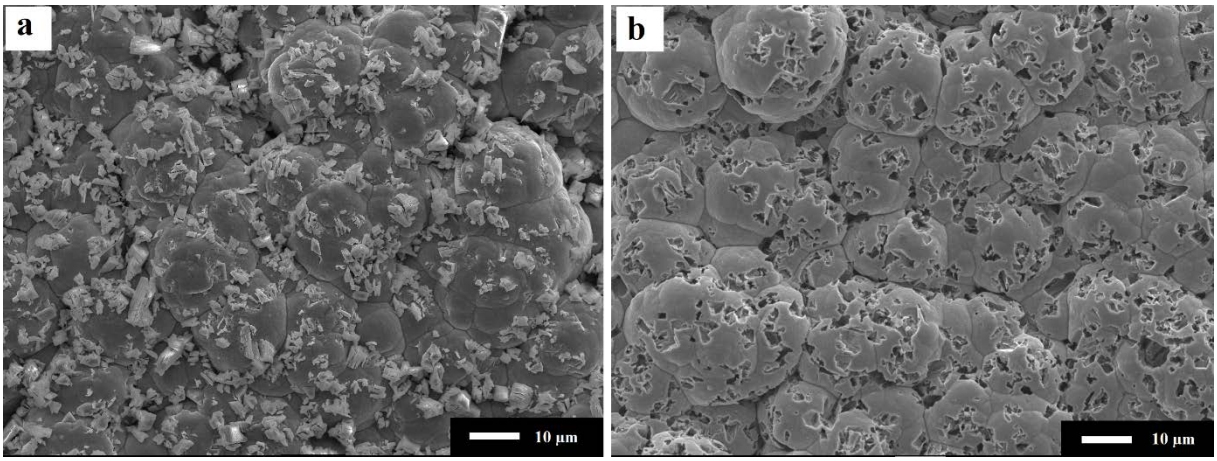


Fig. 2.17 SEM analysis of the surface of deposits before (a) and after (b) the dissolution of concentrated $H_2SO_4$. Deposit was made by optimal conditions: the applied potential was -1.2 V/NHE, the stirring speed was 300 rpm, the $Gd_2O_3$ loading was 6.5 g, and the temperature was 30°C.

Gradient distribution of $Gd_2O_3$ can be affected by many factors, such as stirring speed, initial concentration of loaded $Gd_2O_3$ particles, current density, etc. However, the above parameters remain unchanged in this work. One hypothesis is that $Gd_2O_3$ particles may be more easily captured on nickel substrate than on gold substrate. To verify this hypothesis, two types of deposits were manufactured. The first type is to co-deposit Ni-$Gd_2O_3$ directly on a gold substrate during 1 min, the second type is to firstly deposit a pure Ni layer on a gold substrate during 15 min to cover the gold substrate and then co-deposit Ni-$Gd_2O_3$ on the Ni layer during 1 min. Other experimental parameters remained unchanged: the applied potential was -1.20 V/NHE, the stirring speed was 300 rpm, the $Gd_2O_3$ loading was 6.5 g, and the temperature was 30°C. The morphology of these deposits were compared through SEM analysis (Fig. 2.18), it is clear that more $Gd_2O_3$ can be incorporated directly on the gold substrate than on Ni layer.

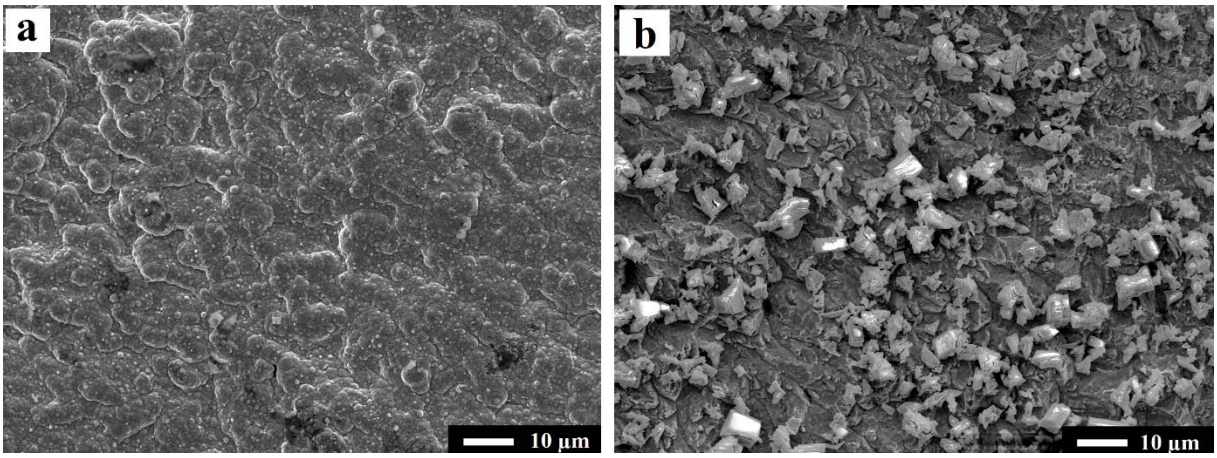


Fig. 2.18 SEM analysis of the surface morphology of (a) a deposit with a pure Ni layer on gold substrate and a Ni-$Gd_2O_3$ layer on Ni layer, and (b) a deposit with simple Ni-$Gd_2O_3$ layer on gold substrate. The applied potential was -1.2 V/NHE, the stirring speed was 300 rpm, the $Gd_2O_3$ loading was 6.5 g, and the temperature was 30°C.

The comparison of two deposits are shown in Table 2.8. The mass of the deposit on the gold substrate is 1.2 mg, which is twice more than that on the nickel substrate. The difference of mass may be due to the difference of electrical conductivity, gold ($44.2\times10^6$ siemens/m) is more conductive than nickel ($14.3\times10^6$ siemens/m), which lead to a more negative current density. The Gd atomic content is over 180 times more in deposit using gold substrate than that using nickel substrate. This means that gold substrate facilitates embedding of $Gd_2O_3$ particles in Ni deposit, the previous hypothesis does not hold.

Table 2.8 Comparison of deposit on a nickel substrate and deposit on a gold substrate

| Substrate material | Nickel | Gold |
|---|---|---|
| Substrate electrical conductivity ($10^6$ Siemens/m) | 14.3 | 44.2 |
| Mass of deposit (mg) | 0.5 | 1.2 |
| Gd atomic content (%) | 0.1 | 18.1 |

Another hypothesis is that as the thickness of the plating increases, the surface roughness of the deposit increases[151]. As verified in section 1.4.1.1, rough surfaces are more beneficial to increase the incorporation rate. To verify this hypothesis, a deposit was first deposited during 10 min (2.3 µm of the thickness) and the surface was analyzed at SEM (Fig. 2.19 (a)), then the deposit was deposited for another 50 min (13.5 µm of the thickness), and the same place of the surface was also analyzed by SEM (Fig. 2.19 (b)). The comparison of the two images proves that the roughness of the deposits does not increase with the increase of deposition time, conversely, the surface of Ni is slightly flattened. The comparison also shows that there are more $Gd_2O_3$ on the surface when the deposit is thicker.

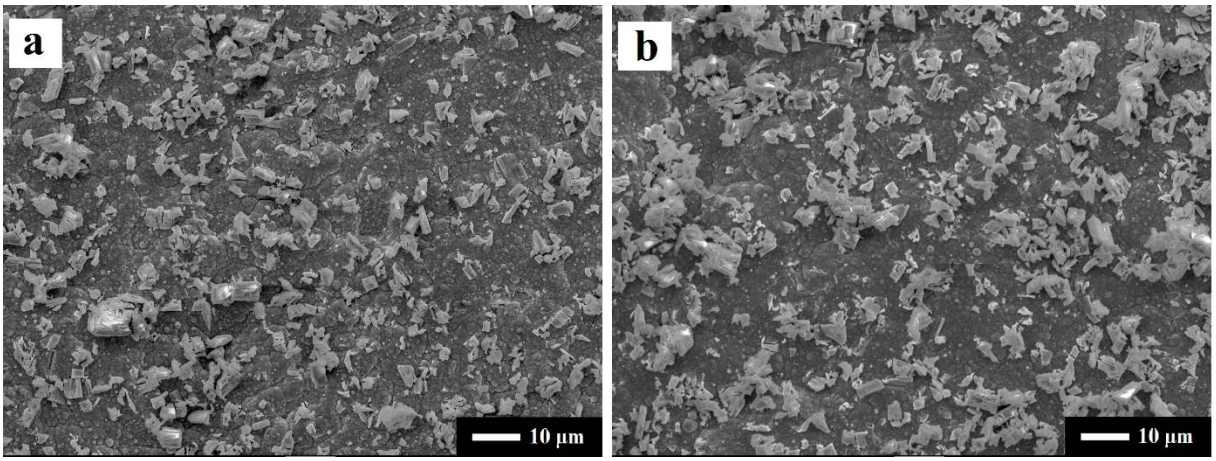

Fig. 2.19 SEM images of the surface of the same deposit at 2.3 µm (a) and at 13.5 µm (b).

The reason for the uneven distribution of $Gd_2O_3$ is not fully explained, but fortunately this uneven distribution in the depth direction is negligible compared to the beam size (1.0 to 1.5 cm of diameter) because the deposit is very thin (10-20 µm).

### 1.4.2. Multilayer deposit

In studying the longitudinal distribution of particles, a sandwich-like "multilayer deposit" scheme had been considered. This multilayer deposit refers to electroplating a thin layer of Ni on top of a thin Ni-$Gd_2O_3$ layer to remove the roughness of the deposit surface and increase conductivity, then another Ni-$Gd_2O_3$ layer is added on the top of Ni layer. If the process is repeated until the desired thickness, a multilayer deposit will be therefore manufactured. The schema of one multilayer deposit with 7 layers is shown in Fig. 2.20.

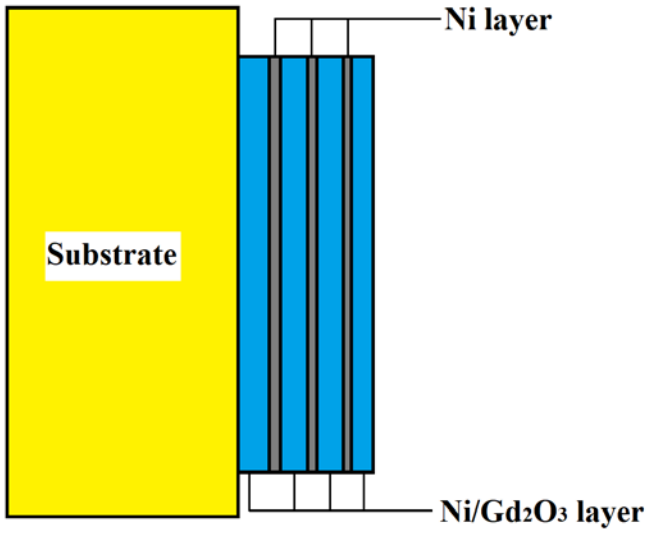

Fig. 2.20 Schema of multilayer deposits with 7 layers. The schema is not drawn to actual scale.

Different stirring modes were applied to deposit only Ni layer or to co-deposit Ni and $Gd_2O_3$ layer. As a screw propeller stirrer was used to stir at 800 rpm to obtain Ni layers, due to the turbulence of solution, almost no gadolinium oxide particles was co-deposited. Meanwhile, a

magnet was used to stir at 300 rpm to catch $Gd_2O_3$ particles and obtain Ni-$Gd_2O_3$ layers. Therefore, while keeping the electrolyte, potential, $Gd_2O_3$ loadings and temperature unchanged, multilayer deposit can be generated only by changing the stirring modes. The SEM image of each layer in the same place of the deposit is shown in Appendix Figure 1 in *Appendix 2.3*.

Several deposits with 7 layers were manufactured: the Ni-$Gd_2O_3$ layer was first co-deposited and then followed by a pure Ni layer, these two types of layers were alternately deposited until the 7th Ni-$Gd_2O_3$ layer. The duration of co-electrodeposition of each Ni-$Gd_2O_3$ layer was 15 min while the duration of each Ni layer was 5 min. The applied potential was -1.20 V/NHE, the stirring speed was 300 rpm, the $Gd_2O_3$ loading was 6.5 g, and the temperature was 30°C. Simple Ni-$Gd_2O_3$ monolayer deposits were also made in the same condition during 65 min. All deposits were dissolved by 12M of HCl for ICP-AES analysis. The comparison of a simple Ni-$Gd_2O_3$ monolayer deposit and a 7-layer-deposit is shown in Table 2.9. All values and their associated errors shown in Table 2.9 are average values.

Table 2.9 Comparison of multilayer deposit and monolayer deposit.

| Parameters | Multilayer | Monolayer |
|---|---|---|
| Thickness (µm) | 15.5 ± 0.8 | 14.9 ± 0.6 |
| The deposition rate (mg/cm²) | 11.0 ± 0.3 | 10.3 ± 0.4 |
| Atomic Gd content | 4.6% ± 0.7% | 3.6% ± 0.6% |

It can be seen that the thickness, the deposition rate, and the Gd content remain similar for multilayer and monolayer deposit when taking into account errors.
However, the objective of this work is to use thin target to measure reaction cross sections. In the case of the same thickness, the content of Gd in the single-layer target is sufficient to measure the reaction cross section. Considering the difficulty of the manufacture multilayer deposit, this method was ultimately not adopted.

After studying various parameters affecting co-electrodeposition, we found the optimal parameters for obtaining high quality deposits: the deposit should be deposited on a smooth gold substrate, with 6.5 g $Gd_2O_3$ loading, at -1.20 V/NHE, and with a stirring speed of 300 rpm.

## 2.3.Co-electrodeposition of Zn and $Gd_2O_3$

### 1.5.1. Optimization of co-electrodeposition parameters of Zn-$Gd_2O_3$

Similar to the research process of Ni-$Gd_2O_3$ composite deposit, several parameters that may affect deposit quality were investigated to determine optimal experimental conditions.

#### 1.5.1.1. Applied potential effects

To choose the potential ranges for a good Zn deposit, voltammetry curves with 5 cycles were performed at 30°C. The sweep potential varied from -0.50 V/NHE to -1.80 V/NHE for 5 cycles, the sweep rate was set at 0.05 V/s and the solution was stirred at 800 rpm with a magnet. The voltammetry curves of solution with or without 1.0 g $Gd_2O_3$ loading is shown in Fig. 2.21. All

curves of each cycle have the same behavior, Fig. 2.21 shows the voltammetry curves associated with the fifth cycle. Unlike nickel, oxidation and reduction of zinc is reversible. For the solution without $Gd_2O_3$, the oxidation of zinc begins at a potential value of -1.50 V/NHE and ends at -1.12 V/NHE, the value of the maximum current density is about 62 mA/cm² at -1.20 V/NHE. Meanwhile, for the solution with 1.0 g $Gd_2O_3$, the oxidation of zinc begins at a potential value of -1.50 V/NHE and ends at -1.10 V/NHE, the value of the maximum current density is about 58 mA/cm² at -1.22 V/NHE. According to the dominance diagram of zinc (subsection 1.3.4.2, Fig. 2.4), zinc ions is in the form of $Zn(OH)_4^{2-}$, the zinc oxidation half-equation is written as *eq. 2.3* according to Gunko et al.[152]:

$$Zn + 4\,OH^- \rightarrow Zn(OH)_4^{2-} + 2e^- \qquad (eq.2.3)$$

The reduction of zinc begins at a potential of -1.50 V/NHE and the current density stabilizes at -25 mA/cm² for the solution without $Gd_2O_3$ or with 1.0 g $Gd_2O_3$. Unlike the oxidation process, there are no reduction peaks; the maximum speed of the deposition kinetics is reached from the potential values mentioned above. The zinc reduction equation can be written as *eq. 2.4* [152]:

$$Zn(OH)_4^{2-} + 2e^- \rightarrow Zn + 4\,OH^- \qquad (eq.2.4)$$

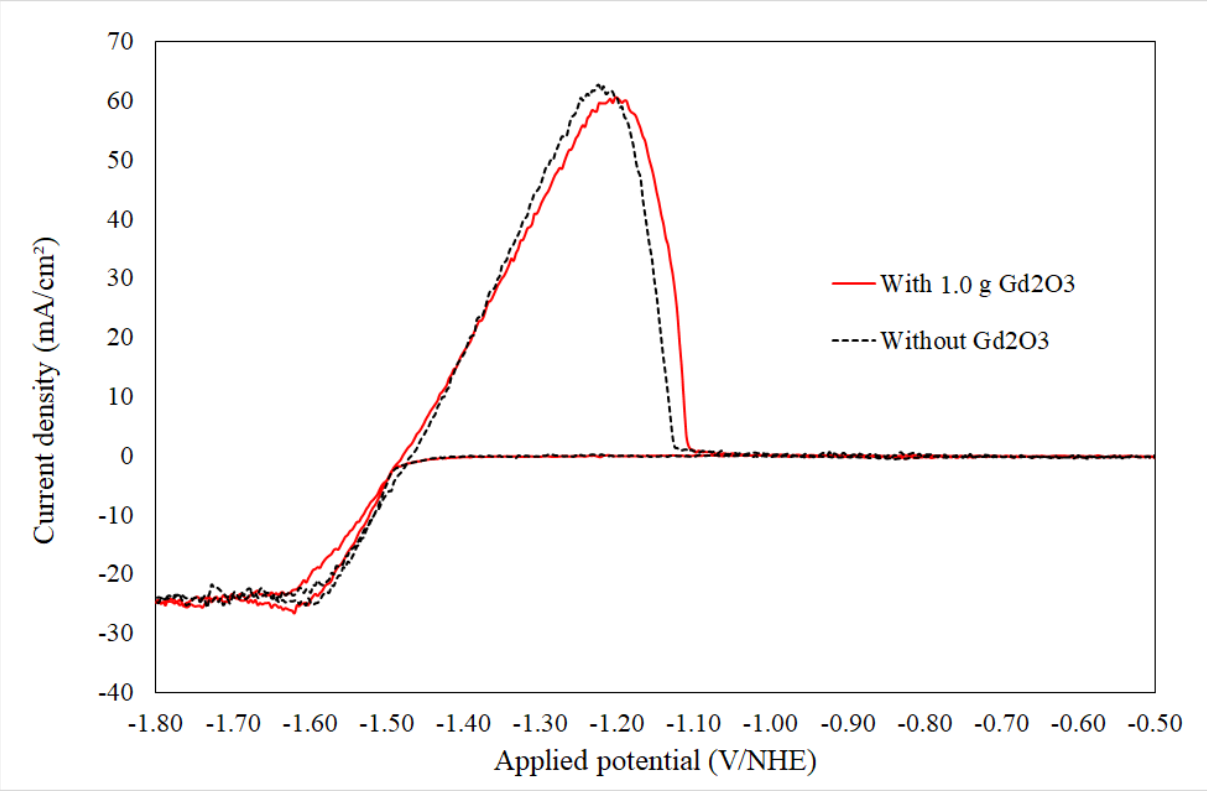


Fig. 2.21 voltammetry curves associated with the fifth cycle in Zn electrolyte without $Gd_2O_3$ loading (black curve) and with 1.0 g $Gd_2O_3$ loading (red curve) at 30°C. The stirring speed was 800 rpm with a magnet.

The voltammetry studies performed above showed that the reduction of zinc begins approximately at -1.50 V/NHE. In order to determine the optimum potential, series of Zn electrodeposition experiments were carried out: -1.52 V/NHE, -1.54 V/NHE, -1.56 V/NHE, -

1.58 V/NHE, -1.60 V/NHE and -1.62 V/NHE. Experiments at each applied potential were repeated three times. The stirring speed was fixed at 800 rpm and the temperature was fixed at 30°C. The morphology of each deposit was investigated by SEM analysis. Images of each deposit in the same applied potential are similar; some of these images are presented in Fig. 2.22. As shown in the figure, the deposit surface shows differences under different applied potential, which is mainly reflected in the grain size. When the applied voltage became more and more negative, the grain size of Zn was larger and had more nodules points, the surface was more rough, and dendrite structure appeared when applied potential was too negative (-1.62 V/NHE). This may because when the applied potential is more negative, the absolute value of current density is bigger, and the current density promotes the deposit deterioration by increasing the nucleation rate[153]. In addition, the increase of hydrogen reduction at low potential may also contribute to the formation of dendrites. This result indicates that the optimal applied potential is around -1.52 V/NHE and -1.54 V/NHE.

Several Zn-$Gd_2O_3$ composite deposits were made to further compare the effects of -1.52 V/NHE and -1.54 V/NHE. The $Gd_2O_3$ loading was 6.5 g, the stirring speed was 800 rpm, the temperature was 30°C, and the duration of co-electrodeposition was 60 min. Details of the comparison are presented in Table 2.10. The comparison shows that the difference between the current density and the areal density of the deposit is not evident under the two applied potentials, and the content of $Gd_2O_3$ is higher (2.7 mg) at -1.52 V/NHE. Therefore, -1.52 V/NHE was chosen as the optimal applied potential.

Table 2.10 Applied potential effects on average current density, deposit areal density, deposited Gd mass and Gd content in Zn-$Gd_2O_3$ composites deposits.

| Applied potential (V/NHE) | Average current density ($mA/cm^2$) | Areal density ($10^{18}$ at/$cm^2$) | Gd quantity (mg) |
|---|---|---|---|
| -1.52 | -10.1 ± 0.4 | 1.52 ± 0.07 | 2.7 ± 0.2 |
| -1.54 | -10.5 ± 0.5 | 1.59 ± 0.08 | 2.0 ± 0.1 |

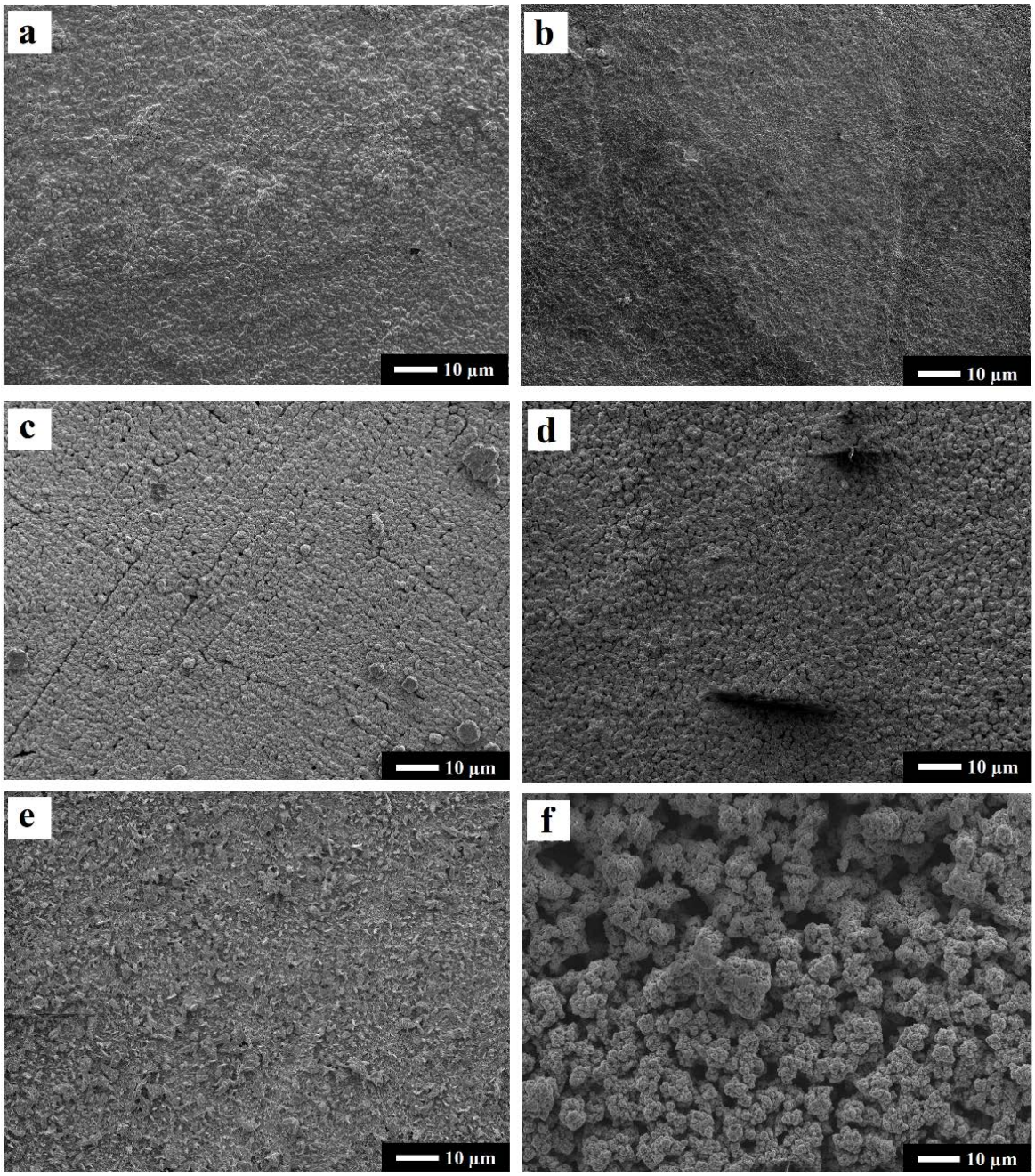


Fig. 2.22 Microscopic images of the morphology of Zn deposits in different applied potential: (a) -1.52 V/NHE, (b) -1.54 V/NHE, (c) -1.56 V/NHE, (d) -1.58 V/NHE, (e) -1.60 V/NHE and (f) -1.62 V/NHE. The stirring speed was 800 rpm and the temperature was 30°C.

#### 1.5.1.2. $Gd_2O_3$ loading quantity effects

Voltammetry curves (Fig. 2.21) show small deviations of current density at the same potential with or without $Gd_2O_3$ loading. In the oxidation wave, with the addition of $Gd_2O_3$, the applied potential range of the oxidation process has grown slightly, and the maximum current density slightly decreases. Meanwhile, no obvious difference has been found in reduction process. Overall, the presence of a small amount of $Gd_2O_3$ (1.0 g) has very little effect on Zn electrodeposition.

However, the presence of $Gd_2O_3$ caused the appearance of dendritic structures in deposits. Fig. 2.23 shows the photo of deposits with different $Gd_2O_3$ loading. The applied potential was -1.52

V/NHE, the stirring speed was 800 rpm, the temperature was 30°C, and the duration of co-electrodeposition was 60 min. When there was no $Gd_2O_3$ loading (Fig. 2.23 a), the Zn deposit was relatively uniform overall. As more $Gd_2O_3$ was added, dendrites became more pronounced, especially at the edge of the deposit (Fig. 2.23 b and Fig. 2.23 c). The edge area is rougher, the particle color is darker under the electron microscope, the middle area is smoother, and the particle color under the electron microscope is brighter. According to Wang et al.[154], the growth of dendrites is closely related to interfacial energy anisotropy and electrolyte conductivity. When $Gd_2O_3$ is added, the anisotropy of the interfacial energy increases with the increase of the loaded powder. The presence of low conductivity $Gd_2O_3$ particles hinders the movement of $Zn^{2+}$, this may lead to a non-uniform distribution of charge. Then, the difference of current density promotes the dendrite formation. The current density tend to be higher at substrate edges[120], so it is easier to form dendrites in the edge areas.

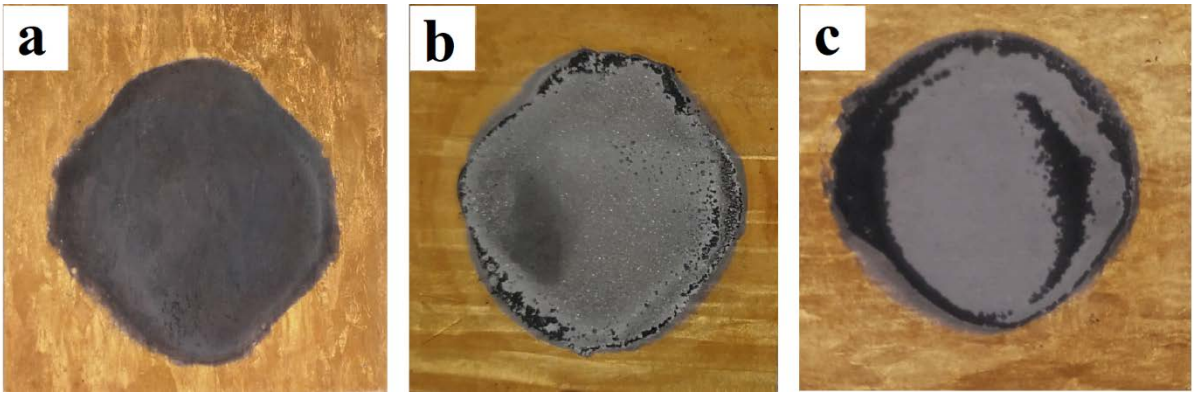


Fig. 2.23 Photo of deposits (a) without $Gd_2O_3$, (b) with 1.0 g $Gd_2O_3$, and (c) with 6.5 g $Gd_2O_3$. The applied potential was -1.52 V/NHE, the sirring speed was 800 rpm, the temperature was 30°C, and the duration of co-electrodeposition was 60 min.

To study the effect of $Gd_2O_3$ on Zn nucleation in areas without dendrites, these areas were investigated by SEM and compared with pure Zn deposit. Fig. 2.24 presents the SEM images of pure Zn deposit (a) and Zn-$Gd_2O_3$ deposit with 6.5 g $Gd_2O_3$ loading (b). For both deposits, the applied potential was -1.52 V/HNE, the stirring speed was 800 rpm, the temperature was 30°C, and the experiment lasted 60 min. It can be seen that the pure Zn deposit in the form of hexagonal plates accumulates layer by layer. This form of Zn deposit has been observed in several studies[155–157], it can be considered as a typical form of Zn electrodeposit. In Fig. 2.24(b), with the help of EDX analysis, the dark geometries at the bottom were identified as Zn deposits, and the brighter, smaller particles at the top were identified as $Gd_2O_3$. It is clear that hexagonal structure can be also observed and the size of the structure is close to the structure of pure Zn. Therefore, the presence of $Gd_2O_3$ does not affect the way that Zn are nucleated. This may be because the amount of trapped Gd is very small.

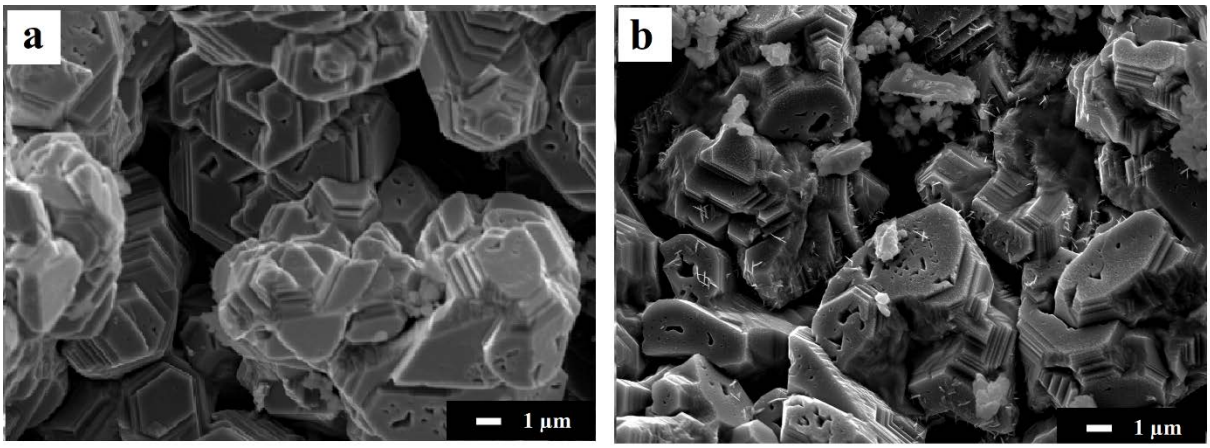


Fig. 2.24 Morphology studies of Zn deposit (a) and Zn-$Gd_2O_3$ co-deposit (b) by SEM. The applied potential was -1.52 V/HNE, the stirring speed was 800 rpm, the temperature was 30°C, and experiment lasted 60 min. For (b), 6.5g $Gd_2O_3$ was added.

To investigate the content of Gd in areas without dendrites in the deposits, EDX analysis was performed on different areas of the deposits. For all deposits, the applied potential was -1.52 V/NHE, stirring speed was 800 rpm, and $Gd_2O_3$ loading was 6.5 g. The EDX spectrum in no-dendrites area is shown in Fig. 2.25. The chemical composition shows that all three elements, Zn, Gd, and O, were detected, and there were no other unmatched peaks, indicating that the deposits did not contain other impurities. To investigate the exact composition content, $K_\alpha$ of Zn, Lα of Gd and Kα of O were used to quantify the atomic percentage of the deposits. The results showed that this area contains 2.0 % of Gd.

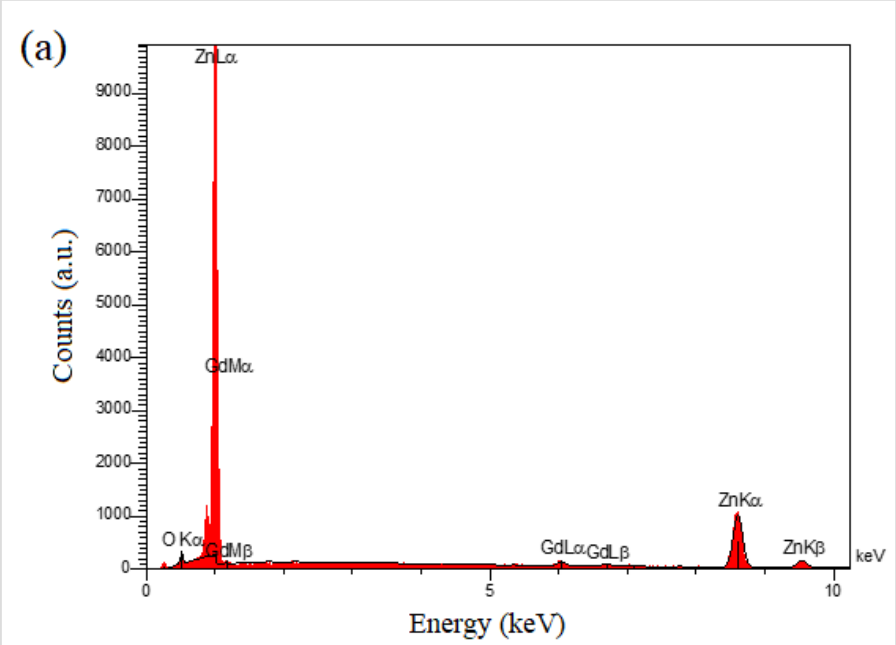


Fig. 2.25 EDX analysis of the chemical composition of the deposits in no-dendrites area. Applied potential was -1.52 V/NHE, stirring speed was 800 rpm, $Gd_2O_3$ loading was 6.5g.

In summary, the presence of $Gd_2O_3$ can easily affect the Zn electroplating and form dendritic structures at the edge of the deposit. However, in the central region of the deposit, the

electrodeposition of Zn is not affected. Since the addition of $Gd_2O_3$ will always result in the formation of dendrites, it is difficult to have a uniform deposit.

#### 1.5.1.3. Stirring speed effects

To study the influence of agitation, several deposits were made with different stirring speed at 400 rpm, 800 rpm and 1200 rpm. The applied potential was -1.52 V/NHE, the $Gd_2O_3$ loading was 6.5 g, the temperature was 30°C, and co-electrodeposition duration was 60 min. When the stirring speed was too small (400 rpm), the deposit was full of dendrites, the zinc deposition is in form of mossy structures (Fig. 2.26). Typically, moss structures appear primarily at low potential, high zinc concentration baths[155,158] and long deposition duration[155]. However, all these parameters were controlled in this experiment. Another possible cause for the formation of moss structures is the change in local current density. According to Otani et al.[155], when the local current density distribution is not uniform, the layer-like structure of Zn (Fig. 2.24a) can easily form a moss structure, which will further aggravate the non-uniform distribution of the local current density and generate more moss structures. At low stirring speed, it is difficult to evenly distribute $Gd_2O_3$ particles, which may lead to the no uniform of local current density.

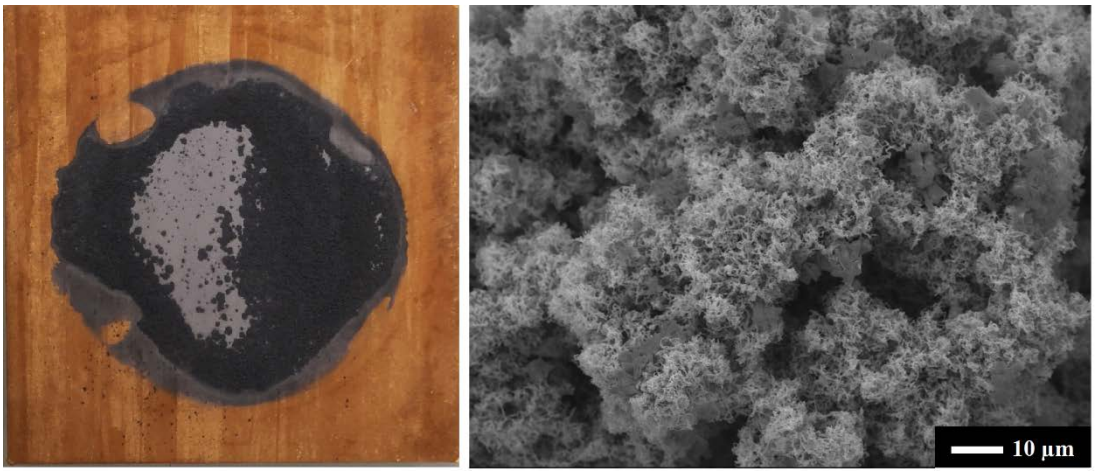


Fig. 2.26 Photo and SEM image of a Zn-$Gd_2O_3$ deposit stirred at 400 rpm. The applied potential was -1.52 V/NHE, the $Gd_2O_3$ loading was 6.5 g, the temperature was 30°C, and co-electrodeposition duration was 60 min.

When the stirring speed increases, the diffusion rate of zinc ions in the electrolyte increases and the concentration gradient decreases, the current density is more uniform, so there is less formation of dendrites. To compare the deposit quality at higher stirring speed (800 rpm and 1200 rpm), the areal density and the mass of Gd atom are compared in Table 2.11.

Table 2.11 Comparison of deposit quality with different stirring speed.

| Stirring speed (rpm) | Areal density ($10^{18}$ at/cm²) | Mass of Gd (mg) |
|---|---|---|
| 800 | 1.52 ± 0.07 | 2.7 ± 0.2 |
| 1200 | 1.57 ± 0.09 | 0.7 ± 0.0 |

We can see that the reduction of Gd incorporation mass under high-speed agitation occurs as it has be seen in Ni-$Gd_2O_3$ deposition. As explained in subsection 1.4.1.4, excessive agitation may

have an effect on the convection layer, and may hinder the process of loose absorption of $Gd_2O_3$ particles.
In summary, 800 rpm is considered to be the optimal stirring speed considering the smoothness and uniformity of deposits and the content of Gd.
In conclusion, this section investigated the effects of applied potential, $Gd_2O_3$ loading, and stirring speed on Zn-$Gd_2O_3$ composite deposits. We have found the optimal applied potential (-1.52 V/NHE) and the optimal stirring speed (800rpm), however, we didn't found the optimal condition of $Gd_2O_3$ loading because of dendrites. Other parameters, such as temperature, substrate roughness, are not investigated because of the poor quality of Zn-$Gd_2O_3$ composite deposits. The next subsection will present the comparison of Ni and Zn composite deposits and explain why Zn-$Gd_2O_3$ composite deposits was excluded in this work.

### 1.5.2. Comparison of Ni-$Gd_2O_3$ and Zn-$Gd_2O_3$ deposits

So far we have studied both Ni-$Gd_2O_3$ and Zn-$Gd_2O_3$ composite deposits, in this section, we will compare the two in terms of deposition difficulty and deposit quality (surface uniformity and Gd incorporation).
In terms of the deposition difficulty, both Ni and Zn are widely studied metals for electrodeposition, and they do not have difficulties to co-deposit with $Gd_2O_3$ in alkaline solution. At the optimal applied potential, their deposit thickness can both reach 10-20 µm for one hour of co-electrodeposition.
In terms of incorporation rate, Gd content was detectable in both deposits after adding 6.5 g of $Gd_2O_3$ powder at the respective optimum application potential, stirring speed and temperature. For Ni-$Gd_2O_3$ deposits, 3.0 mg of Gd was detected under a stirring speed of 300 rpm while only 2.7 mg of Gd was detected in Zn-$Gd_2O_3$ deposits under a stirring speed of 800 rpm. Taking into account the uncertainties associated with the average values, the two results are similar.
In terms of surface uniformity, the surface of Ni-$Gd_2O_3$ deposits is very flat, and the distribution of $Gd_2O_3$ on the surface is very uniform. Meanwhile, the presence of dendrites on the periphery is a very serious disadvantage for Zn-$Gd_2O_3$ composite deposit, because it causes the deposit adherence problem, and the thickness of the perimeter and the middle of the deposit is significantly different. In addition, the presence of dendrites caused significant inhomogeneity of the deposit surface, and the distribution of $Gd_2O_3$ on the target will be difficult to determine. The Gd atoms measured by ICP-AES will not be represented for the irradiated Gd atoms, which means that is unappropriated for cross section measurement.
In addition, for Ni-$Gd_2O_3$ target, Ni is a well-studied monitor in stacked-foil experiments, the production radionuclides $^{56}Co$ and $^{58}Co$ may help to measure the beam flux (see subsection 4.1.1.2).
In summary, Ni-$Gd_2O_3$ deposits have more advantages in surface uniformity and deposit adherence, and are more suitable as thin targets for measuring reaction cross sections.

## 2.4. Reuse of $Gd_2O_3$ loading

After finally confirming the use of Ni-$Gd_2O_3$ deposit, we can make the target with enriched $Gd_2O_3$ powder. In subsection 1.4.1.3, in order to make the contrast significant, 6.5 g of $Gd_2O_3$ was usually loaded during the experiment. However, limited by the high price of enriched materials, only a small amount of powder can be used in the actual production of the target.

Therefore, saving and reuse of raw materials are important. Due to its insolubility in alkaline solution, these $Gd_2O_3$ powders tend to settle at the bottom of the cell when stirring is stopped. After each co-electrodeposition, the electrolyte were removed by a pipette while $Gd_2O_3$ powders remained at the bottom. After taking out the deposited target, new gold substrate and new electrolyte were added to start a new co-electrodeposition.

This work was limited by budget and only 1.0 g of enriched $^{155}Gd_2O_3$ was purchased. When measuring the reaction interface, we need to make at least 10 targets to measure 10 points. To estimate the number of times the loaded powder can be reused, as a test, 1.0 g of natural $Gd_2O_3$ and 0.5 g of natural $Gd_2O_3$ were respectively loaded initially to the cell for 10 depositions. In order to incorporate homogeneously the powder to the electrolyte, the solution was stirred before each deposition. Fig. 2.27 shows the evolution of trapped Gd mass as a function of deposition number with the same electrolyte (concentration and composition remain unchanged). When the loaded powder is only 0.5 g, although there are slight fluctuations, generally the mass of Gd in deposits decreases significantly with the increase of the number of depositions. The mass of Gd in the first deposition was 1.6 mg while in the second deposition was only 0.8 mg. The mass of Gd was smaller than 0.3 mg after five depositions, this number is lower than the Gd contained in the first deposit made with 0.1 g of $Gd_2O_3$ loading (0.4 mg, result in Fig. 2.13). Nevertheless, the Gd content of the fifth deposit made by reusing 0.5 g of powder was higher than that of the five deposits made by no-recycling 0.1 g of powder. This phenomenon is more obvious when loading 1.0 g of powder: when 1.0 g of powder was reused to make 10 deposits, the content of Gd in each deposit was greater than 0.6 mg, which is much higher than that (0.4 mg) with 0.1 g of no-recycling powder. Since the Gd content in the deposit varies slightly under the same experimental condition, we can only roughly estimate that the total amount of Gd that can be obtained by manufacturing 10 targets: loading 10 times of 0.1 g $Gd_2O_3$ can only trap 4 mg of Gd in total while reusing 10 times of 1 g of $Gd_2O_3$ can obtain more than 10 mg of Gd in total. Therefore, even if the incorporation mass of Gd trapped in each deposit decreases with the reuse times (in other words, the number of deposits), more Gd content can still be obtained when the total amount of powder loaded is the same. This conclusion is consistent with the conclusion of 1.4.1.3: the initial addition of larger amounts of $Gd_2O_3$ loading may have a low single-deposition utilization rate, but thanks to the powder reuse process, the powder is not wasted.

Experiments show that the minimum Gd content that can be used for cross section measurement is 0.4 mg (See subsection 4.1.2.4). From the results of Fig. 2.27, it can be seen that with 1.0 g of $Gd_2O_3$ loading, all the 10 deposits have a Gd content bigger than 0.4 mg. Meanwhile, when the loading is 0.5 g, only the first five deposits satisfy the condition. Morphology studies have shown that with 1.0 g of $Gd_2O_3$ loading, the distribution of $Gd_2O_3$ is also homogeneous over the surface. Therefore, for the cross section measurement with enriched Ni/$^{155}Gd_2O_3$ targets, the initial $Gd_2O_3$ loading was fixed at 1.0 g.

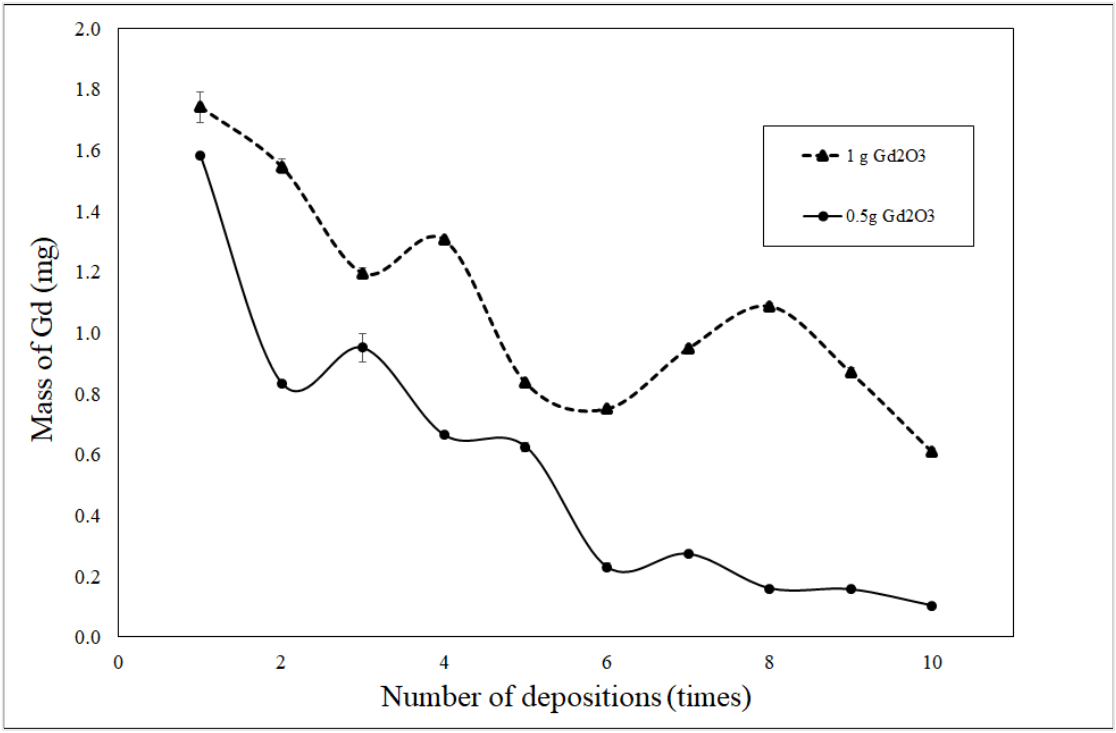


Fig. 2.27 The change of trapped Gd mass with the deposition times. The Gd2O3 loading was 1.0 g and 0.5 g, the applied potential was -1.2 V/NHE, the stirring speed was 300 rpm, and the temperature was 30°C.

## 2.5. Conclusion of this chapter

In conclusion, in this chapter, we have presented and developed two possible thin targets (Ni-$Gd_2O_3$ and Zn-$Gd_2O_3$ targets) through co-electrodeposition method. In both cases, we benefited for well known electrodeposition condition of the method in alkaline solution where $Gd_2O_3$ particle remains chemically stable.

For Ni-$Gd_2O_3$ targets, insoluble $Gd_2O_3$ was mixed in alkaline Ni electrolyte and co-deposited with Ni. Several experimental parameters on their influences to deposit quality were studied with the help of SEM, EDX and ICP-AES analysis. Based on these studies, optimal condition has been found for Ni-$Gd_2O_3$ deposits: the applied potential is -1.20 V/NHE, the stirring speed is 300 rpm, the $Gd_2O_3$ loading is 6.5 g, the temperature is 30°C, and the substrate should be smooth. The surface of the finally obtained deposits was smooth, and Gd and Ni were evenly distributed on the surface. With 6.5 g of $Gd_2O_3$ loading, about 3.0 mg of Gd can be find in the deposit. Multilayer deposits have also been studied in order to get higher Gd content, however, due to the difficulty to characterize the deposit, this approach was eventually abandoned in this work. In addition, limited by the expensive price of enriched $^{155}Gd_2O_3$, the recycling of $Gd_2O_3$ powder has also been studied.

For Zn-$Gd_2O_3$ targets, $Gd_2O_3$ was co-deposited with Zn in alkaline solution. Experimental parameters were also studied to obtain the optimal condition. Unlike Ni-$Gd_2O_3$ co-electrodeposition, Zn-$Gd_2O_3$ co-electrodeposition was very easy to form dendrites, and even under optimal conditions (applied potential was -1.52 V/NHE and agitation was at 800 rpm). Dendrites were still difficult to avoid at the edge of the deposit. The presence of dendrites disrupts the uniformity of the deposit surface, and Zn and Gd in dendrites area could not adhere

well on the substrate. The content of Gd was about 2.7 mg in the deposit with 6.5 g of $Gd_2O_3$ powder loaded. This result is close to that in Ni-$Gd_2O_3$ deposits.

In order to select the most suitable thin target, the morphology, the Gd content, and impurities generated under irradiation of the two composite targets were compared. It can be concluded that Ni has a more uniform surface, has a higher Gd content, and has an advantage for beam flux measurement (used as a monitor thanks to the reaction $^{nat}Ni(d,x)^{58(m)}Co$). Therefore, Ni-$Gd_2O_3$ composite target is finally chosen for the cross section measurement.

One gram of natural $Gd_2O_3$ was recycled to make 10 deposits, each of which eventually contained more than 0.4 mg of Gd (minimum value for cross section measurement). This result has proved that it is feasible to use 1.0 g of enriched $^{155}Gd_2O_3$ to make 10 targets for measuring cross sections. The recovery experiment also confirmed that with the same amount of powder loaded, more Gd can be trapped by adding a large amount of powder at first and recycling the powder.

# Chapter 3:
# Manufacture of thick targets through the pelletizing method

# 3. Manufacture of thick targets through the pelletizing method

This chapter uses the pelletizing method to manufacture Gd-containing-target with thickness ranging from 0.2 to 1.2 mm. In the first section (section 3.1), the principle of this method, the candidate powders, the tools to characterize the pellet and the method to calculate the pellet temperature during irradiation will be introduced. The optimization of the pelletizing process will be investigated to find the optimal experimental conditions. Then, the characterization of the $Gd_2O_3$ pellets, including the densification, the morphology, and the temperature effect will be presented. Finally, the dissolution of the pellet after irradiation and the subsequent recovery of $Gd_2O_3$ will discussed at the end of this section. Limited by the high price of enriched $^{155}Gd_2O_3$ powder, in this section, natural $Gd_2O_3$ powder was used in most studies except for the last one (a pellet made with enriched $^{155}Gd_2O_3$ powder).

## 3.1. Method and materials

### 3.1.1. Principle of the pelletizing method

Pelletizing is an agglomeration process that converts fine powder into the shape of a pellet by compressing and molding.

With the high pressure generated by the press, powders in the pellet dies can be compressed into pellets. There are four steps for the powder to be compacted [60,159–162]:

a) Particle rearrangement: this step happens immediately after pouring the powder into the pellet die, the particle positions are regrouped until all particles can remain in place and the powder reaches a new equilibrium state[159].
b) Deformation of particles: this step occurs after applying force to the powder. According to different studies[60,160,161], the powder particles may undergo elastic deformation first and then plastic deformation.
c) Formation of inter-particulate bonds: in this step, the inter-particulate bonds form thanks to the plastic deformation[60,162]. The inter-particulate bonds lock the particles in a certain position and mechanically bind the powder particles into a whole solid pellet.
d) Elastic recovery: this step happens when the applied pressure is removed. The volume of the pressed pellet rebounds and is fixed to the final volume.

Finally, the powder is transformed to a solid and compact pellet after the pelletizing process.

### 3.1.2. Materials for the pelletizing

#### 3.1.2.1. Hydraulic press and pellet die

In this study, a hydraulic press was used for pelletizing. It uses a hydraulic cylinder to generate a compressive force. The system contains two pistons with different areas and incompressible fluid. The operation principle of the hydraulic press is the Pascal's law, that is, the pressure (P) change of a confined incompressible fluid is transferred without loss to every part of the fluid and to the walls of the container. Therefore as P = F/S, when a small force (F) acts on the small piston (S), the resulting pressure is transmitted through the hydraulic fluid to apply a greater force on the larger piston.

The press used in this work is *A330 Abor Hydraulic press* supplied by *Enerpac*[163]. It has a maximum capacity of $3 \times 10^4$ kg, the maximum applied pressure for a 20-mm-diameter-pellet are 950 MPa. The photo of the press is shown in Fig. 3.1.

Fig. 3.1 Hydraulic press used in this work, the maximum capacity is 950 Mpa for a 20-mm-diameter-pellet.

The pellet die used in this work is a 20-mm-diameter evacuable pellet die bodies supplied by *Specac*. The photo of the pellet die and other relative devices is shown in Fig. 3.2 (left size); the whole structure includes a plunger, two stainless steel replacement pellet, an item for demolding, a die body and an evacuable die base. The maximum load is 22 tons for the pellet die. The right side of the Fig. 3.2 shows a schematic diagram of the assembly of all components when compressing the powder.

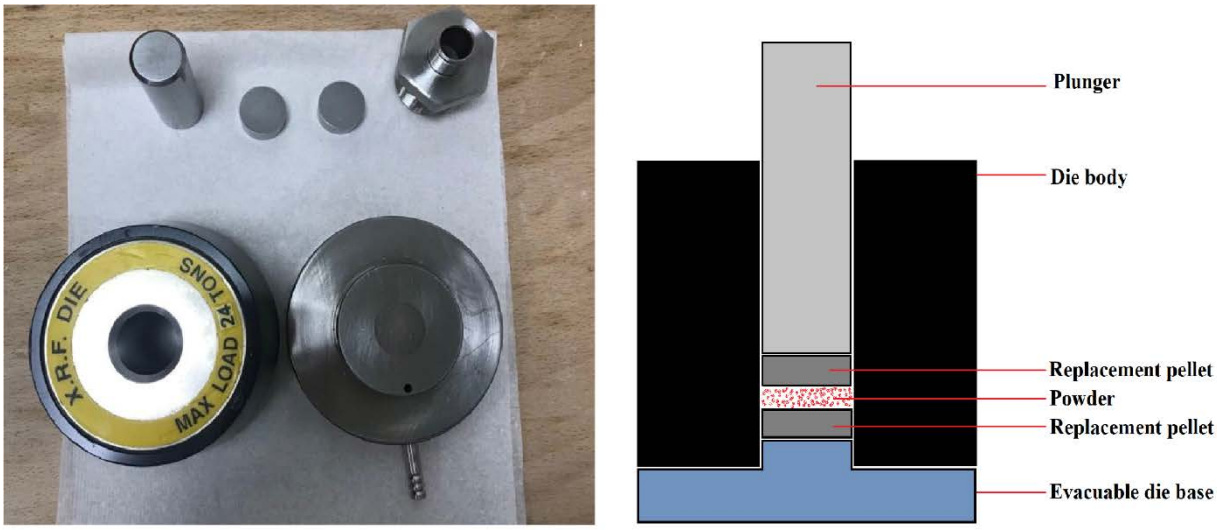


Fig. 3.2 The 20-mm-diameter pellet die used in this work. Left side: photo of the plunger, two replacement pellet, an item for demolding, the die body and the evacuable die base. Right side: the schematic diagram of the pelleting apparatus.

#### 3.1.2.2. Candidate pelleting powders

As mentioned in the previous two chapters, the enriched $^{155}Gd$ powder obtained in this work is in the form of $Gd_2O_3$. The $Gd_2O_3$ is stable at room temperature and has a high melting point (2310°C[164]), so it was selected as a candidate for thick target preparation. Meanwhile, Gd-containing salts, such as $GdCl_3$ and $GdF_3$, can be chemically converted from $Gd_2O_3$. Their melting points are also high enough (609°C[164] and 1231°C[164] respectively) to avoid melting during the irradiation, they were also considered as candidates.

These three powders $Gd_2O_3$, $GdCl_3$ and $GdF_3$ were studied for pelletizing. All these powders were dried and sieved before the pelletizing. The particle size was smaller than 230 mesh to avoid particle size effect on pelletizing.

Limited by the high price of enriched $^{155}Gd_2O_3$, pellets in *section 3.2* were made with natural $Gd_2O_3$ powder supplied by *Sigma-Aldrich*[128]. The enriched powder was supplied by *TraceScience*[129], the composition of the powder is presented in *Appendix 2.*.

### 3.1.3. Materials for the characterization of pellets

The SEM coupled with EDX presented in chapter 2 was used to analyze the surface of the pellets. In addition to that, the following equipment and software were also used to characterize the pellets.

#### 3.1.3.1. Mass and thickness measurement

For each pellet, the *Precisa XB A200* balance with an accuracy of 0.0001 g was used for weighing the mass of the powder before the pelletizing and the mass of the pellet after the pelletizing. An electronic vernier caliper with an accuracy of 0.01 mm was used to measure the thickness of the pellet. The thickness of each pellet was measured three times at different positions and an averaged value was taken to represent the final thickness. The error of the thickness is the sum of the standard deviation of the three measurements and the error of the Vernier caliper itself.

#### 3.1.3.2. X-ray diffraction (XRD)

X-ray diffraction analysis (XRD) is a technique using X-rays to determine the crystallographic structure of a sample. More precisely, XRD uses the diffraction effect of X-rays on electrons to obtain the distribution of electron density in a crystal and then analyze it to obtain information about atomic positions and chemical bonds, that is, crystal structure[165].

In this work, data of X-ray diffraction were acquired from a *D8 Advanced X-ray Diffractometer* of *Brucker*, using Cu/$K_{\alpha 1}$ radiation ($\lambda$ = 1.54056 Å), two theta from 10° to 70º, step size of 0.015° and 2 seconds per step.

#### 3.1.3.3. Thermal conductivity measurement

The conductivity of heat is a major concern for thick target because overheating may cause changes in the shape and physical forms and properties of the target. The major heat source of the target comes from interactions of beam particles with the target: particles transfer part of their energy to the surrounded medium through collisions[74].

To avoid the overheating of thick pellets a cooling system is in place for which it is crucial to have a measure of the thermal conductivity of the pellet to be able to estimate its temperature during irradiation.

The thermal conductivity λ ($W \cdot m^{-1} \cdot K^{-1}$) can be estimated indirectly according to the *eq.3.1:*

$$\lambda(T) = \alpha(T) \cdot \rho(T) \cdot C_p(T) \qquad (eq.\,3.1)$$

Where T (K) is the temperature, α is the thermal diffusivity ($m^2/s$), ρ ($kg \cdot m^{-3}$) is the density and $C_p$ ($J \cdot kg^{-1} \cdot K^{-1}$) is the specific heat capacity.

The thermal diffusivity α was measured by the flash laser method. The principle of this method is to heat one side of the plane-parallel sample with short pulses of energy and detect the temperature evolution on the other side of the sample[166].

The density ρ was determined by the hydrostatic weighing method[167]. The pellet was put in the water-free alcohol, according to the Archimedes' principle, the volume of the displaced liquid (water-free alcohol) is the volume of the immersed pellet. The mass of the sample was measured by a balance in air and in the solution. The density of the pellet $\rho_{pellet}$ ($g/cm^3$) can be calculated as *eq.3.2*:

$$\rho_{pellet} = \frac{m_{air}}{m_{air} - m_{alcohol}} \cdot (\rho_{alcohol} - \rho_{air}) + \rho_{air} \qquad (eq.\,3.2)$$

Where $m_{air}$ (g) and $m_{alcohol}$ (g) are the mass of the pellet in the air and in the water-free alcohol respectively, $\rho_{air}$ ($g/cm^3$) and $\rho_{alcohol}$ ($g/cm^3$) are the density of the air and the water-free alcohol respectively.

The specific heat $C_p$ was measured using a Differential scanning calorimetry (DSC). A sample will absorb or release heat under phase transition to keep the same temperature as the reference object, so the principle of this technique is to measure the heat flux change between the sample and the reference object.

In this work, all these measurements were carried out by SAS CAPACITÉS, a research development subsidiary of Nantes University[168].

#### 3.1.3.4. Temperature estimation during irradiation

As mentioned in the previous subsection, the heat generated in the target comes from the energy loss of beam particles. The internal heat generation per unit volume caused by energy dissipation, note as P ($W \cdot m^{-3}$), depends on the stopping power dE/dx ($MeV \cdot m^{-1}$), the irradiated surface S ($m^2$), the beam intensity I (A), charge state of the accelerated ion $Z$, and the elementary charge $e$. It can be expressed as *eq.3.3* :

$$P = \frac{dE/dx \cdot I}{S \cdot Ze} \qquad (eq.\,3.3)$$

Meanwhile, the target losses heat by conduction, convection and radiation:

- The conduction of heat is the major transfer route in the target. According to Fourier's law of conduction, the heat flux $\varphi_1$ ($W \cdot m^{-2}$) can be expressed as *eq.3.4*:

$$\varphi_1(x) = -\lambda\left(\frac{dT}{dx}\right) \qquad (eq.\,3.4)$$

With λ ($W \cdot m^{-1} \cdot K^{-1}$) the thermal conductivity of the material, dT (K) the temperature differential, and dx (m) the distance differential.

- The convection of heat is caused by the movement of fluid. If the target has a cooling system, the heat of the target can be transferred from the target to the coolant. In the boundary of the target, the convection flux $\varphi_2$ ($W \cdot m^{-2}$) can be expressed as *eq.3.5*:

$$\varphi_2 = h(T_b - T_c) \qquad (eq.3.5)$$

  Where $h$ ($W \cdot m^{-2} \cdot K^{-1}$) is the water flow, and $T_b$ and $T_c$ (K) are the temperature of target boundary and coolant, respectively.
- The radiation heat flux $\varphi_3$ ($W \cdot m^{-2}$) can be expressed as *eq.3.6*:

$$\varphi_3 = \varepsilon\sigma(T_t - T_s)^4 \qquad (eq.3.6)$$

  With $\varepsilon$ (a.u.) is the emitting factor which is equal to 1 for black body or smaller than 1 for other materials, $\sigma$ is the Stefan-Boltzmann constant equals to $5.7 \times 10^{-8}$ $W \cdot m^{-2} \cdot K^{-1}$, $T_t$ and $T_s$ are temperatures (K) of the target and of the surrounding material. For our target, the heat loss by radiation is negligible when target temperature is below 500°C[74]. Therefore, in this work, we first consider heat conduction and heat convection to estimate a rough target temperature.

According to the heat diffusion equation, the temperature T can be expressed as *eq.3.7*:

$$\rho C_p \frac{\partial T}{\partial t} = \nabla(\lambda \nabla T) + P \qquad (eq.3.7)$$

with $\rho$ ($kg \cdot m^{-3}$) the density of the material, $C_p$ ($J \cdot kg^{-1} \cdot K^{-1}$) the specific heat capacity, $\nabla$ the gradient function, $\lambda$ ($W \cdot m^{-1} \cdot K^{-1}$) the thermal conductivity of the material, and P ($W \cdot m^{-3}$) the generated heat.

To simplify the system, the target and the encapsulation system are considered as 1-d model and homogenous (for $Gd_2O_3$ pellet, the verification will be presented in section 3.2.2.1), the thermal conductivity of each layer is constant at every position of the layer, and the whole system is considered in steady-state with heat generation. Therefore, in x-direction, the *eq.3.7* can be simplified as *eq.3.8*:

$$\lambda \frac{\partial^2 T}{\partial^2 x} + P = 0 \qquad (eq.3.8)$$

As explained in Chapter 1, in order to avoid the contamination of the container or beam structures caused by powder particles on the pellet during or after the irradiation, the pellet will be encapsuled after being compressed. The encapsulation material could be Al (see section 3.3) or Nb (see section 4.2.2.3). Since the pellet and the encapsulation material cannot be completely fitted, air exist between them as contact resistance. The schematic diagram is presented in Fig. 3.3 for an encapsulation in Al and the scale shown does not represent the real scale. The encapsulation system has five layers: Al – air – $Gd_2O_3$ pellet – air – Al. The boundary of each layer is noted as $X_i$ (i=0,1,2,…,5), the temperature of the boundary $X_i$ is noted as $T_i$ (i=0,1,2,…,5), and the thickness of layer-i is noted as $e_i$ (i=1,2,…,5). The heat flux is from $X_0$ to $X_5$.

For the irradiation test in this work (section 4.2.2), the system did not have cooling system because the beam intensity (0.5 µA) is low enough (the power will be 4 W for a energy loss of 8 MeV) so that we can suppose the temperature of the pellet could not be so high. However, for

future mass production, the beam intensity will be more than 20 µA, in this case, it will be necessary to have cooling system. This is why Fig. 3.3 presents the water fluent on the two side of the target.

Detailed calculations are shown in *Appendix 3.2* and the cooling system is taken into account to estimate the pellet temperature.

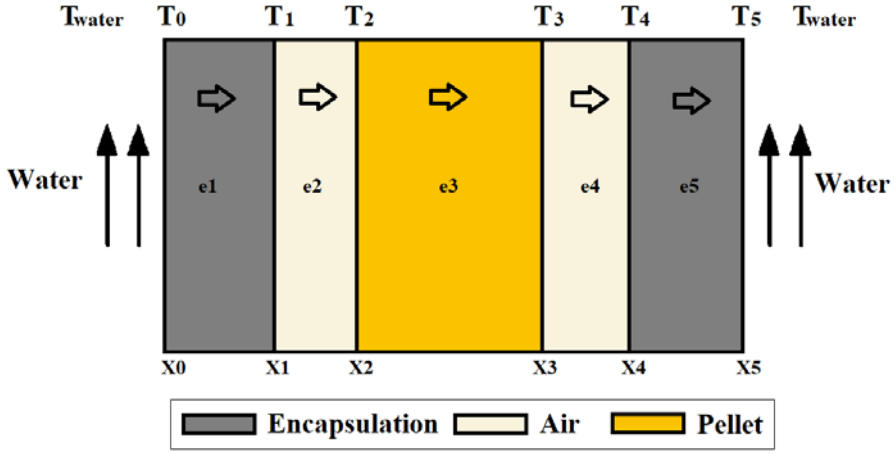


Fig. 3.3 Schematic diagram of the heat transfer of the encapsulated pellet with two-side water-cooling. $X_i$ (i=0,1,2,…,5) represents the boundary of each component of the encapsulated pellet in the lateral direction, $T_i$ (i=0,1,2,…,5) is the temperature of the $X_i$. Thickness of layey-i is noted as $e_i$ (i=1,2,…,5). The direction of heat flux is from $X_0$ to $X_5$, and there is a constant flow of water on $X_0$ and $X_5$. The scale shown does not represent the actual scale.

## 3.2.Pelletizing of no-enriched Gd-containing powder

### 3.2.1. Optimization of pelletizing parameters

#### 3.2.1.1. Selection of pelleting powder

As mentioned in subsection 3.1.2.2, $Gd_2O_3$, $GdCl_3$ and $GdF_3$ were considered as candidate powders.

Since the enriched $^{155}Gd$ is in oxide form, the enriched $GdCl_3$ and $GdF_3$ can only be produced with the help of enriched $Gd_2O_3$. The relevant chemical equations to transfer $Gd_2O_3$ into $GdCl_3$ or $GdF_3$ are as shown in *eq.3.9* and *eq.3.10*, respectively:

$$Gd_2O_3 + 6\,HCl \rightarrow 2\,GdCl_3 + 3\,H_2O \qquad (eq.3.9)$$

$$Gd_2O_3 + 6\,NH_4F + 6\,HCl \rightarrow 2\,GdF_3 + 6\,NH_4Cl + 3\,H_2O \qquad (eq.3.10)$$

For $GdCl_3$ powder, several processes are necessary after the reaction of *eq.3.9*, such as evaporation of solution, drying, grinding, and sieving. Similarly, for $GdF_3$ powder, the precipitation ($GdF_3$) obtained after reaction *eq.3.10* needs to be rinsed several times to remove $NH_4Cl$, as well as evaporation, drying, grinding and sieving processes. The experimental procedures of production are shown in *Appendix 3.1*.

To characterize the composition of $GdCl_3$ and $GdF_3$ obtained powders, EDX analysis have been performed and those spectra are shown in Fig. 3.4. Both two spectra show existence of Cu that is coming from the copper tape used to glue powders and hold them in place during analysis. Therefore, copper is not an impurity of the powders but rather a bias coming from the way the analysis is conducted. According to EDX spectrum of $GdCl_3$, except for Gd and Cl, we see

oxygen in the powder. As the transformation has been made with a larger excess of HCl, we think that there is no residual $Gd_2O_3$ and that this is coming from water molecules contained in the powder as $GdCl_3$ is very hygroscopic and can easily combine with water molecules. For the spectrum of $GdF_3$, except for Gd and F, Cl and O also exist as impurities. As an hygrosocopic species, water molecule can also combine with the powder explaining the presence of O, the presence of Cl may be due to the residual $NH_4Cl$, since there is a peak before O, this might be N in the spectrum.

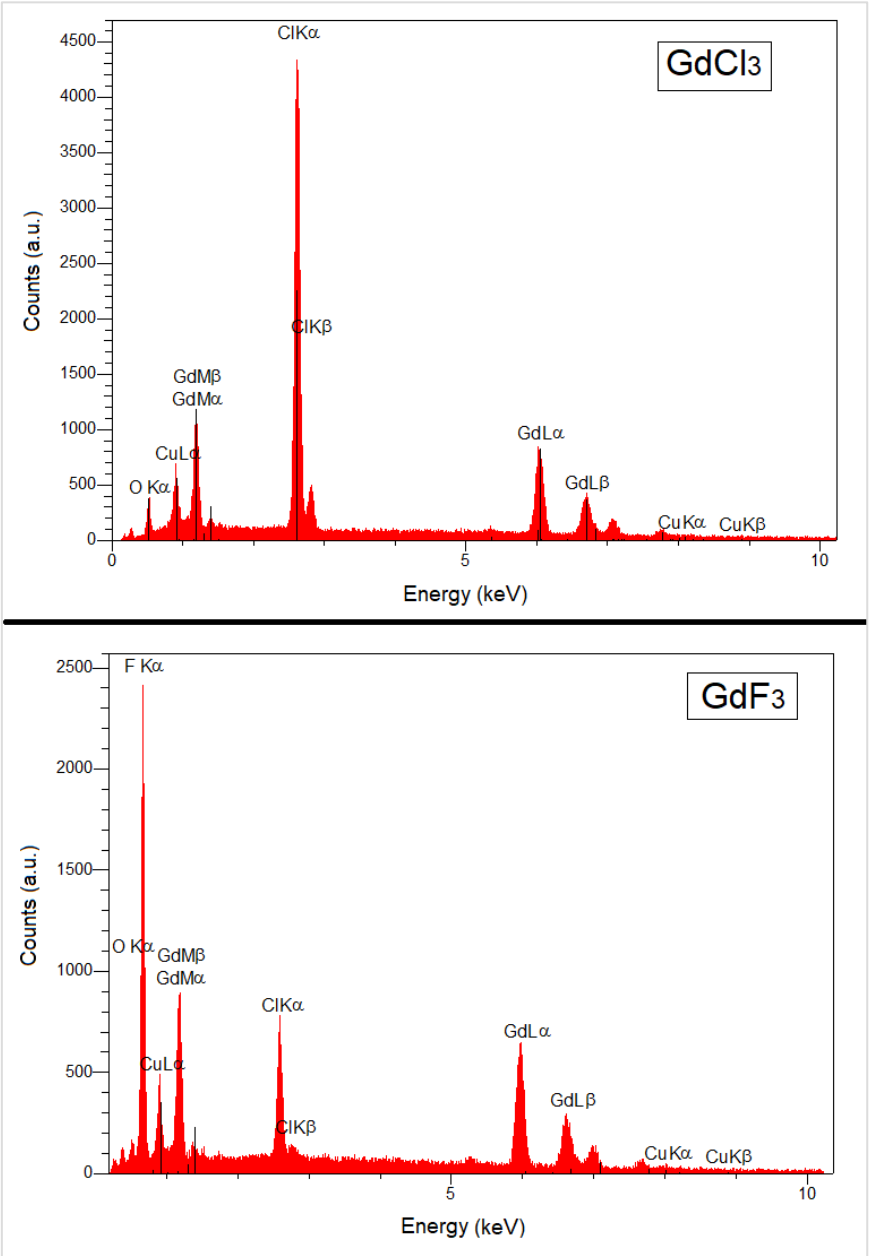


Fig. 3.4 EDX spectra of obtained $GdCl_3$ (above) and $GdF_3$ (below) powders. The tension was 15 keV, the magnification factor was 5000.

To complete these results and better understand the structure of the obtained powders, both powders were then analyzed by XRD and obtained spectra are shown in Fig. 3.5. In each spectrum, the red vertical lines represent the peaks corresponding to standard hexagonal $GdCl_3$ (or monoclinic $GdF_3$) crystals. It is clear that both powders do not match with crystallite

structure of the chosen reference for $GdCl_3$ or $GdF_3$. This conclusion could fit with some remaining of water in the composite.

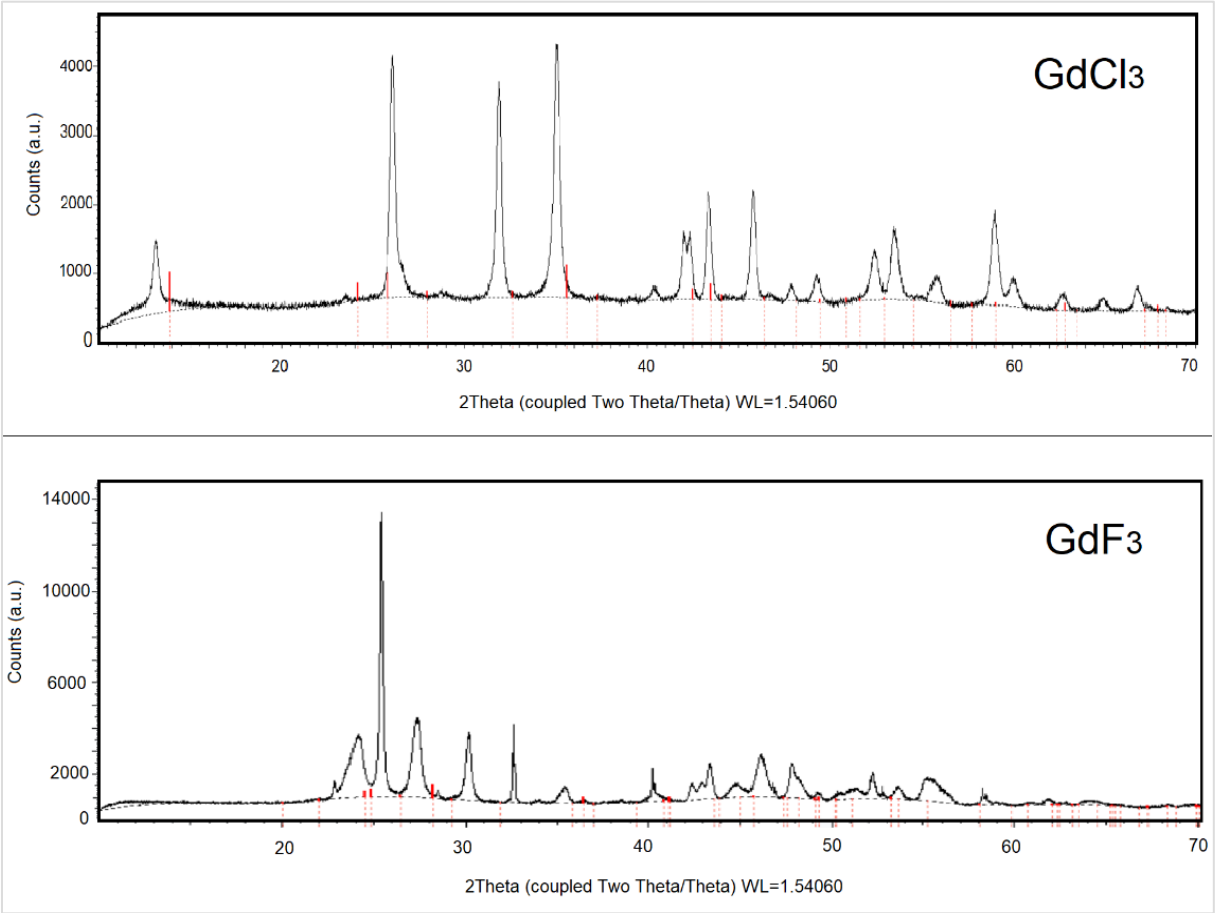


Fig. 3.5 XRD spectra of obtained $GdCl_3$ (above) and $GdF_3$ (below) powders. The red vertical lines in each spectrum represent the peaks corresponding to standard $GdCl_3$ (or $GdF_3$) crystals.

In addition to the problem of sample purity, another drawback is that the two Gd-containing salts themselves are not chemically suitable as targets. For $GdCl_3$, the powder is difficult to obtain due to the strong hygroscopicity. It can easily absorb water to form $GdCl_3 \cdot 6H_2O$. Even if the powder is dried in an oven at 200°C for 2 hours, it absorbed easily water vapor in the air during the pellet making process. To investigate it, 50.175 g of dried powder was exposed at 20°C (lab condition that day), and its mass change with time is shown in Fig. 3.6. It can be seen that the absorption rate of water vapor by the powder is very fast in the first 20 minutes, and the absorption rate slows down then. However, even after 120 minutes of exposure to air, the powder continued to absorb water vapor. Therefore, $GdCl_3$ pellets inevitably contain water.

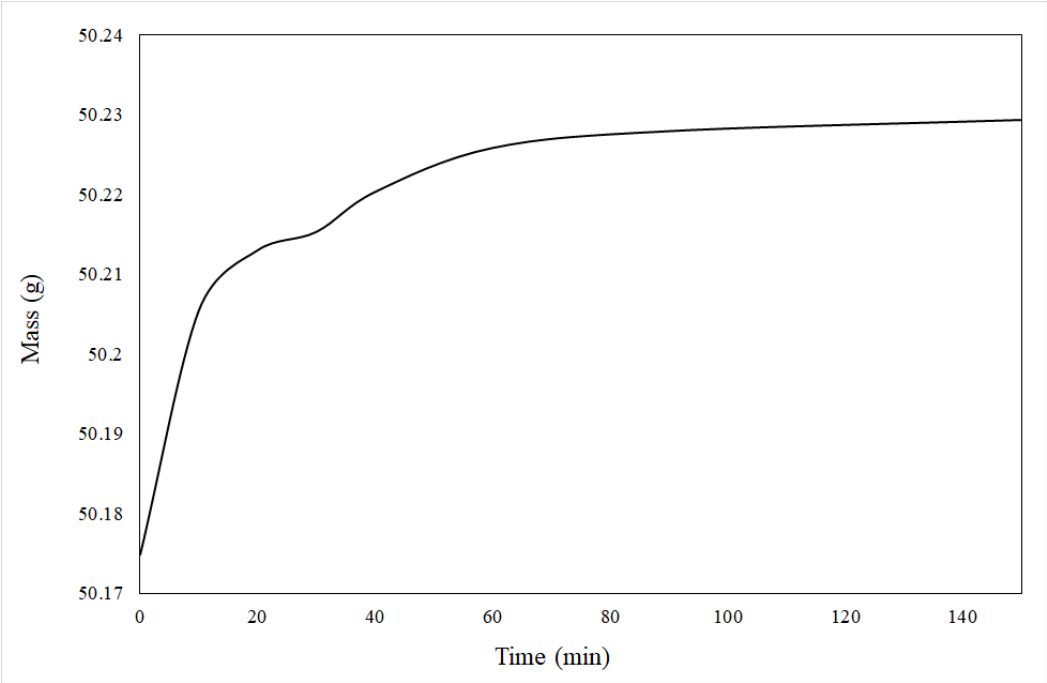


Fig. 3.6 Mass change of 50.17 g of exposed $GdCl_3$ powder with time at 20°C.

This characteristic is very detrimental to the stability of the pellet at high temperature. Fig. 3.7 shows the photo of one $GdCl_3$ pellet before (left photo) and after (right photo) 30 minutes of heating at 300°C. The mass of the pellet is 0.50 g and the diameter is 20 mm. Before heating, the pellet was flat with a tiny crack while after heating the pellet had many bulges and pores, and the crack became more visible. This phenomenon can be explained by the escape of water molecules of the pellet during heating. A mass change was observed before and after heating: after heating, the mass of the pellet is 0.40 g, which is 20% less than that before heating. The same experiment was repeated for two other pellets with a mass of 0.90 g and 0.60 g, and their mass after heating was 0.74 g and 0.47 g, respectively, which were 18% and 22% less than before. Since the pellet will be sealed during irradiation, the escape of gas will increase the internal pressure, which may cause the deformation of the capsule or even its bursting. For this reason, $GdCl_3$ was excluded for target preparation.

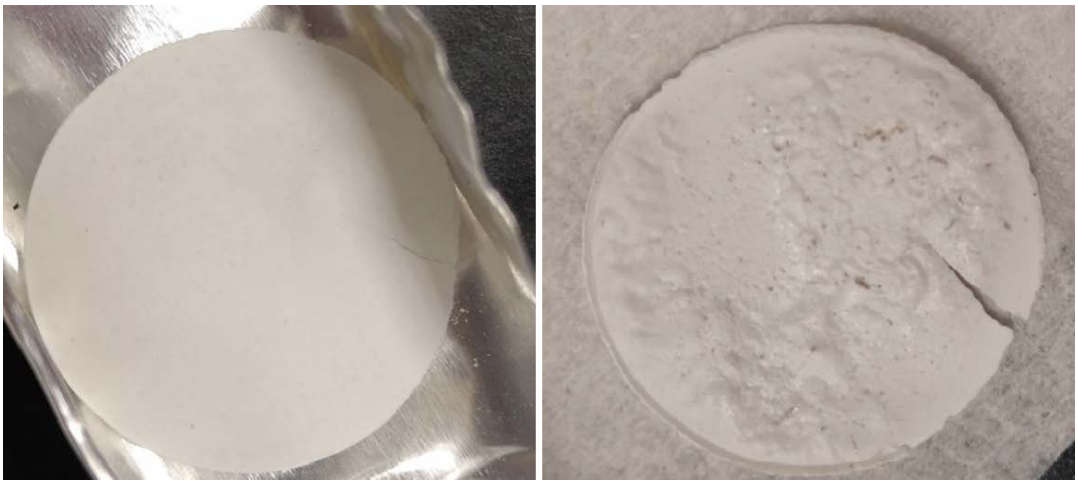

Fig. 3.7 Photo of GdCl3 pellet before heating (left) and after heating at 300 °C for 30 minute (right). The mass of the pellet is 0.50 g, the diameter is 20 mm.

Considering $GdF_3$, the conversion from $Gd_2O_3$ to $GdF_3$ requires more experimental steps (multiple rinsing, drying, grinding, and sieving); the whole experimental process takes more than 24 hours (*Appendix 3.1*). Powder could be inevitably lost during this process (sticking to filter paper, transferring powder before different utensils, etc.). Considering the high price of enriching $Gd_2O_3$, this method is not economical. Moreover, the method to dissolve $GdF_3$ pellet is not well studied. The $GdF_3$ pellets were difficult to dissolve in concentrated nitric acid or hydrochloric acid or even aqua regia. Kylyshkanov et al.[169] have proposed to dissolve $GdF_3$ in a solution of aluminum nitrate, but the exact composition of the solvent agent remains unknown. Qiu et al.[170] proposed dissolving $GdF_3$ in 16 mol/L nitric acid and heat to 190°C with a microwave. This method is complicated for handling pellets containing radionuclides. Consequently, $GdF_3$ pellet was considered less suitable in terms of operability than $Gd_2O_3$.
Compared with $GdCl_3$ and $GdF_3$, $Gd_2O_3$ is easy to obtain, it is not significantly hygroscopic, and it can be easily dissolved by HCl or $HNO_3$. In addition, as the two first compounds must be prepared from oxide when using enriched Gd, $Gd_2O_3$ powder was finally used for pelletizing.

#### 3.2.1.2. Pressure effects

To study the optimum pressure of the pelletizing process, several pressure values (from 400 bars to 600 bars) have been applied to make 18 pellets (6 pellets for each pressure value) using 1.0 g of $Gd_2O_3$ powder. All pellets have a diameter of 20 mm. The duration of each pelletizing process was 60 s. The compressed pellets had to be removed from the pellet die and some pellets were damaged during this process (Fig. 3.8 photo in left). We therefore counted the success rate, which is the number of complete pellets divided by the total number of manufactured pellets.

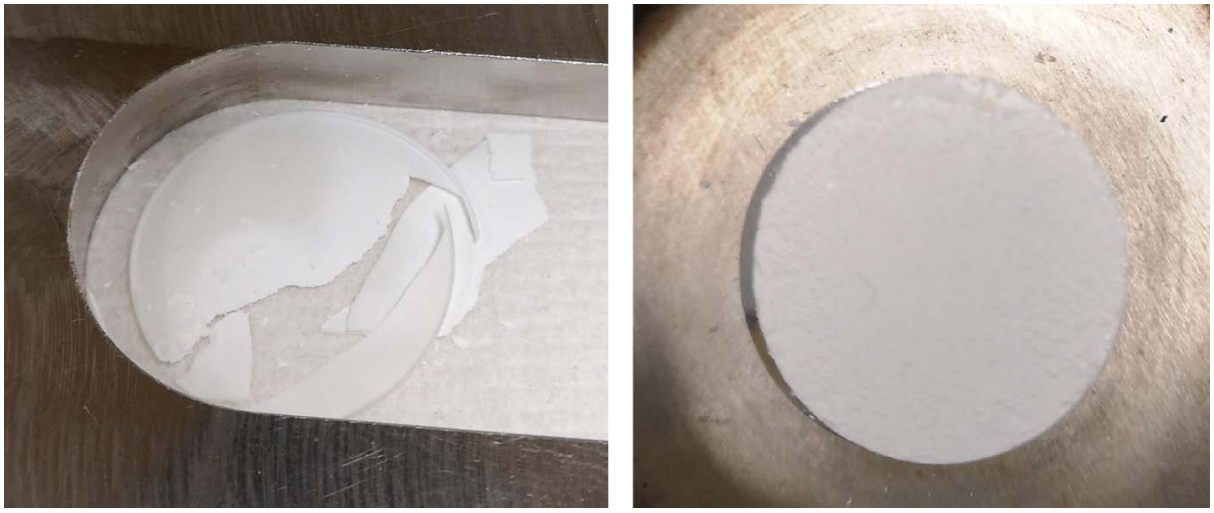

Fig. 3.8 Photos of a damaged pellet (left) and a complete pellet (right) during the recovery process.

The mean thickness of the pellets under different pressure and the success rate are shown in Table 3.1. From the table, the mean thickness decreases with the increase of the pressure, the mean thickness is 0.70 mm at 400 bars and 0.65 mm at 600 bars. With the same mass (1.0 g), the thinner the thickness, the higher the density of the target. Therefore, targets are slightly denser at higher pressure. It can also be seen that as the pressure increase, the magnitude of the thickness change decreases: from 400 bar to 500 bar, the thickness decreased 0.04 mm; while from 500 bar to 600 bar, the thickness decreased only 0.01 mm. Considering the bearing capacity of the mold, the pressure did not be increased more. According to the table, the success

rate is minimum at 500 bar (33%) and maximum at 600 bar (67%). Since only 6 samples have been tested in each pressure, the sample size is too small to conclude a relation between the pressure and the success rate. However, according to the success rate results, 600 bar was first chosen as the experimental pressure to study the pellet density (section 3.2.2.1). During the study, 22 pellets were made, of which 7 were broken and 15 were in good condition, the success rate was 68%, which demonstrates consistency of the result in Table 3.1.

Table 3.1 Mean thickness and success rate under different pressures.

| Pressure (bar) | Mean thickness (mm) | Success rate (%) |
|---|---|---|
| 400 | 0.70 ± 0.04 | 50% |
| 500 | 0.66 ± 0.04 | 33% |
| 600 | 0.65 ± 0.06 | 67% |

#### 3.2.1.3. Pelleting time effects

To verify the effect of the compression time on the target thickness, 6 pellets were compressed for different durations with the same mass (1.50 g). The experiment was repeated three times for each compression time, so there were 18 pellets in total. Fig. 3.9 presents the thickness of the targets for 10, 20, 30, 45, 60, and 120 s of compression, the black dots represent the average thickness of the three pellets, and the red dotted line is the average value of all 18 pellets. For the black dots, the uncertainty of the thickness is the standard deviation of three measurements, and the uncertainty of the duration is considered as 1 s. It is clear that when the compression time varied from 10 s to 120 s, the thickness of each target was very close to 0.9 mm. The average value of all the targets (red dotted line) is 0.91 mm, this value agrees with the average for each compression time (black dots). It can be inferred from the result that the thickness of the sample is independent of the compression time from 10 s to 120 s. The compression time has not been increased further because the press system is manual and it is difficult to continue pressing for longer periods. For the characterization of $Gd_2O_3$ pellet, the compression time was fixed at 60 s (mean value of the studied interval).

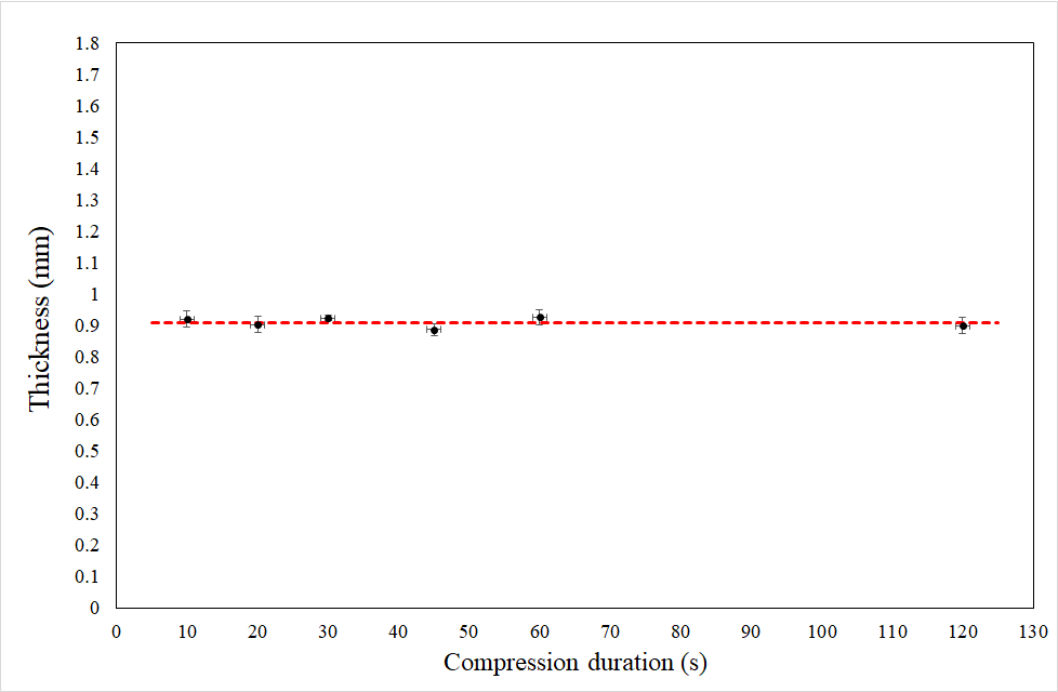


Fig. 3.9 The thickness of the pellet with different compression time. The applied pressure was 600 bars, the mass of the powder was 1.50 g. Black dots represent the average thickness of pellets, red dotted line present the average value of all pellets.

### 3.2.2. Characterization of $Gd_2O_3$ pellet

#### 3.2.2.1. Pellet densification

To evaluate the powder densification, the density of the pellet has been investigated.

Three pellets were made with 1.0 g of powder using an applied pressure of 600 bars and a compression duration of 60 s. Their densities have been measured by the hydrostatic weighting method[167]. This density is noted as hydrostatic density. The average value measured for these pellets is 7.04 g/cm$^3$. The theoretical density of $Gd_2O_3$ is 7.07 g/cm$^3$ [171]. So the densification rate, defined as the ratio of hydrostatic density and theoretical density, is 99.6%. However, this density corresponds to the density reached by the agglomerates formed during compression. It is not the density of the entire pellet since this density measurement ignore possible holes and interstices in the pellet.

In addition to the hydrostatic density, the pellet density has also been evaluated by measuring directly the thickness of the pellet. Twenty-two pellets with different mass were manufactured under 600 bar during 60 s, the thickness of these pellets have been measured to study the relation of mass to thickness, and the results are shown in Fig. 3.10. According to the figure, the thickness of the pellet increases with the increase of the mass. The minimum mass to make a solid and complete pellet is 0.31 g, and the minimum thickness of the target is 0.17 mm. The thickness of the pellet can reach up to 1.23 mm (at 1.99 g). The mass of the powder did not increased beyond 1.99 g because the irradiation experiments did not require a thicker target (see subsection 3.2.2.3). The relation between the mass of the powder (m) in gram and the thickness (th) in millimeter is linear: th (mm) = 0.6267 m (g), with a coefficient of regression $R^2$ equals to 0.9789.

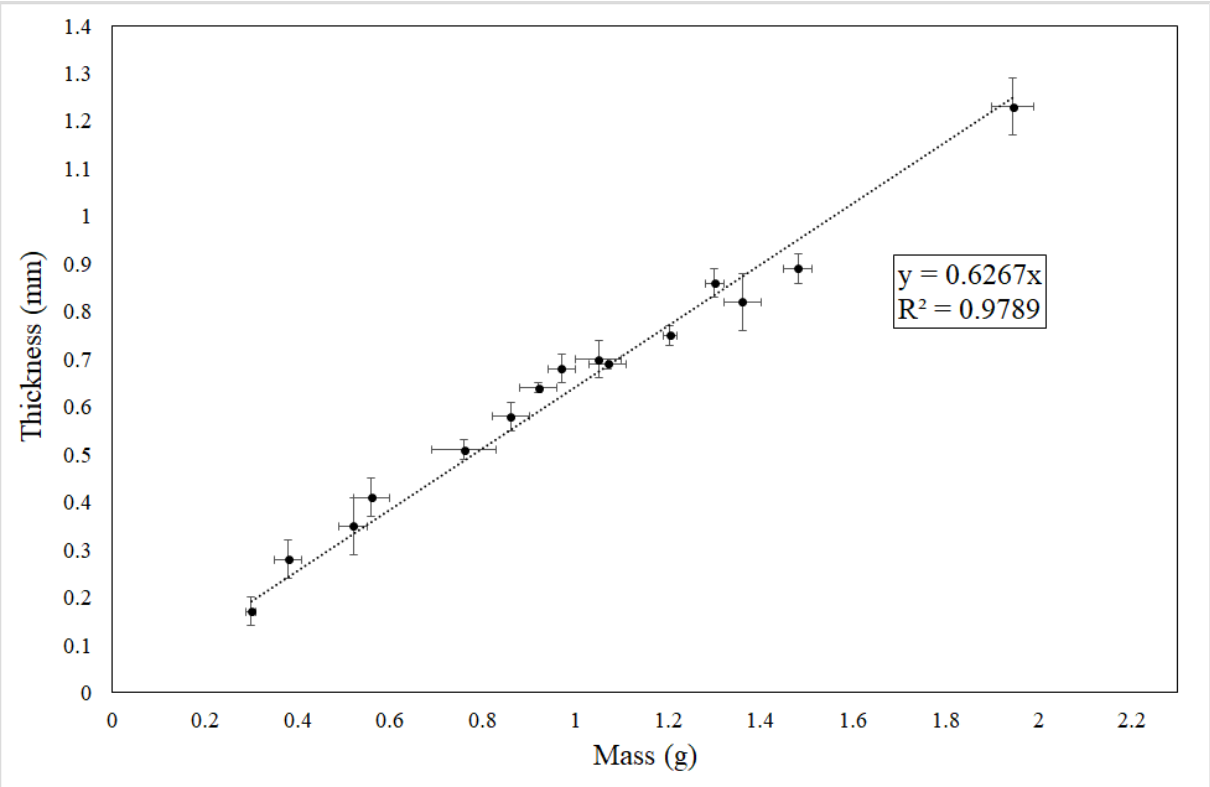


Fig. 3.10 The thickness of the pellets with different mass of $Gd_2O_3$ powder under 600 bar of pressure and 60 s of compression duration.

For a solid pellet, the relation between the density ρ and the mass m is that:

$$\rho = \frac{m}{e \cdot s} \qquad (eq.3.11)$$

Where e is thickness of the pellet and s is the surface of the pellet.

From *eq.3.11*, it can be deduced that:

$$e = \frac{1}{\rho \cdot s} m \qquad (eq.3.12)$$

Therefore, $\frac{1}{\rho \cdot s}$ can be considered as the slope of the trend line (here ρ is the average density for all these pellets). Since the surface of the pellet is known (20 mm of diameter), the density can therefore be deduced. After calculation, the density is about 5.08 g/cm$^3$. This density is noted as geometric density.

Compared with the hydrostatic density (7.04 g/cm$^3$), the geometric density is much smaller (the ratio is only 72% compared with the theoretical density). The difference of the density might be explained by the fact that the pellet is not fully compact and dense. The powder gather together to form aggregates during the compression but there are empty areas and cracks in the pellet.

### 3.2.2.2. Morphology and crystal structure study

The surface morphology of four pellets with a thickness of 0.36 mm, 0.54 mm, 0.85mm and 1.14 mm have been analyzed by SEM. The applied pressure for each pellet was 600 bars and the compression time was 60 s. For each pellet, five position (up, down, left, right and center) were imagined. SEM images of all positions were similar. Therefore, Fig. 3.11 only shows the

image of the center area of each pellet. In the figure, images 1a, 2a, 3a, and 4a represent the pellet with a thickness of 0.36 mm, 0.54 mm, 0.85mm and 1.14 mm after magnification of 1000 times respectively. Whereas, images 1b, 2b, 3b, and 4b represent the same pellets after magnification of 100 times. It can be seen from the figure that after a magnification of 1000 times, the surfaces of the pellets under different thicknesses are very similar. The powder is squeezed together, but instead of forming a complete homogeneous surface, it is gathered together by many rubble-like pieces of different sizes and shapes, with obvious gaps between the pieces. This result is consistent to our hypothesis.

The presence of fissures and cracks are normal in pellet compacting, Gorejava et al.[172] found defects and cracks in the surface of zinc pellets, and Ciezykowska et al.[173] had the same problem for the manufacturing of molybdenum pellets even after 40 min of compression under 8000 bar. Vacancies and voids are unavoidable for pellets obtained by pelletizing. However, these pellets can be used as targets for radionuclide production as they are mechanically self-supporting and do not loose powder. In addition, these defaults are at a microscopic scale as demonstrated by the images obtained with a 100 times of magnification (images 1b, 2b, 3b and 4b of Fig. 3.11) where the surface of the pellet looks much smoother. Several studies confirm the feasibility of radionuclides using pressed pellets: Nelson et al.[174] used compressed $^{68}$Zn pellets to produce $^{68}$Ga, pressed yttrium pellets were used to produce $^{89}$Zr according to the work of Zweit et al.[175], and Favaretto et al.[97] used pressed $Gd_2O_3$ pellet to produce $^{155}$Tb. Therefore, pressed pellet is uniform enough for the production of radionuclide. Experimental thickness and density will be needed to infer irradiation conditions and allow for thermal evaluation during irradiation.

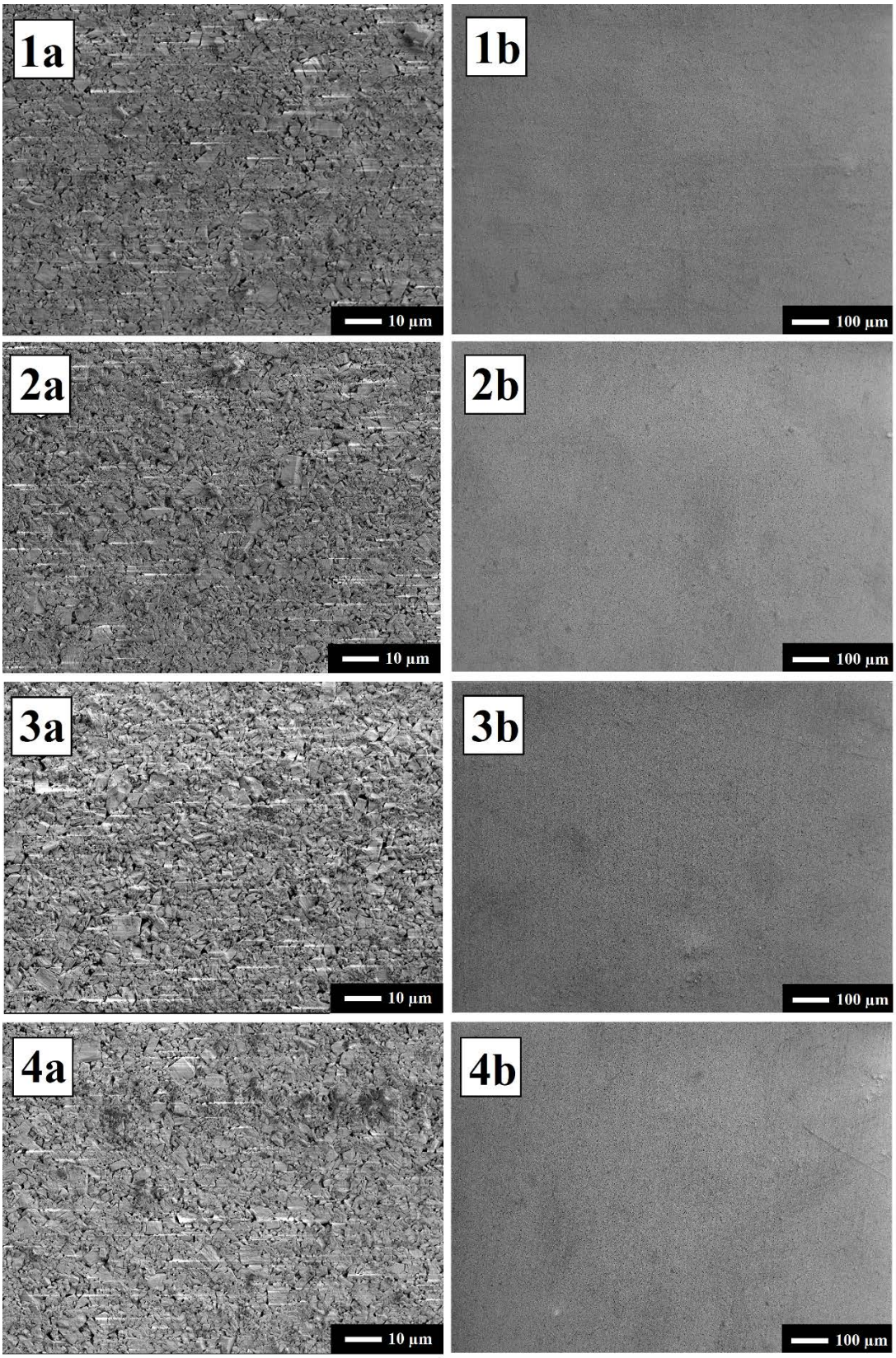


Fig. 3.11 SEM images of the surface of four pellets, images 1a, 2a, 3a, and 4a represent the pellet with a thickness of 0.36 mm, 0.54 mm, 0.85mm and 1.14 mm after magnification of 1000 times respectively. Whereas images 1b, 2b, 3b, and 4b represent the same pellets after magnification of 100 times respectively. The applied pressure was 600 bar and the compression time was 60 s.

### 3.2.2.3. The temperature effects on the pellets

Previous subsection shows that the pellet has voids and cracks inside at microscopic level but the pellet can be regarded as homogeneous as macroscopic level. However, this conclusion is based on the analysis result in room temperature (20-25°C). During irradiation, the temperature of the target (pellet) increases due to the heat deposited by the beam. As explained in Chapter 1, a good knowledge of the thermal properties of the target is needed to verify that it will resist the thermal power caused by irradiation. Therefore, it is necessary to calculate the pellet temperature during the irradiation and to study the heat resistance at high temperature.

**Pellet temperature calculation :**

Before doing any calculation, it is necessary to determine the optimal thickness of the target to be used. The optimal thickness should not only ensure the maximum production of the radionuclide of interest, but also ensure that target material will not be wasted considering the high price of enriched material. After analyse, the optimal thickness of the target is such that considering a given starting energy, the output energy if the beam is lower than energy of the the peak of the cross section and higher to threshold energy (See subsection 4.2.1.3). In this work, we choose the energy interval from 14 MeV (to avoid $^{154}$Tb production), and the threshold energy is about 4 MeV. Details will be presented in Chapter 4.

The RYC (Radionuclide Yield Calculator) program was used to determine the optimal thickness. The experimental macroscopic density of the pellet, 5.08 g/cm$^3$, was used in the simulation. For the irradiation, enriched $Gd_2O_3$ pellet was used, and the enrichment of $^{155}$Gd was 92.8%. According to the simulation, the optimal thickness is 0.52 mm. Using the mass-thickness relation obtained in section 3.2.2.1, the mass of the pellet for this thickness is about 0.83 g.

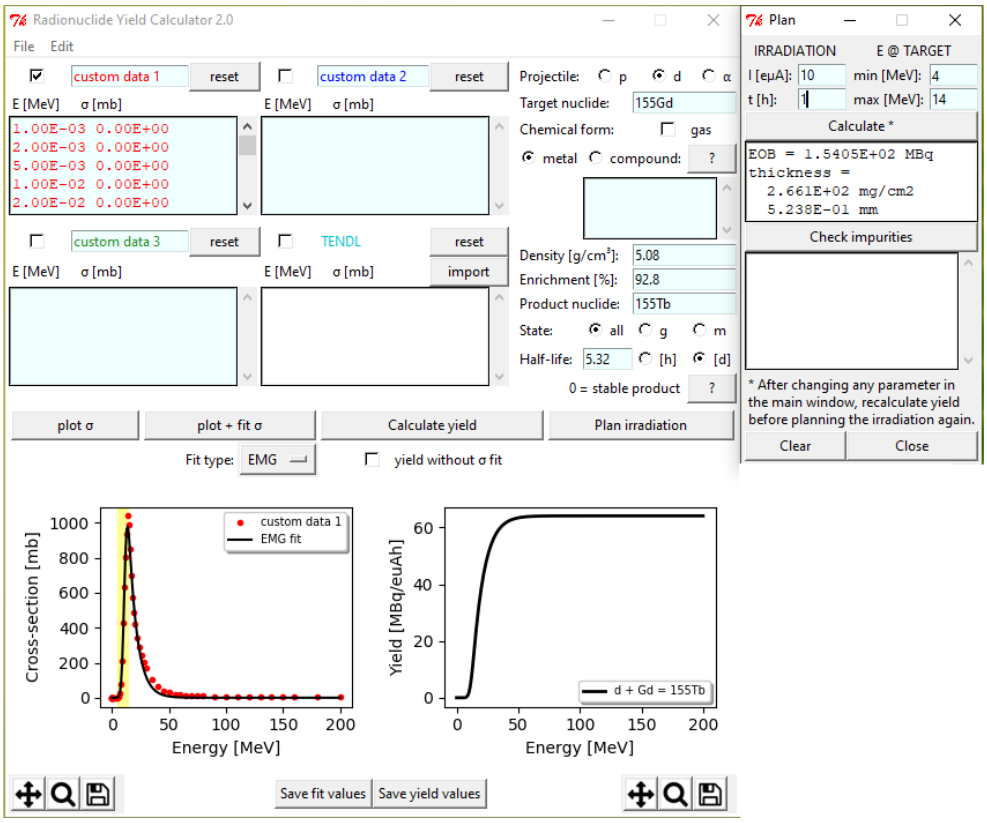


Fig. 3.12 RYC simulation about the optimal thickness for the reaction $^{155}$Gd(d,2n)$^{155}$Tb with the enriched $Gd_2O_3$ used in this work. The cross section data refers to the database Tendl-2019.

To estimate the maximum temperature the pellet can reach, the thermal conductivity of $Gd_2O_3$ pellet has been studied. Three $Gd_2O_3$ pellets with a thickness of 1.0 mm were measured at 24°C, 100°C, 200°C, 300°C, and 400°C. The evolution of the thermal conductivity is shown in Fig. 3.13. The density used for the calculation is the hydrostatic density (7.04 g/cm$^3$). It can be seen that the thermal conductivity of $Gd_2O_3$ decreases with the increase of the temperature, the maximum value is 1.79 $W \cdot m^{-1} \cdot K^{-1}$ at 24°C and the minimum value is 1.27 $W \cdot m^{-1} \cdot K^{-1}$ at 400°C. The change of the thermal conductivity is about -29%, which means it is harder for $Gd_2O_3$ to dissipate heat when the temperature rises.

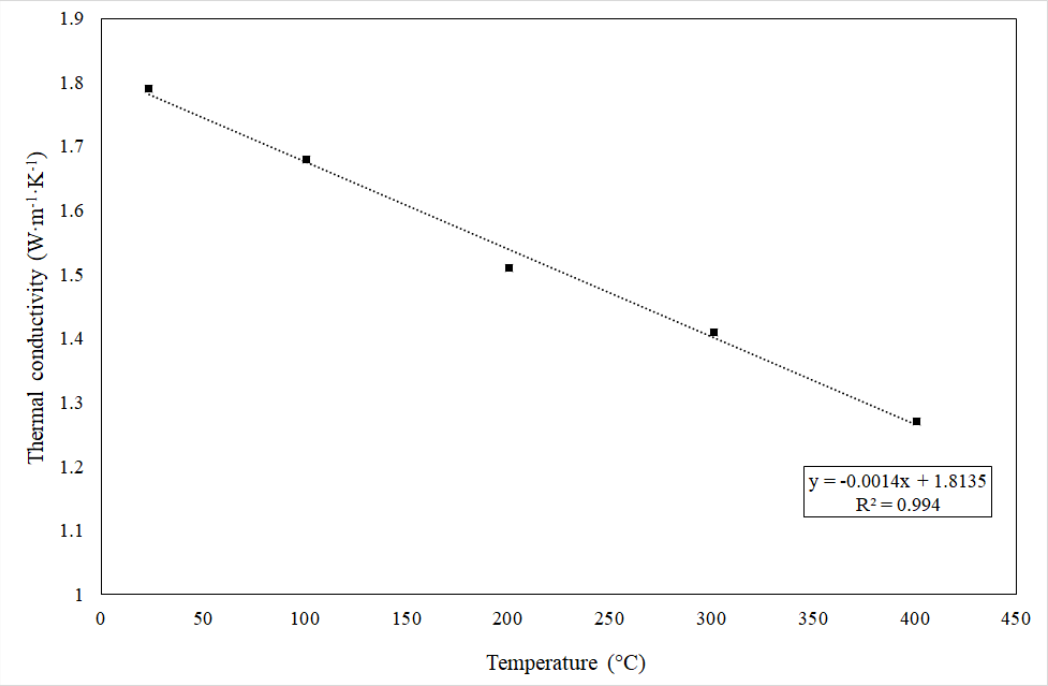


Fig. 3.13 The evolution of the thermal conductivity of $Gd_2O_3$ at 24°C, 100°C, 200°C, 300 °C, and 400°C.

The thermal properties of several pressed solid targets who have already been studied for the production of radionuclide in cyclotron are shown in Table 3.2. According to the table, for metal target, such as Mo and Zn, their thermal conductivities are 138 $W \cdot m^{-1} \cdot K^{-1}$ and 113 $W \cdot m^{-1} \cdot K^{-1}$ respectively, these values are more than 100 times bigger than that of $Gd_2O_3$. For oxide targets, such as CaO and SrO, their thermal conductivities are much smaller than that of metal targets, 19.5 $W \cdot m^{-1} \cdot K^{-1}$ and 17.7 $W \cdot m^{-1} \cdot K^{-1}$ respectively, however, these values are still more than 10 times bigger than that of $Gd_2O_3$. That means that the thermal properties of $Gd_2O_3$ is not as good as other pressed targets. However, the melting point of $Gd_2O_3$ is similar to the melting point of other targets (Mo, CaO, and SrO), and much higher than the melting point of zinc. The high melting point ensures that the pellet will not easily melt in the capsule due to the irradiation. The thermal properties of $Gd_2O_3$ do have some constrains but the irradiation can be carried out by limiting certain parameters (such as the beam intensity and irradiation time) and requiring a good cooling system.

Table 3.2 Thermal properties of different solid targets in room temperature (20-25°C) and their productions.

| Target | Thermal conductivity ($W \cdot m^{-1} \cdot K^{-1}$) | Melting point (°C) | Produced radionuclide |
|---|---|---|---|
| $^{99}Mo$ | 138[176] | 2326 | $^{99m}Tc$ |
| $^{68}Zn$ | 113 | 419.5 | $^{68}Ga$ |
| $^{44}CaO$ | 19.5[177] | 2572 | $^{44}Sc$ |
| $^{86}SrO$ | 17.7[178] | 2531 | $^{87}Y$ |
| $^{155}Gd_2O_3$ | 1.79 | 2420 | $^{155}Tb$ |

For the calculation of the pellet temperature, we used the following parameters :

- a target with a thickness of 0.52 mm,
- encapsulation in a Nb shell (see subsection 4.2.2.4),
- a deuteron beam of 14 MeV,
- a beam intensity of 20 µA and the beam size is 1.0 cm,
- a cooling system having the following characteristics : water cooling on both sides of the encapsulated target, with a temperature of 25°C, the transfer coefficient h = 5000 $W \cdot m^{-2} \cdot K^{-1}$.

Considering all these parameters, he temperature of the target is found between 258°C to 267°C which will not put lots of constrains.

**Heat resistance test :**

The heat resistance test aims to study the changes of pellet mass, morphology and composition at high temperature. In this heat resistance test, four pellets were heated at 100°C, 200°C, 400°C and 600°C. The temperature of this heating resistance test has not be further increased since the temperature of the pellet will be lower than 600°C according to the temperature calculation.
The masses before and after the heating were measured with a scale and the mass change of each pellet is reported in Table 3.3. When the pellet was heated at 100°C and 200°C, the mass of the pellets remained unchanged. However, with the increase of the heating temperature, the mass of the pellets decreases after heating. At 600°C, the pellet has lost 2.3 % of the mass. In general, it can be concluded that the pellet is stable enough at high temperature.

Table 3.3 Mass change of the pellets before and after heating.

| Temperature (°C) | Mass before heating (g) | Mass after heating (g) | Mass change |
|---|---|---|---|
| 100 | 1.60 | 1.60 | 0 % |
| 200 | 1.54 | 1.54 | 0 % |
| 400 | 1.65 | 1.64 | 0.6 % |
| 600 | 1.70 | 1.66 | 2.3 % |

The surface of the same pellets was analyzed by SEM before and after heating. Several zones of the pellets were analyzed and SEM images were similar. The images of the center zone of the pellet before and after heating are shown in Fig. 3.14. The images A, B, C and D represent the image of 4 pellets before the heating; and the images a, b, c and d represent the image of the same pellets after 100°C, 200°C, 400°C and 600°C heating respectively. It can be seen that

there is no evident differences between pellets before and after heating. This illustrates that the morphology of the pellets remains unchanged at 600°C and below.

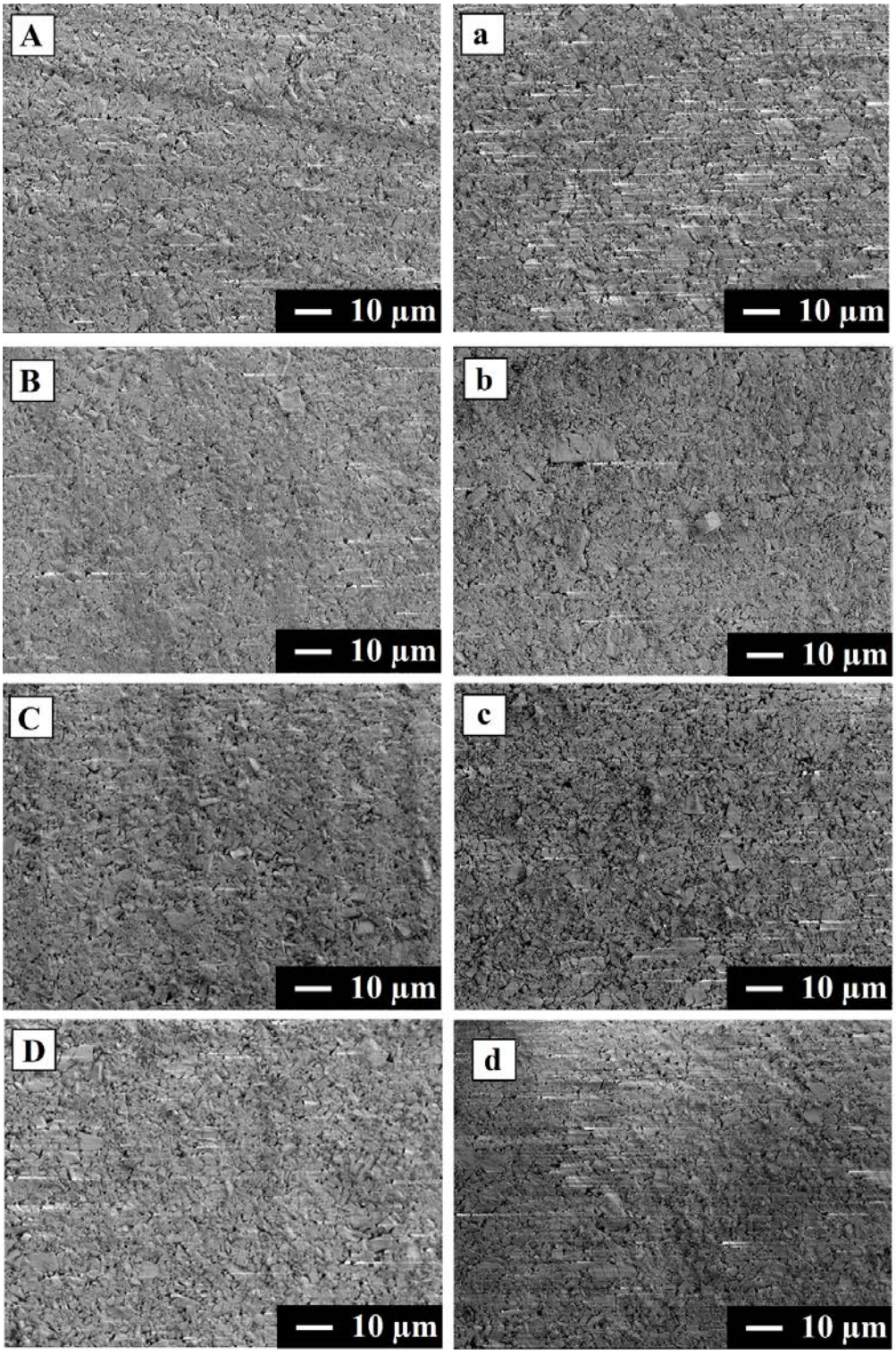


Fig. 3.14 SEM images of four pellets before and after heating. The images A, B, C and D represent the image of 4 pellets before the heating; and the images a, b, c and d represent the image of the same pellets after 100°C, 200°C, 400°C and 600°C of heating respectively.

The composition of the pellet was analyzed by XRD before and after heating at 600°C. The black curve represent the XRD spectrum of pellet before the heating, and the red curve represent

the spectrum after heating at 600°C. Peaks and peak widths of the two spectra are the same, indicating that the composition and crystal structure of the pellet remained unchanged by heating.

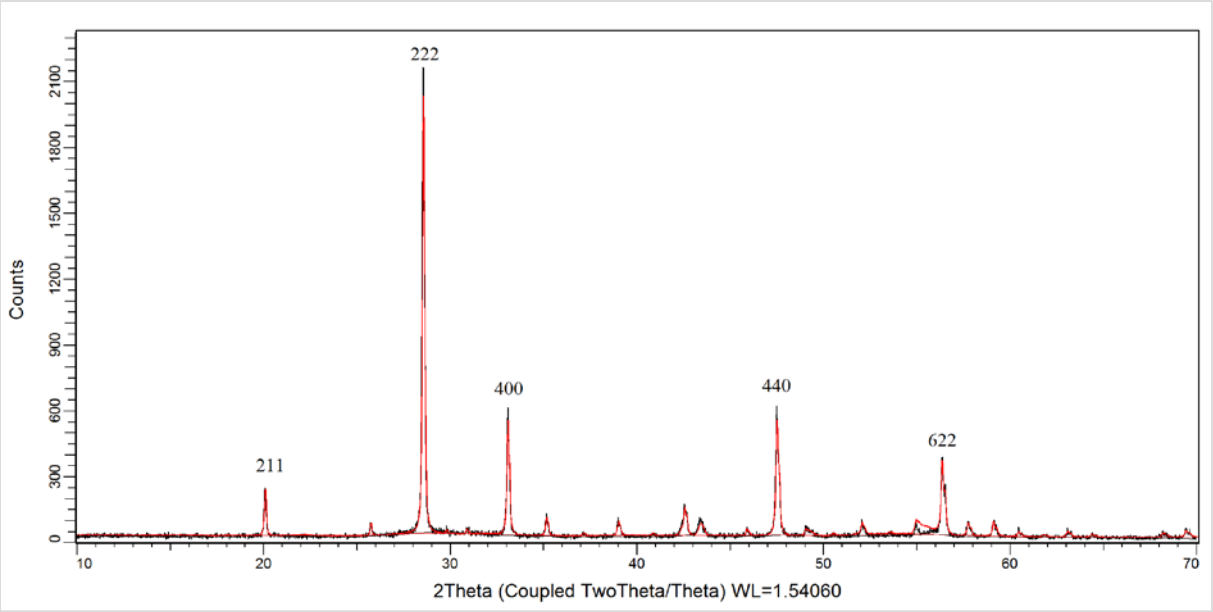


Fig. 3.15 XRD pattern of the $Gd_2O_3$ pellet before (black) and after (red) heating at 600°C.

In summary, the analyses of the mass, morphology and composition of the pellet before and after heating prove that the pellet has a strong stability below 600 °C.

### 3.2.3. Pellet dissolution and recycling of $Gd_2O_3$ powders

Once the pellet is irradiated, it will be dissolved and chemically processed to extract the radionuclide of interest ($^{155}$Tb). Since the half-life of $^{155}$Tb is only 5.32 days, the dissolution process needs to be completed in few hours maximum to reduce the loss of $^{155}$Tb due to decay. In this work, 100 mL of 2 mol/L of HCl was used to dissolve 1.0 g of $Gd_2O_3$. The solution was heated at 90 °C and stirred at 350 rpm. After 1 h, all powder was dissolved.

During irradiation, only a very small part of Gd atoms react with deuterons. After dissolution, $Gd^{3+}$ ions are the main specie in solution. In the case of enriched Gd, these ions need to be recycled to make a new pellet. For this end, oxalic acid was used to generate a gadolinium oxalate decahydrate ($Gd_2(C_2O_4)_3 \cdot 10H_2O$) precipitate, the reaction is shown in *eq.3.13*:

$$2\ Gd^{3+} + 3\ C_2H_4^{2-} + 22\ H_2O \rightarrow\ Gd_2(C_2O_4)_3 \cdot 10H_2O\ (s) + 18\ H_2 \qquad (eq.\ 3.13)$$

This gadolinium oxalate decahydrate can decompose into gadolinium oxide ($Gd_2O_3$) at a high temperature. According to Kaneko et al.[179], $Gd_2(C_2O_4)_3 \cdot 10H_2O$ will first remove water molecules during the heating process to form $Gd_2(C_2O_4)_3$, then $Gd_2(C_2O_4)_3$ will transfer to $Gd_2O_3$ by releasing CO and $CO_2$ above 600°C. The relevant reactions are as follows:

$$Gd_2(C_2O_4)_3 \cdot 10H_2O \rightarrow\ Gd_2(C_2O_4)_3 \cdot 6H_2O \rightarrow\ Gd_2(C_2O_4)_3 \cdot 4H_2O \rightarrow\ Gd_2(C_2O_4)_3 \quad (eq.\ 3.14)$$

$$Gd_2(C_2O_4)_3 \rightarrow\ Gd_2O_2CO_3 \rightarrow\ Gd_2O_3 \qquad (eq.\ 3.15)$$

In this work, after 1.00 g of $Gd_2O_3$ was dissolved in 100 mL of HCl 2 mol/L , 100 mL of oxalic acid 1 mol/L was added to the solution to obtain a precipitate. The precipitate was rinsed three times and gradually heated in an oven. The temperature of the oven increased slowly from 100°C to 700 °C during 7h and then fixed at 800 °C for 8h. After heating, the mass of obtained powder is 0.84 g, so the recovery rate of $Gd_2O_3$ is 84%. Lost powder is mainly due to filtration process and transfer process (from filter paper to drying utensils then to weighing utensils).
To characterize the crystal structure of the obtained powder, XRD was used. The obtained spectrum was compared to the spectrum of $Gd_2O_3$ powder supplied by SigmaAldrich. Fig. 3.16 shows the two spectra with, in black, the recycled powder and in red that from SigmaAldrich. All peaks of both spectra correspond, and these peaks confirm that the obtained powder is $Gd_2O_3$. This result is consistent with the work of Manigandan et al.[180]. However, the peak widths of the recycled powder (black) is wider than that of the reference powder (red). This may be due to the difference of crystallite size of the two powders: the recycled powder may have a smaller crystallite size. The recycled powder can still be compressed into a pellet using the same experimental method and condition, and its mass-thickness relationship is consistent with the relation shown in Fig. 3.10.

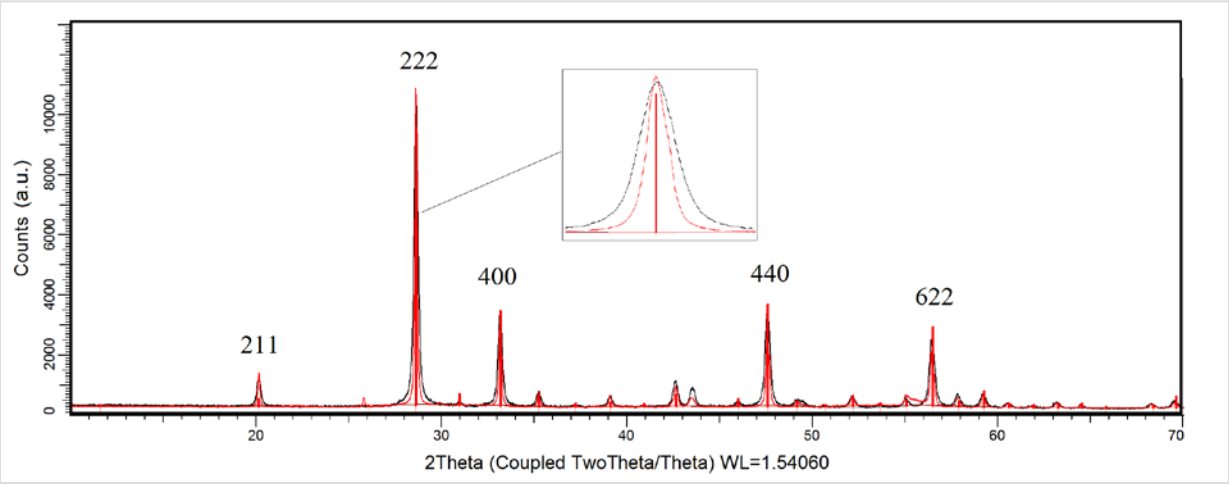


Fig. 3.16 XRD spectra of obtained powder (black) and $Gd_2O_3$ powder supplied by SigmaAldrich (red).

## 3.3. The enriched $^{155}Gd_2O_3$ pellet prepared for irradiation

As mentioned in Chapter 2, 1.0 g of enriched $^{155}Gd_2O_3$ powder was used to make 10 co-electrodeposition targets. Since the powder is insoluble, it sinks to the bottom of the electrolyte after each co-electrodeposition (Fig. 3.17 Left side). The electrolyte and the powder can be easily separated after removing the electrolyte with a pipette, and the $Gd_2O_3$ powder remains in the bottom of the cell (Fig. 3.17 right side).

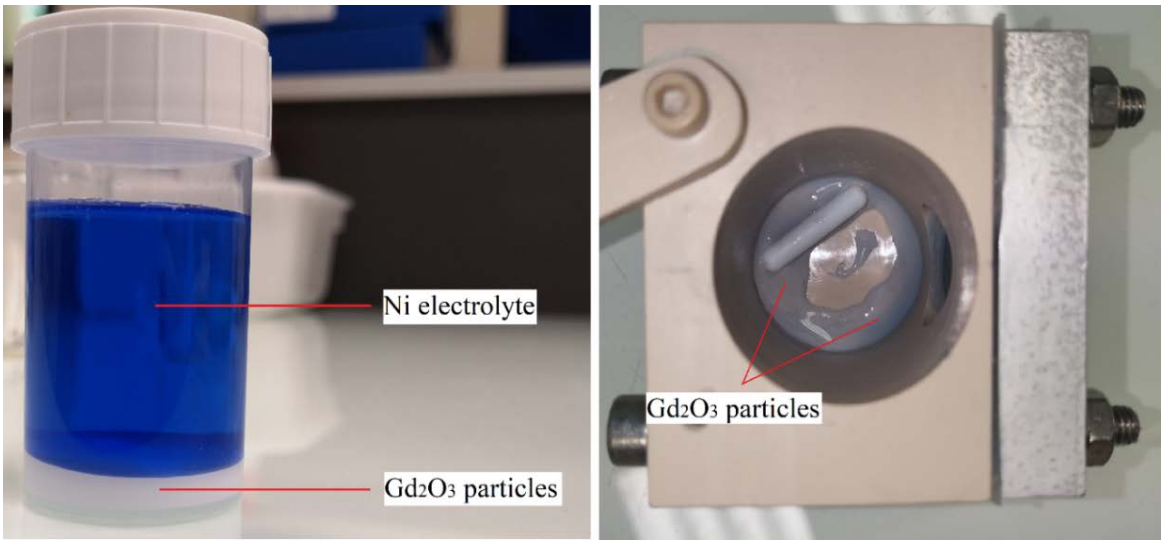


Fig. 3.17 The precipitation of the $Gd_2O_3$ powder in a bottle and in the co-electrodeposition cell. Left side: the layering of the Ni electrolyte and the powder; right side: the powder left in the bottom of the cell after removing the Ni electrolyte with a pipette.

After making 10 co-electrodeposition targets, the remaining powder was collected and rinsed three times, then dried in an oven at 100° for 24 hours, and finally grounded and sieved to limit the particle size to 320 mesh. The mass of the obtained powder is 0.63 g.
Using this powder, a 20 mm in diameter enriched $^{155}Gd_2O_3$ pellet was made (Fig. 3.18) with an applied pressure of 600 bar and a compression duration of 60 s. The thickness of the pellet is 0.39 mm, this result is consistent with the mass-thickness relationship presented in section 3.2.2.1 (Fig. 3.10).

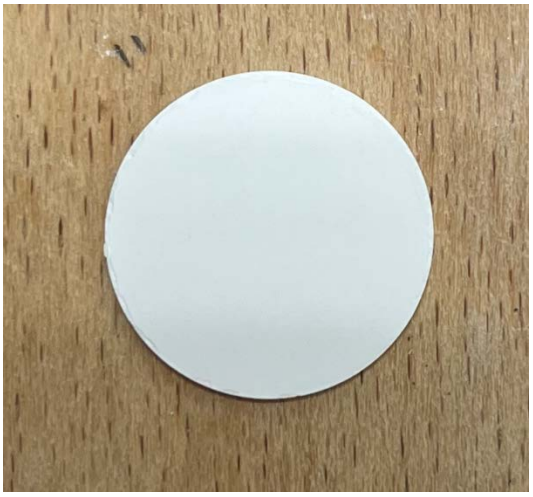

Fig. 3.18 Photo of the pellet made of enriched $^{155}Gd_2O_3$.

The pellet was firstly wrapped by hand in two aluminum foils having each a thickness of 10 µm then the pellet was put into the press and pressed for 60 s under 600 bar to finally get a tightly wrapped pellet. The whole process is shown in Fig. 3.19. This pellet was put in stainless steel holder for irradiation. The design of the capsule and the result of the irradiation will be present in Chapter 4.

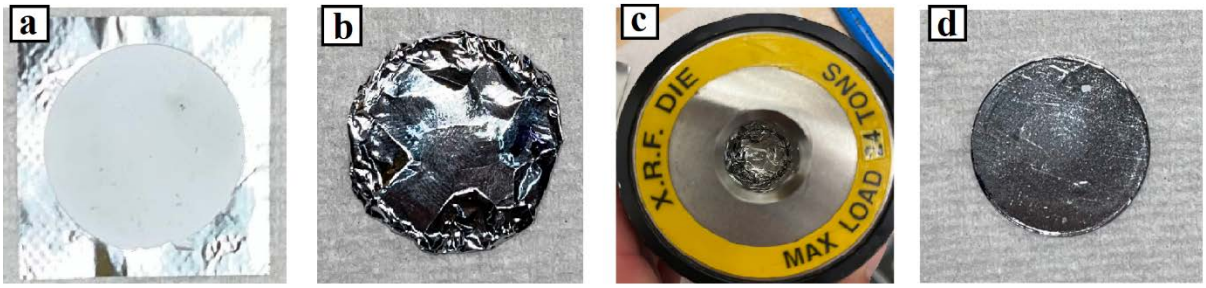


Fig. 3.19 Packaging process of the enriched pellet: (a) the enriched pellet made by the press; (b) the hand wrapped pellet by two aluminum foils; (c) the wrapped pellet in the press die; (d) the tightly wrapped pellet after the compression.

## 3.4. Conclusion of the chapter

In this chapter, the pelletizing method was introduced to manufacture thick targets. A hydraulic press with a capacity of 9500 bar was used to compress powders. Several candidate powders were compared as raw starting material, such as $Gd_2O_3$, $GdF_3$ and $GdCl_3$. The last two were eliminated, on the one hand because of the difficulty of making them, and on the other hand because of their own chemical properties (hygroscopicity or insolubility). Therefore, $Gd_2O_3$ powder was finally chosen as the raw material to make thick targets.

To determine the optimal pelletizing condition, the effects of pressure and the compression time were investigated. Limited by the maximum capacity of our pellet die, the optimal pressure was fixed at 600 bar. Experiments showed that the compression time did not have an impact on the pellet thickness from 10 s to 120 s. The compression time was then fixed at 60 s.

Before making enriched targets, several pellets made with natural $Gd_2O_3$ powder were studied to characterize their physical, chemical and thermal properties. Their density, morphology, crystal structure and thermal conductivity were investigated, and the temperature of the pellet under irradiation was estimated. At the macroscopic level, the measured density was only 5.08 $g/cm^3$, about 72% of the crystal. This low density indicates the existence of pores and voids in the pellet. For pellet with different thickness, their surface morphologies are similar. According to the SEM images, there were cracks and pores on the surface of the pellets when the surface was magnified 1000 times. This observation confirms the hypothesis about the voids in the pellet. Even if these defects can be seen at the microscopic scale, the pellet can still be considered as uniform at the macroscopic scale corresponding to the beam size. This is in addition confirm by looking to the surface with a lower magnification (100 times). The optimal thickness of the target for Tb production was simulated by RYC software considering that we want to avoid $^{154}Tb$. To have an energy variation of the projectile from 14 MeV to 5 MeV, the thickness must be 0.52 mm considering the density experimentally measured. The thermal conductivity of the pellet was measured from 24 °C to 400 °C, this measurement was used to estimate the pellet temperature during irradiation. For a beam energy of 14 MeV and a deuteron beam current of 20 µA, the temperature of the target is between 258°C to 267°C with our cooling system.

Pellets with natural $Gd_2O_3$ powder were also used to study the dissolution of the targets and the recycling of $Gd_2O_3$. Hydrochloric acid was used to dissolve 1 g of $Gd_2O_3$ pellet within 1 h by heating. Oxalic acid was used to recycle $Gd_2O_3$ and a recovery yield of 84% have been obtained.

Finally, a pellet made using 0.64 g of enriched $Gd_2O_3$ powder was prepared for irradiation. Two Al foils were used to wrap the pellet in order to prevent contamination during irradiation. The encapsulation process and the irradiation experiments will be introduced in the next chapter.

# Chapter 4:
# Irradiation of targets for the production of Tb radionuclides

# 4. Irradiation of targets for the production of Tb radionuclides

This chapter is divided into two parts to present the irradiation results obtained with thin targets (co-electrodeposition, Chapter 2) and thick targets (pressed pellets, Chapter 3). The first part presents the cross section measurements of $^{nat}$Gd(d,x)Tb and $^{155}$Gd(d,x)Tb using thin co-electrodeposited targets made with natural $Gd_2O_3$ and enriched $^{155}Gd_2O_3$ respectively. The cross section of $^{nat}$Gd(d,x)Tb has been studied in several other works and the measurements in this work aim to compare our results with published data to validate the reliability of the thin target manufacturing by the developed co-electrodeposition method. Meanwhile, natural Gd target are not suitable for mass production of $^{155}$Tb because of the presence of several impurities (e.g: $^{160}$Tb and $^{156}$Tb) coming from the different Gd isotopes present in natural Gd. Therefore, once the target fabrication method had been validated, targets made by enriched $^{155}Gd_2O_3$ were used to measure the cross sections of $^{155}$Gd(d,x)Tb. These measured results are used to estimate the production yield of thick target. The second part presents an experimental investigation of the $^{155}$Tb production yield using an enriched $^{155}Gd_2O_3$ pellet with a thickness of 0.39 mm. The comparison of theoretical estimation (with TENDL-2019) and experimental values and the determination of irradiation parameters for future production will also be discussed.

## 4.1. Cross section measurement with thin targets

### 4.1.1. Materials and methods

#### 4.1.1.1. The cross section calculation

The nuclear cross section is used to represent the probability to occur of a nuclear reaction between an incident particle and a target nucleus for an incident energy E. The formula of the cross section $\sigma(E)$ was presented in chapter 1 (*eq.1.13*), it is linked with the projectile, the target material and the irradiation parameters.

The study of the cross sections allow, on the one hand, to study the optimum energy for obtaining the maximum production yield of the radionuclide of interest, and on the other hand, to analyze the possibility of producing impurities.

In the case of a thin target (thickness less than 20 µm in this work), the energy loss of the projectile passing through the target is small compared to its initial energy. The cross section can then be considered constant since it varies only slightly over this small energy interval.

Therefore, for a thin, homogenous target hit by a beam that has a size smaller than the surface of the target, the production cross section at energy $E$, $\sigma(E)$ (mb) of the produced nuclei, can be calculated according to *eq.4.1*:

$$\sigma\,(E) = \frac{Act \cdot A}{I \cdot N_A . \rho \cdot \delta x \cdot (1 - e^{-\lambda t})} \qquad (eq.\,4.1)$$

where $\delta x$ is the thickness of the target (cm).

Since all parameters in *eq. 4.1* are independent, estimation of cross section uncertainties is based on combined standard uncertainty estimating in ISO guide[181], as the positive square root of the summation of squares of each parameter (*eq.4.2*).

$$\frac{\Delta\sigma\,(\mathrm{E})}{\sigma\,(\mathrm{E})} = \sqrt{\left(\frac{\Delta I\,(E)}{I\,(E)}\right)^2 + \left(\frac{\Delta\mathrm{Act}\,(\mathrm{E})}{\mathrm{Act}\,(\mathrm{E})}\right)^2 + \left(\frac{\Delta\delta x}{\delta x}\right)^2 + \left(\frac{\Delta\rho}{\rho}\right)^2} \qquad (eq.4.2)$$

It is clear that, to measure the cross section of a given reaction route, it is necessary to measure the number of projectiles per second hitting the target *I*, the activity of produced nuclei *Act(E)*, and the thickness of the target $\delta x$.

#### 4.1.1.2. The stacked foils technique

The stacked foils technique is one of the most used techniques to measure reaction cross sections and obtain the excitation functions (cross section as a function of energy) of projectile-induced nuclear reactions. The principle of this technique is to irradiate a series of thin foils simultaneously[182]. The advantage of the stacked foils technique is that one can measure several cross section values at different energies with only one irradiation. This saves beam time and allows to optimize measurements.

A "stack" is made of several patterns, each containing a target foil, a monitor foil and a degrader foil.

**The target foil:**

The target foil is used to produce the nuclei of interest through a particular nuclear reaction. In this work, the target foil is obtained by co-electrodeposition as presented in Chapter 2. The target is a Ni-$Gd_2O_3$ composited target deposited on a 50-µm-thick gold foil. The thickness of the deposit is between 15-20 µm.

**The monitor foil:**

The monitor foil is placed next to the target and is used to determine the number of the projectiles per second hitting the target (the "*I*" in *eq.4.2*) through a known nuclear reaction. Indeed, using the measured activity of the monitor radionuclide and knowing the characteristics of the foil, it is possible to determine the number of projectiles per second. This number is also the one hitting the target foils as the monitor foil that is just placed after it. Considering that we were using deuteron and the energy range of interest, titanium foils and nickel foils were used as monitors in this work. For these two types of monitors, using *eq. 4.1*, the number of the projectiles per second $I'$ of titanium foils or nickel foils was determined by using the reference cross section $\sigma'(E')$ of the reaction $^{nat}$Ti(d,x)$^{48}$V [121] or the reaction $^{nat}$Ni(d,x)$^{58(m)}$Co [124], respectively. The values of the reference cross section $\sigma'(E')$ were referred by the data of IAEA[183], details can be found in *Appendix 4.1*. The monitor atomic number $N'$ was determined by its mass, its atomic mass, and the Avogadro constant. The number of the projectiles per second hitting the monitor $I'$ was then calculated. Values calculated using the monitor are consistent. This work used an average value of the two monitors, $I''$. Since monitor foils have the same area as targets and are located just next to the target foils, $I''$ is considered equal to $I$. It can be deduced the *eq.4.3*.

$$\sigma\,(E) = \frac{Act(E).A}{I'' \cdot N_A.\rho \cdot \delta x \cdot (1 - e^{-\lambda t})} \qquad (eq.4.3)$$

The monitor foil can also be used as a “catcher” to collect recoil nuclei from the target. In this case, to estimate the produced activity of the desired radionuclide, the value measured in the target and the catcher foil must be summed up. In our case, recoil nuclei from the deposit are stopped on the gold support preventing them to escape to the monitor foil. All monitor foils were provided by *Goodfellow*[132] (99.99% purity).

**The degrader foil:**

The degrader foils are used to adapt the energy of the beam impinging consecutive targets. In this work, aluminum foils were used as beam energy degraders. All degrader foils were provided by *Goodfellow*[132] (99.99% purity).

As mentioned, in a stacked-foils experiment several patterns are irradiated simultaneously. However, to limit energy dispersion and excessive cumulative error in energy calculation due to too many foils[184], we restricted ourselves to 2 patterns in a given irradiation. This also allowed us to leave enough time for the data acquisition. The schematic diagram of one stack made of two patterns corresponding to one typical experiment is presented in Fig. 4.1. For the first target, the titanium and nickel monitor foils were located just before and after the target foil respectively. The particle flux of the target is the average value of the flux determined by the two monitors. However, for the second target, as in some cases the energy impinging the deposit was low leading projectiles to stop into the target foil, the two monitor foils were both put in front of the target. Since the co-electrodeposited targets contain nickel, to avoid the recoil nickel nuclei from the target contaminating the nickel monitor (according to our measurement and estimation, the recoil nuclei can reach up to 1% of the number of atoms the nickel monitor), titanium foil was placed between the nickel monitor and the target.

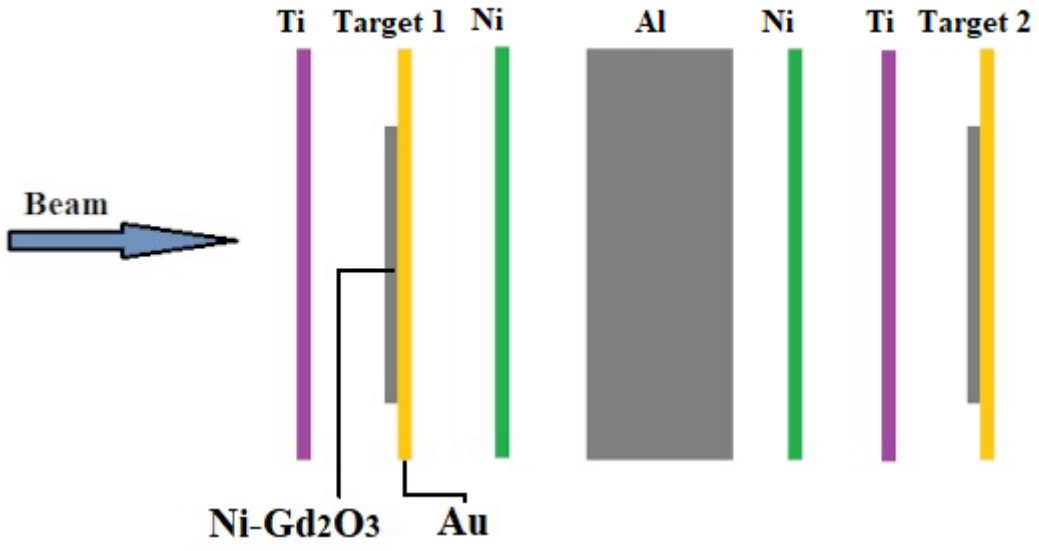


Fig. 4.1 Schematic diagram of the stack composition used for a typical experiment where we irradiated two targets simultaneously. The size and thickness of the foils are not drawn according to the actual scale.

The stack was placed in air 6 cm downstream of the beam output window, made of a 50 µm thick Kapton foil.

#### 4.1.1.3. The energy calculation for each foil

The thickness of foils is not the same for each experiment and needs to be estimated based on the co-electrodeposited deposit characteristics and the targeted energy. To this end, the beam energy loss in each foils needs to be estimated.

When a charged particle moves through a matter, it transmits its energy to the matter. The stopping power is the rate of energy loss by the ion in the target, it is expressed as $\frac{dE}{dx}$, the energy loss per unit distance in the target. The stopping power can be estimated using the Bethe-Bloch formula with density correction and shell correction:

$$-\frac{dE}{dx} = 2\pi N_a r_e^2 m_e c^2 \rho \frac{Z}{A}\frac{z^2}{\beta^2}\left[\ln\left(\frac{2m_e\beta^2c^2W_{max}}{I^2(1-\beta^2)}\right) - 2\beta^2 - \delta - 2\frac{C}{Z}\right] \qquad (eq.4.4)$$

with $N_a$ (mol$^{-1}$) the Avogadro's number, $r_e$ (cm) the classical electron radius, $m_e$ (g) the mass of the electron, $\rho$ (g·cm$^{-3}$) the density of absorbing material, Z (a.u.) the atomic number, $A$ (g· mol$^{-1}$) the atom weight of the absorbing material, $z$ the charge of the incident particle in units of e, $\beta$ (a.u.) the ratio of the incident particle speed to the light speed $\frac{v}{c}$, $I$ (eV) the mean excitation potential, $W_{max}$ (eV) the maximum energy transferred in one collision, $\delta$ is the density correction and $C$ is the shell correction.

The energy loss of the charged particle as a function of the path can be presented by the Bragg curve. An evidence peak in the Bragg curve is called the Bragg peak, this peak occurs just before the rest of the charged particle. In the plateau region before the peak, the energy of particles decrease through ionization of target atoms. Meanwhile, near the peak region, particle energy causes permanent damages of the target structure by disrupting interatomic bonds.

The Stopping and Range of Ions in Matter (SRIM) is a collection of programs using Monte Carlo code to simulate the stopping power and range of ions into the matter, the ion implantation, the sputtering, the ion transmission, and the ion beam therapy[185,186]. The program TRIM of SRIM was used to simulate the transport of charged particles (ions) in targets including the distribution of ions and other kinetic phenomena associated with the ion's energy loss, such as the target damage and sputtering[186]. This work only considered the energy loss and the distribution of ions. TRIM can simulate single-layer or multi-layer targets, whether single composition or composite compound. The newest version of this program, SRIM-2013, was used in this work to calculate the energy loss in thin and thick targets.

Since the thickness of our targets is only 10-20 µm, the energy loss is small. Therefore, the energy in the middle of each target's thickness is considered as the energy of the whole thin target. During the TRIM simulation, all foils were considered homogeneous. The target was regarded as to be composed of Gd, O, and Ni three components. The number of atoms of each component and the density of the target were the one determined according to the ICP-AES analysis results (see subsection 1.3.5.3 in Chapter 2).

For the cross section measurement, the energy uncertainty includes the uncertainty due to energy straggling in TRIM estimation and the beam energy uncertainty (± 0.25 MeV, according to the ARRONAX cyclotron's supplier IBA) calculated by the cyclotron manufacturer.

#### 4.1.1.4. Activity measurements

According to *eq.4.1*, the activity of the nuclei of interest should be measured to be able to calculate the reaction cross section value. In this work, we were interested to $^{155}$Tb, several coproduced impurities, $^{153}$Tb, $^{154}$Tb, $^{156}$Tb, $^{161}$Tb and monitor radionuclides that are all gamma emitters. To get these activities, we used a high-purity germanium detector (HPGe).

**Gamma detection:**

When a photon enters a material, it may interacts through different processes among which the following three processes are the most important to be considered: the photoelectric effect, the Compton effect, and the pair production effect. The probability associated to these phenomenon depends on the photon energy as presented by Lee at al [187] using the linear attenuation coefficient for these three processes ( see Fig. 4.2).

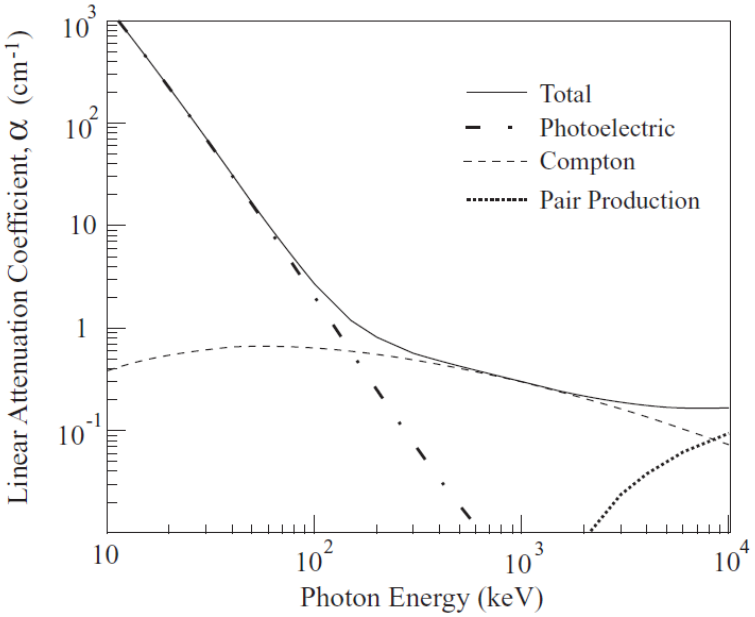


Fig. 4.2 Linear attenuation coefficient of the photoelectric interaction, Compton interaction and pair-production interaction for germanium, figure made by Lee et al[187].

On this figure, we can clearly see that the photoelectric effect dominates at lower photon energies. The photoelectric effect consists on the full transfer of the energy of the incident photon to one electron of the medium leading to the excitation of the atom and ejection of the electron (called photoelectron). This electron will then interact strongly with matter leading to full energy transfer. The schematic representation of photoelectric effect is shown in Fig. 4.3.

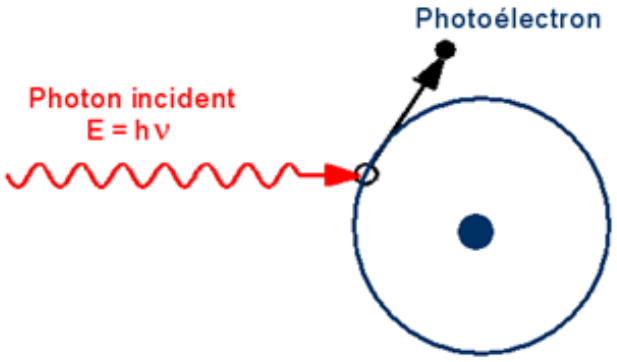


Fig. 4.3 Schematic representation of the photoelectric effect.

As seen in Fig. 4.2, the Compton effect is dominant at medium energy (around 1 MeV). In this case, the photon and an electron slightly bonded to the atom interact together. The Compton effect is an inelastic scattering of the photon by the electron. Part of the energy of the photon is given to the electron that leave the atom whereas a lower energy electromagnetic radiation is deviated. The schematic representation of this effect is shown in Fig. 4.4.

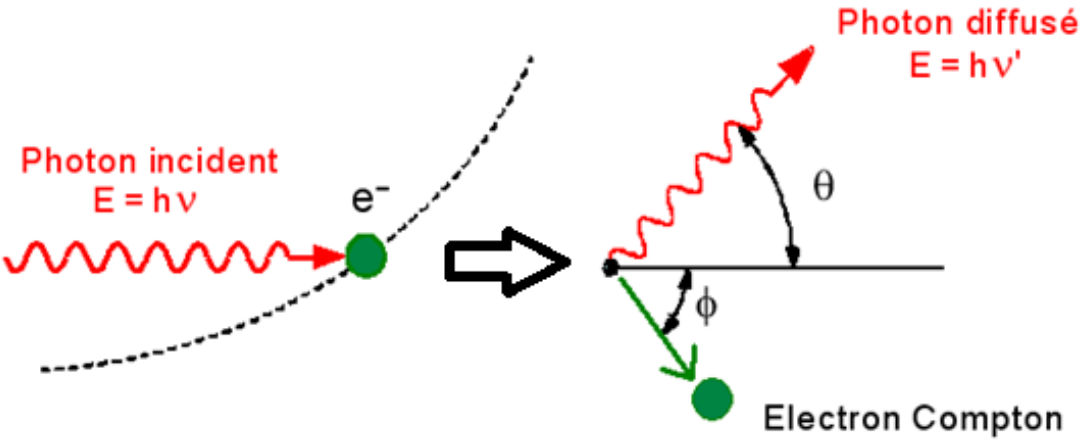


Fig. 4.4 Schematic representation of the Compton effect.

The pair production effect is dominant for high gamma energies as shown in Fig. 4.2. It consists to the annihilation of the photon in the Coulomb field generated by the nucleus and the creation of an electron/positron pair. It is a threshold reaction that can only occurs if the photon energy is higher than sum of the rest mass energy of the electron and the positron (E >1.022 MeV). This process is shown in Fig. 4.5.

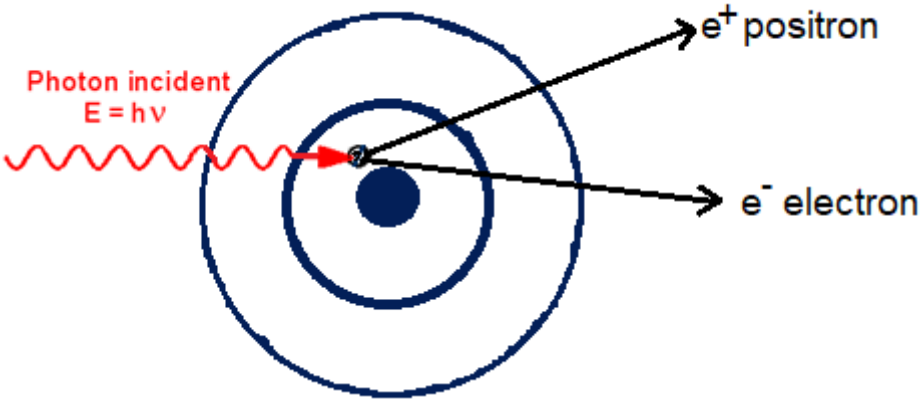


Fig. 4.5 schematic representation of the pair production effect.

Semiconductors are commonly used as gamma detectors, especially germanium crystals. A characteristic of semiconductor materials is that the energy to cross the band gap and to reach the conduction band is small ($E_{gap}$ = 0.67 eV). Such low value requires operating the detector at cryogenic temperatures to avoid band crossing by thermal effect. When crossing the HPGe (High Purity Germanium), the photon will release energy that will be used to create electron-hole pairs. The number of electron-hole pairs is proportional to the released energy in the semiconductor. These electron-hole pairs will be collected and be converted into current signal[188]. The signal is amplified and reaches the analog-digital converter, where it is recorded in a channel of the analyzer.

The detector used in this work is an HPGe detector supplied by *CANBERRA.* A photo of the detector is shown in Fig. 4.6. The cooling system is located on the bottom of the detector (position 1 in Fig. 4.6), it uses liquid nitrogen to keep low temperature (77 K). The Germanium crystal (position 2), placed in vacuum and covered by an aluminum endcap, is in a square shielded chamber made of lead walls covered with copper layers (inside) to eliminate X-rays created in the shielding. A high counting position (position 3) is located 19 cm above the detector. It is surrounded by lead shields to limit worker exposure.
The useful energy range of this detector is from 40 keV to 10 MeV[189]. This detector provide two geometries for solid and liquid samples and samples can be placed at 0 cm or 19 cm from the detector. This allows us to adjust the counting conditions to the activity of the source and in particular, to make sure that dead time[1] is always below 10%.

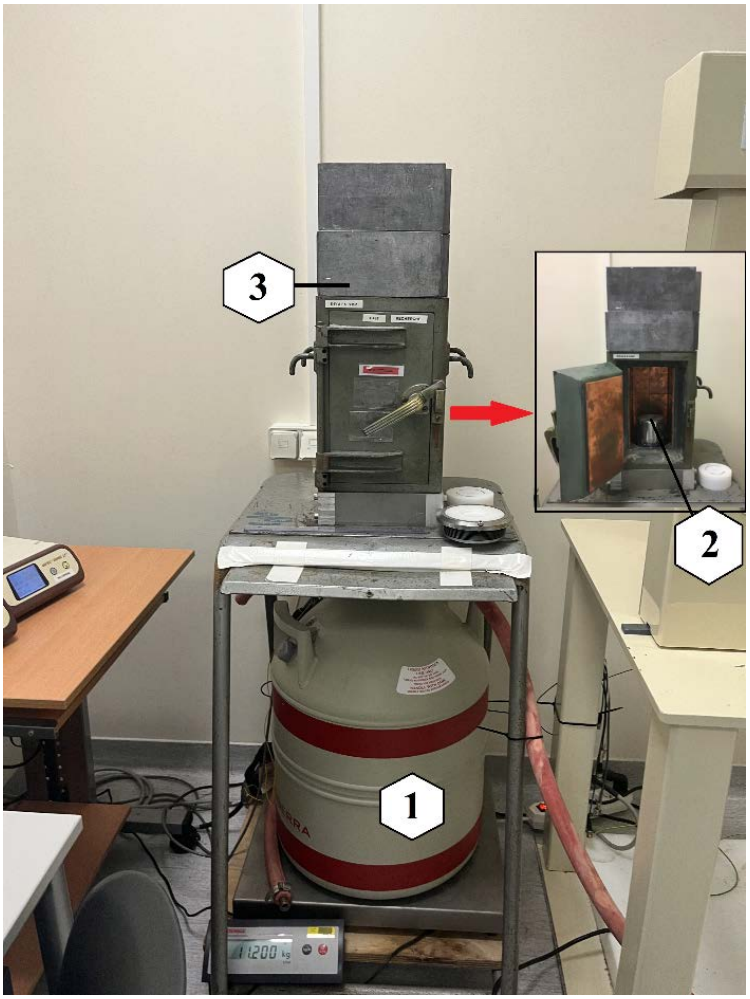


Fig. 4.6 CANBERRA HPGe detector used in this work: (1) cryostat and cooling system with liquid nitrogen, (2) Ge crystal covered with aluminum endcap, (3) high position (19 cm) above the detector, surrounded by lead shield.

[1] Dead time: When a sample is highly radioactive, it is possible that one gamma ray arrives to the detector whereas one gamma ray is already being processed, therefore it will be lost since the detector needs a certain time to record one event and during this time it cannot record another event. This time interval is called dead-time of the detection system[190].

**Energy and Efficiency calibration**:
Before any use, the detector needs to be calibrated for energy and for efficiency using known reference sources (well known source with a known activity and geometry).
The energy calibration aims to find the relationship between a channel number and the photon energy, this relation is linear for semiconductors. The photon energy $E_\gamma$ can be expressed as *eq.4.5*:

$$E_\gamma = a \cdot C + b \qquad (eq. 4.5)$$

Where a and b are two constants, C is the channel number.
The efficiency calibration is intended to determine the ratio of the number of photons detected by the detector to the number of photons emitted by the sample at each photon energy. The efficiency ε can be expressed as *eq.4.6*:

$$\varepsilon(E) = \frac{N_{detected}(E)}{N_{emitted}(E)} \times 100\% \qquad (eq. 4.6)$$

Where $N_{detected}$ is the number of detected photons by the detector and $N_{emitted}$ is the number of emitted photons by the sample. It depends on the energy of the photon as well as the geometry of the sample and the counting position.
The number of emitted photons $N_{emitted}$ decreased with time and follows an exponential relation:

$$N_{emitted}(E) = N_0(1 - e^{-\lambda t_m}) \cdot I(E) \qquad (eq. 4.7)$$

Where $N_0$ is the initial photon number at the beginning of the counting, λ is the decay constant of produced nuclei, $t_m$ is the measurement duration, and I is the intensity at energy E.
Therefore, the efficiency can be finally expressed as *eq.4.8*:

$$\varepsilon(E) = \frac{N_{detected}(E)}{N_0(1 - e^{-\lambda t_m}) \cdot I(E)} \times 100\% \qquad (eq. 4.8)$$

In this work, two reference sources were used for energy and efficiency calibrations. They both have gamma rays emitted over a wide energy range for a precise definition of energy dependence of the efficiency calibration. One is a $^{152}$Eu source for calibrating solid samples; the other is a multi-gamma source provided by GIP ARRONAX for the calibration of liquid samples, it is mixed with various radionuclides, such as $^{210}$Pb, $^{241}$Am, $^{109}$Gd, are used. List of the radionuclides in this source are shown in *Appendix 4.2*. These two sources had the same geometry as samples, and they were placed at the same place as the samples. Details of energy calibration and efficiency calibration are shown in *Appendix 4.2*.

**Sample measurements:**
After irradiation, each target foil (the deposit) was dissolve to be able to separate the gold substrate which is activated and will increase the background during measurement. Details will be presented in section 4.1.2.4. For each stacked foils experiment, 5 mL of dissolved solution sample was placed at 0 cm above the detector and the data acquisition began 20 h after the end

of bombardment (EOB) for the first target and 38 h after EOB for the second target. The counting duration was between 8 h to 14 h for each sample.
Solid titanium monitor foils were measured by the same detector 19 days after EOB [191] to allow the full decay of $^{48}$Sc ($T_{1/2}$ = 43.67 h, E = 983.526 keV, $I_\gamma$ = 100.1%) and avoid interferences. Similarly, solid nickel monitor foils were measured 2 months after EOB [125] to avoid interferences of $^{56}$Ni ($T_{1/2}$ = 6.075 d, E = 811.85 keV, $I_\gamma$ = 86.0%). All targets and foils were counted from 8 h to 14 h at higher position (19 cm from the detector). The dead time for liquid samples was between 5% and 1% and close to 0% for solid samples.

#### 4.1.1.5. Activity data processing

For a gamma emitter, the relationship between the initial photon number $N_0$ and the activity at the beginning of the counting $A_0$ of this radionuclide is shown as *eq.4.9*:

$$A_0(t) = \lambda N_0(t) \qquad (eq.4.9)$$

Therefore, *eq.4.8* can be reformulated to *eq.4.10*:

$$A_0 = \frac{\lambda \cdot N_{detected}(E)}{\varepsilon(E)(1 - e^{-\lambda t_m}) \cdot I(E)} \times 100\% \qquad (eq.4.10)$$

So *eq.4.10* indicates the relation between the count number of a given channel and the initial activity of the radionuclide.
Further, the activity of the EOB $A_{EOB}$ can be deduced:

$$A_{EOB} = A_0 e^{-\lambda \Delta t} \qquad (eq.4.11)$$

with $\Delta t$ the duration from the EOB to the beginning of the counting.
Two types of software were used in this work to determine the activity of the EOB.
The LViS[192] software was associated to the HPGe detector to collect the gamma spectrum. It is an emulation, acquisition and analysis software for gamma spectrometry developed by *Hi-Tech Detection Systems (HTDS)*[192]. This software can search, visualize, analyze and store peaks, has a tool for calculating sum peak corrections as well as efficiency transfer corrections for gamma spectrometry[192].
The *Fitzpeaks Gamma Analysis*[193] software was used in this work to determine the activity of radionuclides. The mathematical algorithm of this software is based on the gamma spectrum analysis program SAMPO80[194] developed in 1980s. The peak search algorithm is based on finding the minimum value in the smoothed second-order difference of the spectral data, and the peak fitting is based on a linear least squares procedure to fit the data to a Gaussian function[193]. A library of radionuclide lists and their decay information (half-life, chosen gamma energy and its intensity) should be created manually, and then the radionuclide identification and activity calculation are done by forming interference matrices and solving for interference sets using weighted least squares[193]. In this work, the maximum peak area uncertainty is 65%.

#### 4.1.1.6. Thickness measurement

All foils for monitors, degraders, and gold substrates of the deposit are of high purity and supplied by *Goodfellow*. To estimate the thickness, we consider them homogeneous and can then use *eq.4.12*:

$$e = \frac{m}{\rho \cdot S} \qquad (eq.\,4.12)$$

Where m (g) is the mass of the foil, ρ (g/cm$^3$) is the density of the foil, and S (cm²) is the surface. Since all parameters in *eq.4.12* are independent, the uncertainty of the thickness can be expressed as the positive square root of the summation of squares of each parameter:

$$\frac{\Delta e}{e} = \sqrt{\left(\frac{\Delta m}{m}\right)^2 + \left(\frac{\Delta \rho}{\rho}\right)^2 + \left(\frac{\Delta S}{S}\right)^2} \qquad (eq.\,4.13)$$

To determine the mass, all foils were weighed with a balance of an accuracy of 0.0001 g before being irradiated.

To determine the surface, foils were scanned by a high-resolution scanner *Epson Perfection V600 Photo*[195] before irradiation. The scanned image was then processed with *GIMP 2.10* [196] to determine the surface of the foil by comparing the number of pixels in the foil with the total number of pixels in the image. Since the shape of the foils is regular (almost a square with a side length of about 2.5 cm), the error in selecting the number of pixels in the foil area is small. The final surface is the average of three estimations with an error of less than 0.5%.

For Ni-$Gd_2O_3$ deposits, the distribution of $Gd_2O_3$ particles is not homogeneous along the thickness (section 2.2.2 in chapter 2). However, since the quantity of $Gd_2O_3$ is much smaller than that of Ni, the number of Gd atoms is less than 5% of the number of total atoms, so the effect of the inhomogeneous distribution of Gd is negligible for calculating the thickness. Therefore, *eq.4.12* can also be applied to the calculation of the deposit thickness.

The density of the deposit $\rho_{tot}$ can be estimated as *eq.4.14*:

$$\rho_{tot} = \rho_{Ni}\frac{N_{Ni}}{N_{tot}} + \rho_{Gd2O3}\frac{N_{Gd2O3}}{N_{tot}} \qquad (eq.\,4.14)$$

Where $\rho_{Ni}$ and $\rho_{Gd2O3}$ are the density of Ni and $Gd_2O_3$, respectively, $N_{Ni}$ and $N_{Gd2O3}$ are the atom number of Ni and $Gd_2O_3$, respectively, and $N_{tot}$ is the total atom number. The atom numbers are calculated according to ICP-AES analysis. The error of the density is related to the proportion error of Gd and Ni estimated by ICP-AES, which is smaller than 0.5%.

#### 4.1.1.7. Irradiation experimental set-up

The irradiation process were carried out at the GIP ARRONAX facility. Fig. 4.7 shows the AX3 beam line used in this work. This is a low intensity light particle (proton, deuteron, alpha particle) beam line. The beam direction is marked as a red arrow, particles are coming from the cyclotron sitting on the other side of the back wall to the end of the beam (1). The whole capsuled stack is situated 6 cm away from the end of beam line closed by a Kapton foil (2). Normally the beam will be stopped at (2), but for the purpose of redundant design for radiation protection, a stopper

made of aluminum (3) is located downstream the stack location to stop the beam. The energy of the deuteron beam is limited to 35 MeV. According to theoretical analysis, the maximum cross section appears in the energy interval of 8-30 MeV, so this energy range is selected in this work.

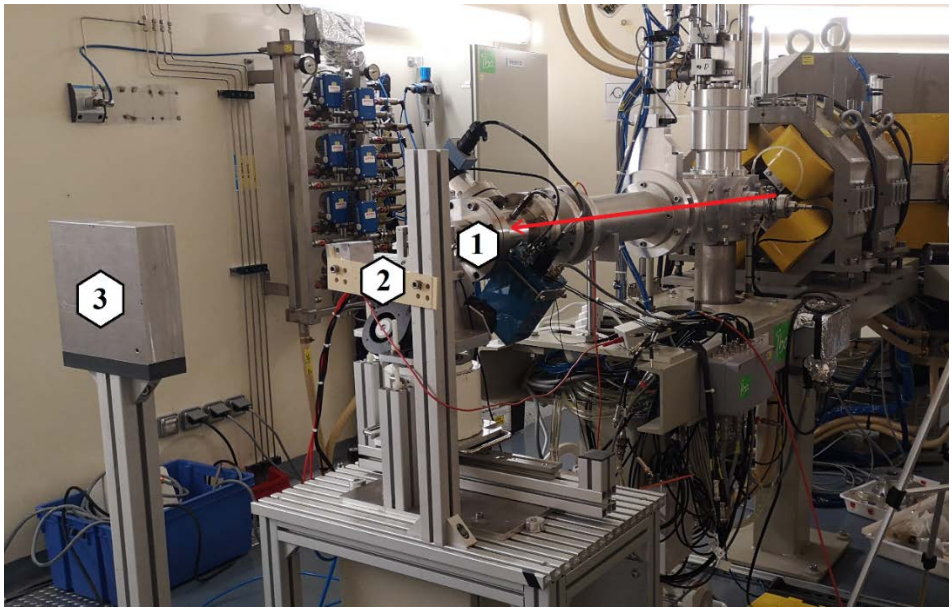


Fig. 4.7 Photo of the beam line used at GIP ARRONAX facility. 1: the end of bombardment (EOB), 2: the position of the stack, 3: aluminum beam stopper for stopping particles.

For irradiation, all foils are stacked according to the define partner and sealed in a stainless steel metal ring capsule with a 2 cm diameter hole in the middle (Fig. 4.8 (a)). The center of the capsule is aligned with the center of the beam. The beam form is approximately circular, its diameter is about 1-1.5cm. So the beam will pass through the hole and irradiate directly the encapsulated foils without touching the capsule.

During irradiation, a lead pot (Fig. 4.8 (b)) was situated below the encapsulated stack. After irradiation, the entire device was cooled for 14 hours to allow short-life radionuclides to decay, reducing the overall activity of the encapsulation. Then the capsule was dropped directly into the lead cylinder to be collected.

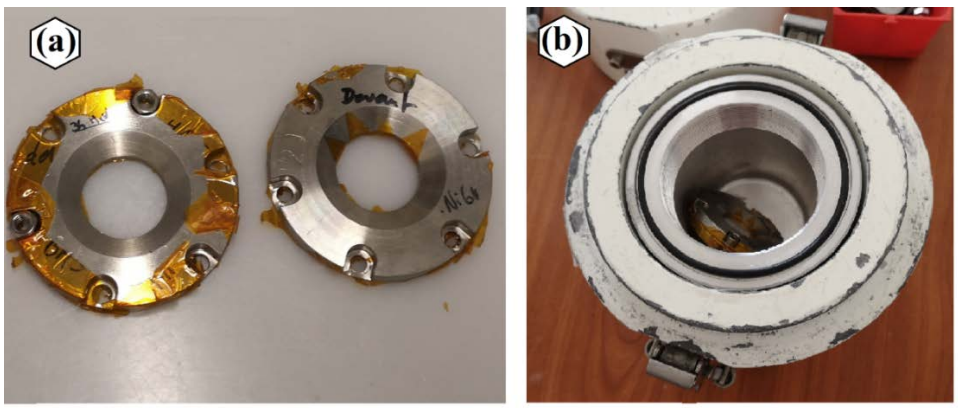


Fig. 4.8 The stainless steel ring capsule (a) and the lead pot for collecting the encapsulation (b).

### 4.1.2. Activation cross sections of deuteron-induced reactions on natural Gd

#### 4.1.2.1. Theoretical analysis of the production $^{nat}$Gd(d,x)Tb

The composition of natural gadolinium and the abundance of each isotope are listed in Table 4.1.

Table 4.1 Composition of natural gadolinium and abundance of each isotope.

| Isotope $^{i}$Gd | $^{154}$Gd | $^{155}$Gd | $^{156}$Gd | $^{157}$Gd | $^{158}$Gd | $^{160}$Gd |
|---|---|---|---|---|---|---|
| Abundance $r_i$ (%) | 2.18% | 14.80% | 20.47% | 15.65% | 24.84% | 21.86% |

Before the irradiation, the theoretical production of terbium isotopes by natural gadolinium was studied using TENDL. TENDL[96] is a nuclear data library using both default and adjusted theoretical simulation of TALYS code with experimental inputs. This nuclear database, mainly developed by IAEA[197], provides outputs of nuclear reactions for more than 2800 isotopes involving several types of incident particles: neutron, light charged particles and gamma-ray, in the 1 keV-200 MeV energy range[96]. In this work, TENDL-2019 was used to simulate the theoretical production of terbium isotopes by gadolinium isotopes using deuterons or protons.
For each Tb radionuclide $^{j}$Tb with *j* the terbium mass number, the cross section produced by natural Gd ($\sigma_{nat}$) is linked with the cross sections produced by each Gd isotope ($\sigma_i^j$ for the reaction $^{i}$Gd(d,x)$^{j}$Tb with *i* the gadolinium mass number) and the abundance ratio of the isotope $r_i$, which can be expressed as *eq.4.15*:

$$\sigma_{nat}^{j} = \sum_{i} r_i \sigma_i^j \qquad (eq.\,4.15)$$

Where i = 154, 155, 156, 157, 158 and 160, and j = 153, 154, 155, 156, 157, 158, and 160.
The Fig. 4.9 presents simulated production cross sections of terbium isotopes by deuteron-induced reactions on natural Gd. It can be seen that between 0-35 MeV, $^{153}$Tb, $^{154}$Tb, $^{155}$Tb, $^{156}$Tb, $^{157}$Tb, $^{158}$Tb and $^{160}$Tb are produced. In this figure, the curves of $^{154}$Tb, $^{156}$Tb and $^{158}$Tb represent cumulative cross section of all fundamental and metastable states of $^{154}$Tb, $^{156}$Tb and $^{158}$Tb, respectively. Visually, the cross section of $^{155}$Tb begins at 4 MeV, and it reaches about 385 mb at around 26 MeV, then it decreases with energy between 25-30 MeV before rising again. The co-production of other terbium isotopes is unavoidable in the energy range 5-30 MeV where the cross section is maximum.

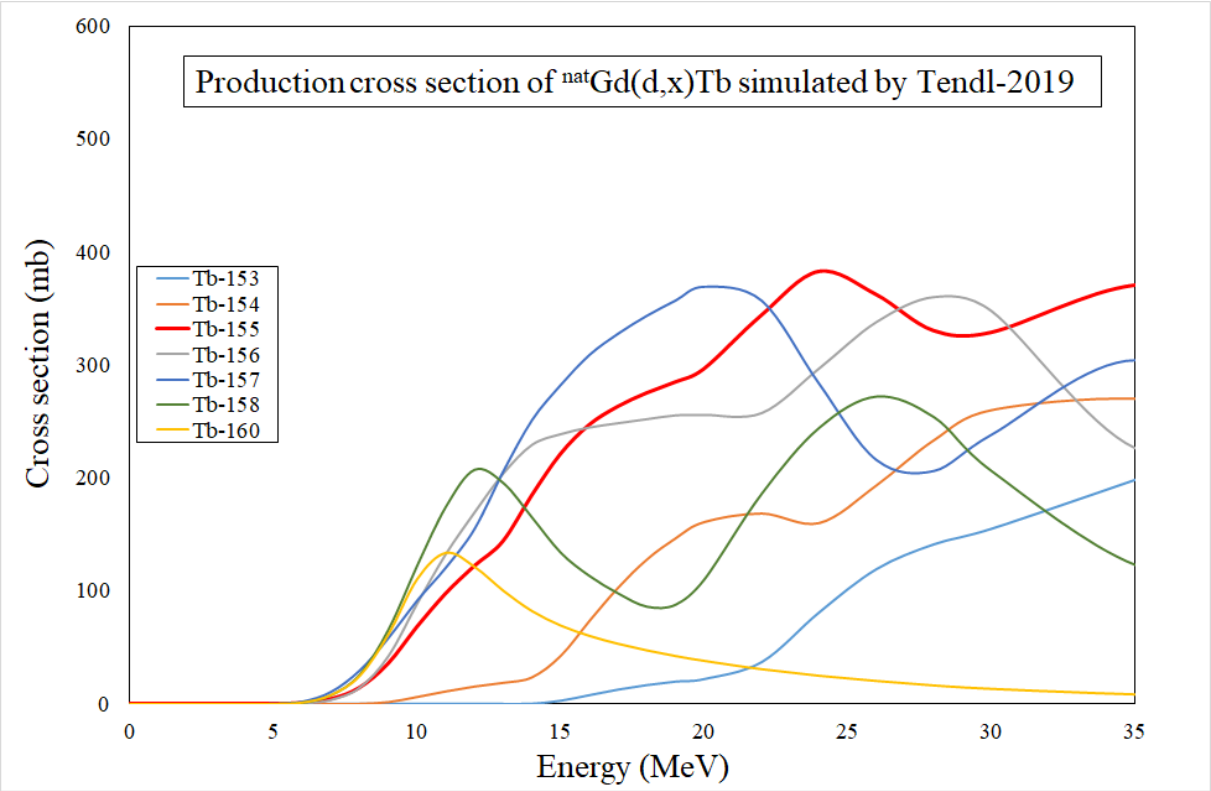


Fig. 4.9 Simulated production cross section of Tb isotopes by deuteron induced reactions on natural Gd target.

The decay information of these radionuclides and relative production reactions are listed in Table 4.2. The $E_{thresold}$ marked in the last column corresponds to the threshold energy for producing ground state radionuclides. For the radionuclide of interest, $^{155}$Tb ($T_{1/2}$ = 5.32 d), all the Gd isotopes have contributions to its production. According to the table, when the deuteron energy is between 0 to 3.88 MeV, the unique reaction for $^{155}$Tb production is $^{154}$Gd(d,n)$^{155}$Tb; when energy is limited between 3.88 MeV and 12.52 MeV, only $^{154}$Gd and $^{155}$Gd produce $^{155}$Tb; and so on. Since the threshold energy of the reaction $^{160}$Gd(d,7n)$^{155}$Tb is 40.56 MeV, the contribution of $^{160}$Gd in the production of $^{155}$Tb could not be observed in this work.

To limite some impurities in the final product, one can play with some decay time to let short lived impurities decay. This is what can be done for some extend with $^{154g}$Tb, $^{154m1}$Tb, and $^{154m2}$Tb as their half-lives are less than 23 h (Table 4.2). The quantity of $^{154}$Tb can be greatly reduced by allowing enough decay time (e.g. 10 days). After 10 days of decay, the activity of $^{155}$Tb will be reduced by about 4 times.

Another possibility is to define an energy range below some energy thresholds. As an example, $^{153}$Tb can be produced by deuteron interaction with $^{154}$Gd, $^{155}$Gd and $^{156}$Gd and have a threshold energy of 13.65 MeV (Table 4.2), this means that when energy is limited below, this impurity can be avoided. At 13.65 MeV, the cross section of $^{155}$Tb is about 150 mb (Fig. 4.9).

In some other cases, the only possibility will be to use enriched Gd targets. This is for example the case for $^{156g}$Tb, $^{157}$Tb, $^{158g}$Tb and $^{160}$Tb that have longer half-lives than that of $^{155}$Tb, and the threshold energies are similar to that of $^{155}$Tb.

Table 4.2 Decay information and reaction information of terbium radionuclides[8,113,198].The $E_{thresold}$ corresponds to the threshold energy for producing ground state radionuclides.

| Radionuclide | Half-life | $E_\gamma$ (keV) | $I_\gamma$ (%) | Reaction | $E_{thresold}$ (MeV) |
|---|---|---|---|---|---|
| $^{153}$Tb | 2.34 d | 212.00 | 28.5 | $^{154}$Gd (d, 3n) | 13.65 |
| | | | | $^{155}$Gd (d, 4n) | 20.17 |
| | | | | $^{156}$Gd (d, 5n) | 28.81 |
| $^{154g}$Tb | 21.5 h | 1291.326 | 6.9 | $^{154}$Gd (d, 2n) | 6.64 |
| $^{154m1}$Tb | 9.4 h | 540.18 | 20 | $^{155}$Gd (d, 3n) | 13.16 |
| | | | | $^{156}$Gd (d, 4n) | 21.81 |
| $^{154m2}$Tb | 22.7 h | 426.78 | 17 | $^{157}$Gd (d, 5n) | 28.25 |
| $^{155}$Tb | 5.32 d | 180.08 | 7.5 | $^{154}$Gd (d, n) | 0 |
| | | | | $^{155}$Gd (d, 2n) | 3.88 |
| | | | | $^{156}$Gd (d, 3n) | 12.52 |
| | | | | $^{157}$Gd (d, 4n) | 18.96 |
| | | | | $^{158}$Gd (d, 5n) | 27.00 |
| | | | | $^{160}$Gd (d, 7n) | 40.56 |
| $^{156g}$Tb | 5.35 d | 534.29 | 67 | $^{155}$Gd (d, n) | 0 |
| | | 1222.44 | 31 | $^{156}$Gd (d, 2n) | 5.52 |
| $^{156m1}$Tb | 24.4 h | 49.630 | 74.1 | $^{157}$Gd (d, 3n) | 11.96 |
| $^{156m2}$Tb | 5.3 h | 88.4 | 1.15 | $^{158}$Gd (d, 4n) | 20.00 |
| | | | | $^{160}$Gd (d, 6n) | 33.56 |
| $^{157}$Tb | 71 y | 54.548 | 0.0084 | $^{156}$Gd (d, n) | 0 |
| | | | | $^{157}$Gd (d, 2n) | 3.106 |
| | | | | $^{158}$Gd (d, 3n) | 11.14 |
| | | | | $^{160}$Gd (d, 5n) | 24.71 |
| $^{158g}$Tb | 180 y | 944.189 | 44.4 | $^{157}$Gd (d, n) | 0 |
| $^{158m1}$Tb | 10.70 s | 110.3 | 0.92 | $^{158}$Gd (d, 2n) | 4.28 |
| $^{158m2}$Tb | 0.40 ms | 171.07 | 50.4 | $^{160}$Gd (d, 4n) | 17.84 |
| $^{160}$Tb | 72.3 d | 298.5783 | 26.1 | $^{160}$Gd (d, 2n) | 3.15 |
| | | 879.378 | 30.1 | | |
| | | 966.166 | 25.1 | | |

#### 4.1.2.2. Characterization of Tb radionuclides

To identify $^{155}$Tb in our γ-spectra, according to Table 4.2, we restrict ourselves on one gamma line ($E_\gamma$ = 180.08 keV, $I_\gamma$ = 7.5%). Gamma lines at low energy $E_\gamma$ = 86.55 keV and $E_\gamma$ = 105.318 keV are in a region where the efficiency evolve rapidly with energy whereas the gamma line at $E_\gamma$ = 262.27 keV is also populated by $^{156}$Tb decay ($E_\gamma$ = 262.579 keV, $I_\gamma$ = 5.29%) leading to interferences. During the irradiation, the gold substrate of the target is activated and many radionuclides, including $^{198m}$Au are produced. This impurity has a gamma line with an energy $E_\gamma$ = 180.31 keV and an intensity $I_\gamma$ = 50%, which will interfere the detection of $^{155}$Tb. This is

why the deposit needs to be dissolved after irradiation to separate it from the gold substrate before data acquisition. In addition, the separation of the deposit and the substrate also have a positive impact on the dead time of data acquisition.

For $^{153}$Tb, the gamma line $E_\gamma$ = 212.00 keV, $I_\gamma$ = 28.5% was used to determine its activity.

$^{154}$Tb has a ground state $^{154g}$Tb ($T_{1/2}$ = 21.4 h) and two metastable states, $^{154m1}$Tb ($T_{1/2}$ = 9.4 h) and $^{154m2}$Tb ($T_{1/2}$ = 22.7 h). The m2 state $^{154m2}$Tb decays with 98.2 % ε to $^{154}$Gd and 1.8% IT to the m1 state $^{154m1}$Tb[90,91,199]. The m1 state $^{154m1}$Tb decays to $^{154}$Gd (EC = 78.2%) as well as the ground state $^{154g}$Tb (IT = 21.8%)[90,91,199]. The ground state $^{154g}$Tb decays with almost 100% ε to $^{154}$Gd and less than 0.1% $\beta^-$ to $^{154}$Dy. The decay chains between $^{154g}$Tb, $^{154m1}$Tb, and $^{154m2}$Tb are shown in *eq.4.16*:

$$^{154m2}Tb \xrightarrow{1.8\%} {}^{154m1}Tb \xrightarrow{21.8\%} {}^{154g}Tb \qquad (eq.4.16)$$

The Bateman equation was applied to determine the activity of each state in this decay chain. If we use A,B, and C to denote $^{154m2}$Tb, $^{154m1}$Tb and $^{154g}$Tb, respectively, then their activities $A_A$, $A_B$, $A_C$ can be expressed as *eq.4.17* to *eq.4.19*:

$$A_A(t) = A_{A0}e^{-\lambda_A t} \qquad (eq.4.17)$$

$$A_B(t) = \frac{\lambda_B}{\lambda_B - \lambda_A} \cdot A_{\mathrm{A0}}\left(e^{-\lambda_A t} - e^{-\lambda_B t}\right) \cdot \mathrm{BR_A} + A_{\mathrm{B0}}e^{-\lambda_B t} \qquad (eq.4.18)$$

$$A_c(t) = \Lambda'\left((\lambda_C - \lambda_B)e^{-\lambda_A t} - (\lambda_C - \lambda_A)e^{-\lambda_B t}\right) + \mathrm{X}'e^{-\lambda_B t} + (A_{\mathrm{C0}} + (\lambda_B - \lambda_A)\Lambda' - \mathrm{X}')e^{-\lambda_c t} (eq.4.19)$$

Where $\Lambda' = \frac{\lambda_C\lambda_B A_{\mathrm{A0}}\cdot \mathrm{BR_B}\cdot \mathrm{BR_A}}{(\lambda_B-\lambda_A)(\lambda_C-\lambda_A)(\lambda_C-\lambda_B)}$, $\mathrm{X} = \frac{\lambda_C A_{\mathrm{B0}}\cdot \mathrm{BR_B}}{(\lambda_C-\lambda_B)}$; $\mathrm{BR_A}$ and $\mathrm{BR_B}$ are the branching ratio of the decay from $^{154m2}$Tb to $^{154m1}$Tb and from $^{154m1}$Tb to $^{154g}$Tb, respectively; $A_{A0}$, $A_{B0}$ and $A_{C0}$ are the initial activity of $^{154m2}$Tb, $^{154m1}$Tb and $^{154g}$Tb at t= 0, respectively; and $\lambda_{A0}$, $\lambda_{B0}$ and $\lambda_{C0}$ are the decay constant of $^{154m2}$Tb, $^{154m1}$Tb and $^{154g}$Tb, respectively.
Details of calculation are explained in *Appendix 4.3*.
The gamma radiation information of $^{154m1}$Tb and $^{154m2}$Tb is not listed in Nudat 3.0, so this information is taken from the *Lund/LBNL nuclear data search*[113]. These three states interfere with each other for certain gamma lines, so only the gamma lines listed in Table 4.2 were used to determine their activity.

For $^{156}$Tb, it has also a ground state $^{156g}$Tb ($T_{1/2}$ = 5.35 d) and two metastable states, $^{156m1}$Tb ($T_{1/2}$ = 24.4 h) and $^{156m2}$Tb ($T_{1/2}$ = 5.3 h). The m2 state $^{156m2}$Tb decays with almost 100% to the m1 state $^{156m1}$Tb, and the m1 state decays 100% to the ground state $^{156g}$Tb. The gamma energies of the two metastable states are low ($E_\gamma$ = 49.630 keV for $^{156m1}$Tb and $E_\gamma$ = 88.4 keV for $^{156m2}$Tb), making them difficult to measure with our detection system. Therefore, only the cross section of the ground state $^{156g}$Tb was measured in this work. S. This cumulative value is noted as $^{156g}$Tb. The gamma lines $E_\gamma$ = 534.29 keV, $I_\gamma$ = 67% and $E_\gamma$ = 1222.44 keV, $I_\gamma$ = 31% were used to determine the activity.

For $^{157}$Tb has a half-life of 71 years and it has only one gamma line $E_\gamma$ = 54.5 keV and $I_\gamma$ = 0.0084%, which makes it difficult to measure. Therefore, we did not study the cross section of $^{157}$Tb in this work.

$^{158}$Tb was not study in this work. The long half-life of the ground state (180 y) did not allow us to get enough statistics during our counting (the counting time is adjusted according to the half-life of $^{155}$Tb).

Finally, for $^{160}$Tb, three gamma lines shown in Table 4.2 were used for the data acquisition.

#### 4.1.2.3. Irradiation conditions

In order to measure the cross sections of $^{155}$Tb and other terbium impurities and compare them to the theoretical simulations, a series of irradiation of co-electrodeposited targets have been carried out.

$Gd_2O_3$ powder made of natural gadolinium (noted as $^{nat}Gd_2O_3$) was used to manufacture co-electrodeposition targets. Eight Ni-$^{nat}Gd_2O_3$ composite targets were irradiated by deuterons in 5 different experiments (target n°1 and n°7 were irradiated together, target n°5 and n°8 were irradiated together all other where irradiated alone) for the cross section measurement on $^{nat}$Gd. Each irradiation lasted for 30 min or 60 min. Thanks to the Arronax deuteron beam that can be varied from 16 MeV up to 33 MeV, the activation cross sections were measured over the energy range from 8 MeV to 30 MeV.

All information about targets and beam parameters are shown in Table 4.3. For target n°2, the Gd content is much smaller than others, this is due to the co-electrodeposition duration that stand only 10 min in this case while the duration to manufacture other targets was 60 min. This target helps to investigate the minimum Gd content in the target for which the reaction cross section can be measured. Mean beam intensity varied slightly within one irradiation when two targets are irradiated together: for target n°1 and target n°7, the mean beam intensity is 63.9 nA and 59.1 nA, respectively, and for target n°5 and target n°8 it is 55.0 nA and 52.8 nA.

Table 4.3 Target information and beam parameters of cross section measurement on $^{nat}$Gd.

| Target number | Gd content in the target (mg) | Mean beam intensity (nA) | Energy (MeV) | Irradiation time (min) |
|---|---|---|---|---|
| 1 | 3.1 | 63.9 ± 4.6 | 8.7 ± 0.5 | 30 |
| 2 | 2.6 | 57.2 ± 2.4 | 10.4 ± 0.6 | 60 |
| 3 | 0.4 | 57.8 ± 4.7 | 13.2 ± 0.5 | 60 |
| 4 | 1.7 | 79.3 ± 6.0 | 14.2 ± 0.4 | 60 |
| 5 | 2.6 | 55.0 ± 4.0 | 19.5 ± 0.6 | 30 |
| 6 | 1.8 | 88.6 ± 6.7 | 24.0 ± 0.5 | 60 |
| 7 | 2.6 | 59.1 ± 4.5 | 24.4 ± 0.3 | 30 |
| 8 | 2.5 | 52.8 ± 4.1 | 29.5 ± 0.3 | 30 |

#### 4.1.2.4. The cross section of $^{nat}$Gd(d,x)$^{155}$Tb

Cross section values for $^{155}$Tb production induced by deuteron on a $^{nat}$Gd target were successfully extracted for all targets. All measured values and associated uncertainties are presented in Table 4.4. When the deuteron energy varies from 8 MeV to 30 MeV, the cross

section increases until it reaches a maximum of 394.8 mb, at 24.4 MeV. Then, the cross section values decrease with the increase of the incident energy. The relative error Δ, which is the ratio of the error to the measured value, varies between 9.1% and 16.9%. Most of the uncertainties are slightly below 10% except for target n°3, n°4 and n°7 for which the relative error is equal to 16.9%, 13.7% and 11.3%, respectively. Referring to Table 4.3, the Gd contents of the three targets are 0.4 mg, 1.7 mg and 1.8 mg, respectively, which are much smaller than the Gd contents of other targets (2.5-3 mg). This low content of Gd in the composite explains this large relative uncertainty.

Table 4.4 Measured cross section values of the reaction $^{nat}$Gd(d,x)$^{155}$Tb.

| Target n° | Energy (MeV) | σ $^{155}$Tb (mb) | Δ $^{155}$Tb (%) |
|---|---|---|---|
| 1 | 8.7 ± 0.5 | 22.3 ± 2.2 | 9.9 |
| 2 | 10.4 ± 0.6 | 32.9 ± 3.2 | 9.6 |
| 3 | 13.2 ± 0.5 | 93.7 ± 15.8 | 16.9 |
| 4 | 14.2 ± 0.4 | 103.4 ± 14.2 | 13.7 |
| 5 | 19.5 ± 0.6 | 199.6 ± 18.3 | 9.2 |
| 6 | 24.0 ± 0.5 | 325.2 ± 29.6 | 9.1 |
| 7 | 24.4 ± 0.3 | 394.8 ± 44.6 | 11.3 |
| 8 | 29.5 ± 0.3 | 305.0 ± 29.4 | 9.6 |

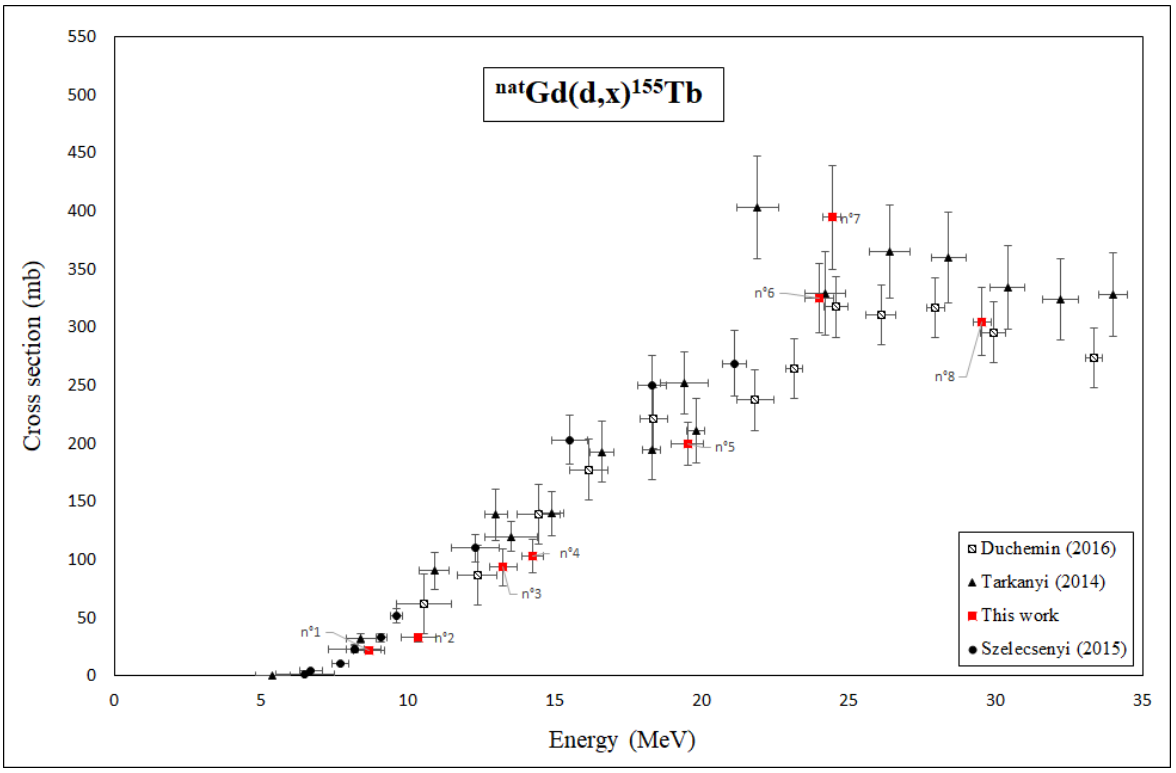


Fig. 4.10 Experimental cross section of $^{nat}$Gd(d,x)$^{155}$Tb reactions measured in this work (red points) and other existing data in the literature [91–93].

On Fig. 4.10, the measured cross sections (red points) were compared with existing data in the literature (black points)[91–93]. In general, the measurement results of this work are in good

agreement with other data. The experimental errors of this work are relatively smaller than others at lower energy (8-20 MeV), and are similar to the ones in the literature data at higher energy (20-30 MeV). Moreover, despite a very small Gd quantity (0.4 mg), the cross section value obtained for target n°3 is closed to other data in the literature. Cross section of target n°7 is found higher than that of target n°6 who has a similar energy but they are compatible if one takes into accounts the associated uncertainties.

#### 4.1.2.5. Cross sections of impurities produced by deuteron irradiation on $^{nat}Gd_2O_3$ targets

As shown in the simulation results (Fig. 4.9), several Tb radionuclides will be co-produced during irradiation and will be considered as impurities as the goal is to produce $^{155}$Tb. Along with $^{155}$Tb, we measured cross sections for several Tb isotopes: $^{153}$Tb, $^{154g,m1,m2}$Tb, $^{156(cum)}$Tb, and $^{160}$Tb. Cross section values, σ, and the associated relative uncertainty, Δ, are listed in Table 4.5. Some radionuclides were not detected even the energy is above the threshold energy, this may because their activity is below the detection limit. Considering the gamma energy, the intensity and the half-life of each radionuclides, the limit of the detection is considered as 3 times of the background noise value in the area near the gamma energy (± 10 keV).

Table 4.5 Measured deuteron-induced reactions cross section values of $^{153}$Tb, $^{154g,m1,m3}$Tb, $^{156(cum)}$Tb, and $^{160}$Tb on natural Gd targets.

| Target n° | Energy (MeV) | σ $^{153}$Tb (mb) | Δ $^{153}$Tb (%) | σ $^{154m1}$Tb (mb) | Δ $^{154m1}$Tb (%) | σ $^{154m2}$Tb (mb) | Δ $^{154m2}$Tb (%) |
|---|---|---|---|---|---|---|---|
| 1 | 8.7 ± 0.5 | - | - | < 19.2 | - | < 5.0 | - |
| 2 | 10.4 ± 0.6 | - | - | < 19.2 | - | < 5.0 | - |
| 3 | 13.2 ± 0.5 | - | - | < 19.2 | - | < 5.0 | - |
| 4 | 14.2 ± 0.4 | < 0.6 | - | < 19.2 | - | < 5.0 | - |
| 5 | 19.5 ± 0.6 | 14.4 ± 1.5 | 10.4 | 104.9 ± 19.7 | 18.8 | 5.29 ± 0.9 | 17.5 |
| 6 | 24.0 ± 0.5 | 42.5 ± 3.9 | 9.1 | 196.4 ± 34.7 | 17.6 | 12.7 ± 2.3 | 17.9 |
| 7 | 24.4 ± 0.3 | 64.9 ± 6.1 | 9.5 | 247.3 ± 39.7 | 20.7 | 15.4 ± 3.1 | 20.1 |
| 8 | 29.5 ± 0.3 | 139.3 ± 12.9 | 9.2 | 216.2 ± 33.5 | 16.8 | 15.3 ± 2.3 | 18.6 |
| Target n° | Energy (MeV) | σ $^{154g}$Tb (mb) | Δ $^{154g}$Tb (%) | σ $^{156}$Tb (mb) | Δ $^{156}$Tb (%) | σ $^{160}$Tb (mb) | Δ $^{160}$Tb (%) |
| 1 | 8.7 ± 0.5 | < 3.7 | - | 27.2 ± 2.6 | 9.5 | 68.3 ± 18.5 | 27.1 |
| 2 | 10.4 ± 0.6 | < 3.7 | - | 44.0 ± 4.9 | 11.2 | 197.9 ± 38.6 | 19.5 |
| 3 | 13.2 ± 0.5 | < 3.7 | - | 128.3 ± 12.3 | 9.6 | 111.7 ± 35.8 | 32.0 |
| 4 | 14.2 ± 0.4 | < 3.7 | - | 125.3 ± 11.9 | 9.5 | 126.0 ± 33.1 | 26.3 |
| 5 | 19.5 ± 0.6 | 41.2 ± 7.1 | 17.3 | 197.8 ± 17.8 | 9.0 | 26.9 ± 5.8 | 21.4 |
| 6 | 24.0 ± 0.5 | 59.3 ± 9.2 | 26.5 | 226.6 ± 20.3 | 9.0 | 28.4 ± 8.5 | 30.1 |
| 7 | 24.4 ± 0.3 | 73.3 ± 12.3 | 16.8 | 312.3 ± 28.9 | 9.2 | 30.8 ± 6.1 | 20.4 |
| 8 | 29.5 ± 0.3 | 69.4 ± 15.6 | 22.5 | 282.4 ± 25.8 | 9.1 | 14.8 ± 3.2 | 21.8 |

As expected from the threshold energy, the cross section of $^{153}$Tb was measured for the target n°5-8 but the radionuclide was not detected in targets n°1-4. According to Table 4.2, the threshold energy to produce $^{153}$Tb is 13.65 MeV, so it is normal that $^{153}$Tb did not be produced in the targets n°1-3. For target n°4, the deuteron energy is just slightly larger than the threshold energy, due to the small cross section and the small amount of Gd in the deposit, the produced $^{153}$Tb was not enough to be detected by the HPGe detector. Considering the detection limit, the cross section in this energy is less than 0.6 mb. For targets n°5-8, the cross section increases with the deuteron energy, and reaches to the highest value at 29.5 MeV (139.3 mb). The relative uncertainties are between 9 - 11% for all targets, which are similar to the uncertainty rates of $^{155}$Tb. As a result, it is possible to limit the $^{153}$Tb impurity by decreasing the deuteron energy below 14.2 MeV.

The three states $^{154g}$Tb, $^{154m1}$Tb and $^{154m2}$Tb were detected only in targets n°5-8 (Table 4.5). The minimum energy to produce $^{154g}$Tb, $^{154m1}$Tb, and $^{154m2}$Tb are 6.64 MeV (Table 4.2), 6.76 MeV and 7.06 MeV [96] respectively. It is produced from interaction on $^{154}$Gd which is only present as 2.18% in $^{nat}$Gd. Significant production will start with interaction on $^{155}$Gd (14.80%) for which the threshold energies are respectively 13.16 MeV, 13.27 MeV and 13.57 MeV for $^{154g}$Tb, $^{154m1}$Tb, and $^{154m2}$Tb. This is why we were able to measure $^{154}$Tb only for the high-energy part of our measurements. For the measured cross section, the reaction cross sections of the three states have the same trend as a function of energy. Cross sections increase from 19.5 MeV to 24.4 MeV and then slightly decrease as the energy increase. For $^{154m2}$Tb, the cross sections are very small compared with other states, the maximum value is 15.4 mb at 24.4 MeV. On the contrary, the cross sections of $^{154m1}$Tb are more than 14 times larger than those of $^{154m2}$Tb, and the maximum value is 247.3 mb at 24.4 MeV. Since the branching ratio of the decay from $^{154m2}$Tb to $^{154m1}$Tb is only 1.8%, it can be concluded that the contribution of $^{154m2}$Tb is negligible for the production of $^{154m1}$Tb. Meanwhile, for $^{154g}$Tb, the contribution of the decay of $^{154m1}$Tb is not negligible because of the large cross section and the relatively larger branching ratio (21.8%). However, due to the high experimental relative uncertainty of the $^{154m1}$Tb activity (18-20%), despite the Bateman's equation, we decided to not determine $^{nat}$Gd(d,x)$^{154g}$Tb but rather the cumulated cross section.

The cumulative cross section values for $^{156g}$Tb were measured for all targets. According to Table 4.5, the cross section increases from 8 MeV to 25 MeV with the maximum value equals to 312.3 mb at 24.4 MeV, and the cross section decreases to 282.4 mb at 29.5 MeV. It should be noted that at low energy (less than 14.2 MeV), the cross sections of $^{156(cum)}$Tb (Table 4.5) are bigger than the cross sections of $^{155}$Tb (Table 4.4). And even in higher energy, the cross sections of $^{156(cum)}$Tb is very close to the cross sections of $^{155}$Tb. As the two radionuclides have similar half-lives, this is a big problem for the purity of $^{155}$Tb produced from $^{nat}$Gd and deuteron beam. $^{160}$Tb cross sections were also extracted for every target. The maximum cross section is found equal to 197.9 mb at 10.4 MeV while the simulation value is 130 mb at 12 MeV. After 14.2 MeV, the cross section decreases with energy, this trend is similar to the simulation results. The relative uncertainty of our measurements are between 19% to 32%, which is almost twice larger than that of other radionuclides. This is linked to the fact that we were focusing our measurements on $^{155}$Tb and that as the half-life of $^{160}$Tb is relatively long (72.3 d), the duration of data acquisition in this work (8-14 h) was not sufficient to obtain a good statistics. Also, the background noise is relatively large for $^{160}$Tb during the counting.

The obtained cross sections had been compared with existing data[91,92] and results are presented in Fig. 4.11-Fig. 4.16.

The comparison of the measurement values and literature results of $^{153}$Tb is shown in Fig. 4.11. It can be seen that the overall trend of the measurement values agrees with other published data.

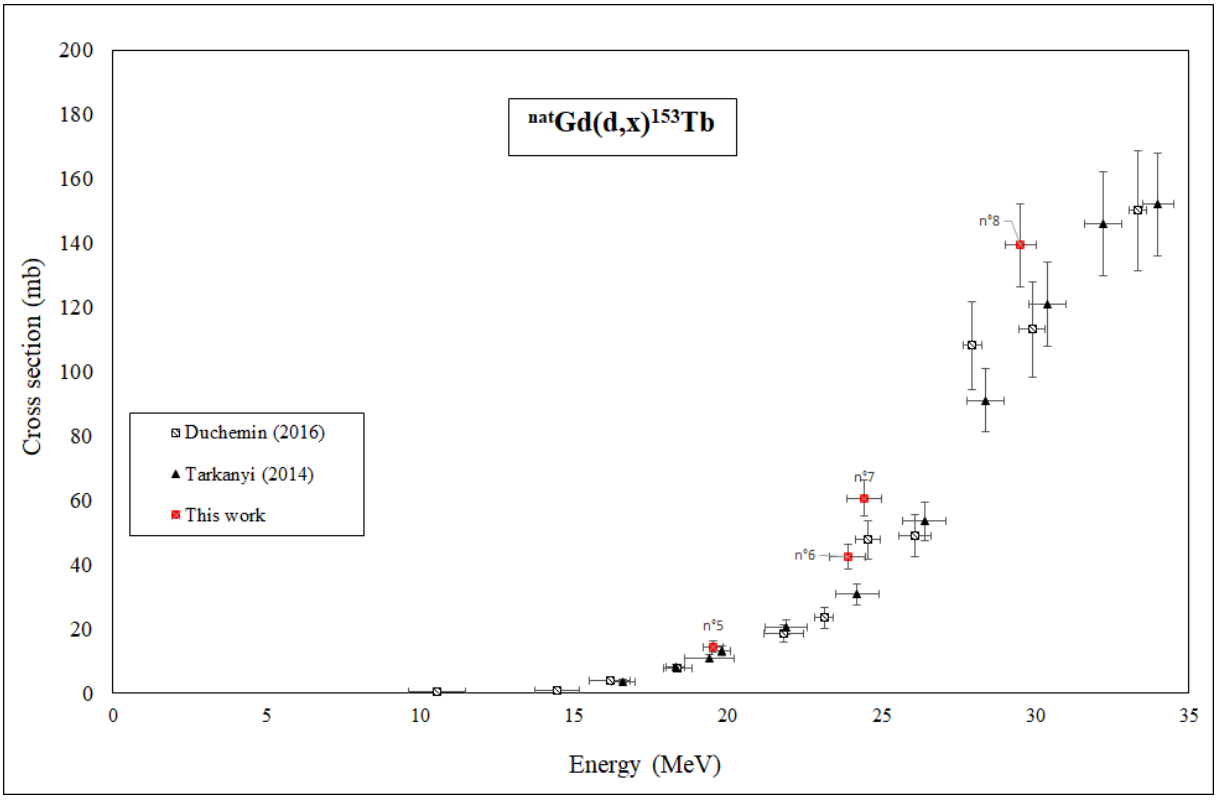


Fig. 4.11 Experimental cross section of $^{nat}$Gd(d,x)$^{153}$Tb reactions measured in this work (red points) and other existing data in the literature[91,92].

The cross sections comparison between the results in this work and other existing data[91,92] for $^{154m2}$Tb, $^{154m1}$Tb and $^{154g}$Tb are shown in Fig. 4.12, Fig. 4.13 and Fig. 4.14, respectively. For $^{154m2}$Tb and $^{154m1}$Tb, our measured results show good agreement with the results of Duchemin et al., and of Tarkanyi et al.. For $^{154g}$Tb, the only existing data comes from the work of Tarkanyi et al., the comparison shows that the measured values of this work are much smaller.

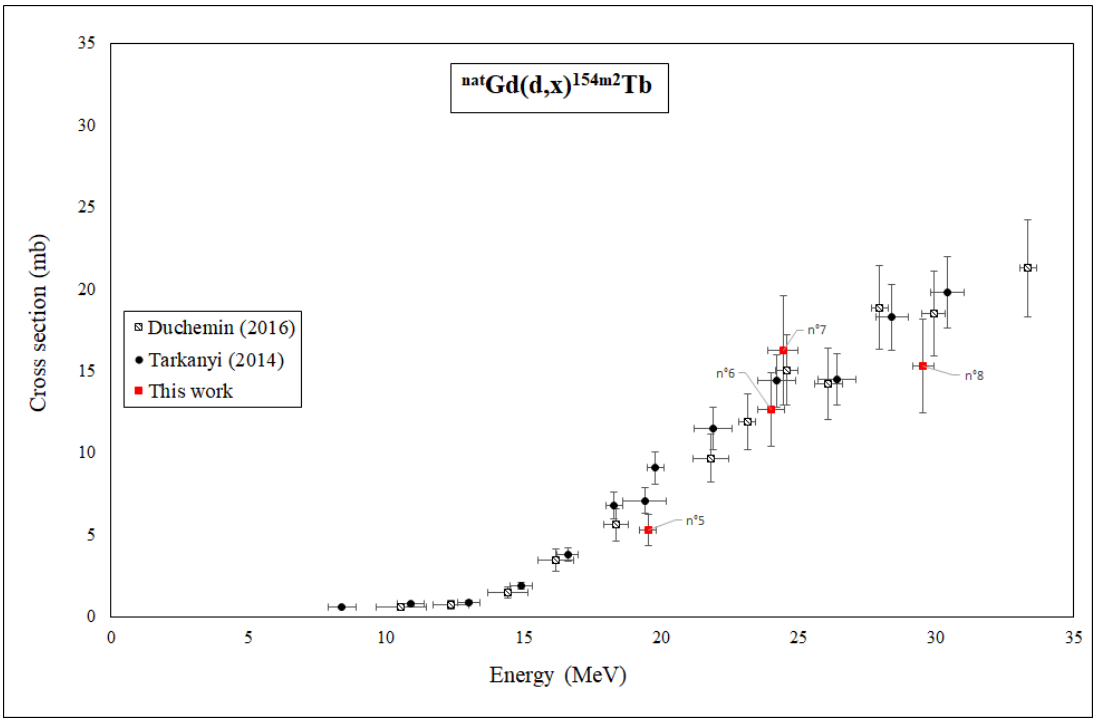


Fig. 4.12 Experimental cross section of $^{nat}Gd(d,x)^{154m2}Tb$ reactions measured in this work (red points) and other existing data in the literature[91,92].

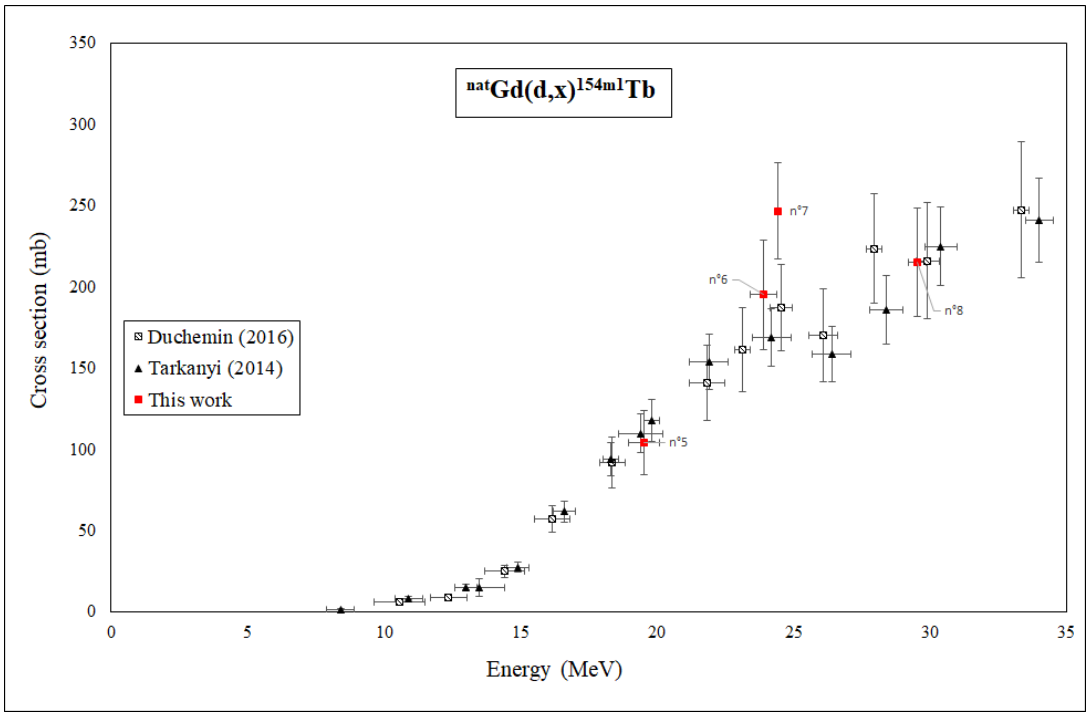


Fig. 4.13 Experimental cross section of $^{nat}Gd(d,x)^{154m1}Tb$ reactions measured in this work (red points) and other existing data in the literature[91,92].

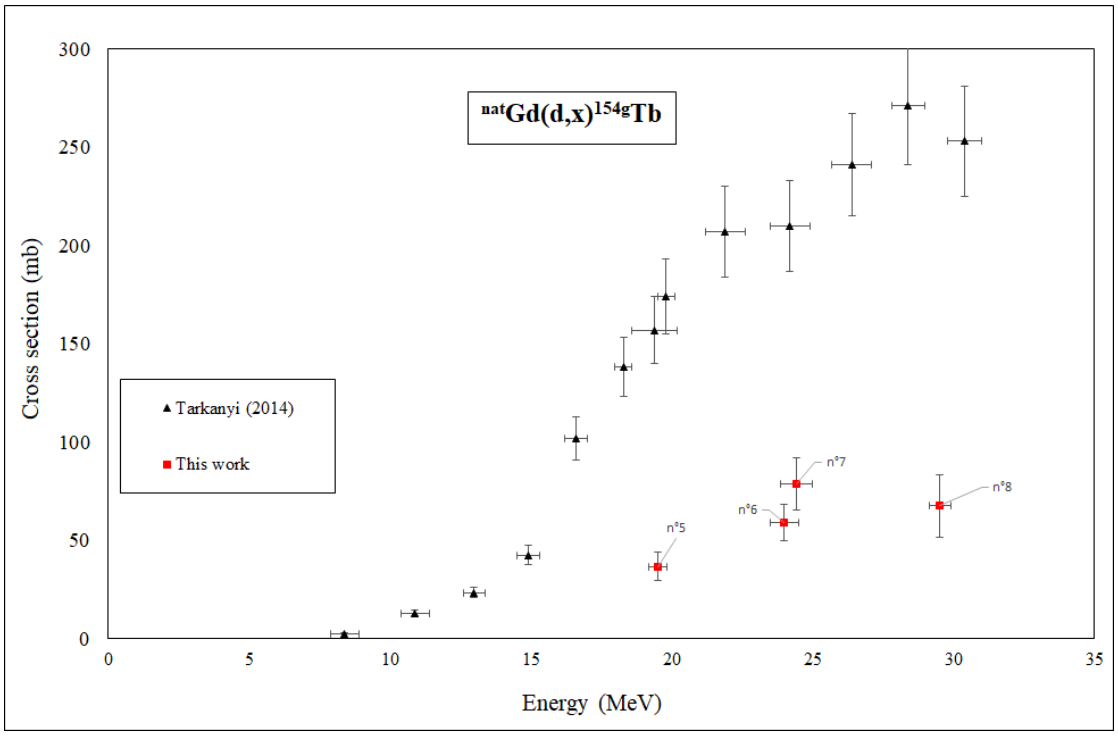


Fig. 4.14 Experimental cross section of $^{nat}Gd(d,x)^{154g(cum)}Tb$ reactions measured in this work (red points) and other existing data in the literature[91].

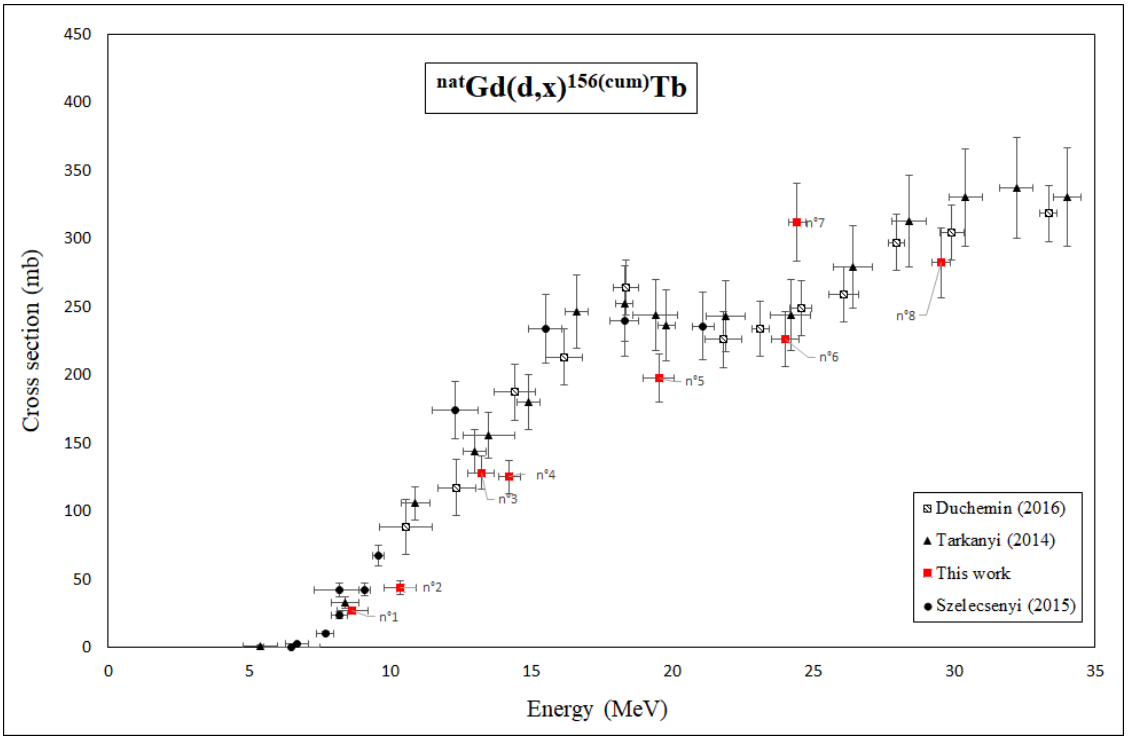


Fig. 4.15 Experimental cross section of $^{nat}Gd(d,x)^{156}(cum)Tb$ reactions measured in this work (red points) and other existing data in the literature[91,92].

Fig. 4.15 presents the comparison of the cross section of $^{156(cum)}Tb$ measured in this work (red points) and the existing data[91–93](black points). All results are in agreement with the existing data except for the target n°7 that is far off.

Fig. 4.16 compares the measured cross sections of $^{160}$Tb in this work (red points) and in existing data[91,92] (black points). In general, these measured values are consistent with those measured by Tarkanyi et al. and by Duchemin et al., except for the value of target n°2.

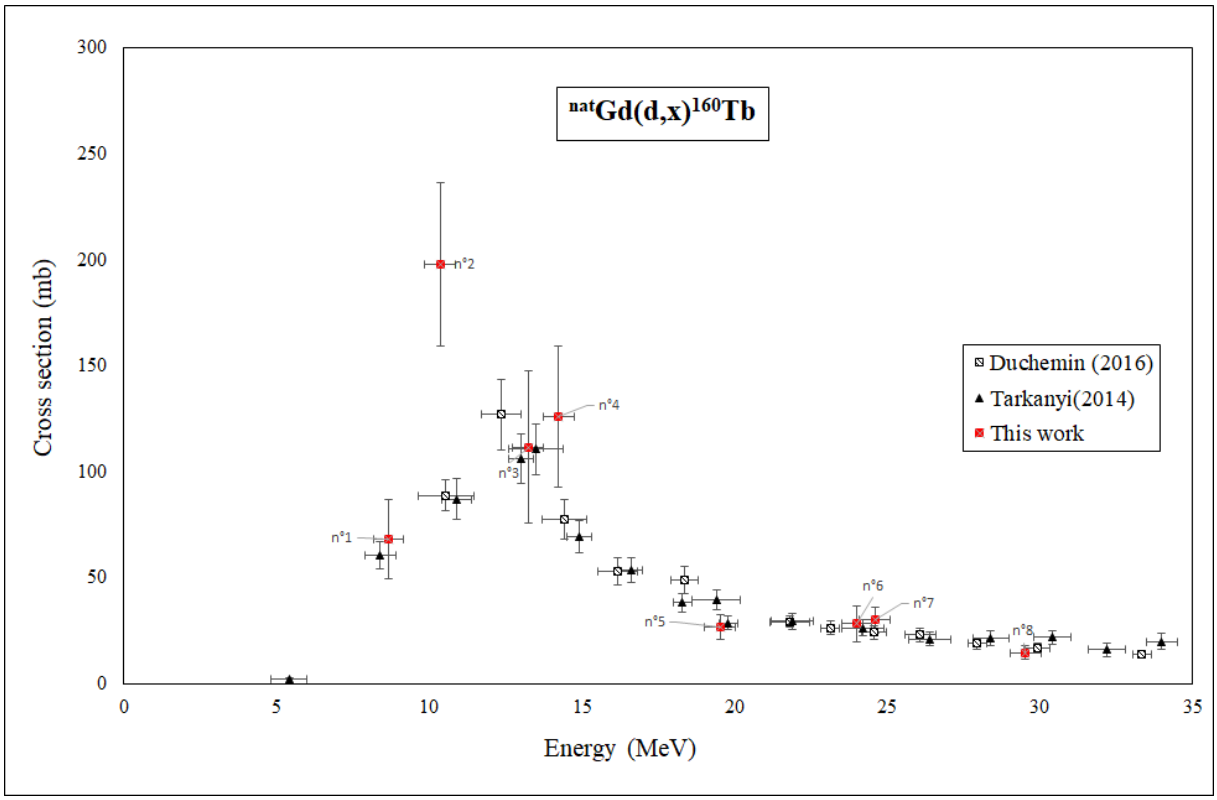


Fig. 4.16 Experimental cross section of $^{nat}$Gd(d,x)$^{160}$Tb reactions measured in this work (red points) and other existing data in the literature[91,92].

#### 4.1.2.6. Comparison with TENDL simulation

The TENDL-2019 library was also compared with our measurements, comparisons of $^{155}$Tb and $^{156}$Tb cross sections are shown in Fig. 4.17. For $^{155}$Tb, the overall trend of the cross section agrees with the simulated value calculated by TENDL-2019. However, the maximum measured value (394.8 mb) is bigger than that of simulation (385 mb). If the measurement error is taken into account (± 44.6 mb), the two values basically match. For $^{156}$Tb, similar to the case of $^{155}$Tb, the measured cross sections are generally smaller than simulated values. Fig. 4.17 also indicates that the measured cross sections of $^{155}$Tb and $^{156}$Tb are quite close at all energies except for at 24 MeV.

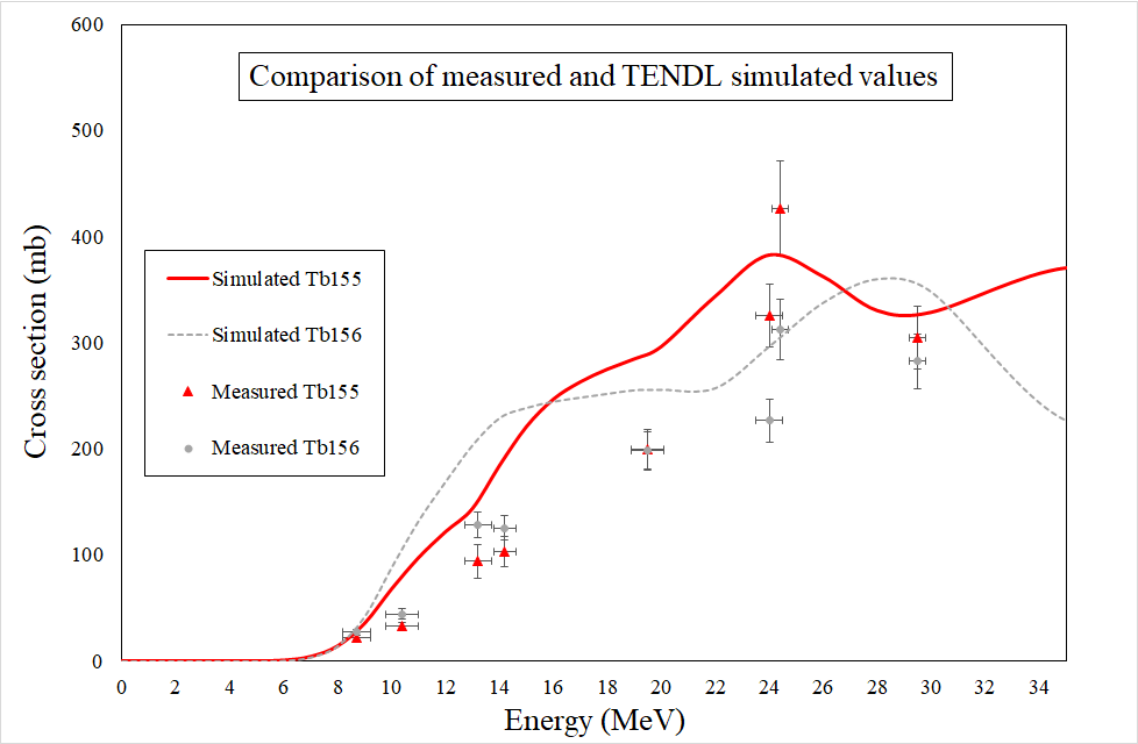


Fig. 4.17 Comparison of measured and TENDL simulated values of $^{155}$Tb and $^{156}$Tb cross sections.

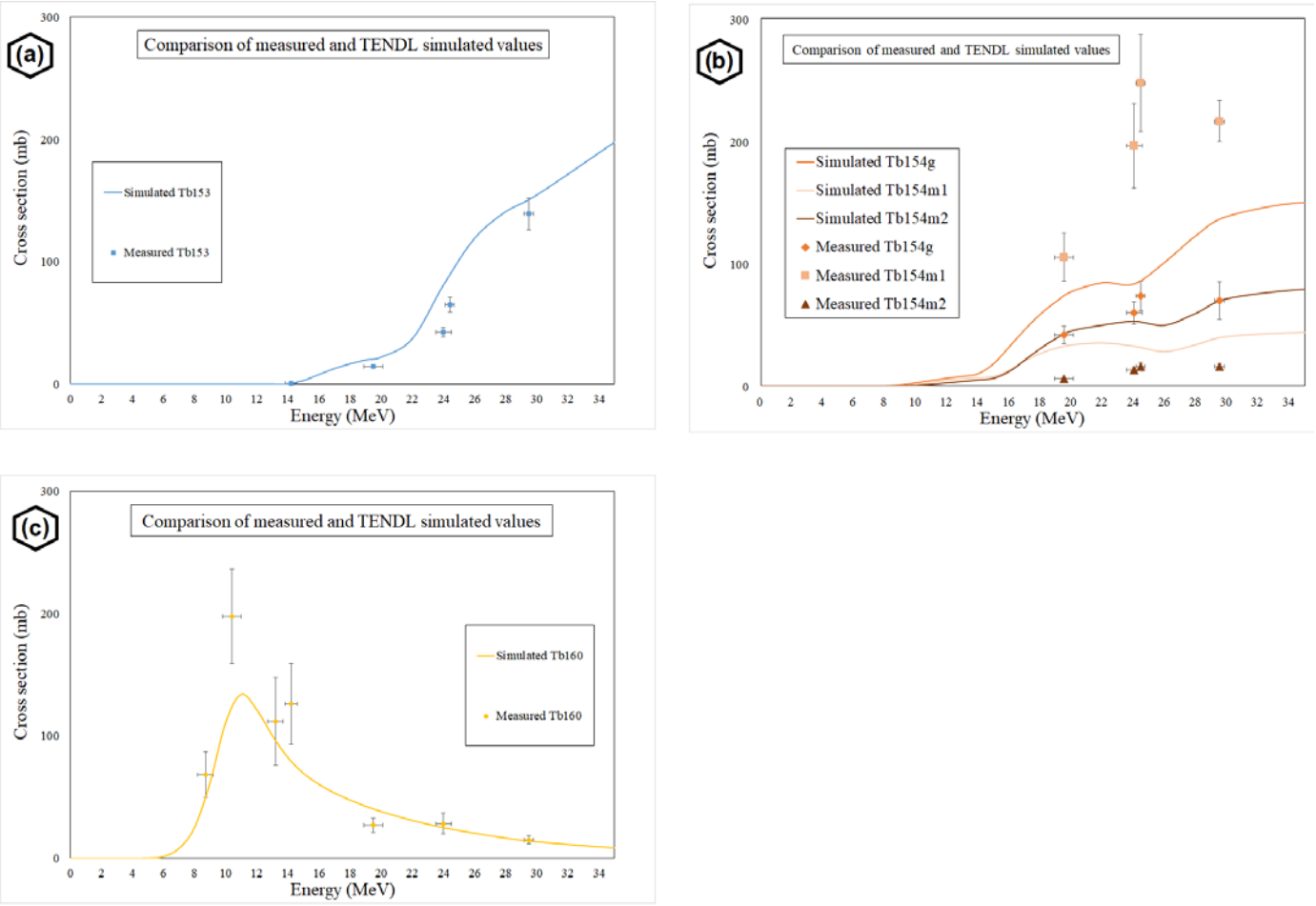


Fig. 4.18 Comparison of measured and TENDL simulated values of $^{153}$Tb, $^{154g,m1,m2}$Tb and $^{160}$Tb cross sections.

Fig. 4.18 shows the comparison between measured and simulated values of $^{153}$Tb, $^{154g,m1,m2}$Tb and $^{160}$Tb cross sections. For $^{153}$Tb (Fig. 4.18 (a)), the measured values are very similar to the simulated values. For three states of $^{154}$Tb (Fig. 4.18 (b)), there are differences between the measured values and simulated values, especially for $^{154m1}$Tb. The gaps of cross sections are obvious especially for $^{154m1}$Tb and $^{154m2}$Tb. For $^{154g}$Tb, the difference between measured values and simulated values is smaller. For $^{160}$Tb (Fig. 4.18 (c)), the global trend of the measured values are agree with the simulated results, except for the value at 10 MeV.

#### 4.1.2.7. Summary of this section

In this section, production cross sections of the reaction $^{nat}$Gd(d,x)Tb were measured experimentally and the results were compared with TENDL simulation. The main goal was to qualify our target manufactured by co-electrodeposition in order to prepare experiments with enriched material.

Data obtained for $^{155}$Tb is consistent with existing measurement data. Data obtained for other Tb isotopes demonstrate the co-production of other Tb impurities as for example $^{153}$Tb, $^{154}$Tb, $^{156}$Tb and $^{160}$Tb. Fortunately, $^{153}$Tb and $^{154}$Tb can be avoided by working at low energy and/or having some decay time. However, $^{156}$Tb and $^{160}$Tb cannot be avoided as they are produced over the whole energy range of $^{155}$Tb production and having long half-lives cannot be eliminated by decay. According to the measured cross sections, the dominant radionuclides ($^{155}$Tb, $^{156}$Tb or $^{160}$Tb) under different energies were analyzed; the results are shown in Fig. 4.19.

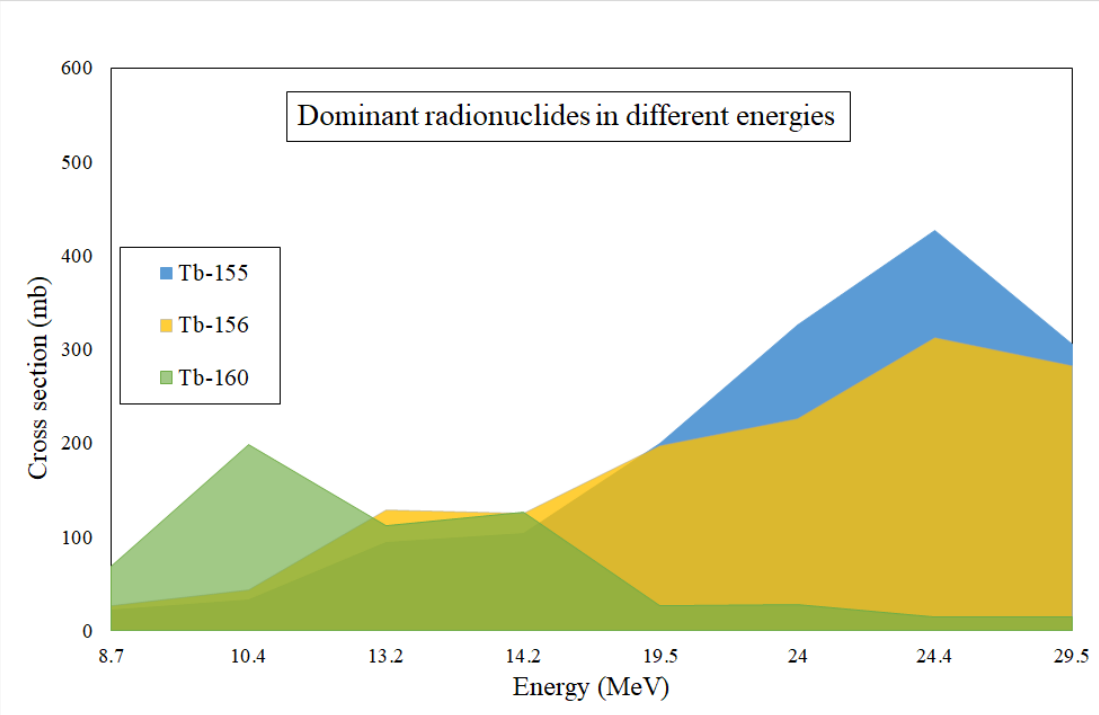


Fig. 4.19 Dominant radionuclides at different energies according to the measured cross sections.

It is clear that at lower energy, the production of $^{160}$Tb is dominant while at moderate energy the production of $^{156}$Tb is dominant; even at high energy, the proportion of $^{156}$Tb is quite large. If one wants to use $^{nat}$Gd as target material, the only way to eliminate these impurities is to use the mass separation, a technique that still needs improvement in terms of yield (see Chapter 1).

Going to proton irradiation will not change this picture as the main issue is linked to the abundance of Gd isotopes in $^{nat}$Gd.
In conclusion, these experiments validate the feasibility of manufacturing Gd targets by the co-electrodeposition method for cross section measurements. The simulation and experimental analysis in this section confirm that producing $^{155}$Tb from $^{nat}$Gd targets ends up with Tb contaminants in the final product. Therefore, in the next section, co-deposited enriched Gd targets were used for the cross section measurements of the reaction $^{155}$Gd(d,x)Tb.

### 4.1.3. Production cross sections of deuteron-induced reactions on enriched 155Gd

In order to reduce the production of many Tb isotopes coming from the interaction of the projectile with the different Gd isotopes composing $^{nat}$Gd (In natural Gd, the total proportion of $^{156}$Gd, $^{157}$Gd, $^{158}$Gd and $^{160}$Gd isotopes are 82.82% (Table 4.1)), it will be interesting to work with enriched$^{155}$Gd. In our work, we used 92.8% enriched $^{155}$Gd, the remaining part is made of $^{156}$Gd (about 5.7%) and $^{157}$Gd, $^{158}$Gd and $^{160}$Gd for less than 1% each.

#### 4.1.3.1. Theoretical analysis of the production Tb through enriched Gd

The enriched Gd used in this work is in the form of $Gd_2O_3$, the proportion of each Gd isotopes are listed in Table 4.6. In this work, Gd with this composition is noted as *Gd, and this enriched oxide power is noted as *$Gd_2O_3$.

Table 4.6 Isotopic composition of enriched $Gd_2O_3$.

| Isotope | $^{155}$Gd | $^{156}$Gd | $^{157}$Gd | $^{158}$Gd | $^{160}$Gd |
|---|---|---|---|---|---|
| Proportion (%) | 92.8 | 5.7 | 0.8 | 0.5 | 0.2 |

To estimate the theoretical production cross section of the enriched powder, TENDL-2019 database was used along with each Gd isotope and its proportion. Using *eq.15*, the cross section to produce an isotope of Tb ($^{j}$Tb) can be written as *eq.4.20*. Here $\sigma_i$ (i=155,156,157,158,160) is the cross section of the reaction $^{i}$Gd(d,x)$^{j}$Tb with i and j the mass number of Gd and Tb respectively:

$$\sigma^{j}_{enriched} = 92.8\,\% \cdot \sigma^{j}_{155} + 5.7\,\% \cdot \sigma^{j}_{156} + 0.8\,\% \cdot \sigma^{j}_{157} + 0.5\,\% \cdot \sigma^{j}_{158} + 0.2\,\% \cdot \sigma^{j}_{160} \quad (eq.4.20)$$

The simulated production of Tb isotopes using the enriched *$Gd_2O_3$ is shown Fig. 4.20.

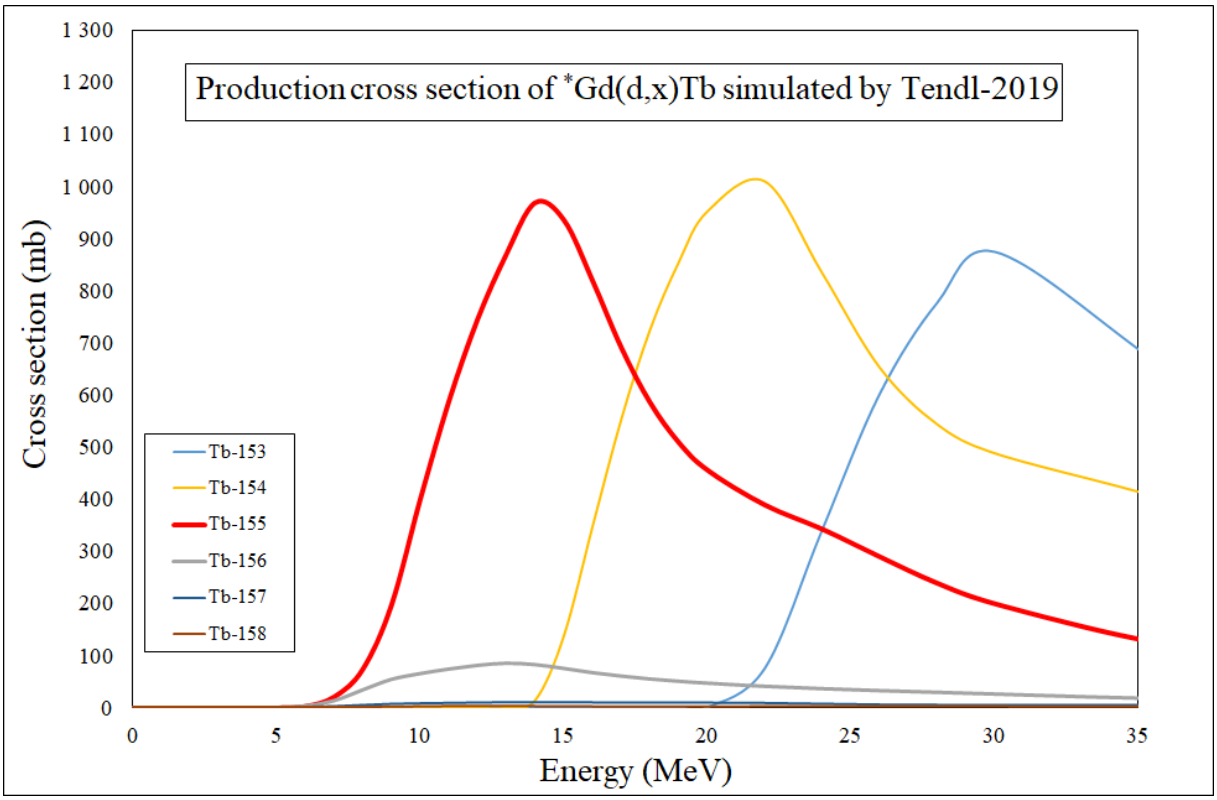


Fig. 4.20 Simulated production cross section of Tb isotopes by deuteron induced reactions on enriched *Gd.

According to Fig. 4.20, between 5 – 30 MeV, the main produced Tb isotopes are $^{153}$Tb, $^{154}$Tb, $^{155}$Tb and $^{156}$Tb. The $^{157}$Tb and $^{158}$Tb are also produced but the cross sections are small. According to Table 4.2, the threshold energies for $^{153}$Tb, $^{154}$Tb, $^{155}$Tb and $^{156}$Tb are 20.17 MeV, 13.16 MeV, 3.88 MeV and 0 MeV, respectively. That means the co-production of $^{153}$Tb and $^{154}$Tb can be avoided by limiting the reaction energy while the co-production of $^{156}$Tb is not avoidable under all energy. Going to higher enrichment may help reduce the amount of $^{156}$Tb. Another possibility will be to shift to proton irradiations.

For the radionuclide of interest, $^{155}$Tb, cross section values are peaked at 15 MeV with a maximum value at 970 mb which is twice larger than data estimated from natural Gd target (385 mb at 25 MeV) and the one measured for the proton induced reaction $^{155}$Gd(p,n)$^{155}$Tb (440 mb at 11 MeV). Therefore, $^{155}$Tb production through the deuteron route is valuable from the yield point of view. The contribution of each Gd isotope to the cross section is presented in Fig. 4.21. The red dotted line represents the total cross section, which is equivalent to the red solid line in Fig. 4.20. In general, the production of $^{155}$Tb is mainly from the reaction $^{155}$Gd(d,2n)$^{155}$Tb (blue line), while in higher energy (more than 15 MeV), the contribution of $^{156}$Gd(d,3n)$^{155}$Tb is not negligible (orange line) and can be clearly seen at about 25 MeV (distortion on the red dotted line). The contribution of $^{157}$Gd and $^{158}$Gd are very small.

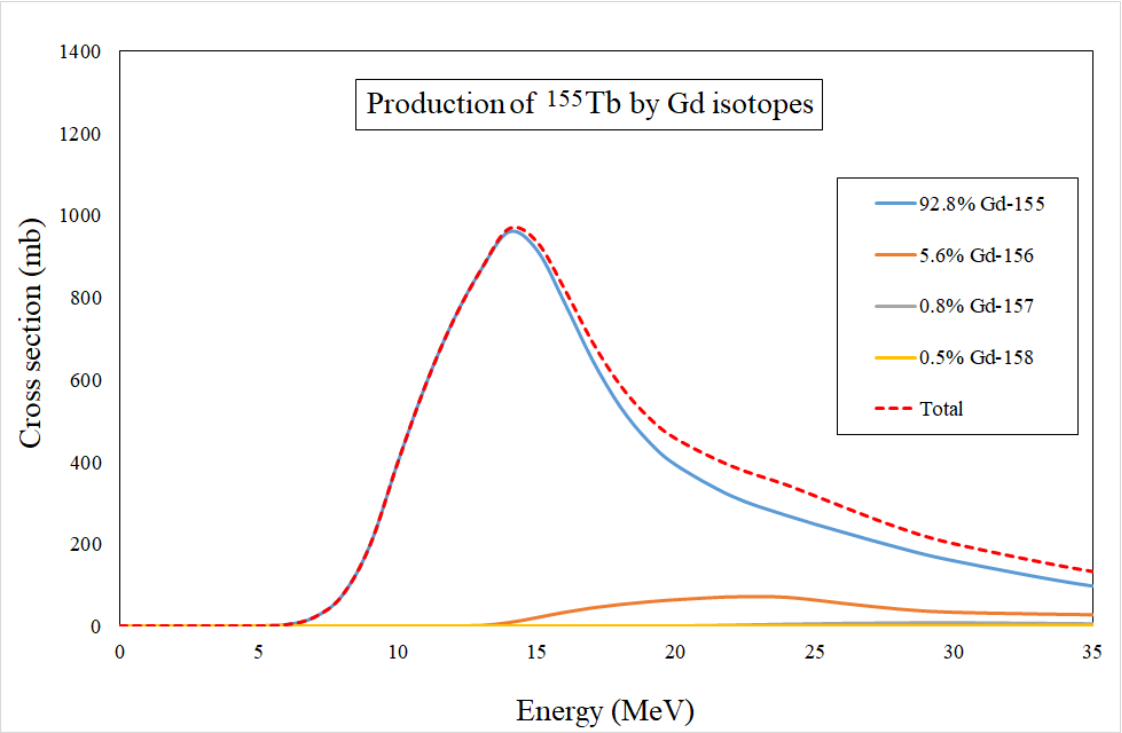


Fig. 4.21 Contribution of the production of 155Tb by Gd isotopes.

For the production of impurities, according to Fig. 4.20, the cross section of $^{154}$Tb begins at its threshold energy (13.16 MeV) and increases to the maximum value (1000 mb) at 24 MeV, the cross section of $^{153}$Tb begins at 20.17 MeV and increases until 900 mb at 30 MeV. The production of $^{156}$Tb begins at 0 MeV with cross section values always below 100 mb, the maximum value is 85 mb at 14 MeV, almost 10 times smaller than that of $^{155}$Tb at the same energy (870 mb).

From the point of view of improving the purity, when the energy is limited below 13.16 MeV, there is only one impurity, $^{156}$Tb. As the half-lives of the two radionuclides are almost the same, the relative amount of each species ($^{156}$Tb/$^{155}$Tb) will be equivalent to that of the cross sections. Therefore, the use of enriched targets increase the production yield while reducing impurities.

#### 4.1.3.2. Irradiation conditions

Ten targets were made with enriched $Gd_2O_3$, the co-electrodeposition duration was 35 min for each targets. These were irradiated by pair in five experiments, referenced as A, B, C, D and E. It should be noted that the target number is going from small to large in accordance with the energy and not the manufacturing order. Details on the Gd content in each target and beam energy used to irradiate them are listed in Table 4.7. According to the table, the Gd content varies between 0.7 to 2.0 mg, and the irradiation energy covers the energy range from 8.1 MeV to 29.7 MeV. Compared with Table 4.3, the Gd content is in general lower and due to the deposition duration decreased from 60 min to 35 min. It can also be seen from Table 4.7 that usually the energies corresponding to each experiment are not adjacent but staggered. This is to limit the measurement errors in a certain energy interval caused by experimental operations, for example, a shift of energy.

For each experiment, the beam intensity was 50 nA and the irradiation time was 30 min. The stacks were assembled as shown in Fig. 4.1, the encapsulation and the data acquisition remained the same as experiments of natural Gd targets.

Table 4.7 Target information of the irradiation for enriched targets.

| Experiment reference | Target number | Gd content in the target (mg) | Energy (MeV) |
|---|---|---|---|
| A | 1 | 1.5 | 8.1 ± 0.4 |
| B | 2 | 1.0 | 10.4 ± 0.4 |
| C | 3 | 1.6 | 11.2 ± 0.4 |
| B | 4 | 1.5 | 12.4 ± 0.3 |
| D | 5 | 1.2 | 14.0 ± 0.4 |
| A | 6 | 1.5 | 14.2 ± 0.3 |
| C | 7 | 2.0 | 16.0 ± 0.3 |
| D | 8 | 1.4 | 19.4 ± 0.3 |
| E | 9 | 0.7 | 24.4 ± 0.4 |
| E | 10 | 0.7 | 29.7 ± 0.3 |

#### 4.1.3.3. The cross section of $^{155}$Gd(d,2n)$^{155}$Tb

The cross sections of the reaction *Gd(d,x)$^{155}$Tb (noted as $\sigma_{enriched}$) were successfully measured in all targets, the values of $\sigma_{enriched}$ and the associated relative uncertainty are listed in Table 4.8.

From Table 4.8, it can be seen that the cross section increases from 8.1 MeV to 14.2 MeV where it reaches the highest value of 797.9 mb, then as the energy continues to increase, the cross section decreases. Even if the maximum cross sections of enriched or natural Gd target do not appear at the same energy, if only the numerical values are compared, the maximum cross section of the enriched target is doubled. The measured uncertainties are between 9.3 - 13.5%, these values are similar to those of natural Gd targets (Table 4.4). The highest relative uncertainty values are for targets having the lower Gd content which is somewhat expected.

Table 4.8 Measured cross section values of the reaction *Gd(d,x)$^{155}$Tb.

| Target n° | Energy (MeV) | $\sigma_{enriched}$ (mb) | $\Delta\sigma_{enriched}$ (%) |
|---|---|---|---|
| 1 | 8.1 ± 0.4 | 72.8 ± 9.2 | 12.6 |
| 2 | 9.0 ± 0.4 | 170.3 ± 18.6 | 10.9 |
| 3 | 11.2 ± 0.4 | 256.5 ± 24.9 | 9.7 |
| 4 | 12.4 ± 0.3 | 471.3 ± 48.2 | 10.2 |
| 5 | 14.0 ± 0.4 | 720.8 ± 67.4 | 9.3 |
| 6 | 14.2 ± 0.3 | 797.9 ± 77.8 | 9.7 |
| 7 | 16.0 ± 0.3 | 709.0 ± 66.3 | 9.4 |
| 8 | 19.4 ± 0.3 | 501.0 ± 49.9 | 10.0 |
| 9 | 24.4 ± 0.4 | 343.4 ± 46.7 | 13.5 |
| 10 | 29.7 ± 0.3 | 180.6 ± 24.0 | 13.3 |

For target n°1-4, the energy is smaller than the threshold energy of the reaction $^{156}$Gd(d,3n)$^{155}$Tb, only $^{155}$Gd can produce $^{155}$Tb. According to *eq.4.20*, the measured values correspond to 92.8% of the cross section of the reaction $^{155}$Gd(d,2n)$^{155}$Tb. Therefore, the cross section of $^{155}$Gd(d,2n)$^{155}$Tb can be converted. The results are shown in Table 4.9.

Table 4.9 Cross section of the reaction $^{155}$Gd(d,2n)$^{155}$Tb converted from measured values of $^{*}$Gd(n,x)$^{155}$Tb.

| Energy (MeV) | $\sigma_{155}$ (mb) |
|---|---|
| 8.1 ± 0.4 | 78.4 ± 9.9 |
| 9.0 ± 0.4 | 183.5 ± 20.0 |
| 11.2 ± 0.4 | 276.4 ± 26.8 |
| 12.4 ± 0.3 | 507.9 ± 51.9 |

Since these measured cross sections of *Gd(d, x)$^{155}$Tb are the first experimental values, there is no comparable data in literature.

The comparison of the measured results and simulated results are shown in Fig. 4.22. The red curve in the figure represents simulated values using *eq.4.20* (cross section taking into account the proportions of each isotope and the cross sections of each reaction), the black points represent the experimental with *$Gd_2O_3$ targets (values in Table 4.8), and the orange points represent the modified experimental values with natural $Gd_2O_3$ targets ($\sigma'_{modified}$) which will be explained later. Compared the measured results (black) and the simulated results, we can see that the position of the maximum value (about 14 MeV) is compatible between the two results. The maximum measured value is 797.9 mb at 14.2 MeV, this measured value is about 10% smaller than the simulated value (870 mb) situated at the same energy. Between 9-15 MeV, experimental curve rises more slowly than the simulation, and the measured cross sections are smaller than simulated result, this phenomenon is similar to the comparison with natural Gd targets (Fig. 4.17 in subsection 4.1.2). However, the experimental curve shows a good agreement with the simulated data above 15 MeV.

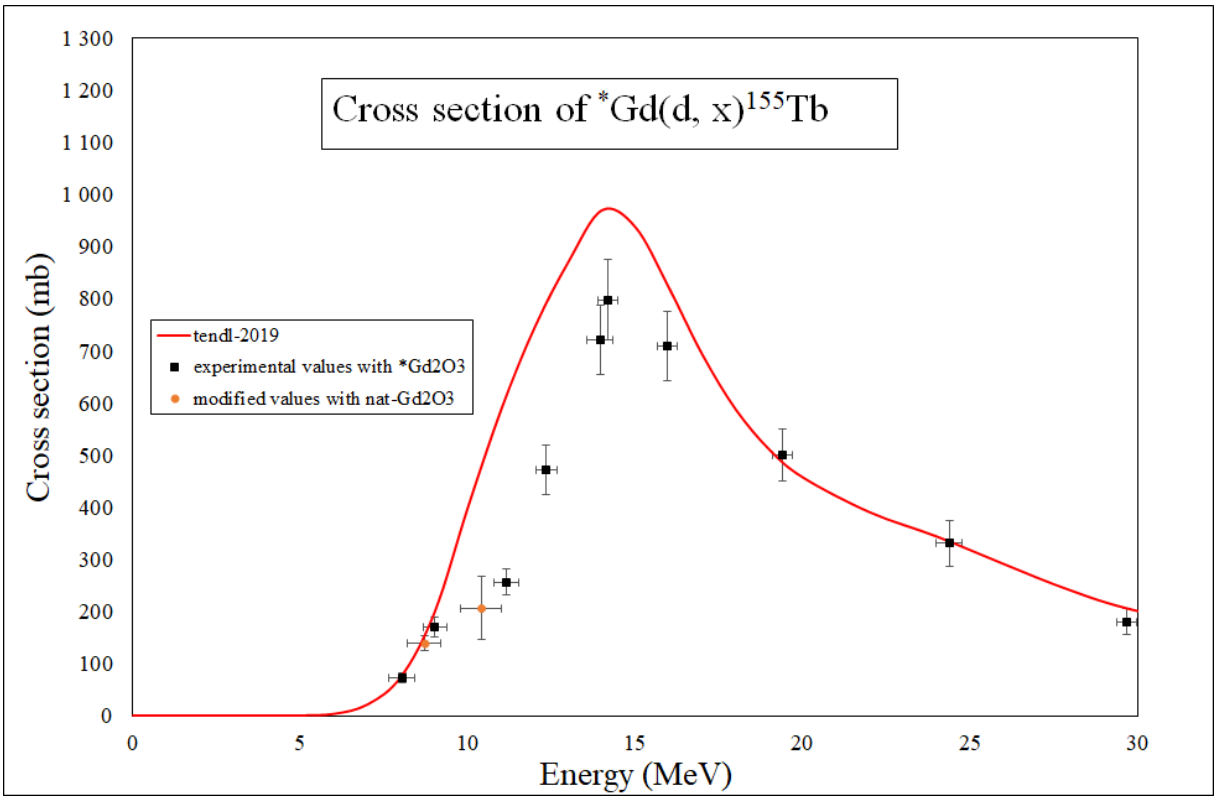


Fig. 4.22 Comparison of measured cross sections and simulated values of the reaction *Gd(d,x)$^{155}$Tb. Red curve: simulated values using eq.4.20; black points: measured values using enriched *$Gd_2O_3$ targets; orange points: modified measured values using naturel $Gd_2O_3$ targets according to eq.4.23.

In order to further compare the experimental values, the measured cross sections of natural $Gd_2O_3$ targets can be used to compare with these results at lower energy because when the deuteron energy is inferior to 12.52 MeV, only $^{154}$Gd and $^{155}$Gd produce $^{155}$Tb. Using *eq.4.15*, the measured cross section of natural $Gd_2O_3$ targets $\sigma'_{nat}$ can be expressed as *eq.4.21*:

$$\sigma'_{nat} = 2.18\,\% \cdot \sigma'_{154} + 14.8\% \cdot \sigma'_{155} \qquad (eq.\,4.21)$$

Where $\sigma'_{154}$ and $\sigma'_{155}$ are the experimental cross sections of $^{154}$Gd(d,n)$^{155}$Tb and $^{155}$Gd(d,2n)$^{155}$Tb, respectively. To be compared with the enriched results and taking into account the absence of $^{154}$Gd in the enriched target, the $\sigma'_{nat}$ was modified by taking the same enrichment of $^{155}$Gd. Using *eq.4.21*, the modified results $\sigma'_{modified}$ is expressed as:

$$\sigma'_{modified} = \frac{92.8\%}{14.8\%} \cdot \sigma'_{nat} \qquad (eq.\,4.22)$$

Using *eq.4.21*, the expression of $\sigma'_{modified}$ can be converted in to *eq.4.23*:

$$\sigma'_{modified} \approx 13.7\% \cdot \sigma'_{154} + 92.8\% \cdot \sigma'_{155} = 13.7\,\% \cdot \sigma'_{154} + \sigma'_{enriched} \qquad (eq.\,4.23)$$

Where $\sigma'_{enriched}$ is the estimated cross section of *Gd(d,2n)$^{155}$Tb according to the measured cross section of natural $Gd_2O_3$ targets $\sigma'_{nat}$.

Unfortunately, $\sigma'_{154}$ has not been measured experimentally in this work, so $\sigma'_{enriched}$ can not be deduced from experiment. However, the simulated cross section can be used for a rough

comparison. According to TENDL-2019, the cross section of $^{154}$Gd(d,n)$^{155}$Tb is about 150 - 180 mb at 9 - 11 MeV. Therefore, the $\sigma'_{modified}$ is about 20 - 25 mb higher than $\sigma'_{enriched}$. There are two available modified data at 8.7 MeV and 10.4 MeV (Table 4.4), the original value and the modified value are listed in Table 4.10.

Table 4.10 The original measured cross section and the modified cross section using natural $Gd_2O_3$ targets.

| Energy (MeV) | $\sigma'_{nat}$ (mb) | $\sigma'_{modified}$ (mb) |
|---|---|---|
| 8.7 ± 0.5 | 22.3 ± 2.2 | 139.8 ± 13.8 |
| 10.4 ± 0.6 | 32.9 ± 3.2 | 206.3 ± 20.1 |

These two values are also presented in Fig. 4.22 (orange points). For the two series of measured data, the modified values with natural $Gd_2O_3$ targets are in general consistent with those with enriched *$Gd_2O_3$ targets. This consistency indirectly shows that we can be confident with the accuracy of the enriched target cross section measurement, as the natural target cross section measurement are in agreement with existing literature data (subsection 4.1.2.4).

### 4.1.3.4. Cross section of impurities with enriched *$Gd_2O_3$ targets

Impurities such as $^{153}$Tb, $^{154}$Tb and $^{156}$Tb have been measured in several targets. The measured cross sections and associated uncertainties are listed in Table 4.11. It is worth noting that the cross sections of $^{156g}$Tb are cumulated values by considering contribution of its metastable states.

Table 4.11 Measured deuteron-induced reactions cross section values of $^{153}$Tb, $^{154}$Tb, and $^{156}$Tb on enriched *Gd targets.

| Target n° | Energy (MeV) | σ $^{153}$Tb (mb) | σ $^{154m2}$Tb (mb) | σ $^{154m1}$Tb (mb) | σ $^{154g}$Tb (mb) | σ $^{156g}$Tb (mb) |
|---|---|---|---|---|---|---|
| 1 | 8.1 ± 0.4 | - | - | - | - | 23.1 ± 2.7 |
| 2 | 9.0 ± 0.4 | - | - | - | - | 41.6 ± 4.5 |
| 3 | 11.2 ± 0.4 | - | - | - | - | 53.0 ± 5.2 |
| 4 | 12.4 ± 0.3 | - | - | - | - | 57.3 ± 5.9 |
| 5 | 14.0 ± 0.4 | - | < 5.1 | < 19.2 | < 5.0 | 78.2 ± 7.4 |
| 6 | 14.2 ± 0.3 | - | < 5.1 | < 19.2 | < 5.0 | 83.1 ± 8.1 |
| 7 | 16.0 ± 0.3 | - | < 5.1 | < 19.2 | < 5.0 | 71.4 ± 6.7 |
| 8 | 19.4 ± 0.3 | - | 31.6 ± 3.5 | 104.5 ± 14.8 | 188.0 ± 26.6 | 62.8 ± 6.2 |
| 9 | 24.4 ± 0.4 | 98.3 ± 12.7 | 43.8 ± 6.3 | 79.9 ± 11.5 | 51.3 ±7.4 | 56.4 ± 6.1 |
| 10 | 29.7 ± 0.3 | 837.6 ± 78.8 | 76.6 ± 9.8 | 116.9 ± 17.0 | 134.4 ± 19.5 | 37.2 ± 4.1 |

The $^{153}$Tb was only detected in two targets at high energies (24.4 MeV and 29.7 MeV). This is expected as the threshold energy of $^{*}$Gd(d,x)$^{153}$Tb is 20.17 MeV. These values are compared with data of TENDL-2019 in Fig. 4.23. The global trend of the cross section values with the energy is comparable. At 29.7 MeV, the measured cross section is 837.6 mb, which is in agreement with the value of TENDL-2019 (875.4 mb) considering the associated uncertainties of the measured value. At 24.4 MeV, our measured value (98.3 mb) is much smaller than that of TENDL-2019 (341.3 mb).

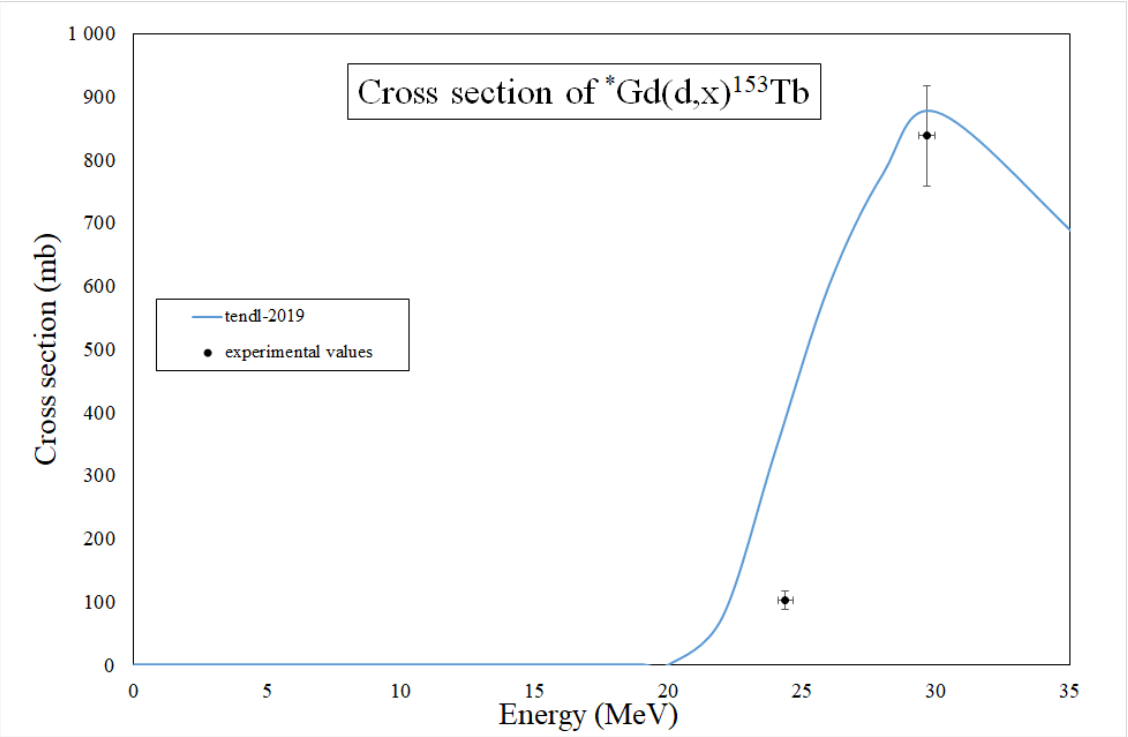


Fig. 4.23 Comparison of measured cross sections and simulated values of the reaction *Gd(d,x)$^{153}$Tb. Blue curve: simulated TENDL-2019 values; black points: measured values using enriched *$Gd_2O_3$ targets.

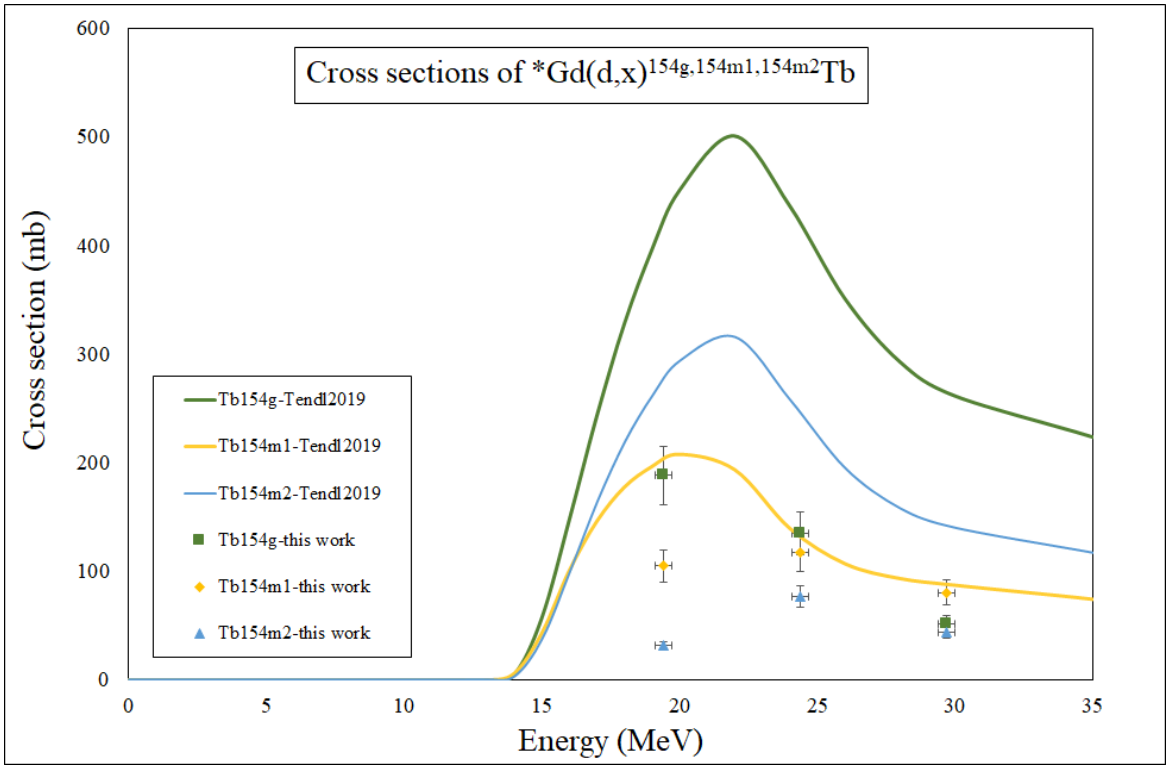


Fig. 4.24 Comparison of measured cross sections and simulated values of the reaction *Gd(d,x)$^{154g,m1,m2}$Tb. Green, yellow and blue curves reprensent the simulated TENDL-2019 values of $^{154g}$Tb, $^{154m1}$Tb and $^{154m2}$Tb, respectively; green, yellow and blue points represent measured values of $^{154g}$Tb, $^{154m1}$Tb and $^{154m2}$Tb, respectively.

For $^{154}$Tb, the three states were detected in three targets (n°8-10) at high energy, above 19.4 MeV. As the threshold energies for *Gd(d,x) $^{154g,154m1,154m2}$Tb are 13.16 MeV, 13.27 MeV and 13.57 MeV respectively, $^{154g,154m1,154m2}$Tb can be produced in the irradiation conditions of target n°5-7. However, the values were smaller than the detection limits. The cross sections of $^{154m2}$Tb, $^{154m1}$Tb, and $^{154g}$Tb are maximum at 24.4 MeV, the values are 76.6 mb, 116.9 mb, and 134.4 mb, respectively. The measured cross sections were compared with those simulated with TENDL-2019. Fig. 4.24 shows the comparison, it is clear that all measured results are much smaller than those of simulation. In higher energy, the measured cross sections of $^{154m1}$Tb are similar to the simulated values, while the measured values of $^{154g}$Tb and $^{154m2}$Tb are quite different from the simulation.

For $^{156}$Tb, it is detected in all target, this is consistent with the theoretical analysis: the co-production of $^{156}$Tb is not avoidable in the energy range studied in this work (8-30 MeV). The cross section reaches a maximum of 85mb at 15 MeV. This $^{156}$Tb is coming from interaction on $^{155}$Gb and $^{156}$Gd, which explains why values in this case are smaller than those obtain in $^{nat}$Gd above 14 MeV (125-312 mb). The measured cross section values of $^{156}$Tb are also compared with values of TENDL-2019 in Fig. 4.25. As for $^{155}$Tb values, TENDL-2019 overestimates values in the energy range from 8 to 14 MeV, while it is globally in agreement with the experimental data above 14 MeV. As stated previously, neighbor data points were measured in different irradiation session that prevent any systematic error coming from one experiment giving us confidence on our results .

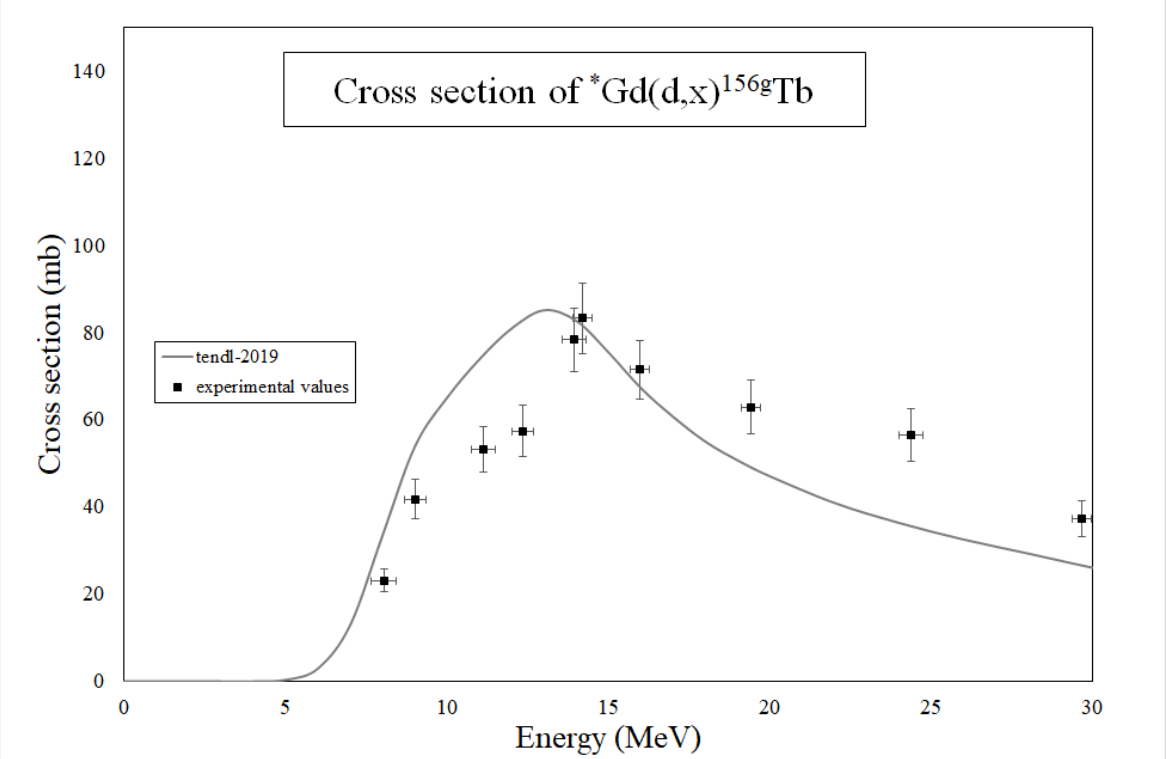


Fig. 4.25 Comparison of measured cross sections and simulated values of the reaction *Gd(d,x)$^{156g}$Tb. Gray curve: simulated TENDL-2019 values using eq.4.16; black points: measured values using enriched *$Gd_2O_3$ targets

Since the co-production of $^{156}$Tb exists from 0-30 MeV, and its half-life is similar to that of $^{155}$Tb, it is interesting to compare their cross sections. The results are presented in Fig. 4.26 . The gap is biggest at 14.2 MeV, the two radionuclides both reach their maximum value, 83.1 mb for $^{156}$Tb and 797.9 mb for $^{155}$Tb. The ratio of the cross sections is 10.4 % at this energy. The production purity of $^{155}$Tb will be presented in the next section (section 4.2).

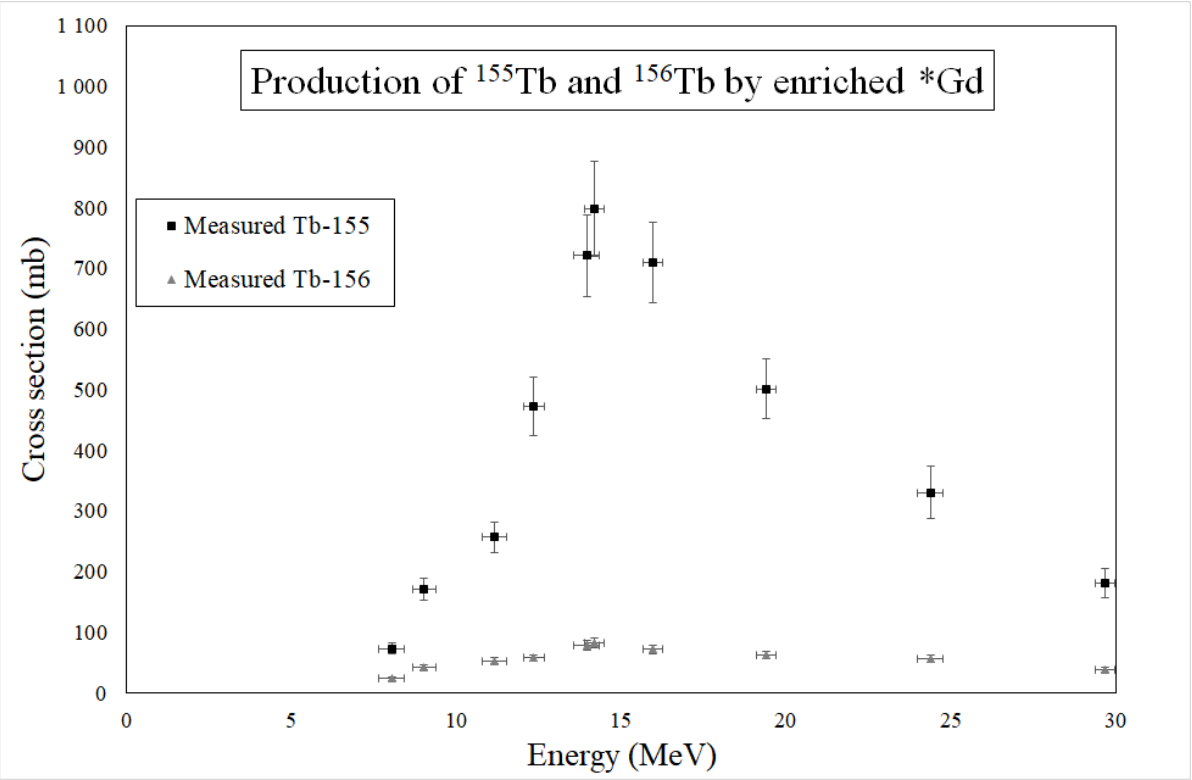


Fig. 4.26 Measured cross section values of $^{155}$Tb and $^{156}$Tb.

#### 4.1.3.5. Comparison with proton induced reaction of enriched $^{155}$Tb

As explained in Chapter 1, theoretic analysis shows that deuteron-induced reaction on enriched $^{155}$Tb is more productive than that of proton-induced reaction. To validate the theoretical analysis, the experimental cross sections of $^{155}$Tb measured in this work are also compared with those of proton-induced reaction at 9-20 MeV. The compared data comes from the work of Dellepiane et al. [98]. The enrichment level of $^{155}$Gd in their targets is 91.90%, which is a little bit smaller than the enrichment level of our targets (92.8%).

Fig. 4.27 shows the comparison of $^{155}$Tb cross sections produced by proton and deuteron induced reactions on enriched $^{155}$Gd. From the comparison, in a similar enrichment level, the deuteron-induced reaction has a huge advantage at 14-20 MeV. The maximum cross section of $^{155}$Tb is about 800 mb through deuteron induced reaction while this value decreases to 400 mb through proton induced reaction.

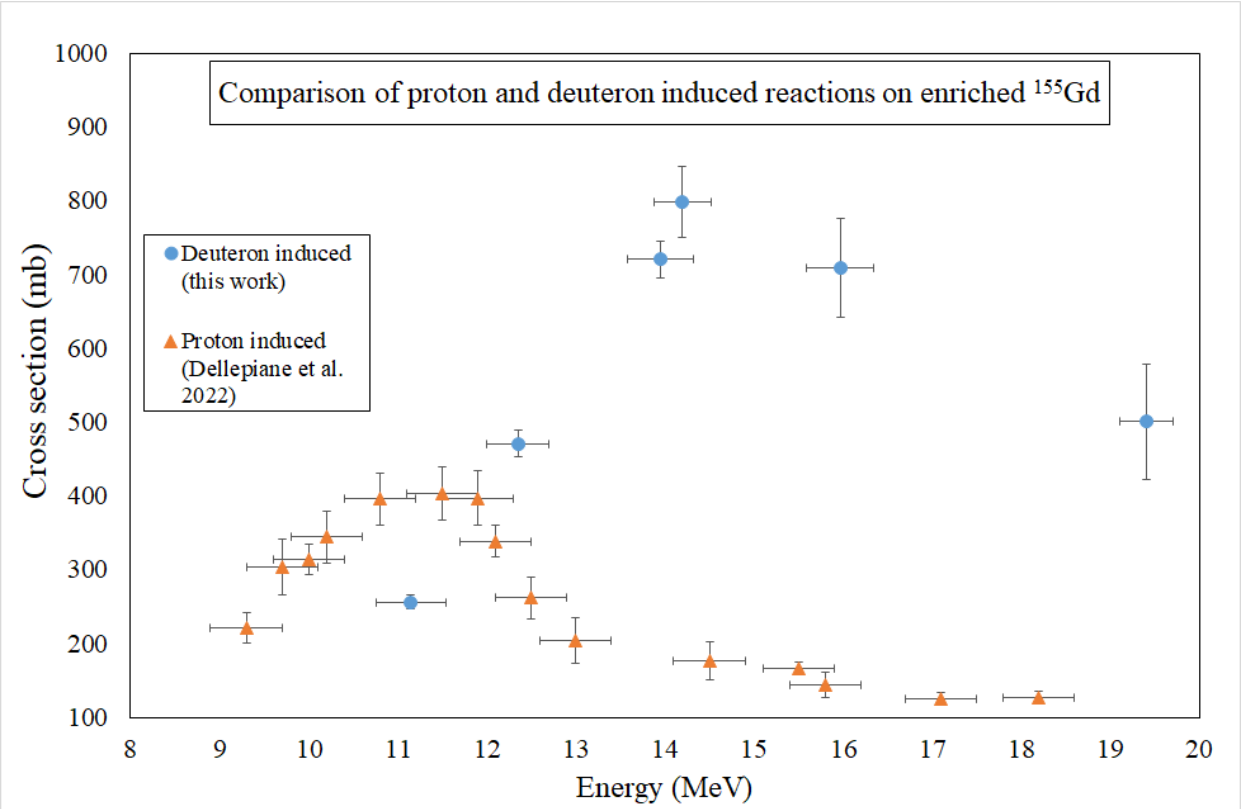


Fig. 4.27 Comparison of $^{155}$Tb cross sections produced by proton induced and deuteron induced reactions of enriched $^{155}$Gd.

#### 4.1.3.6. Summary of this section

In this section we reported production cross section of $^{155}$Tb and other Tb impurities obtained by irradiation of enriched $^{155}$Gd (92.8%) by a deuteron beam with energy up to 30 MeV. Experiments were conducted using the stacked foils technique and target foils made of codeposited *$Gd_2O_3$ with Ni.

Calculation of TENDL-2019 are used and compared with the collected data, the calculations are in overall agreement with our results. Data shows that $^{155}$Tb production is more effective with deuteron and an enriched $^{155}$Gd target than with $^{nat}$Gd target or proton induced reaction on enriched $^{155}$Tb. However, $^{156}$Tb is co-produced when using deuteron at the experimental energy range. The next section will estimate and experimentally validate the purity of $^{155}$Tb.

## 4.2. Thick target Production of $^{155}$Tb

### 4.2.1. Theoretical analysis

#### 4.2.1.1. The production yield and the thick target yield (TTY)

The production yield of a radionuclide represents the efficiency of the production during an irradiation process; it is related to the number of the radionuclides produced and the irradiation conditions (irradiation time, beam intensity and so on). As explained in Chapter 1, the number of the produced nuclei $Y(t)$ can be expressed as *eq.1.14*:

$$Y(t) = tI_0 \int_{E_1}^{E_0} dE \left(-\frac{1}{\rho}\frac{dE}{dx}\right)^{-1} \sigma(E)/(Ze) \qquad (eq.\,1.14)$$

For a radionuclide with a decay constant λ, the change of the number of the nuclei $\frac{dN(t)}{dt}$ satisfy the following equation:

$$\frac{dN(t)}{dt} = \frac{dY(t)}{dt} - \lambda N(t) = I_0 y - \lambda N(t) \qquad (eq.4.24)$$

Since the production yield $y$ can be expressed as eq.1.15 (explained in Chapter 1):

$$y = x \int_{E_1}^{E_0} dE \left(-\frac{1}{\rho}\frac{dE}{dx}\right)^{-1} \sigma(E)/(Ze) \qquad (eq.1.16)$$

The solution of this differential equation is:

$$N(t) = \frac{I_0 y}{\lambda}\left(1 - e^{-\lambda t}\right) \qquad (eq.4.25)$$

Thus, the production yield can be expressed as *eq.4.26*:

$$y = \frac{\lambda N(t)}{I_0(1 - e^{-\lambda t})} = \frac{Act(t)}{I_0(1 - e^{-\lambda t})} \qquad (eq.4.26)$$

When the irradiation time is very long, t ≫ 1 , the production yield y reaches to the saturation production yield, it can be approximately equal to the ratio of activity to the beam intensity:

$$y = \frac{Act(t)}{I_0} \qquad (eq.4.27)$$

The unity of the production yield is thus in MBq/µAh.
Another quantity to evaluate the production is the thick target yield (TTY), it is the production yield of a target who reduce the particle energy from maximum energy to the threshold energy. The formula is the same as *eq.1.15* by replacing $E_1$ to the threshold energy.

#### 4.2.1.2. Production yield simulated by RYC

Since the production yield is a function of the cross section, the target characteristics and the beam energy, it is possible to estimate the production yield using the excitation function.
In this work, the RYC program was used to estimate the production yield and the TTY. It is a free GUI program developed by GIP ARRONAX[6]. It is written in python programming language[200] using the TKinter module and compiled with PyInstaller software[201]. RYC uses SRIM module[185] to calculate the stopping-power of the projectiles[202] and calculates the production yield and activity of radioisotopes based on irradiation parameters and excitation functions[202–204].
The fitted excitation functions using the Experimentally Modified Gaussian (EMG) distribution provided by RYC are shown in Fig. 4.28. Curves A1 and B1 are respectively the excitation functions of $^{*}$Gd(d,2n)$^{155}$Tb and $^{*}$Gd(d,n)$^{156}$Tb using measured cross section.

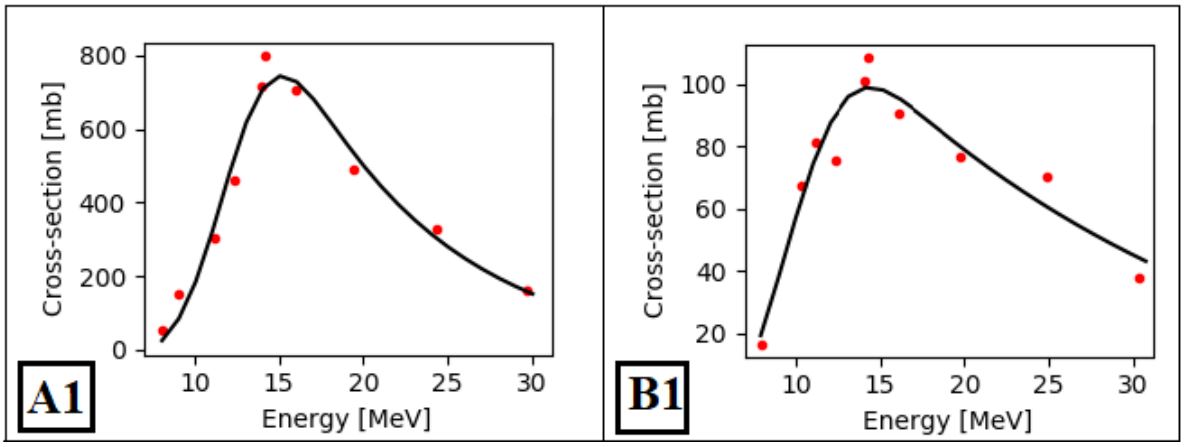


Fig. 4.28 Fitted excitation function of $^{155}$Tb and $^{156}$Tb with Experimentally Modified Gaussian (EMG) distribution fitting function. A1: inputs of cross sections of $^{155}$Tb measured in this work;B1: inputs of cross sections of $^{156}$Tb measured in this work.

From these fitted excitation functions, the production yields can be estimated using the formula *eq.4.27*. As a target, we used a pressed pellet of $Gd_2O_3$ with a density equals to 5.08 g/cm$^3$, the one corresponding to the manufactured pellet presented in Chapter 3. The Fig. 4.29 shows the RYC estimation of the production yield, the orange curve and blue curve represent respectively the production yield of $^{155}$Tb and $^{156}$Tb using measured data. It should be noted that the value shown in the figure is the production yield for a target supposed thick enough to stop the beam. For $^{155}$Tb, the production yield increased slowly when the incident energy increase from 8 to 13 MeV, then, the production yield increases rapidly as the energy continues to increase at 13-19 MeV and finally slow down again at 19-30 MeV. From this is curve, it is possible to determine the value for any energy interval (incident energy E1, output energy E2) by just making the difference between the yields corresponding to E1 and E2. For example, when the incident energy is 14 MeV and the output energy is 8 MeV, the production yield of $^{155}$Tb is 6.9 MBq/µAh. Meanwhile, when the incident energy is 16.5 MeV and the output energy is 14 MeV, the production yield of $^{155}$Tb remains unchanged. Therefore, the production yields corresponding to different incident and output energy intervals may be the same. However, the target thicknesses and produced radionuclides corresponding to these energy intervals may vary, which will be discussed in the next subsection (4.2.1.3).

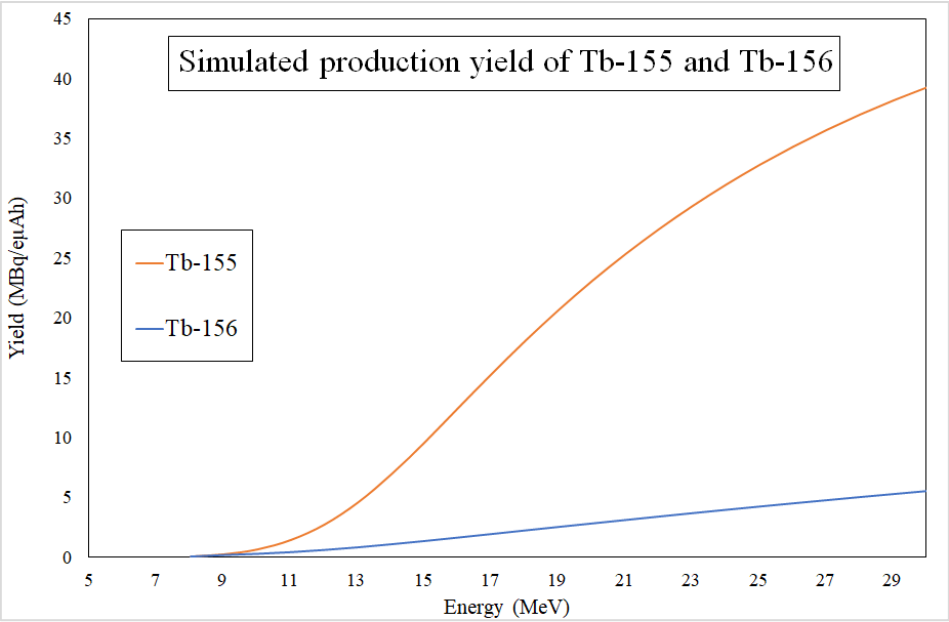


Fig. 4.29 RYC simulation of production yield of $^{155}$Tb and $^{156}$Tb using measured data.

From the RYC simulation of production yields, the ratio of the production yield of $^{155}$Tb to the production yield of $^{156}$Tb ($\frac{y_{155}}{y_{156}}$) can thus be estimated (Fig. 4.30). The ratio increases from 60% to 89% when energy increases from 9 MeV to 18 MeV, and remains unchanged at 18-22 MeV, then the ratio slightly decreases to 87% when energy increases to 30 MeV. As explained before, when energy is between 9 and 13.16 MeV ($E_{hhreshold}$ of $^{154}$Tb), only $^{155}$Tb and $^{156}$Tb can be produced, so the ratio $\frac{y_{155}}{y_{156}}$ is in fact the purity of the production ($^{155}$Tb). When energy is larger than 13.16 MeV, this ratio can be considered as the purity of the production after a period long enough to allow $^{154}$Tb (and $^{153}$Tb when energy is above 20.17 MeV) to decay to a negligible amount.

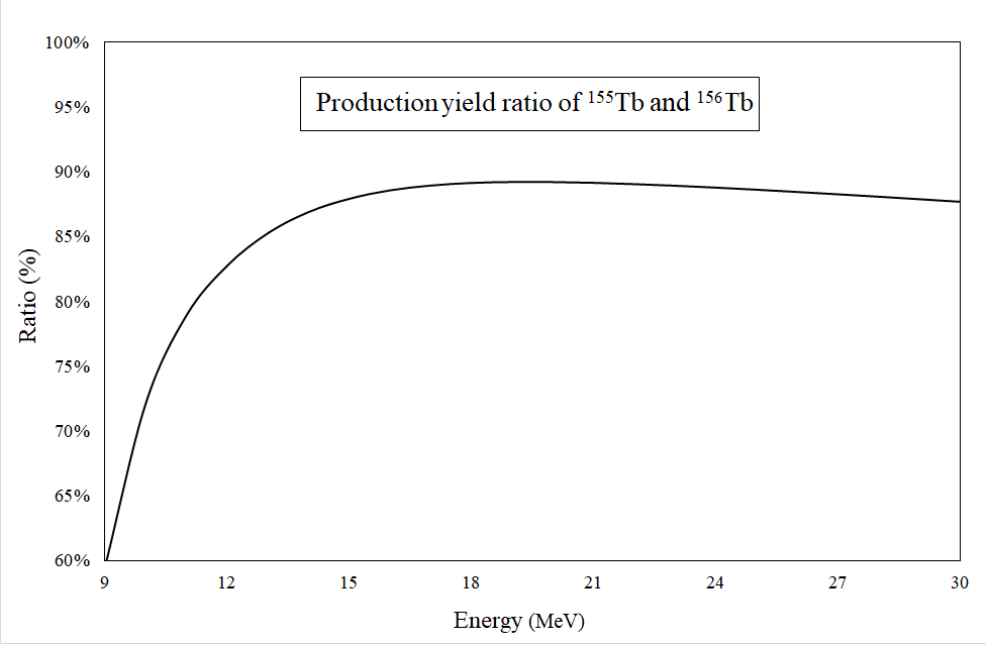


Fig. 4.30 The ratio of the production yield of $^{155}$Tb and $^{156}$Tb as a function of energy using the data simulated by RYC.

#### 4.2.1.3. Optimal target thickness and energy window

For a target, an ideal thickness needs to meet three conditions:

- it should not be too thin, otherwise the production yield will be limited and mechanical performance may not be sufficient to sustain irradiation;
- it should not be too thick, otherwise the particle energy decreases below the threshold energy of the required nuclear reaction leading to additional thermal energy in the target to evacuate and possibly production of contaminant;
- the Bragg peak must not take place in the target otherwise there can be local overheating in the target which can weaken it and may cause issues during irradiation.

As mentioned in the previous subsection (4.2.1.2), in the case of the consistent production yield, the target thicknesses corresponding to different energy windows are different. For a target with an incident energy at 14 MeV and an output energy at 8 MeV, the thickness of the target is 340 µm; meanwhile, the thickness decreases to 140 µm when the incident and output energies are respectively 16 MeV and 14 MeV. From the point of view of saving target material, the latter is better. However, more $^{154}$Tb is generated in the latter energy window, which affects the purity of $^{155}$Tb.

Therefore, two cases were considered to choose the optimal energy window.

**Case 1:** the incident energy is 13.16 MeV and the output energy is 8 MeV.

In this case, the estimated target thickness is about 290 µm according to TRIM while the production yields for $^{155}$Tb and $^{156}$Tb are respectively 4.9 MBq/µAh and 0.8 MBq/µAh according to Fig. 4.29. Since only $^{155}$Tb and $^{156}$Tb are produced in this energy window, and their half-lives are very close, the purity of $^{155}$Tb remains almost unchanged after irradiation. It is about 86%.

**Case 2:** the incident energy is 16 MeV and the output energy is 12 MeV.

In this case, the estimated target thickness is about 270 µm and the estimated production yields for $^{155}$Tb and $^{156}$Tb are respectively 9.8 MBq/µAh and 1.0 MBq/µAh. Except for $^{155}$Tb and $^{156}$Tb, the three states of $^{154}$Tb will also be produced in this energy window but there cross sections are very small (Table 4.11). To increase the purity of $^{155}$Tb, the target can be cooled for 10 days (>10 times of the half-lives of $^{154g,m1,m2}$Tb) to keep the amount of $^{154}$Tb low enough (> 1024 times lower). After 10 days, the production yields of $^{155}$Tb and $^{156}$Tb decrease respectively to 2.7 MBq/µAh and 0.3 MBq/µAh. The purity is about 90%.

Comparing these two cases, with similar target thickness, the former has a higher final yield but a slightly lower purity, and the latter has a lower final yield but a slightly higher purity. Considering that the former does not need to wait for the target to cool, and it completely avoids the generation of $^{154}$Tb, it is more advantageous in terms of operability. Therefore, for the experimental production, we prefer to limit the incident energy below 13.16 MeV.

### 4.2.2. Experimental production of $^{155}$Tb

After theoretical analysis, an enriched *$Gd_2O_3$ target with a thickness of 0.39 mm was encapsulated by 2 foils of Al (see Chapter 3) and irradiated to determine thick target production yield of $^{155}$Tb.

#### 4.2.2.1. Capsule conception and irradiation condition

The capsule used in this experiment is an existing stainless steel capsule designed and manufactured by GIP ARRONAX for another project. The capsule is divided into two parts: the front part is thin in the center and the surrounding area is thick, the center thickness is about 0.66 mm, and the rear part has a groove with a depth of 2.0 mm and a diameter of 280 mm to position the target. As this capsule was not initially designed for that project, the enriched *$Gd_2O_3$ target is too small and we had to add a natural $Gd_2O_3$ target encapsulated with 2 Al foils behind the enriched target to reach a total thickness of 1.5 mm and have a solid system. We also used 4 balls made of Al to center the targets. Fig. 4.31 shows the empty capsule (a), the assembly of the enriched target (b), and the closed capsule.

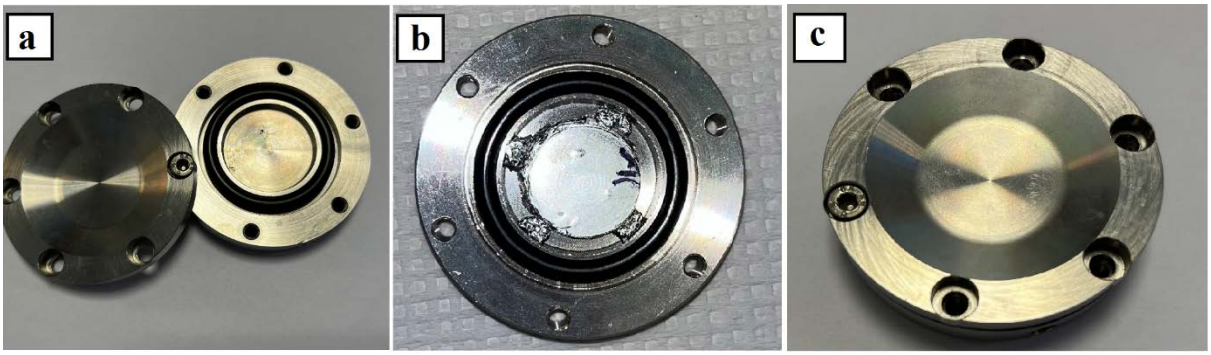


Fig. 4.31 The capsule and the assembly of the target. a: empty capsule; b: assembly of enriched targets fixed by Al balls and natural target; c: closed capsule.

The enriched *$Gd_2O_3$ target was irradiated by deuterons with an incident energy of (12.72 ± 0.5) MeV, and a beam intensity of 500 nA for 1h. According to the SRIM simulation, the exit energy from the enriched pellet (not including the Al foil) is (3.77 ± 0.85) MeV. A Ti foil with a thickness of 10 µm was put before the enriched pellet in order to get a measurement of the incident beam intensity through a monitor reaction. The schematic of the assembly is shown in Fig. 4.32.

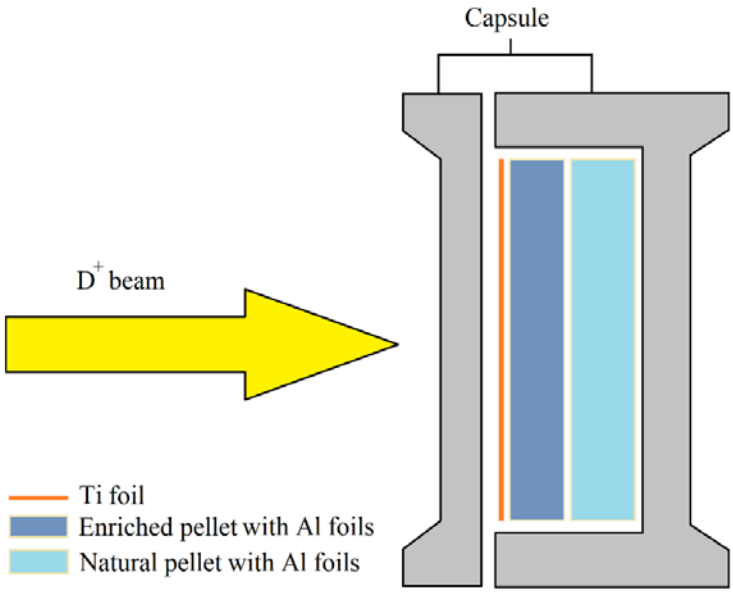


Fig. 4.32 Schematic diagram of the assembly of Ti foil and pellets in the capsule.

After irradiation, the whole assembly was stored in a lead pot for 9 days for decay. The enriched pellet, including his aluminum wrapping foils, was then dissolved by 100 mL of HCl (2 mol/L). The dissolved solution was diluted by a factor 100 and an aliquot was collected for the data acquisition (triplicate). Samples were counted 3 times on our HPGe detector 9–14 days after EOB (0 cm from the detector). Each counting lasted 24 hours, and the dead times were 10%, 9%, and 6%, respectively. The activities of radionuclides are average values of three counts.

#### 4.2.2.2. Experimental production yield and purity of $^{155}$Tb

Measured activity recalculated at EOB were (3.75 ± 0.06) MBq for $^{155}$Tb and (0.48 ± 0.01) MBq for $^{156}$Tb. Meanwhile, except for $^{155}$Tb and $^{156}$Tb, several peaks of $^{154g}$Tb were also detected. Activities of $^{154g}$Tb during the two first counting are respectivley 16 kBq and 0.4 kBq, and it was not detected during the last counting. No $^{154m1}$Tb or $^{154m2}$Tb were detected during the three counting, so the activity for $^{154g}$Tb at EOB remains unknown. One spectrum of the diluted samples (counted 9 days after EOB) is shown in Fig. 4.33. It can be seen that the gamma lines $E_\gamma$ = 704.9 keV and $E_\gamma$ = 1291.326 keV of $^{154g}$Tb are evident in the spectrum. It should be noted that the half-life of $^{154g}$Tb is 21.5 h, so $^{154g}$Tb undergoes ten decay period (9 days) when the sample was counted. This means that there might be a problem for the incident energy.

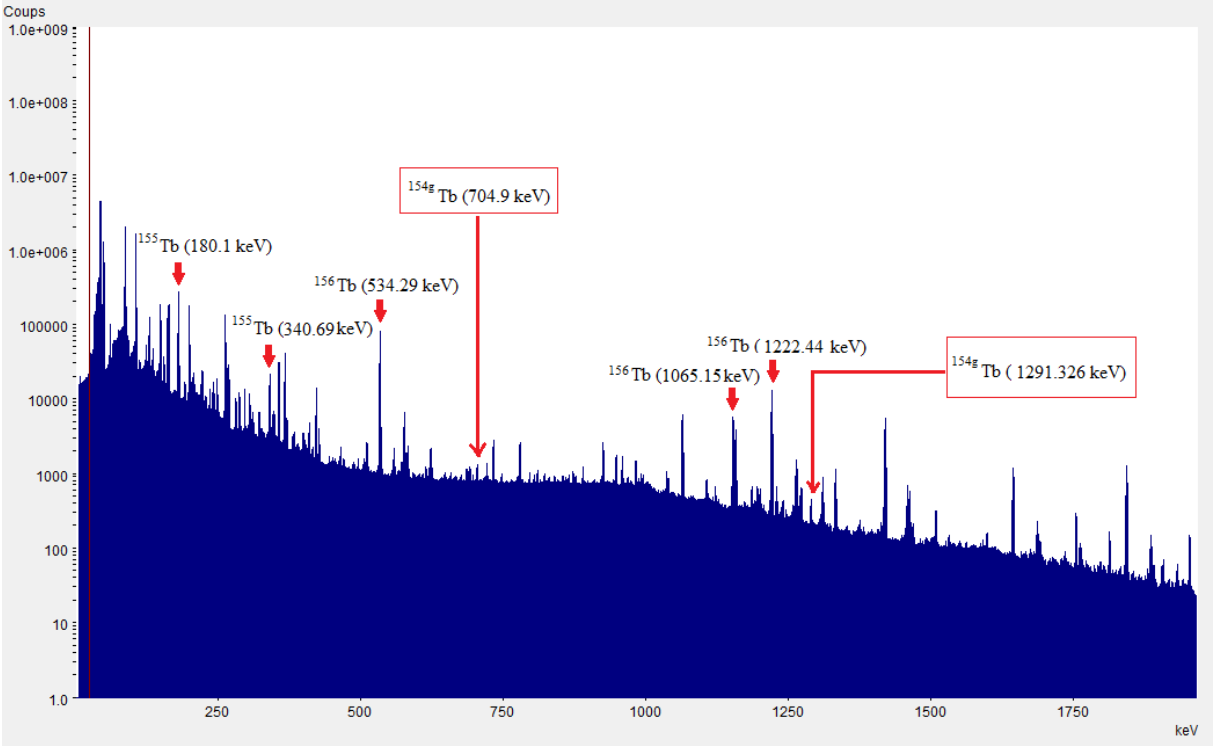


Fig. 4.33 Spectrum of a diluted sample which is counted 9 days after EOB.

To verify the incident energy and the beam intensity in the experiment, the Ti monitor was used thanks to the 2 monitor reactions $^{nat}$Ti(d,x)$^{46}$Sc and $^{nat}$Ti(d,x)$^{48}$V.

The excitation function of the reaction $^{nat}$Ti(d,x)$^{46}$Sc is shown in Fig. 4.34, the data in the figure come from IAEA[121]. It can be seen that when energy varies between 13-16 MeV, the reaction cross section varies little (between 35 mb to 30 mb). Therefore, the reaction $^{nat}$Ti(d,x)$^{46}$Sc can be used to estimate the beam intensity. The estimated beam intensity was then used to calculate the cross section of the reaction $^{nat}$Ti(d,x)$^{48}$V. The excitation function of $^{nat}$Ti(d,x)$^{48}$V is shown

in Appendix Figure 7 (in *Appendix 4.1*), it can be seen that the cross section changes with energy: when energy varies from 13 MeV to 16 MeV, cross section varies from 258 mb to 325 mb. We will use this reaction to verify the incident energy.

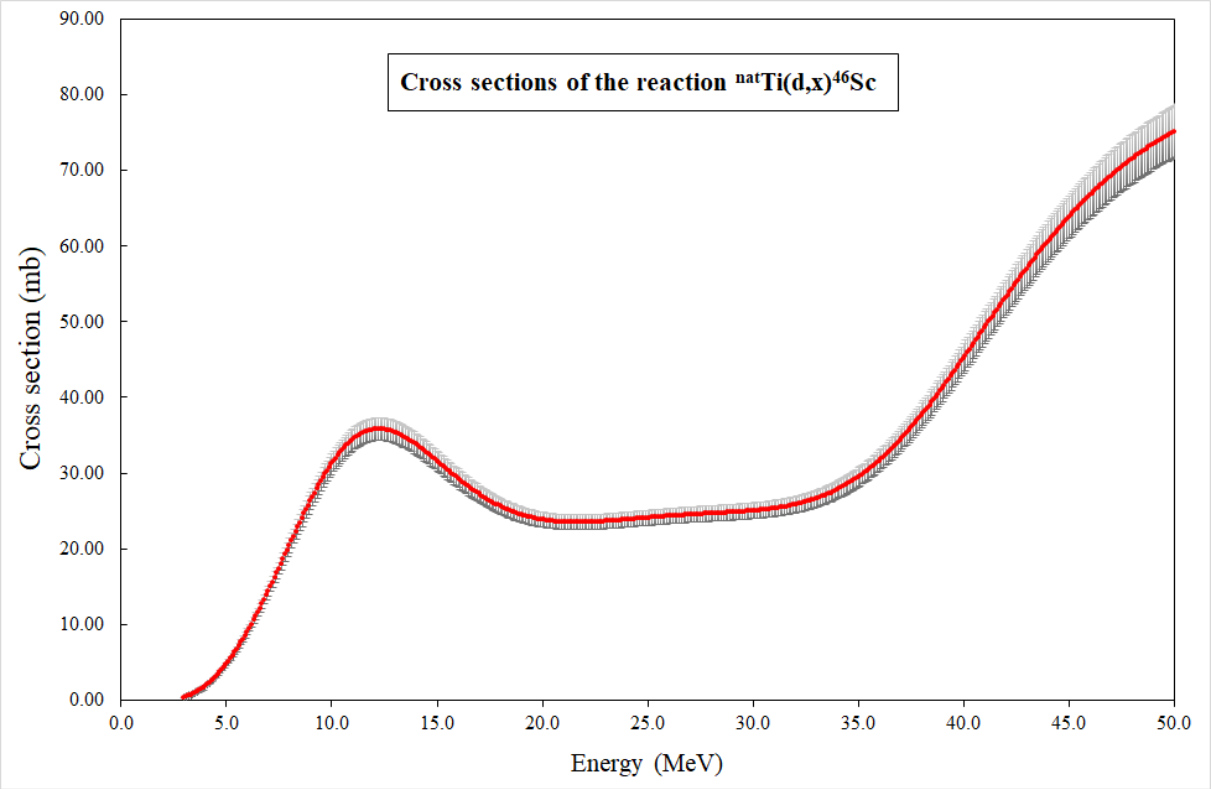


Fig. 4.34 Activation cross section data of the $^{nat}$Ti(d, x)$^{46}$Sc reaction with estimated uncertainties according to data of IAEA.

The analysis of the Ti monitor results to a beam intensity of (368 ± 26) nA and an incident energy in the monitor of (15.3 ± 1.5) MeV. This leads to an incident energy in our pellet equal to (15.1 ± 1.5) MeV and an exit energy of (8.6 ± 0.8) MeV. This incident energy is very different from the desired energy; the deviation may be due to the wrong estimation of the capsule thickness or the problem of mechanical adjustment.

Using the measured beam intensity, the production yields of the enriched *$Gd_2O_3$ target were estimated. The production yield of $^{155}$Tb is (10.2 ± 0.7) MBq/µAh while the production yield of $^{156}$Tb is (1.3 ± 0.1) MBq/µAh. These experimental production yields have been compared with our cross section measurement using the corrected incident energies. We found a very good agreement with estimated production yields of $^{155}$Tb and $^{156}$Tb, which are 10.1 MBq/µAh and 1.2 MBq/µAh, respectively. These thick target yields are consistent with our cross section values.

The purity of $^{155}$Tb, which is calculated as the ratio of the activity of $^{155}$Tb to the total activity of all radionuclides ($^{154}$Tb, $^{155}$Tb and $^{156}$Tb), was estimated according to the first counting. The change of purity over time is shown in Fig. 4.35. It is clear that the purity increases with cooling time but in low proportion: from 9 days after EOB to 14 days after EOB, the purity increases from 87.6% to 88.6%. The purity remains almost unchanged after 14 days. The final production yield for $^{155}$Tb is (3.2 ± 0.2) MBq/µAh after 9 days of decay and (1.6 ± 0.2) MBq/µAh after 14 days of decay.

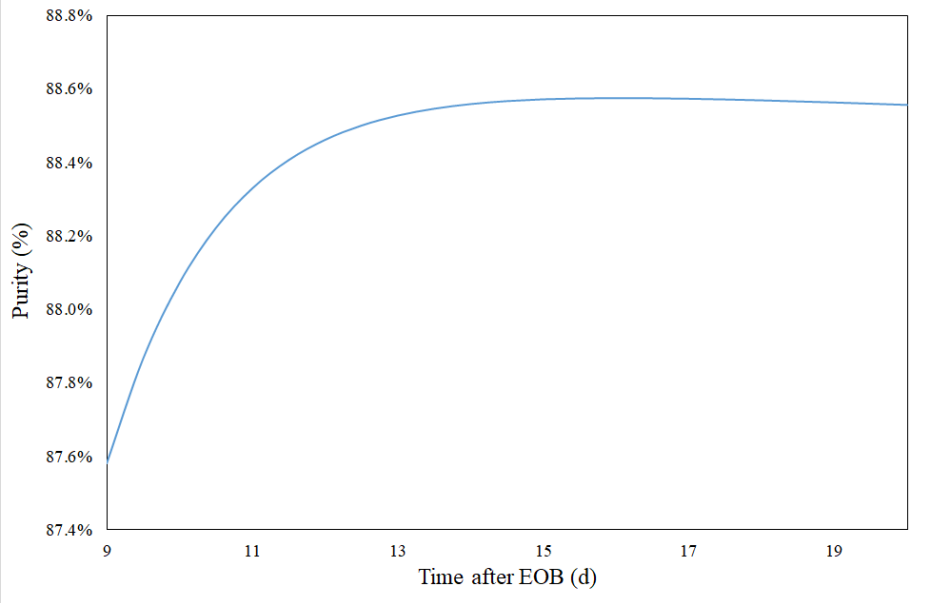


Fig. 4.35 Purity change of $^{155}$Tb as a function of time after irradiation.

The experimental production yield of $^{155}$Tb has also been compared with other proton induced production route. The comparison is presented in Table 4.12. It can be seen that, under the respective optimum experimental conditions, the production yield of this work is more than twice larger than that of the production with protons ($^{155}$Gd(p,n)$^{155}$Tb) as expected from cross section data. However, the purity of this work is slightly smaller than the proton production route.

Table 4.12 Comparison of different production routes of $^{155}$Tb

| Production route | Target mass (mg) | Beam incident energy (MeV) | Production yield EOB (MBq/μAh) | Maximum purity (%) | Reference |
|---|---|---|---|---|---|
| $^{155}$Gd(d,2n)$^{155}$Tb | 630 | 15.1 | 10.2 ± 0.7 | 89% | This work |
| $^{155}$Gd(p,n)$^{155}$Tb | 37-40 | 10.4 | 3.4 ± 0.5 | 93% | Dellepiane et al.[98] |

### 4.2.2.3. Future target material

The comparison in the previous subsection shows that for the target with enrichment as high as 92 ± 1%, the deuteron induced reaction has more advantage in production yield but is slightly weaker in terms of purity. In fact, whether it is proton or deuteron, the final purity of their product ($^{155}$Tb) is far from the requirements in clinical medicine. The purity of most radionuclides used in clinics is greater than 99.9% ($^{99}$Mo) or even 99.995% ($^{131}$I) [205].

To increase the purity, one solution is to increase the enrichment level. For a pure target of $^{155}$Gd, the calculated (TENDL-2019) cross sections of Tb radionuclides from 0-30 MeV is shown in Fig. 4.36. For proton-induced reactions, the cross section of $^{156}$Tb is very small in that energy range while that for deuteron is relatively large.

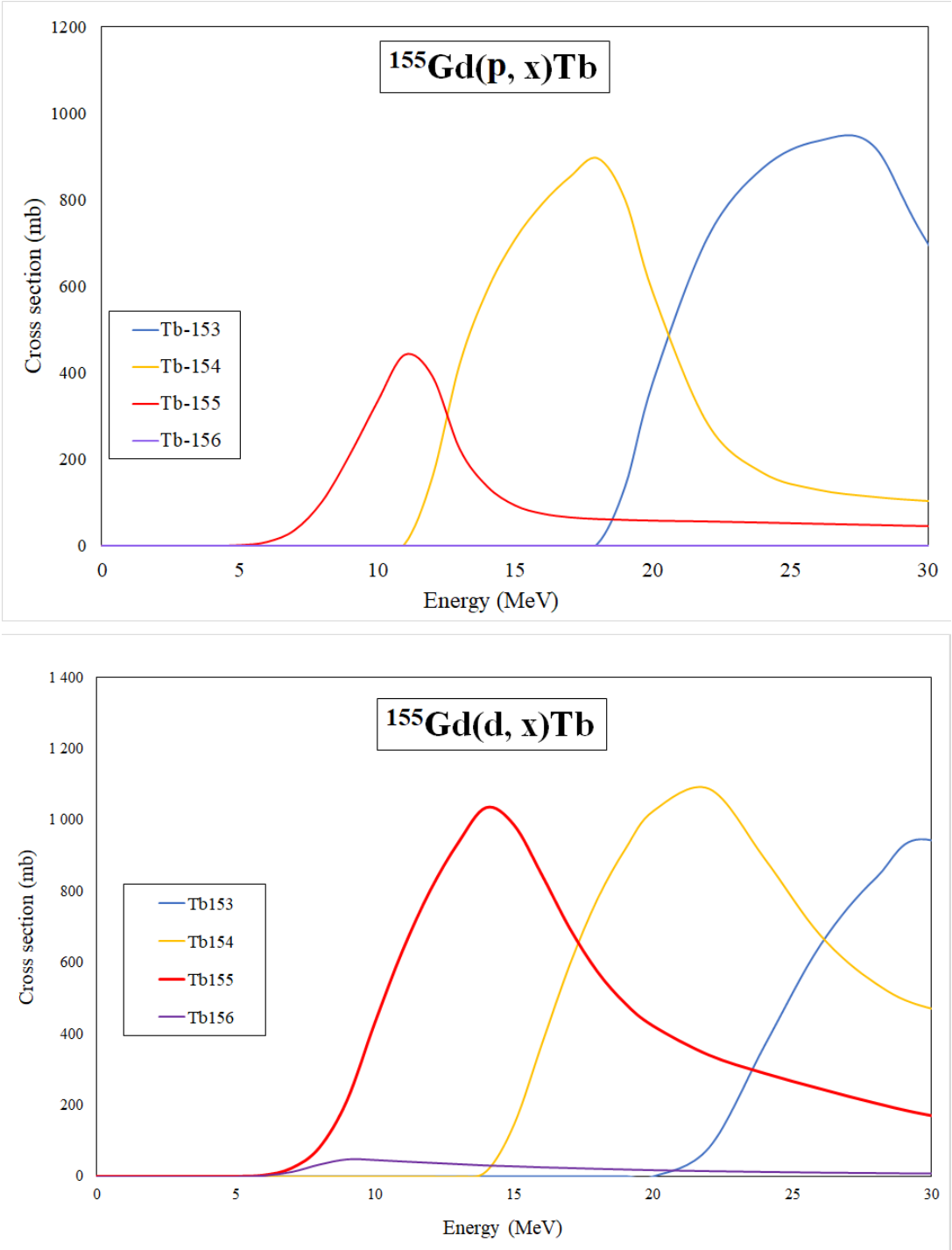


Fig. 4.36 Cross sections of Tb radionuclides of proton induced (on top) or deuteron induced (on bottom) reactions on pure $^{155}$Gd target. Data calculated by TENDL-2019.

Using this calculated data, the production yield and the ratio $\frac{y_{155}}{y_{156}}$ were estimated by RYC. Fig. 4.37 shows the ratio $\frac{y_{155}}{y_{156}}$ as a function of energy. For proton-induced reaction, the ratio increases when energy increases from 0 to 11 MeV, then reaches a maximum value 99.9%, and slightly decreases when energy continues to increase. For deuteron-induced reaction, the ratio decreases firstly until 8 MeV, and then increases up to 95% as the increase of the incident energy.

In terms of purity, the deuteron production route is better from 0-2 MeV, but the production yield of $^{155}$Tb is only $2.5\times10^{-6}$ MBq/µAh. This is not suitable for mass production. For proton production route however, when energy is between 10 to 11 MeV, the ratio $\frac{y_{155}}{y_{156}}$ is above 99.9%. Thus, in the future, if the target enrichment level can be improved until 100%, proton production route is more advantageous than deuteron.

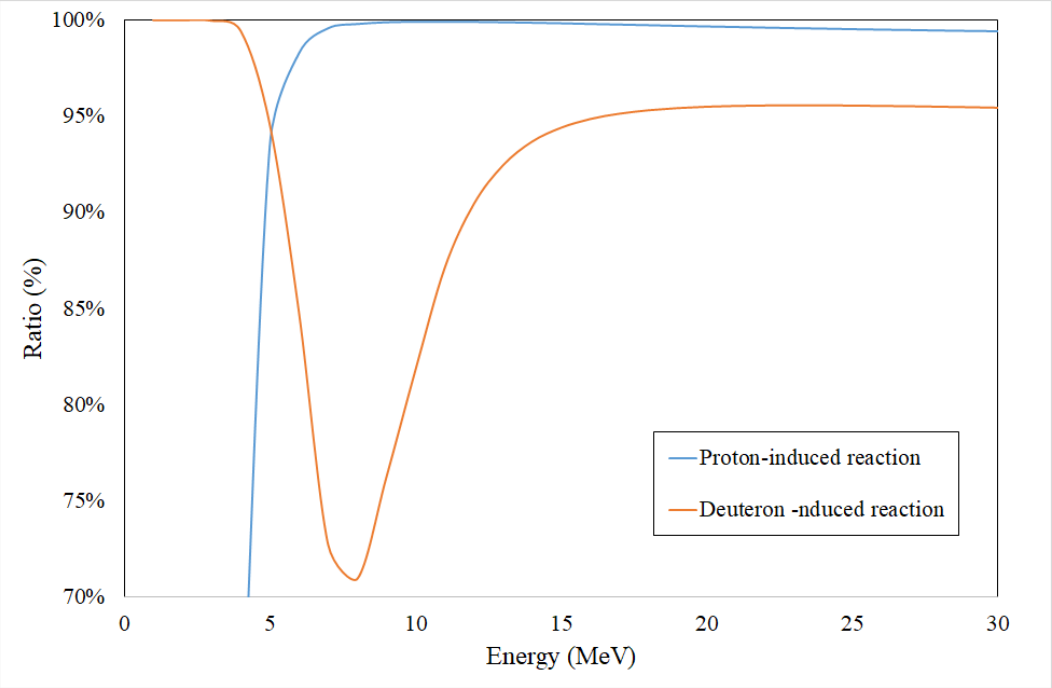


Fig. 4.37 The ratio of the $^{155}$Tb yield to the $^{156}$Tb yield as a function of energy.

#### 4.2.2.4. Future capsule conception

The experimental device presented in section 4.2.2.1 has many disadvantages. First, the size of the capsule does not match with the size of the target. Secondly, this capsule is not designed for high beam intensity. Therefore, another capsule design is considered to be used for future production. The capsule made of Nb will be used to wrap the pellet and the assembly will be laser welded. After irradiation, the perimeter of the capsule will be cut by a specific machine in a hot cell to open the capsule and get the pellet out of the target. Fig. 4.38 shows the same principle applied to a stainless steel welded capsule before (A) and after opening (B).

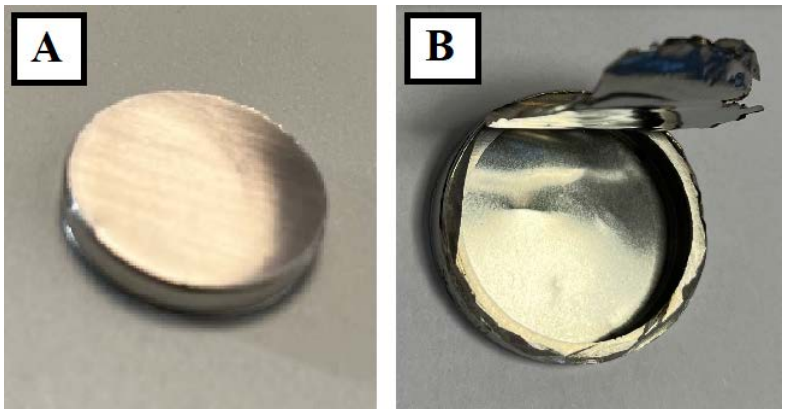


Fig. 4.38 Welded Nb capsule (A) and opened capsule (B).

To irradiate at high intensity, the capsule will be placed in a rabbit system that allow moving target to our high intensity irradiation station. (Fig. 4.39). This rabbit can be adapted to house different types of targets and allows efficient cooling. This kind of rabbit is commonly used at high intensity (150 µA).

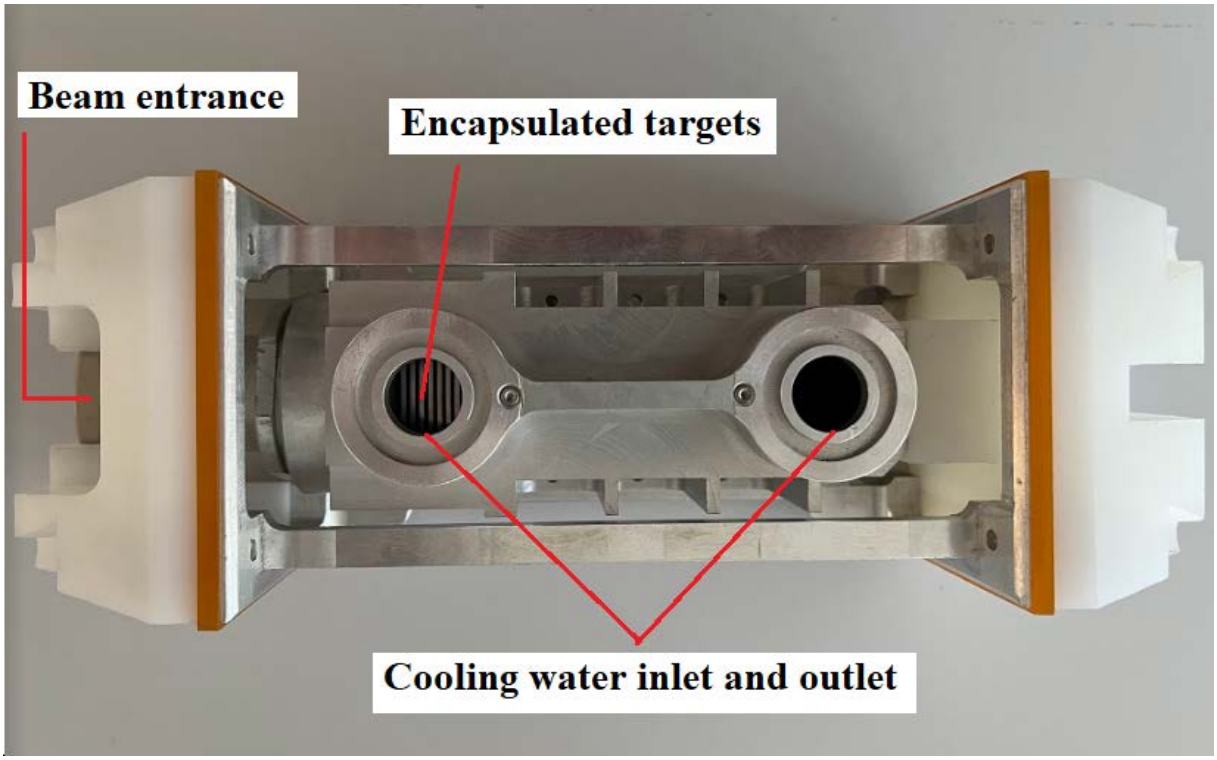


Fig. 4.39 Shuttle used for placing the encapsulated targets. The shuttle has two holes as inlet and outlet of cooling water.

## 4.3.Conclusion of the chapter

In this chapter, cross sections have been extracted from co-deposited $Gd_2O_3$ targets. First, experiments with $^{nat}Gd$ have been conducted to insure the feasibility of the measurements. A good overall agreement with existing data have been obtained. Then, cross section measurements have been conducted for enriched $^{155}Gd$. These are the first data available for such enriched material. Finally, a thick target yield measurement have been conducted using a thick target made of enriched $^{155}Gd_2O_3$. Results obtained for the pellet are in good agreement with cross section data showing that the whole process is under control and allowing to prepare irradiation with a new generation of dedicated capsule that can be accommodate in our high intensity target station.

# Conclusion

# 5. Summary and conclusion of this thesis

This thesis proposed an alternative route to produce Tb isotopes using enriched Gd solid targets and light charged particles. The production of $^{155}$Tb was taken as a study case. Thin and thick targets were both developed in this work for cross section measurement and mass production respectively.

The co-electrodeposition method was used to fabricate thin targets. Through this method, insoluble $Gd_2O_3$ particles were mechanically transported and physically embedded into a growing deposited metal layer. Nickel and Zinc were selected as the deposited metals at the beginning of the work. Using natural $Gd_2O_3$ powder, several parameters affecting experimental performance were investigated to determine optimal experimental conditions, such as the applied potential, the $Gd_2O_3$ loading quantity, the stirring speed, the temperature of the electrolyte, and the substrate roughness. For Ni-$Gd_2O_3$ targets, experiments showed that the optimal experiment condition was under -1.20 V/NHE, with as much as possible $Gd_2O_3$ powder, with a stirring speed of 300 rpm, at 30°C and deposited on a smooth gold substrate. In this condition, targets with a thickness of 10-20 µm were obtained within 60 min, The Gd content in the target was 3.0 ± 0.4 mg according to the ICP-AES results. SEM images showed that $Gd_2O_3$ particles were distributed uniformly on the surface of the deposit. Experiments also showed that the longitudinal distribution of particles along the thickness was not uniform, with more $Gd_2O_3$ particles on the surface than inside the deposit. However, this inhomogeneous distribution is at very small scales (tens of micrometers) and is negligible for the scale of the beam (1.0-1.5 cm). The reuse of $Gd_2O_3$ loadings was also investigated in this work, 1.0 g of powder was added to make 10 deposits, compared with adding 10 times of 0.1 g of powder to make 10 deposits, the reuse of 1.0 g of powder method can trap more Gd in the deposit. For Zn-$Gd_2O_3$ targets, the quality of the deposit was better under -1.52 V/NHE and with a stirring speed of 800 rpm. However, compared with Ni-$Gd_2O_3$ targets, Zn-$Gd_2O_3$ targets have adherence problem on the boundary because of dendrites. In addition, Ni is more advantageous for cross section measurement because it is a well-studied monitor, which can help to determine the target beam flux. Therefore, Ni-$Gd_2O_3$ target was finally chosen as the thin target used for cross section measurement.

The stacked-foils technique was used to measure the cross section. Before measuring the cross sections of $^{*}$Gd(d,x)Tb (where $^{*}$Gd represents enriched Gd), proof of concept experiments were performed firstly using natural Ni-$^{nat}Gd_2O_3$ targets. Eight Ni-$^{nat}Gd_2O_3$ composite targets were irradiated at GIP ARRONAX cyclotron facility with a deuteron beam on target ranging from 8-30 MeV during 30 or 60 min. The radionuclide of interest $^{155}$Tb, and other impurities, $^{153}$Tb, $^{154}$Tb, $^{156}$Tb, and $^{160}$Tb were detected and their excitation functions were investigated. The measured values of the production route $^{nat}$Gd(d,x)Tb were compared with existing data. The consistency of the measured values proved the reliability of the composite Ni-$Gd_2O_3$ targets. Then, the cross sections of *Gd(d,x)Tb were measured using 10 enriched composite Ni-$^{*}Gd_2O_3$ targets. Both $^{155}$Tb and $^{156}$Tb were detected in these 10 targets. The maximum cross section of $^{*}$Gd(d,x)$^{155}$Tb is 797.9 mb at 14.2 MeV while the maximum cross section of $^{*}$Gd(d,x)$^{156}$Tb is 83.1 mb at the same energy. Four of the ten targets had energies below 12.52 MeV (the threshold energy for $^{156}$Gd to produce $^{155}$Tb), which allowed to measure 4 cross section values of the reaction $^{155}$Gd(d,2n)$^{155}$Tb. Theoretically, the co-production of $^{153}$Tb or $^{154}$Tb is available when

energy is smaller than 13.16 MeV, however, these two radionuclides were only detected when energy of the target was higher than 19.4 MeV. Thanks to these excitation functions, the energy window for $^{155}$Tb production was chosen as 4-14 MeV. The production yields of $^{155}$Tb and $^{156}$Tb were estimated using the excitation functions of $^{155}$Tb and $^{156}$Tb. The thick target yield in the chosen energy window is 6.9 MBq/µAh. The maximum purity of $^{155}$Tb increases from 60% to 89% when energy increases from 9 MeV to 16 MeV.

In parallel, the fabrication of thick targets was investigated for mass production of $^{155}$Tb. The pelletizing technique was applied to manufacture thick targets. $Gd_2O_3$, $GdCl_3$ and $GdF_3$ were considered as candidate powder at first, but the latter two were eliminated because of hygroscopicity and insolubility respectively. Using natural $Gd_2O_3$ powder, the pressing pressure and the pelleting time were investigated to find the optimal conditions. The pressure was proven to have an effect on the integrity of the target leading to an optimal pressure of 600 bar. The pelleting time did not show any evident effect on target quality, therefore, the final pelleting time was fixed at 60 s. In these conditions, the average density of obtained pellet is 5.08 g/cm$^3$. This density is only 72% of theoretical density, which indicates the presence of voids in the target. SEM images confirmed the presence of voids on the surface and obtained images were similar for all pellets even if the thicknesses were different. However, these non-uniformities are negligible compared to the size of the beam. The temperature reached by the pellet was estimated using heat transfer equations. It has been found to be between 258°C to 267°C considering our cooling system and irradiation conditions. Our pellet was heated until 600°C in an oven; SEM results showed that the surface of the pellet did not change under high temperature, which indicated the good heat resistance of the pellet.

The study of natural $Gd_2O_3$ target demonstrated good quality of thick target using the pelletizing technique, thus, enriched $Gd_2O_3$ was used to make enriched target. As first test, 0.63 g of enriched $Gd_2O_3$ powder was compressed to make a pellet with a thickness of 0.39 mm and a diameter of 20 mm. This pellet was wrapped with two 10 µm thick aluminum foils and encapsulated in a stainless steel capsule. The target was irradiated by deuteron beam with an incident energy of (15.1 ± 1.5) MeV and an exit energy of (8.6 ± 0.8) MeV for 1 h. The beam intensity was (368 ± 26) nA. The measured production yield of $^{155}$Tb was 10.2 MBq/µAh while the production yield of $^{156}$Tb was 1.3 MBq/µAh. These results showed consistency with the estimated values obtained from cross section data, which were 10.1 MBq/µAh for $^{155}$Tb and 1.2 MBq/µAh for $^{156}$Tb. Compared with other production route, such as proton-induced reaction who has a production yield about 3 MBq/µAh, the deuteron-induced reaction triples the production yield. After 14 days of decay, the purity of $^{155}$Tb was 89%, this result agreed with estimated purity.

The dissolution of the pellet and the recycling of $Gd_2O_3$ powders were also investigated using natural $Gd_2O_3$. 100 mL of 2 mol/L of HCl was allowed to dissolve 1 g of $Gd_2O_3$ in 60 min with a stirring speed of 350 rpm and a temperature of 90°C. To recovery $Gd_2O_3$, 100 mL of 1 mol/L of oxalic acid was added to the solution to obtain the precipitation of $Gd_2(C_2O_4)_3 \cdot 10H_2O$. The precipitation was then heated until 800°C to transfer to $Gd_2O_3$. XRD analysis indicated that the crystal structure of the obtained powder was that of $Gd_2O_3$. Finally, the recovery rate reached to 84%.

This work involved various aspects of radioisotope production, including the fabrication and encapsulation of solid targets, measurement of excitation functions, estimation of production

yields, thick target production, dissolution of targets, and recovery of targets. On the one hand, this work is of great significance for the production of Tb radionuclides using low-and-medium-energy cyclotron facilities around the world. The cross section measurement gives the first experimental values of the reaction $^{155}$Gd(d,2n)$^{155}$Tb and *Gd(d,x)Tb, which not only can be used to evaluate production yields, but also has important implications for validating physical models of nuclear reactions and improving simulation models. On the other hand, the techniques developed in this work are useful for the production of other medical radionuclides. The co-electrodeposition method can be used to manufacture other thin targets, such as dysprosium (Dy) and neodymium (Nd), which have also a very negative reduction potential (-2.3 V/NHE for the two element). Dy target can be used to produce $^{166}$Ho, a potential candidate for $\beta^-$ therapy; and Nd target can be used to produced $^{153}$Sm, a $\beta^-$ emitter that can used for theranostics. This work also prove that the use of deuteron is a good way to produce radionuclide in cyclotrons. In the future, other medical radionuclides can also be produced by deuteron induced reactions, such as the $\beta^-$ emitter $^{67}$Cu (the relative reaction is $^{70}$Zn(d,x)$^{67}$Cu) [191].

However, several studies have to do to complete this work. First, limited by the supply in the market, the enrichment of $^{155}$Gd used in this work is only 92.8%. The presence of other Gd isotopes makes it difficult to measure the exact cross section of $^{155}$Gd(d,2n)$^{155}$Tb. Therefore, it will be interesting to repeat the cross section measurement using pure $^{155}$Gd targets. This kind of target may be available using electromagnetic isotope separator in the future. Secondly, this work only carried out one test of thick target irradiation, more experiments with different energy windows and with higher beam intensities need to be performed to validate the accuracy of the yield estimates and to optimize the experimental procedure. In order to withstand higher intensity and longer irradiation time, pure metal Gd targets need be developed, because metal targets have better thermal conductivity. Thirdly, as mentioned in chapter 4, the encapsulation system needs to be improved in order to better fit the target and get efficient cooling. A specific Nb capsule and a stainless steel target holder should be fabricated to encapsulate and place the target in the beam line. In addition, even though this work covers almost all aspects of radionuclide production of Tb, the extraction and purification of radionuclides have not been involved in this work. For future work, it is necessary to study the method to extract Tb from Gd, and to work on mass separation to see how to separate efficiently $^{155}$Gd and $^{156}$Gd.

## Appendix 2.1: Dissolution of $Gd_2O_3$ in acid solutions

The electrodeposition of Ni and Zn can be carried out both in acid and alkaline solutions. To determine the pH condition for the co-electrodeposition, a series of experiments on the dissolution of $Gd_2O_3$ with or without the presence of $NiSO_4$ and $ZnSO_4$ was carried out between pH 2 and pH 4. For each experiment, 10 g/L of $Gd_2O_3$ were added to the acid solutions (acidified with HCl or $H_2SO_4$) at 30°C. The experimental duration was 30 min, and the solution was stirred with a magnet at 800 rpm. The pH of the solution was measured before and after the process at 20°C. After the filtration with a 0.2 µm nylon filter, the solution were analyzed by ICP-AES to determine the concentration of Gd. The presence of Gd in the solution means that partial or total dissolution of the $Gd_2O_3$ powder has taken place. The difference in mass value before and after dissolution was calculated to obtain the dissolution rate. The pH changes and the dissolution rate in each solution are shown in Appendix Table 1.

Appendix Table 1 Dissolution of $Gd_2O_3$ in acid solutions

| Solution | Initial pH | Final pH | Dissolution rate (%) |
|---|---|---|---|
| 10 g/L $Gd_2O_3$ + HCl | 1.99 | 6.14 | 4.5% |
| 10 g/L $Gd_2O_3$ + $H_2SO_4$ | 1.97 | 6.32 | 4.5% |
| 10 g/L $Gd_2O_3$ +10 g/L $NiSO_4$ + $H_2SO_4$ | 2.01 | 6.84 | 11.8% |
| 10 g/L $Gd_2O_3$ +10 g/L $ZnSO_4$ + $H_2SO_4$ | 2.07 | 6.16 | 37.0% |
| 10 g/L $Gd_2O_3$ +10 g/L $NiSO_4$ + $H_2SO_4$ | 4.03 | 6.84 | 4.9% |
| 10 g/L $Gd_2O_3$ +10 g/L $ZnSO_4$ + $H_2SO_4$ | 3.99 | 6.16 | 29.6% |

According to Appendix Table 1, the final pH of each solution increased after 30 min, which means that $Gd_2O_3$ has been dissolved in all solutions. The reaction can be written as:

$$Gd_2O_3 + 6\,H^+ = 2\,Gd^{3+} + 3\,H_2 \qquad (eq.A2.1)$$

The solubility of $Gd_2O_3$ in HCl or $H_2SO_4$ solutions is similar: the pH of solutions increased from 2 to 6, the dissolution rate of Gd were about 4.5%. However, after adding zinc and nickel ions, the dissolution rate increased. The addition of zinc cations favored the dissolution of $Gd_2O_3$ significantly, the dissolution rate was 37% at pH 2 and 29.6% at pH 4. Meanwhile, these values were 11.8% at pH 2 and 4.9% at pH 4 with the addition of nickel cations.

In conclusion, $Gd_2O_3$ cannot be considered as inert particles in acid solutions because of the dissolution. Meanwhile, it has been experimentally proven that $Gd_2O_3$ is insoluble in alkaline solution. Therefore, in this work, alkaline solutions were chosen for co-electrodeposition.

## Appendix 2.2: Component of enriched $Gd_2O_3$

The enriched $Gd_2O_3$ powder bought from *Tracescience*[129] has a enrichment level of 92.8%, the isotopic composition is presented in *Appendix Table 2*.

Appendix Table 2 Isotopic composition of enriched $Gd_2O_3$.

| Isotope | $^{152}Gd$ | $^{154}Gd$ | $^{155}Gd$ | $^{156}Gd$ | $^{157}Gd$ | $^{158}Gd$ | $^{160}Gd$ |
|---|---|---|---|---|---|---|---|
| Enrichment (%) | - | - | 92.8 | 5.7 | 0.8 | 0.5 | 0.2 |

Other impurities are shown in Appendix Table 3. The data is provided by *Tracesciences international*[99].

Appendix Table 3 Chemical impurities in enriched $Gd_2O_3$ powder.

| Element | Symbol | Impurity measurement (ppm) |
|---|---|---|
| Aluminum | Al | < 40 |
| Calcium | Ca | 90 |
| Chromium | Cr | < 30 |
| Copper | Cu | < 10 |
| Dysprosium | Dy | < 400 |
| Erbium | Er | < 300 |
| Europium | Eu | < 400 |
| Iron | Fe | 20 |
| Potassium | K | 70 |
| Magnesium | Mg | 10 |
| Sodium | Na | 80 |
| Nickel | Ni | 30 |
| Neodymium | Nd | < 400 |
| Lead | Pb | 80 |
| Silicon | Si | 40 |
| Samarium | Sm | < 300 |
| Tin | Sn | < 30 |
| Terbium | Tb | < 800 |
| Ytterbium | Yb | < 800 |

## Appendix 2.3: SEM images for multilayer deposit

During the multilayer deposition, in order to investigate the changes of the deposit surface after each new deposited layer, five places of the deposit were marked and analyzed by SEM after performing each new layer. The results of each marked point are similar, and the SEM images of each layer at one point is shown in *Appendix Figure 1*. The number marked in the image refers to the layer number. Layer 1, 3, 5, and 7 are Ni-$Gd_2O_3$ composite layer while layer 2, 4, and 6 are Ni layer. The figure shows the effect of Ni layers on reducing the surface roughness of the deposit, while not all $Gd_2O_3$ were covered due to the short deposition time of the Ni layers.

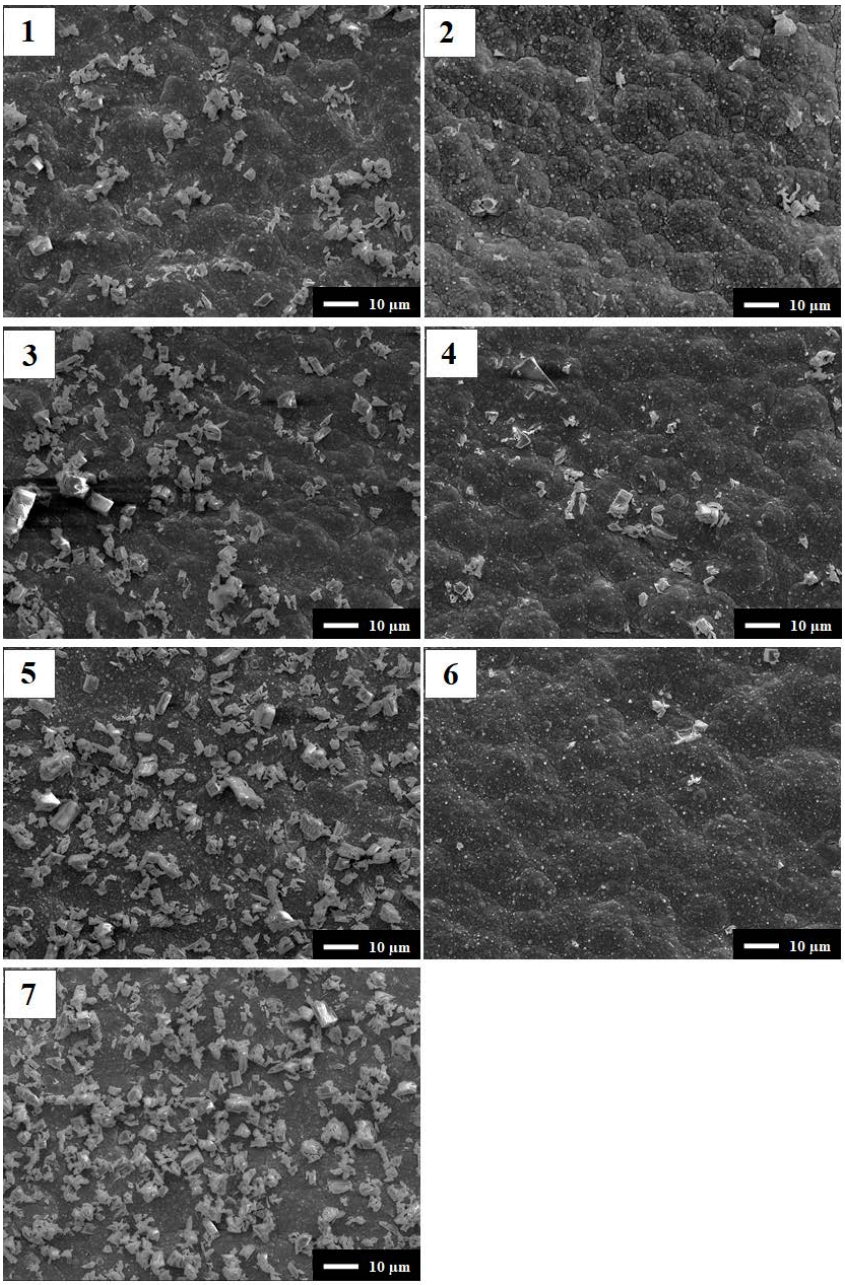


Appendix Figure 1 SEM images of each layer in the same place of a multilayer deposit. The number marked in the image refers to the layer number. Layer 1,3,5,7 are Ni-$Gd_2O_3$ composite layers while layer 2, 4, and 6 are Ni layers.

## Appendix 2.4: EDX analysis of Ni-$Gd_2O_3$ deposit under -1.30 V/NHE

To investigate the distribution of $Gd_2O_3$ particles on the surface of the deposit, the same place of the deposit shown in Fig. 2.11 (h) were magnified 5000 times and studied by EDX. The result is presented in *Appendix Figure 2*. It can be seen that the peaks of Gd are evident compared to the peaks of Ni. The quantification shows that there are almost 70% of Gd atoms in this place while the atomic percentage of Ni is only about 20%. From this, it can be inferred that $Gd_2O_3$ particles were mainly accumulated in the craters.

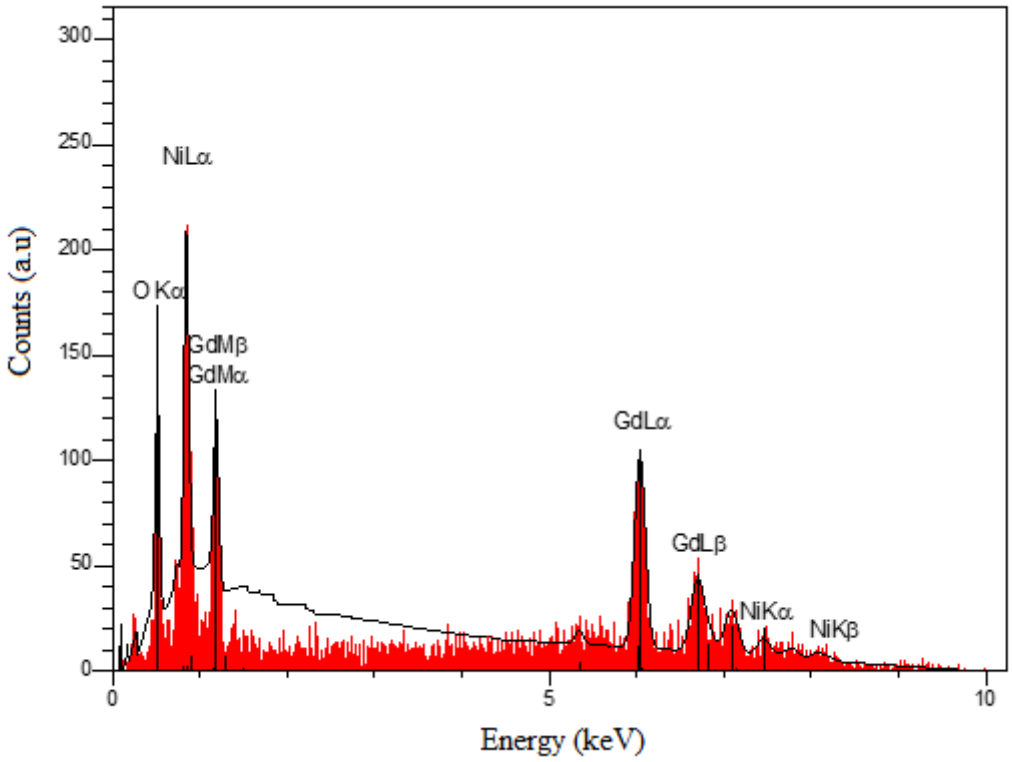


Appendix Figure 2 EDX analysis of the chemical composition of the deposit shown in Fig. 2.11(h). Applied potential was -1.30 V/NHE, stirring speed was 300 rpm, $Gd_2O_3$ loading was 6.5g, $Ni^{2+}$ concentration was 0.14 mol/L, pH = 9.8.

Here, different KLM lines are shown in the spectrum. The name of these lines are defined according to their shell in which the initial vacancy occurs, and the notion α, β and γ depends on whether the electron filling the vacancy comes from an adjacent shell, two shells apart, or three shells apart. For example, if the vacancy occurs in L shell, and the electron filling the vacancy comes from the M shell, this line is named as Lα. The most commonly appeared lines are shown in *Appendix Figure 3* [206].

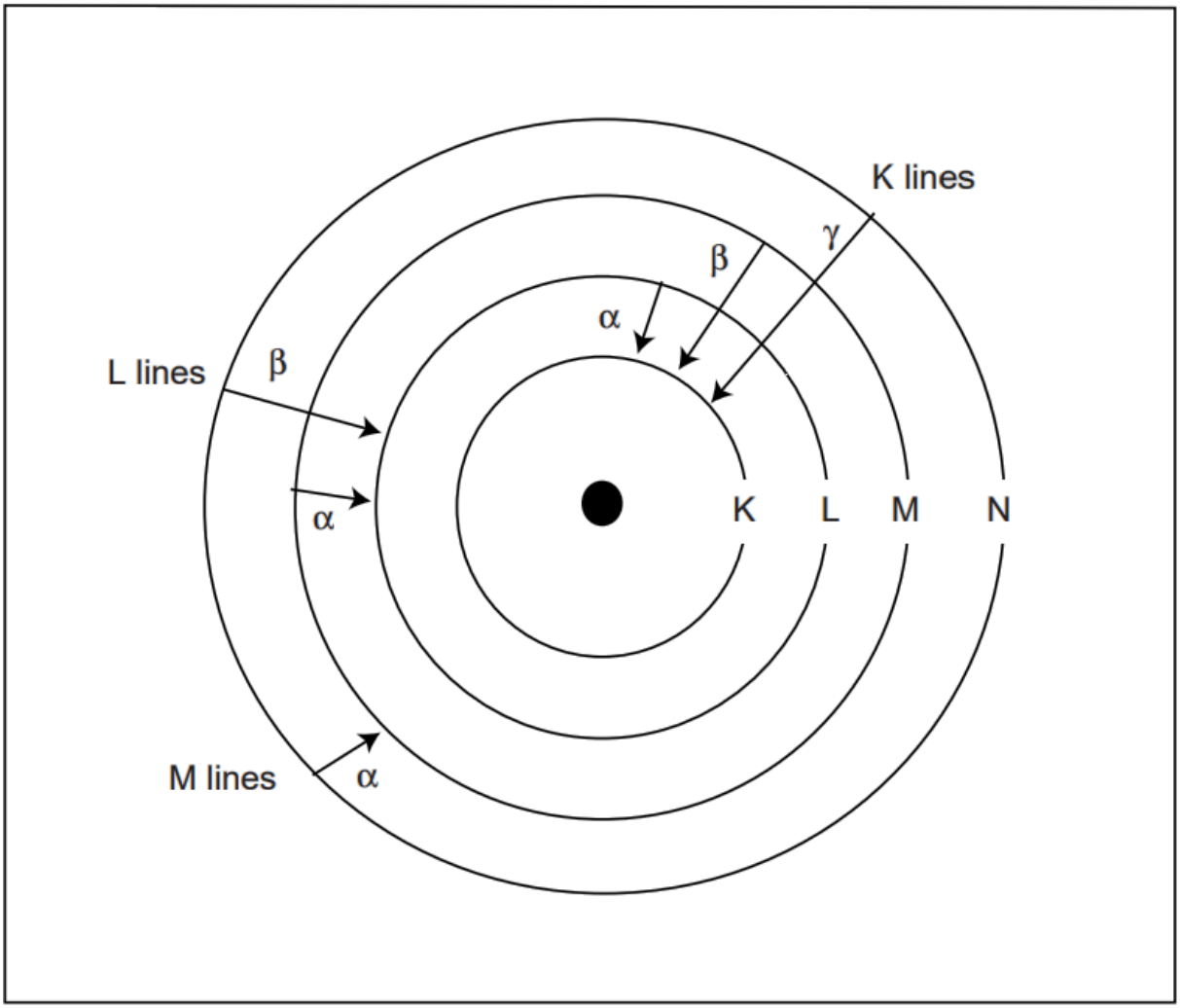


Appendix Figure 3 Some typical line types in EDX spectrum [206].

## Appendix 3.1: Experimental procedures to produce $GdCl_3$ and $GdF_3$

To produce $GdCl_3$, the diluted 2 mol/L of HCl were used to dissolve $Gd_2O_3$ and generate $GdCl_3$. After the $Gd_2O_3$ was completely dissolved, the solution was heated to evaporate the water and excess HCl. After multiple rinsing and evaporation, the $GdCl_3$ solid was obtained. The final powder is obtained by grinding the solids and sifting through a 120 mesh sieve. The experimental procedures are shown in *Appendix Figure 4*.

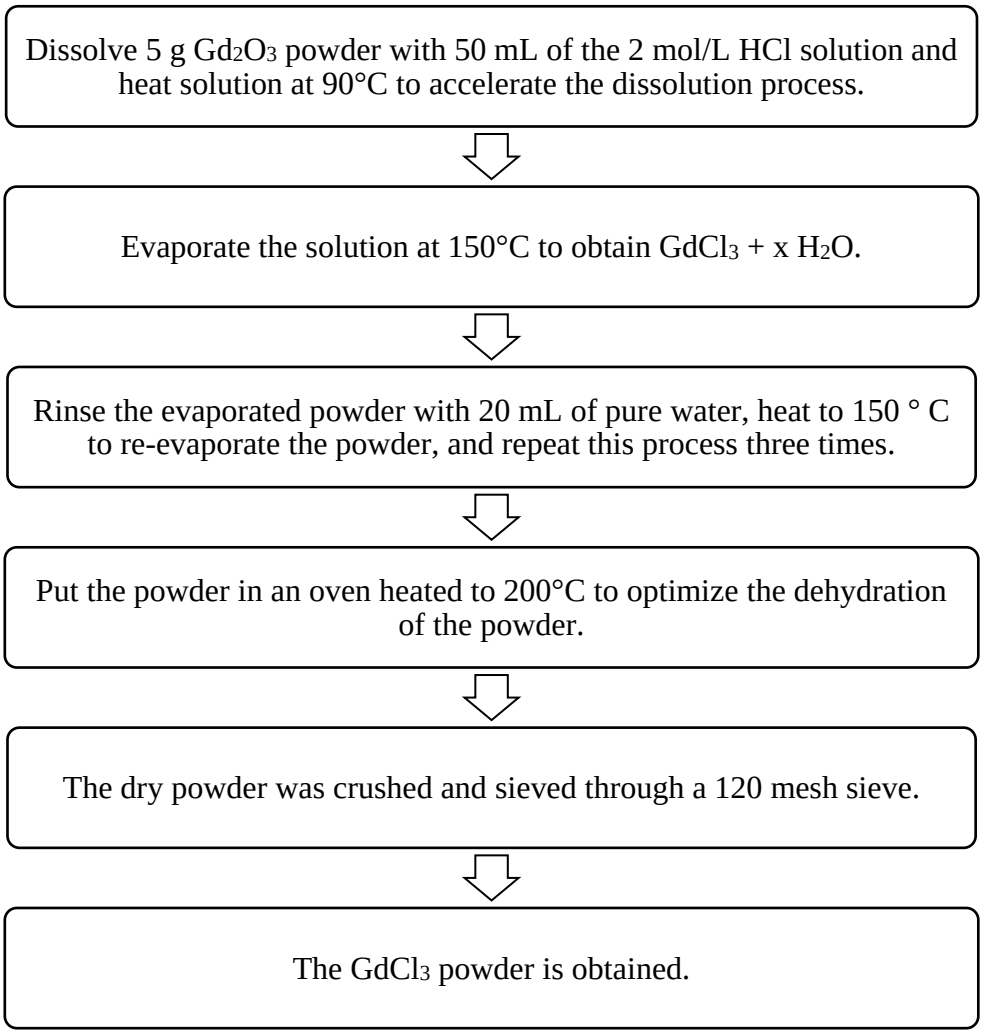


Appendix Figure 4 Experimental procedures to obtain $GdCl_3$ powder from $Gd_2O_3$ powder.

To produce $GdF_3$, the diluted 2 mol/L of HCl were used to dissolve $Gd_2O_3$ and pure water was used to dissolve the $NH_4F$. The two dissolved solutions were mixed together to generate $GdF_3$ precipitation. After the $GdF_3$ was completely precipitated, the precipitation was rinsed with pure water 3 times in order to eliminate $NH_4Cl$ and HCl or HF acids. After multiple rinsing, the precipitation was put in the oven to dry. The final powder is obtained by grinding the solids and sifting through a 120 mesh sieve. The experimental procedures are shown in *Appendix Figure 5*.

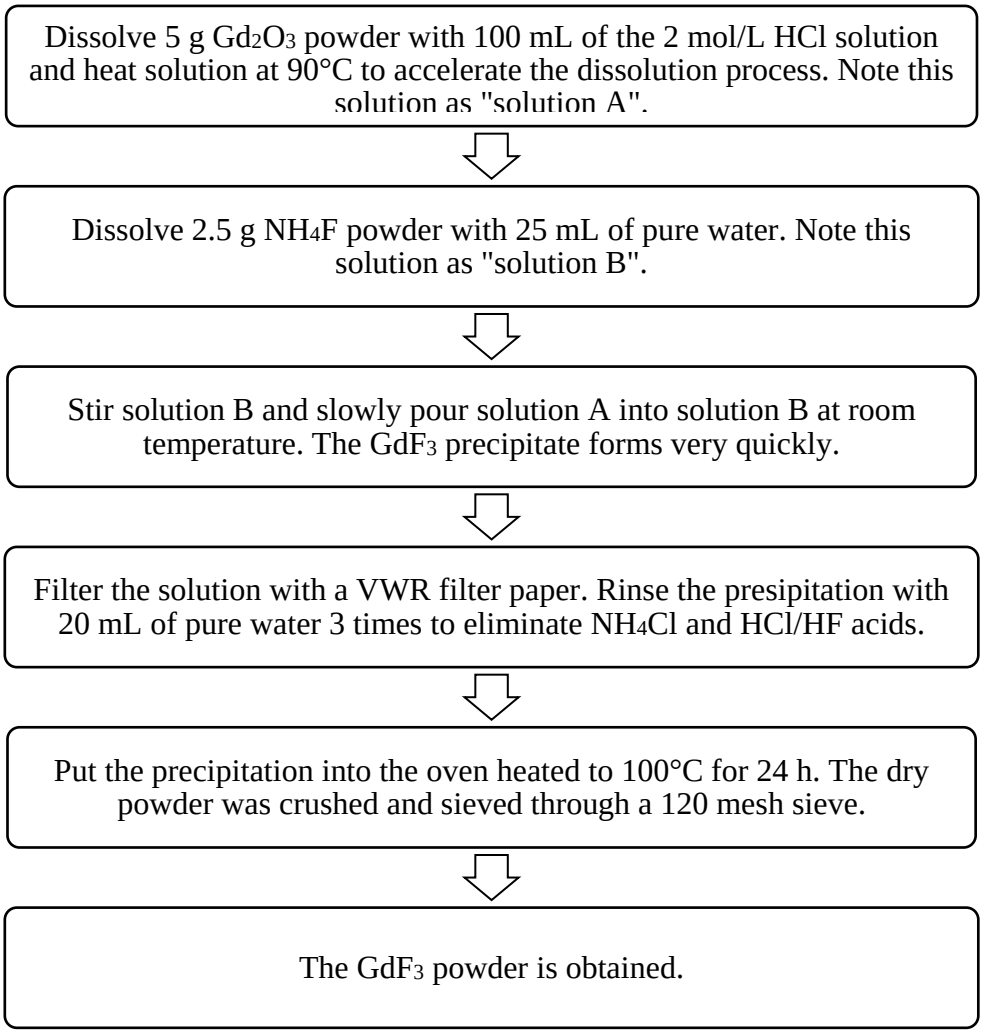


Appendix Figure 5 Experimental procedures to obtain $GdF_3$ powder from $Gd_2O_3$ powder.

## Appendix 3.2: Heat transfer calculation in the target

The heat transfer in a targetry system can be considered as a classical model in heat transfer problem: the heat transfer through multi-layer walls. *Appendix Figure 6* presents the "multi-layer walls" model: multiple layers are placed together in parallel, with heat flow from left to right. $X_i$ (i=0,1,2,…,n+1) represents the boundary of each component of the encapsulated pellet in the lateral direction, $T_i$ (i=0,1,2,…,n+1) is the temperature of the $X_i$. The generated energy per volume, the thickness, and the thermal conductivity of layey-i is noted as $P_i$, $\lambda_i$, and $e_i$, (i=0,1,2,…,n+1), respectively. On the two sides of the multi-layer walls, water is used as coolant with a flow $h_c$.

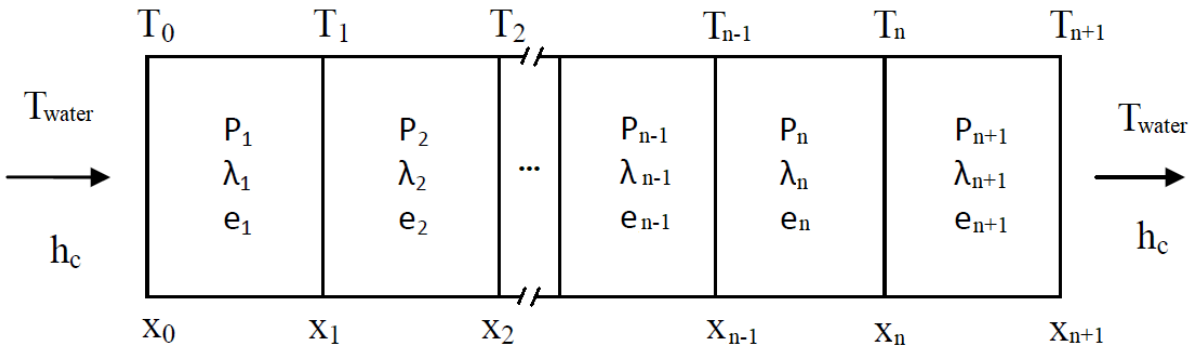


Appendix Figure 6"Multi-layer walls" model in heat transfer problem. $X_i$ (i=0,1,2,…,n+1) represents the boundary of each component of the encapsulated pellet in the lateral direction, $T_i$ (i=0,1,2,…,n+1) is the temperature of the $X_i$. The generated energy per volume, the thickness, and the thermal conductivity of layey-i is noted as $P_i$, $\lambda_i$, and $e_i$, (i=1,2,…,n+1), respectively.

As explained in subsection 3.1.3.4, for a steady-state targetry system, if each layer is isotopic and homogenous, the temperature T and the generated heat P has a relation written as *eq.3.8*:

$$\lambda \frac{\partial^2 T}{\partial^2 x} + P = 0 \qquad (eq.3.8)$$

The solution of *eq.3.8* can be expressed as:

$$T(x) = -\frac{P_n}{2\lambda_n} x^2 + A\,x + B \qquad (eq.A3.1)$$

With A and B two constants.
Using the Fourier's law, the heat flux can be expressed as:

$$\varphi(x) = -\lambda\left(\frac{dT}{dx}\right) = P_n x - \lambda A \qquad (eq.A3.2)$$

Since *eq.A3.1* is valid everywhere in the walls, so on the surface $X_n$ and $X_{n-1}$, *eq.A3.3* and *eq.A3.4* can be deduced:

$$T(x_n) = T_n = -\frac{P_n}{2\lambda_n} x_n^2 + A' x_n + B' \qquad (eq.A3.3)$$

$$T(x_{n-1}) = T_{n-1} = -\frac{P_n}{2\lambda_n} x_{n-1}^2 + A' x_{n-1} + B' \qquad (eq.A3.4)$$

And the expression of $A'$ can be obtained using *eq.A3.3* and *eq.A3.4*:

$$A' = \frac{(T_n - T_{n-1})}{(x_n - x_{n-1})} + \frac{P_n}{2\lambda_n}((x_n + x_{n-1}) \qquad (eq.A3.5)$$

It should be noted that:

$$x_n - x_{n-1} = e_n \qquad (eq.A3.6)$$

$$x_n + x_{n-1} = e_n + 2\sum_{n-1} e_{n-1} \qquad (eq.A3.7)$$

The heat flux on the left side of the surface $X_n$ can be therefore expressed as *eq.A3.8* (except for the surface $X_0$):

$$[\varphi(X_n)]_L = \frac{1}{2} P_n e_n + \frac{\lambda_n}{e_n}(T_{n-1} - T_n) \qquad (eq.A3.8)$$

In the same way, the heat flux of the right side of the surface $X_n$ can be expressed by using $T(X_i)$ and $T(X_{i+1})$, and the formula is as *eq.A3.9* (except for the surface $X_{n+1}$):

$$[\varphi_n(x_n)]_R = -\frac{1}{2} P_{n+1} e_{n+1} + \frac{\lambda_n}{e_n}(T_n - T_{n+1}) \qquad (eq.A3.9)$$

For the first surface $X_0$ and the last surface $X_{n+1}$, the convection heat flux (left side) equals to the conduction heat flux (right side), so *eq.A3.10* and *eq.A3.11* can be deduced:

$$[\varphi(X_0)]_L = h_w (T_{water} - T_0) = [\varphi(X_0)]_R \qquad (eq.A3.10)$$

$$[\varphi(X_5)]_L = [\varphi(X_5)]_R = h_w (T_5 - T_{water}) \qquad (eq.A3.11)$$

Where $h_w$ ($W \cdot m^{-1} \cdot K^{-2}$) is the water flow, and $T_{water}$ (K) is the water temperature.
Therefore,

$$T_0 = b_1 T_1 + \frac{1}{2\left(\frac{\lambda_1}{e_1} + h_c\right)} \alpha_1 + \frac{h_c}{\left(\frac{\lambda_1}{e_1} + h_c\right)} T_{water} \qquad (eq.A3.12)$$

With

$$H_{c1} = \frac{h_c}{a_1}; a_1 = \frac{\lambda_1}{e_1} + h_c;\ b_1 = \frac{\lambda_1}{e_1 a_1};\ \alpha_1 = p_i e_i \qquad (eq.A3.13)$$

For the other surface $X_i$ (i=1,2…n), the heat flux is also conserved on both sides same surface, combining *eq.A3.8* and *eq.A3.9*, it can be deduced that:

$$T_i = b_{i+1} T_{i+1} + \frac{1}{2a_{i+1}} D_i + H_{c(i+1)} T_{water}\ (i = 0,1, \ldots n) \qquad (eq.A3.14)$$

With

$b_n = \frac{\lambda_n}{e_n a_n}; \alpha_n = P_n e_n; \beta_n = \alpha_n b_n$

$H_{c(n)} = H_{c(n-1)} \frac{\lambda_{n-1}}{e_{n-1} a_n}; a_n = -\frac{\lambda_{n-1} b_{n-1}}{e_{n-1}} + \frac{\lambda_{n-1}}{e_{n-1}} + \frac{\lambda_n}{e_n}$

$\mathrm{D}_1 = \alpha_1 + \alpha_2 + \beta_1$

$\mathrm{D}_2 = \alpha_2 + \alpha_3 + \beta_2 + \alpha_1 b_2 + \beta_1 b_2$

$\mathrm{D}_3 = \alpha_3 + \alpha_4 + \beta_3 + \alpha_2 b_3 + \beta_2 b_3 + \alpha_1 b_2 b_3 + \beta_1 b_2 b_3$

$\mathrm{D}_4 = \alpha_4 + \alpha_5 + \beta_4 + \alpha_3 b_4 + \beta_3 b_4 + \alpha_2 b_3 b_4 + \beta_2 b_3 b_4 + \alpha_1 b_2 b_3 b_4 + \beta_1 b_2 b_3 b_4$

$\mathrm{D}_5 = \alpha_5 + \alpha_6 + \beta_5 + \alpha_4 b_5 + \beta_4 b_5 + \alpha_3 b_4 b_5 + \beta_3 b_4 b_5 + \alpha_2 b_3 b_4 b_5 + \beta_2 b_3 b_4 b_5 + \alpha_1 b_2 b_3 b_4 b_5 + \beta_1 b_2 b_3 b_4 b_5$

D6=… and so on.

For the last surface,

$$T_{n+1} = \frac{1}{2m_{n+1}} \mathrm{K}_{n+1} - \left(\frac{h_c}{m_{n+1}} + \frac{\lambda_{n+1}}{e_{n+1} m_{n+1}} H_{cn+1}\right) T_{water} \qquad (eq. A3.15)$$

Wit

$$m_{n+1} = \left(-\frac{\lambda_{n+1} b_{n+1}}{e_{n+1}} + \frac{\lambda_{n+1}}{e_{n+1}} + h_c\right); \; K_{n+1} = D_{n+1} - \alpha_{n+2} \qquad (eq. A3.15)$$

## Appendix 4.1 Ti and Ni Monitor reactions

Ti and Ni are both well studied monitors since their reaction cross sections have been measured by several researchers[3,4,24–26].

For natural titanium, the main productions of the deuteron induced reactions are $^{44g}$Sc, $^{44m}$Sc, $^{46}$Sc, $^{47}$Sc, $^{48}$Sc, $^{47}$V, $^{48}$V and $^{51}$Ti. Among them, two radionuclides are of particular interest, $^{48}$V and $^{48}$Sc. Information associated to these two radionuclides are presented in *Appendix Table 4*. $^{48}$V can be characterized by the gamma energiy $E_\gamma$ = 983.525 keV with an intensity of 99.98%. However, there will have interference cause by $^{48}$Sc for since it has also a gamma energy $E_\gamma$ = 983.526 keV with an intensity of 100%. Since the half-life of $^{48}$Sc is only 43.67 h, in order to eliminate its interference, the data acquisition of $^{48}$V should be carried out after the complete decay of $^{48}$Sc. According to Nigron et al[191], 19 days after the EOB is most of the time enough to get enough $^{48}$Sc decay (more than 10 $T_{1/2}$ of $^{48}$Sc).

Appendix Table 4 Decay data of $^{48}$V and $^{48}$Sc[8].

| Radionuclide | Half-life $T_{1/2}$ | $E_\gamma$ (keV) | $I_\gamma$ (%) |
|---|---|---|---|
| $^{48}$V | 15.9735 d | 944.129 | 7.870 |
| | | 983.525 | 99.98 |
| | | 1312.105 | 98.2 |
| $^{48}$Sc | 43.67 h | 175.361 | 7.47 |
| | | 983.526 | 100 |
| | | 1037.522 | 97.5 |
| | | 1312.120 | 100 |

In this work, the reaction $^{nat}$Ti(d, x)$^{48}$V used was referred to the data of IAEA Monitor Reactions 2017[121]. The cross sections for the reaction is shown in *Appendix Figure 7*. The cross section has been measured from 1 MeV to 50 MeV, the maximum value (320 mb) appears at 18.5 MeV. Between 12-22 MeV, the estimated uncertainties are relatively big (± 40 mb), and the difference between measurement values is obvious in this energy range. This indicates that the error of calculation is relative large when we calculate the number of the projectiles per second I′ with this data in this energy range.

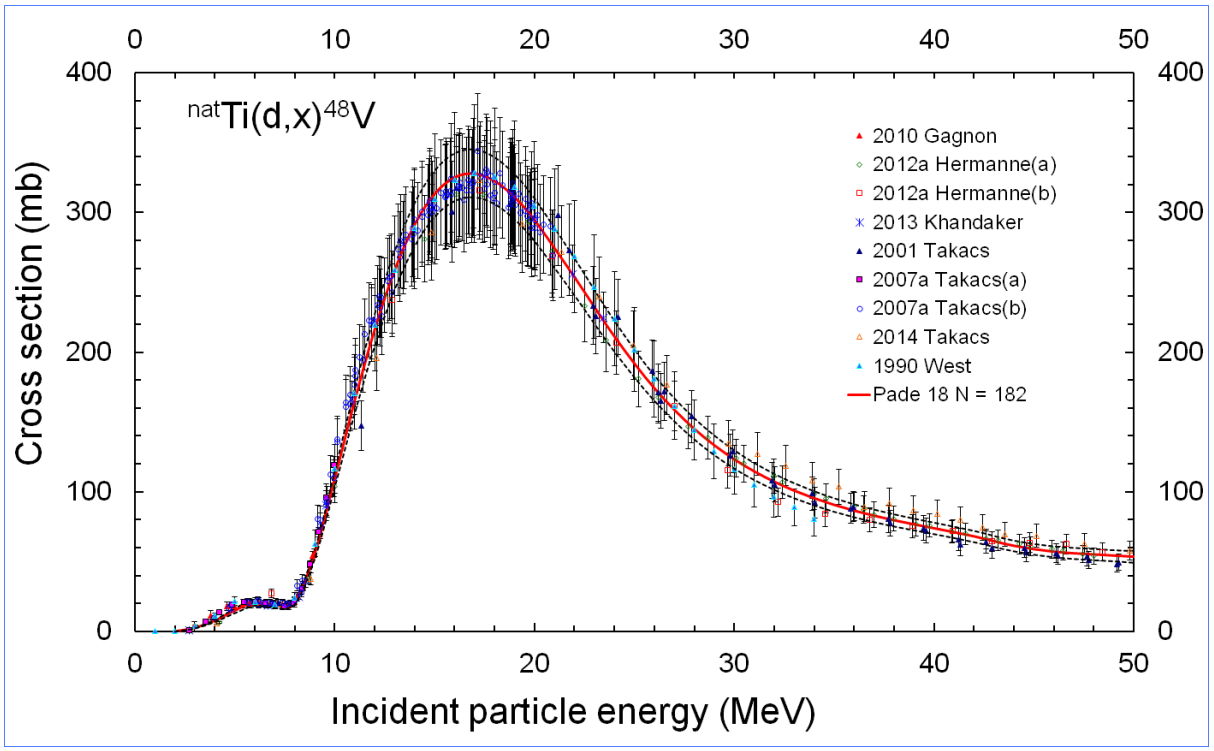


Appendix Figure 7 Activation cross section data of the $^{nat}$Ti(d, x)$^{48}$V reaction with estimated uncertainties, figure made by Hermanne et al[121].

For natural nickel monitors, the main radionuclides produced by deuteron induced reactions are $^{56}$Ni, $^{57}$Ni, $^{55}$Co, $^{56}$Co, $^{57}$Co, $^{58(m)}$Co, $^{52}$Mn, $^{54}$Mn and $^{51}$Cr. Among them, $^{58(m)}$Co was used to measure the number of the projectiles per second of the beam, the reaction involved is $^{nat}$Ni(d, x)$^{58(m)}$Co. The gamma line $E_\gamma$ = 810.7593 keV was used to characterize $^{58(m)}$Co, but there is an interference from $^{56}$Ni (see *Appendix Table 5*). To eliminate the contribution of $^{56}$Ni, the data acquisition of $^{58(m)}$Co has been carried out 2 months after EOB[125] to let enough decay time.

Appendix Table 5 Decay information of $^{58g}$Co and $^{56}$Ni[8].

| Radionuclide | Half-life $T_{1/2}$ | $E_\gamma$ (keV) | $I_\gamma$ (%) |
|---|---|---|---|
| $^{58g}$Co | 70.86 d | 810.7593 | 99.450 |
| $^{56}$Ni | 6.075 d | 158.38 | 98.8 |
| | | 811.85 | 86 |

In this work, the cross sections of $^{nat}$Ni(d, x)$^{58(m)}$Co was referred to the data of IAEA Monitor Reactions 2017[121]. The activation cross sections are shown in *Appendix Figure 8*. As shown in the figure, the cross section has been measured from 3 MeV to 50 MeV, and the maximum value (240 mb) appears at 18.0 MeV. Between 15-25 MeV, the estimated uncertainties are relatively big (± 20 mb), and the difference between measurement values is obvious in this energy range. Compared with the activation cross sections curve of the reaction $^{nat}$Ti(d, x)$^{48}$V (*Appendix Figure 7*), the uncertainty is smaller at 12-15 MeV and bigger at 22-25 MeV. In order to minimize the calculation error caused by uncertainties reaction cross sections, an average value I″ of the number of the projectiles per second I′ calculated by the two monitors was used to estimate the particle flux.

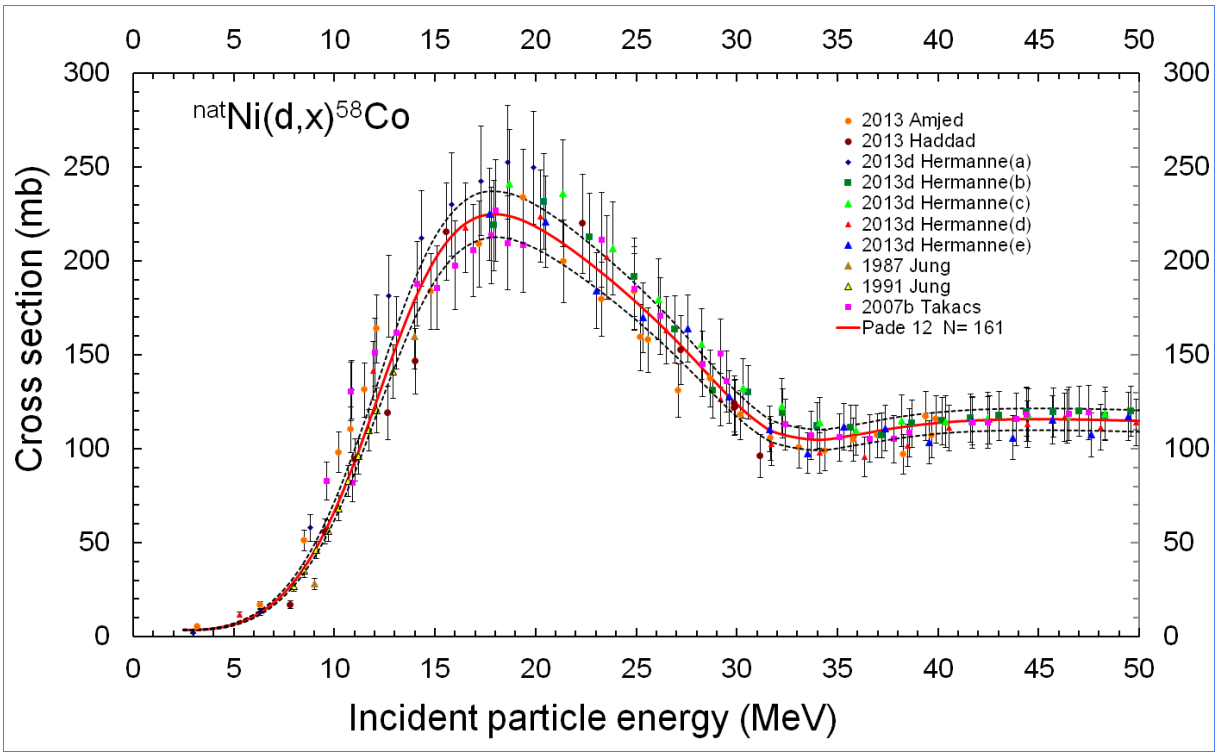


Appendix Figure 8 Activation cross section data of the $^{nat}Ni(d, x)^{58(m)}Co$ reaction with estimated uncertainties, figure made by Hermanne et al[121].

## Appendix 4.2 Energy and efficiency calibration of gamma detector

In this work, solid samples (nickel and aluminum foils) were counted at 19 cm from the detector, and liquid samples (dissolved targets) were counted at 0 cm from the detector in a 5mL geometry. Before counting, two standard sources, solid source $^{152}$Eu and the liquid source SG05, with the same geometries of solid samples and liquid samples, were used for energy and efficiency calibration.

The radioisotope $^{152}$Eu ($T_{1/2}$ = 13.517 y) has been used as an energy calibration source for a long time[210,211]. The chosen gamma energies and intensities are shown in *Appendix Table 6*.

Appendix Table 6 Chosen gamma energies and intensities emitted by $^{152}$Eu for energy and efficiency calibration.

| Gamma energy Eγ (keV) | Intensity (%) |
|---|---|
| 121.8 | 28.6 |
| 244.7 | 7.6 |
| 344.3 | 26.5 |
| 411.1 | 2.2 |
| 444.0 | 3.1 |
| 778.9 | 12.9 |
| 867.4 | 4.2 |
| 964.1 | 14.6 |
| 1085.9 | 10.2 |
| 1112.1 | 13.6 |
| 1212.9 | 1.4 |
| 1299.1 | 1.6 |
| 1408.0 | 21.0 |

The energy calibration was carried out on 6$^{th}$ July 2021. Using *eq.4.5*, the values of a and b were obtained: a = 0.12024 and b = 0.39511.

The efficiency of the detector for solid target at 19 cm above the detector was also obtained by $^{152}$Eu solid source. The efficiency curve as a function of gamma energy is shown in *Appendix Figure 9*.

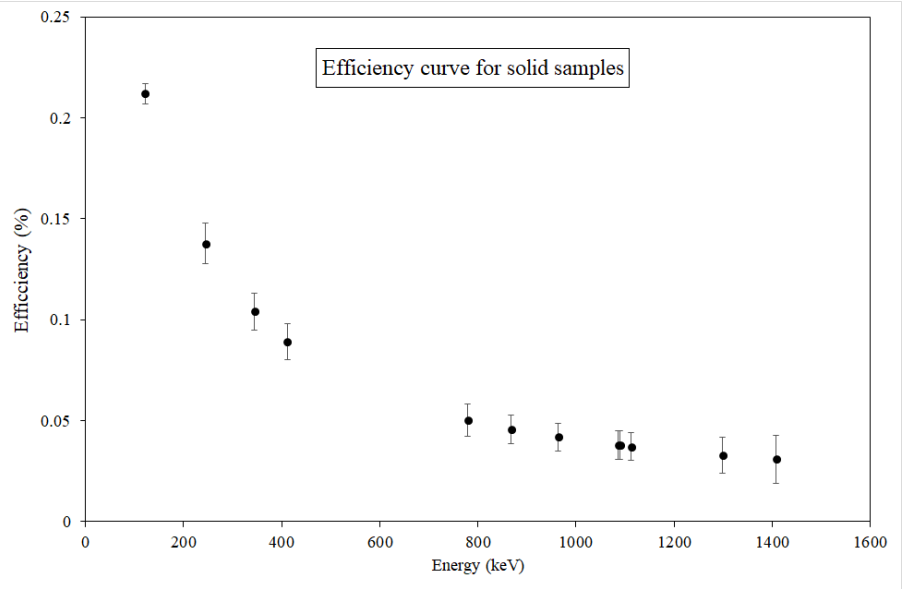


Appendix Figure 9 Efficiency curve for solid samples using $^{152}$Eu solid source at 19 cm above the detector.

The liquid source named SG05 was prepared by GIP ARRONAX. The radionuclides contained in the source and their half-lives and activities (on 1$^{st}$ January 2021) are shown in *Appendix Table 7*.

Appendix Table 7 Radionuclides informations contained in SG05 liquid source

| Radionuclides | Half-life | Activity (Bq) |
|---|---|---|
| $^{210}$Pb | 138.3763 d | 7630 |
| $^{241}$Am | 432.6 y | 588 |
| $^{109}$Gd | 461.4 d | 8295 |
| $^{57}$Co | 271.80 d | 188 |
| $^{139}$Ce | 137.641 d | 284 |
| $^{203}$Hg | 46.594 d | 584 |
| $^{113}$Sn | 115.09 d | 487 |
| $^{85}$Sr | 64.850 d | 597 |
| $^{137}$Cs | 30.05 y | 239 |
| $^{88}$Y | 106.626 d | 791 |
| $^{60}$Co | 5.2711 y | 379 |

The chosen gamma energies and intensities of each radionuclide are shown in *Appendix Table 8*.

Appendix Table 8 Chosen gamma energies and intensities emitted by SG05 multi-gamma source for energy and efficiency calibration.

| Radionuclides | Chosen gamma energy (keV) | Intensity (%) |
|---|---|---|
| $^{210}$Pb | 46.5 | 4.3 |
| $^{241}$Am | 57.9 | 0.01 |
| $^{109}$Gd | 88.0 | 3.6 |
| $^{57}$Co | 122.1 | 85.6 |
| $^{139}$Ce | 165.9 | 80.0 |
| $^{203}$Hg | 279.2 | 81.0 |
| $^{113}$Sn | 391.7 | 64.0 |
| $^{85}$Sr | 514.0 | 96.0 |
| $^{137}$Cs | 661.7 | 85.1 |
| $^{88}$Y | 988.0 | 93.7 |
| | 1836.1 | 99.2 |
| $^{60}$Co | 1173.2 | 100.0 |
| | 1332.5 | 100.0 |

The energy calibration was carried out on 18$^{th}$ Mars 2021. Using *eq.4.5*, the values of A and B were obtenu: A = 0.12026 and B = 0.34410.

The efficiency curve of the detector for liquid samples at 0 cm using SG05 liquid source is shown in *Appendix Figure 10*.

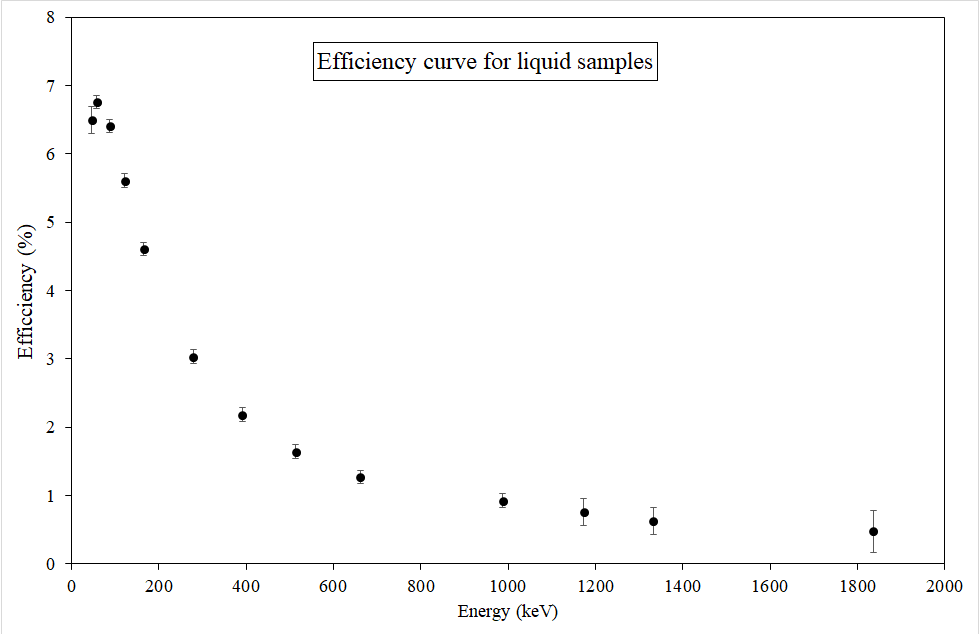


Appendix Figure 10 Efficiency curve for solid samples using SO05 liquid source at 0 cm above the detector.

Although these energy calibrations were performed only once, according to the study of Nigron et al.[212] on the same detector, the changes in the parameters A and B of the energy calibration

during the one year are very small. A metrological follow-up attached on the detectors also shows that there are no deviations

## Appendix 4.3 Activities of radionuclides in a decay chain

Some radionuclides decay more than one step to transform into stable atoms, this process produces several radionuclides as decay products. The series of these decay products is called a decay chain. The Bateman equation can be applied to determine the activity of each radionuclide in the decay chain.

For a decay chain of 3 radionuclides A, B, and C and a stable element D, there are 3 steps of decay: A decays to B with a branching radio $BR_A$, B decays to C with a branching radio $BR_C$, and C decays to D with a branching radio $BR_C$. The decay constants of A, B, and C are $\lambda_A$, $\lambda_B$, and $\lambda_C$, respectively.

We need to solve the following system of differential equations:

$$\frac{dN_A(t)}{dt} = -\lambda_A N_A(t) \qquad (eq.A4.1)$$

$$\frac{dN_B(t)}{dt} = \lambda_A N_A(t) \cdot \mathrm{BR_A} - \lambda_B N_B(t) \qquad (eq.A4.2)$$

$$\frac{dN_C(t)}{dt} = \lambda_B N_B(t) \cdot \mathrm{BR_B} - \lambda_C N_C(t) \qquad (eq.A4.3)$$

$$\frac{dN_D(t)}{dt} = \lambda_C N_C(t).BR_C \qquad (eq.A4.3)$$

For radionuclide A, it can be deduced that

$$N_A(t) = N_{A0} e^{-\lambda_A t} \qquad (eq.A4.4)$$

With $N_{A0}$ the atom number at t = 0.

Combining *eq.A4.2* and *eq.A4.4*, it can be obtained that:

$$\frac{dN_B(t)}{dt} = \lambda_A N_{A_0} e^{-\lambda_1 \cdot t} \cdot \mathrm{BR_A} - \lambda_B N_B(t) \qquad (eq.A4.5)$$

This is a first-order linear inhomogeneous differential equation that can be simplified as *eq.A4.6*:

$$\frac{dN_B(t)}{dt} = p(t)N_B(t) + f(t) \qquad (eq.A4.6)$$

With

$$p(t) = -\lambda_B \qquad (eq.A4.7)$$

$$f(t) = \lambda_A N_A e^{-\lambda_A t} \cdot \mathrm{BR_A} \qquad (eq.A4.8)$$

The general solution of this differential equation can be expressed as:

$$N_B(t) = \mathrm{K}e^{P(t)} + v(t)e^{P(t)} \qquad (eq.A4.9)$$

With K a constant, P(t) an antiderivative of p(t) and $v'(t) = e^{-P(t)}f(t)$.

So $N_B(t)$ can be finally obtained:

$$N_B(t) = \frac{\lambda_A}{\lambda_B - \lambda_A} N_{A0} e^{-\lambda_A t} \cdot \mathrm{BR_A} + K e^{-\lambda_B t} \qquad (eq.A4.10)$$

If the number of B atoms is noted as $N_{B0}$ at t = 0, *eq.A4.11* can be written as:

$$N_B(t) = \frac{\lambda_A}{\lambda_B - \lambda_A} N_{\mathrm{A0}}\left(e^{-\lambda_A t} - e^{-\lambda_B t}\right)\mathrm{BR_A} + N_{\mathrm{B0}} e^{-\lambda_B t} \qquad (eq.A4.11)$$

Using eq.A4.11 and multiply both sides of the equation by $e^{\lambda_c t}$, *eq.A4.3* can be expressed as:

$$\frac{dN_C(t)}{dt} e^{\lambda_c t} + \lambda_C N_C(t) e^{\lambda_c t} = e^{\lambda_c t} \lambda_B \mathrm{BR_B}(t) \left(\frac{\lambda_A}{\lambda_B - \lambda_A} N_{\mathrm{A0}}\left(e^{-\lambda_A t} - e^{-\lambda_B t}\right)\mathrm{BR_A} + N_{\mathrm{B0}} e^{-\lambda_B t}\right) (eq.A4.12)$$

And the initial condition is that the number of C atoms is $N_{C0}$ at t = 0.

So for radionuclide C, the number of atoms of C can be expressed as:

$$N_c(t) = \Lambda\left((\lambda_C - \lambda_B)e^{-\lambda_A t} - (\lambda_C - \lambda_A)e^{-\lambda_B t}\right) + \mathrm{X} e^{-\lambda_B t} + (N_{\mathrm{C0}} + (\lambda_B - \lambda_A)\Lambda - \mathrm{X}) e^{-\lambda_c t} \; (eq.A4.13)$$

Where $\Lambda = \frac{\lambda_A \lambda_B N_{\mathrm{A0}} \cdot \mathrm{BR_B} \cdot \mathrm{BR_A}}{(\lambda_B - \lambda_A)(\lambda_C - \lambda_A)(\lambda_C - \lambda_B)}$ and $\mathrm{X} = \frac{\lambda_B N_{\mathrm{B0}} \cdot \mathrm{BR_B}}{(\lambda_C - \lambda_B)}$.

Since the relation between the activity of one radionuclide and its number of atoms is:

$$\mathrm{A(t)} = \lambda \mathrm{N(t)} \qquad (eq.4.9)$$

The activity of A can be deduced using *eq.4.16*:

$$A_A(t) = A_{A0} e^{-\lambda_A t} \qquad (eq.4.16)$$

Where $A_{A0}$ is the initial activity of A and $A_{B0}$ the initial activity of B.

The activity of B can be deduced using *eq.4.17*:

$$A_B(t) = \frac{\lambda_B}{\lambda_B - \lambda_A} \cdot A_{\mathrm{A0}}\left(e^{-\lambda_A t} - e^{-\lambda_B t}\right) \cdot \mathrm{BR_A} + A_{\mathrm{B0}} e^{-\lambda_B t} \qquad (eq.4.17)$$

Where $A_{B0}$ is the initial activity of B at t = 0.

And the activity of C can be deduced using *eq.A.4.13*:

$$A_c(t) = \Lambda' e^{-\lambda_A t} + \mathrm{X}' e^{-\lambda_B t} + (A_{\mathrm{C0}} - \Lambda' - \mathrm{X}') e^{-\lambda_c t} \qquad (eq.4.18)$$

Where $\Lambda' = \frac{\lambda_C \lambda_B A_{A0} \cdot BR_B \cdot BR_A}{(\lambda_B - \lambda_A)(\lambda_C - \lambda_A)}$, $X' = \frac{\lambda_C A_{B0} \cdot BR_B}{(\lambda_C - \lambda_B)} - \frac{\lambda_C \lambda_B A_{A0} \cdot BR_B \cdot BR_A}{(\lambda_B - \lambda_A)(\lambda_C - \lambda_B)}$, and $A_{C0}$ is the initial activity of C at t = 0.

# Reference


1. Khalil, M. *Basic Sciences of Nuclear Medicine*. (Springer Science & Business Media, 2010).
2. Otuka, N. & Takács, S. Definitions of radioisotope thick target yields. *Radiochimica Acta* **103**, 1–6 (2015).
3. Stephens, K. New PET Tracer Detects Hallmark of Alzheimer's Disease Years Before Symptoms Emerge. *AXIS Imaging News* (2021).
4. Naqvi, S. A. R. & Imran, M. B. *Medical Isotopes*. (BoD – Books on Demand, 2021).
5. Madsen, M. T. Recent Advances in SPECT Imaging. *Journal of Nuclear Medicine* **48**, 661–673 (2007).
6. Qaim, S. M. Nuclear data for production and medical application of radionuclides: Present status and future needs. *Nuclear Medicine and Biology* **44**, 31–49 (2017).
7. Müller, C. *et al.* Future prospects for SPECT imaging using the radiolanthanide terbium-155 — production and preclinical evaluation in tumor-bearing mice. *Nuclear Medicine and Biology* **41**, e58–e65 (2014).
8. NuDat 3. https://www.nndc.bnl.gov/nudat3/.
9. McQuade, P., Rowland, D. J., Lewis, J. S. & Welch, M. J. Positron-Emitting Isotopes Produced on Biomedical Cyclotrons. *Current Medicinal Chemistry* **12**, 807–818.
10. Kapoor, V., McCook, B. M. & Torok, F. S. An Introduction to PET-CT Imaging. *RadioGraphics* **24**, 523–543 (2004).
11. Turkington, T. G. Introduction to PET Instrumentation. *JOURNAL OF NUCLEAR MEDICINE TECHNOLOGY* **29**, 8 (2001).
12. Deng, X. *et al.* Chemistry for Positron Emission Tomography: Recent Advances in 11C-, 18F-, 13N-, and 15O-Labeling Reactions. *Angewandte Chemie International Edition* **58**, 2580–2605 (2019).
13. Müller, C. *et al.* A Unique Matched Quadruplet of Terbium Radioisotopes for PET and SPECT and for α- and β−-Radionuclide Therapy: An In Vivo Proof-of-Concept Study with a New Receptor-Targeted Folate Derivative. *Journal of Nuclear Medicine* **53**, 1951–1959 (2012).
14. Carter, L. M. *et al.* The Impact of Positron Range on PET Resolution, Evaluated with Phantoms and PHITS Monte Carlo Simulations for Conventional and Non-conventional Radionuclides. *Mol Imaging Biol* **22**, 73–84 (2020).
15. Livieratos, L. Technical Pitfalls and Limitations of SPECT/CT. *Seminars in Nuclear Medicine* **45**, 530–540 (2015).
16. Mariani, G. *et al.* A review on the clinical uses of SPECT/CT. *Eur J Nucl Med Mol Imaging* **37**, 1959–1985 (2010).
17. Beyer, T. *et al.* A combined PET/CT scanner for clinical oncology. *Journal of nuclear medicine* **41**, 1369–1379 (2000).
18. Dendale, R. *et al.* [Proton therapy in France in 2019]. *Cancer Radiother* **23**, 617–624 (2019).
19. Pisansky, T. M. External-Beam Radiotherapy for Localized Prostate Cancer. *New England Journal of Medicine* **355**, 1583–1591 (2006).
20. Kassis, A. I. & Adelstein, S. J. Radiobiologic Principles in Radionuclide Therapy. 9.
21. Das, T. & Pillai, M. R. A. Options to meet the future global demand of radionuclides for radionuclide therapy. *Nuclear Medicine and Biology* **40**, 23–32 (2013).
22. Qaim, S. M. Therapeutic radionuclides and nuclear data. *Radiochimica Acta* **89**, 297–304 (2001).
23. Ku, A., Facca, V. J., Cai, Z. & Reilly, R. M. Auger electrons for cancer therapy – a review. *EJNMMI Radiopharmacy and Chemistry* **4**, 27 (2019).
24. Yordanova, A. *et al.* Theranostics in nuclear medicine practice. *Onco Targets Ther* **10**, 4821–4828 (2017).

25. Herzog, H. *et al.* Measurement of pharmacokinetics of yttrium-86 radiopharmaceuticals with PET and radiation dose calculation of analogous yttrium-90 radiotherapeutics. *J Nucl Med* **34**, 2222–2226 (1993).
26. Qaim, S. M., Scholten, B. & Neumaier, B. New developments in the production of theranostic pairs of radionuclides. *J Radioanal Nucl Chem* **318**, 1493–1509 (2018).
27. Dalm, S. U. *et al.* 68Ga/177Lu-NeoBOMB1, a Novel Radiolabeled GRPR Antagonist for Theranostic Use in Oncology. *Journal of Nuclear Medicine* **58**, 293–299 (2017).
28. Scarpa, L. *et al.* The 68Ga/177Lu theragnostic concept in PSMA targeting of castration-resistant prostate cancer: correlation of SUVmax values and absorbed dose estimates. *Eur J Nucl Med Mol Imaging* **44**, 788–800 (2017).
29. Baum, R. P. & Rösch, F. *Theranostics, Gallium-68, and Other Radionuclides: A Pathway to Personalized Diagnosis and Treatment*. (Springer Science & Business Media, 2012).
30. Dash, A., Pillai, M. R. A. & Knapp, F. F. Production of (177)Lu for Targeted Radionuclide Therapy: Available Options. *Nucl Med Mol Imaging* **49**, 85–107 (2015).
31. RRDB. https://nucleus.iaea.org/rrdb/#/reports/utilization-report/isotopeProduction.
32. Hasan, S. & Prelas, M. A. Molybdenum-99 production pathways and the sorbents for 99Mo/99mTc generator systems using (n, γ) 99Mo: a review. *SN Appl. Sci.* **2**, 1782 (2020).
33. Ogbomo, K. *et al.* Production, separation and validation of Tc99m from accelerator transmutation of sintered enriched Mo100. *Journal of Nuclear Medicine* **53**, 1489–1489 (2012).
34. Mirzadeh, S., Mausner, L. F. & Garland, M. A. *Reactor-Produced Medical Radionuclides*. *Handbook of Nuclear Chemistry* 1857 (2011). doi:10.1007/978-1-4419-0720-2_38.
35. IAEA-TECDOC, M. 1340. Manual for reactor produced radioisotope. *Vienna: International Atomic Energy Agency* (2003).
36. The History of the Cyclotron | SpringerLink. https://link.springer.com/chapter/10.1007/978-3-0348-5520-4_133.
37. Cyclotron Produced Radionuclides: Operation and Maintenance of Gas and Liquid Targets. https://www.iaea.org/publications/8783/cyclotron-produced-radionuclides-operation-and-maintenance-of-gas-and-liquid-targets (2016).
38. Cyclotrons used for Radionuclide Production. *Nucleus* https://nucleus.iaea.org/sites/accelerators.
39. Increasing Radiopharmaceutical Production with Cyclotrons. https://www.iaea.org/newscenter/news/increasing-radiopharmaceutical-production-with-cyclotrons (2022).
40. Currie, G., Wheat, J., Davidson, R. & Kiat, H. Radionuclide production. *Radiographer* **58**, 46–52 (2011).
41. van der Meulen, N. P. *et al.* Cyclotron production of 44Sc: From bench to bedside. *Nuclear Medicine and Biology* **42**, 745–751 (2015).
42. Qaim, S. M. Cyclotron Production of Medical Radionuclides. in *Handbook of Nuclear Chemistry* (eds. Vértes, A., Nagy, S., Klencsár, Z., Lovas, R. G. & Rösch, F.) 1903–1933 (Springer US, 2011). doi:10.1007/978-1-4419-0720-2_39.
43. Qaim, S. M. Nuclear data for medical radionuclides. *J Radioanal Nucl Chem* **305**, 233–245 (2015).
44. Dos Santos Augusto, R. M. *et al.* CERN-MEDICIS (Medical Isotopes Collected from ISOLDE): A New Facility. *Applied Sciences* **4**, 265–281 (2014).
45. David, J.-C. Spallation reactions: A successful interplay between modeling and applications. *The European Physical Journal A* **51**, 1–57 (2015).
46. Duchemin, C. *et al.* CERN-MEDICIS: A UNIQUE FACILITY FOR THE PRODUCTION OF NONCONVENTIONAL RADIONUCLIDES FOR THE MEDICAL RESEARCH. in

*11th International Particle Accelerator Conference* (2020). doi:10.18429/JACoW-IPAC2020-THVIR13.
47. Dewit, B. Towards the first collection of 44Sc at CERN MEDICIS. (Leuven U.).
48. Armbruster, P. *et al.* Measurement of a Complete Set of Nuclides, Cross Sections, and Kinetic Energies in Spallation of U 238 1 A G e V with Protons. *Physical review letters* **93**, 212701 (2004).
49. Rösch, F. & Knapp, F. F. Radionuclide Generators. in *Handbook of Nuclear Chemistry* (eds. Vértes, A., Nagy, S., Klencsár, Z., Lovas, R. G. & Rösch, F.) 1935–1976 (Springer US, 2011). doi:10.1007/978-1-4419-0720-2_40.
50. Themes, U. F. O. Radionuclide Generator Systems Represent Convenient Production Systems to Provide Therapeutic Radionuclides. *Radiology Key* https://radiologykey.com/radionuclide-generator-systems-represent-convenient-production-systems-to-provide-therapeutic-radionuclides/ (2017).
51. Naidoo, C., van der Walt, T. & Raubenheimer, H. Cyclotron production of 68 Ge with a Ga 2 O target. *Journal of Radioanalytical and Nuclear Chemistry* **253**, 221–225 (2002).
52. Vereshchagin, Y. I., Zagryadskiy, V. A. & Prusakov, V. N. Cyclotron 82Sr production for medical applications. *Nuclear Instruments and Methods in Physics Research Section A: Accelerators, Spectrometers, Detectors and Associated Equipment* **334**, 246–248 (1993).
53. Ghergherehchi, M. & Sardari, D. Production of 62 Zn/62 Cu generator by cyclotron.
54. Human Health Campus - Principles of radionuclide generators. https://humanhealth.iaea.org/HHW/Radiopharmacy/VirRad/Eluting_the_Generator/Generator_Module/Principles_of_radionuclide_generators/index.html.
55. Dash, A., Knapp, F. F. (Russ) & Pillai, M. R. A. 99Mo/99mTc separation: An assessment of technology options. *Nuclear Medicine and Biology* **40**, 167–176 (2013).
56. Mirzadeh, S. & Knapp, F. F. Biomedical radioisotope generator systems. *Journal of Radioanalytical and Nuclear Chemistry, Articles* **203**, 471–488 (1996).
57. Ziadi, M. C., Dekemp, R. A., Yoshinaga, K. & Beanlands, R. S. Chapter 19 - Diagnosis and Prognosis in Cardiac Disease Using Cardiac PET Perfusion Imaging. in *Clinical Nuclear Cardiology (Fourth Edition)* (eds. Zaret, B. L. & Beller, G. A.) 309–331 (Mosby, 2010). doi:10.1016/B978-0-323-05796-7.00037-0.
58. Haji-Saeid, M. *et al. Standardized High Current Solid Targets for Cyclotron Production of Diagnostic and Therapeutic Radionuclides*. (2004).
59. Stolarz, A. Target preparation for research with charged projectiles. *J Radioanal Nucl Chem* **299**, 913–931 (2014).
60. Halahakoon, A. *Principles of Powder compression and Compaction*. (2020). doi:10.13140/RG.2.2.32065.99688.
61. Sugai, I., Takeda, Y. & Kawakami, H. Preparation of thick enriched isotopic Si targets by the HIVIPP method. *Nuclear Instruments and Methods in Physics Research Section A: Accelerators, Spectrometers, Detectors and Associated Equipment* **561**, 38–44 (2006).
62. Skliarova, H. *et al.* Medical Cyclotron Solid Target Preparation by Ultrathick Film Magnetron Sputtering Deposition. *Instruments* **3**, 21 (2019).
63. Maier, H. J. Preparation of nuclear accelerator targets by vacuum evaporation. *IEEE Transactions on Nuclear Science* **28**, 1575–1583 (1981).
64. Crespo, M. T. A review of electrodeposition methods for the preparation of alpha-radiation sources. *Applied Radiation and Isotopes* **70**, 210–215 (2012).
65. Skliarova, H. *et al.* HIVIPP deposition and characterization of isotopically enriched 48Ti targets for nuclear cross-section measurements. *Nuclear Instruments and Methods in Physics Research Section A: Accelerators, Spectrometers, Detectors and Associated Equipment* **981**, 164371 (2020).

66. Alves, V., do Carmo, S., Alves, F. & Abrunhosa, A. Automated Purification of Radiometals Produced by Liquid Targets. *Instruments* **2**, 17 (2018).
67. do Carmo, S. J. C., Scott, P. J. H. & Alves, F. Production of radiometals in liquid targets. *EJNMMI Radiopharmacy and Chemistry* **5**, 2 (2020).
68. Alves, F. *et al.* Production of copper-64 and gallium-68 with a medical cyclotron using liquid targets. *Mod. Phys. Lett. A* **32**, 1740013 (2017).
69. Zacchia, N. A., Martinez, D. M. & Hoehr, C. Radiolysis reduction in liquid solution targets for the production of 89Zr. *Applied Radiation and Isotopes* **155**, 108791 (2020).
70. Pandey, M. K., Engelbrecht, H. P., Byrne, J. F., Packard, A. B. & DeGrado, T. R. Production of 89Zr via the 89Y (p, n) 89Zr reaction in aqueous solution: effect of solution composition on in-target chemistry. *Nuclear medicine and biology* **41**, 309–316 (2014).
71. Zhuikov, B. & Ermolaev, S. Adsorption from liquid metals: an approach for recovery of radionuclides from irradiated targets. *Radiochimica Acta* **109**, 99–107 (2021).
72. Rovais, M. R. A. *et al.* Design and manufacture of krypton gas target for 81Rb production at a 30 MeV cyclotron. *Nukleonika* 225–231 (2010).
73. Sumiya, L. C. A. & Sciani, V. Evaluation of irradiation parameters of enriched 124Xe target for 123I production in cyclotrons. *Applied Radiation and Isotopes* **66**, 1337–1340 (2008).
74. Radionuclides, C. P. Principles and practice. *International Atomic Energy Agency, Vienna* (2008).
75. Steyn, G., Vermeulen, C. & Isaacs, E. Encapsulation methods for solid radionuclide production targets at a medium-energy cyclotron facility. in *AIP Conference Proceedings* vol. 1962 030016 (AIP Publishing LLC, 2018).
76. Beyer, G.-J. *et al.* Targeted alpha therapy in vivo: direct evidence for single cancer cell kill using 149Tb-rituximab. *Eur J Nucl Med Mol Imaging* **31**, 547–554 (2004).
77. Durán, M. T. *et al.* Determination of 161Tb half-life by three measurement methods. *Appl Radiat Isot* **159**, 109085 (2020).
78. Alcocer-Ávila, M. E. *et al.* Radiation doses from 161Tb and 177Lu in single tumour cells and micrometastases. *EJNMMI Phys* **7**, 33 (2020).
79. Baum, R. P. *et al.* First-in-humans application of 161Tb: A feasibility study using 161Tb-DOTATOC. *Journal of Nuclear Medicine* **62**, 1391–1397 (2021).
80. Lehenberger, S. *et al.* The low-energy β− and electron emitter 161Tb as an alternative to 177Lu for targeted radionuclide therapy. *Nuclear Medicine and Biology* **38**, 917–924 (2011).
81. Tárkányi, F. *et al.* Cross-section measurement of some deuteron induced reactions on 160Gd for possible production of the therapeutic radionuclide 161Tb. *J Radioanal Nucl Chem* **298**, 1385–1392 (2013).
82. Gracheva, N. *et al.* Production and characterization of no-carrier-added 161Tb as an alternative to the clinically-applied 177Lu for radionuclide therapy. *EJNMMI Radiopharmacy and Chemistry* **4**, 12 (2019).
83. Webster, B. L. The chemical separation of terbium for applications in nuclear medicine. (University of Surrey, 2022).
84. Maiti, M. New measurement of cross sections of evaporation residues from the nat Pr+ 12 C reaction: A comparative study on the production of 149 Tb. *Physical Review C* **84**, 044615 (2011).
85. Allen, B. J. *et al.* Production of terbium-152 by heavy ion reactions and proton induced spallation. *Applied Radiation and Isotopes* **54**, 53–58 (2001).
86. Zaitseva, N. G. *et al.* Terbium-149 for nuclear medicine. The production of 149Tb via heavy ions induced nuclear reactions. *Czech J Phys* **53**, A455–A458 (2003).

87. Lahiri, S. *et al.* Separation of carrier free152, 153Dy and151–153Tb from16O7+ irradiated CeO2 by liquid-liquid extraction. *Journal of radioanalytical and nuclear chemistry* **241**, 201–206 (1999).
88. Nayak, D., Lahiri, S., Ramaswami, A., Manohar, S. B. & Das, N. R. Separation of carrier free 151,152 Tb produced in 16O irradiated lanthanum oxide matrix. *Applied radiation and isotopes* **51**, 631–636 (1999).
89. Blakely, E. A. The 20th Gray lecture 2019: health and heavy ions. *The British journal of radiology* **93**, 20200172 (2020).
90. Formento-Cavaier, R., Haddad, F., Alliot, C., Sounalet, T. & Zahi, I. New excitation functions for proton induced reactions on natural gadolinium up to 70 MeV with focus on 149Tb production. *Nuclear Instruments and Methods in Physics Research Section B: Beam Interactions with Materials and Atoms* **478**, 174–181 (2020).
91. Tárkányi, F. *et al.* Activation cross-sections of deuteron induced reactions on natGd up to 50MeV. *Applied Radiation and Isotopes* **83**, 25–35 (2014).
92. Duchemin, C., Guertin, A., Haddad, F., Michel, N. & Métivier, V. Deuteron induced Tb-155 production, a theranostic isotope for SPECT imaging and auger therapy. *Applied Radiation and Isotopes* **118**, 281–289 (2016).
93. Szelecsényi, F., Kovács, Z., Nagatsu, K., Zhang, M.-R. & Suzuki, K. Investigation of deuteron-induced reactions on natGd up to 30 MeV: possibility of production of medically relevant 155Tb and 161Tb radioisotopes. *J Radioanal Nucl Chem* **307**, 1877–1881 (2016).
94. Steyn, G. F. *et al.* Cross sections of proton-induced reactions on 152Gd, 155Gd and 159Tb with emphasis on the production of selected Tb radionuclides. *Nuclear Instruments and Methods in Physics Research Section B: Beam Interactions with Materials and Atoms* **319**, 128–140 (2014).
95. Moiseeva, A. N. *et al.* Cross section measurements of 151Eu(3He,5n) reaction: new opportunities for medical alpha emitter 149Tb production. *Sci Rep* **10**, 508 (2020).
96. TENDL-2019 nuclear data library. https://tendl.web.psi.ch/tendl_2019/tendl2019.html.
97. Favaretto, C. *et al.* Cyclotron production and radiochemical purification of terbium-155 for SPECT imaging. *EJNMMI Radiopharmacy and Chemistry* **6**, 37 (2021).
98. Dellepiane, G. *et al.* Cross-section measurement of terbium radioisotopes for an optimized 155Tb production with an 18 MeV medical PET cyclotron. *Applied Radiation and Isotopes* 110175 (2022) doi:10.1016/j.apradiso.2022.110175.
99. Stable Isotopes Supplier. http://www.tracesciences.com/index.html.
100. Arronax Nantes. *Arronax Nantes* https://www.arronax-nantes.fr/.
101. Haddad, F. *et al.* ARRONAX, a high-energy and high-intensity cyclotron for nuclear medicine. *Eur J Nucl Med Mol Imaging* **35**, 1377–1387 (2008).
102. Lide, D. R. *CRC Handbook of Chemistry and Physics, 85th Edition*. (CRC Press, 2004).
103. Gucik, M. L. *et al.* Electrodeposition of Gadolinium Metal from Organic Solvents. *Meet. Abstr.* **MA2020-02**, 1517–1517 (2020).
104. Kovács, Z., Szelecsényi, F. & Brezovcsik, K. Preparation of thin gadolinium samples via electrodeposition for excitation function studies. *J Radioanal Nucl Chem* **307**, 1861–1864 (2016).
105. Small, L. J., Sears, J. M., Lambert, T. N., Boyle, T. J. & Hess, R. F. Electroreduction of Er3+ in nonaqueous solvents. *RSC Adv.* **6**, 89564–89571 (2016).
106. Caravaca, C., de Córdoba, G., Tomás, M. J. & Rosado, M. Electrochemical behaviour of gadolinium ion in molten LiCl–KCl eutectic. *Journal of Nuclear Materials* **360**, 25–31 (2007).
107. POURBAIX, M. Atlas of Electrochemical Equilibria in Aqueous Solution. *NACE* **307**, (1974).

108. Walsh, F. C. & Ponce de Leon, C. A review of the electrodeposition of metal matrix composite coatings by inclusion of particles in a metal layer: an established and diversifying technology. *Transactions of the IMF* **92**, 83–98 (2014).
109. Celis, J. P., Roos, J. R. & Buelens, C. A Mathematical Model for the Electrolytic Codeposition of Particles with a Metallic Matrix. *J. Electrochem. Soc.* **134**, 1402 (1987).
110. Williams, R. V. & Martin, P. W. Electrodeposited Composite Coatings. *Transactions of the IMF* **42**, 182–188 (1964).
111. Grahame, D. C. The Electrical Double Layer and the Theory of Electrocapillarity. *Chem. Rev.* **41**, 441–501 (1947).
112. Hovestad, A. & Janssen, L. J. J. Electrochemical codeposition of inert particles in a metallic matrix. *J Appl Electrochem* **25**, 519–527 (1995).
113. Decay data search. http://nucleardata.nuclear.lu.se/toi/.
114. Reid, J. Copper electrodeposition: principles and recent progress. *Japanese journal of applied physics* **40**, 2650 (2001).
115. Ballesteros, J. C., Chainet, E., Ozil, P. & Trejo, G. Electrodeposition of Copper from Non-Cyanide Alkaline Solution Containing Tartrate.
116. Skitał, P. M., Sanecki, P. T., Saletnik, D. & Kalembkiewicz, J. Electrodeposition of nickel from alkaline NH4OH/NH4Cl buffer solutions. *Transactions of Nonferrous Metals Society of China* **29**, 222–232 (2019).
117. Yuan, L., Ding, Z., Liu, S., Shu, W. & He, Y. Effects of additives on zinc electrodeposition from alkaline zincate solution. *Transactions of Nonferrous Metals Society of China* **27**, 1656–1664 (2017).
118. Qiao, X., Li, H., Zhao, W. & Li, D. Effects of deposition temperature on electrodeposition of zinc–nickel alloy coatings. *Electrochimica Acta* **89**, 771–777 (2013).
119. Vidrine, A. B. & Podlaha, E. J. Composite electrodeposition of ultra®ne c-alumina particles in nickel matrices Part I: Citrate and chloride electrolytes. 8.
120. Abelha Carrijo Gonçalves, G., Campos, P. M., Veloso, T. & Capelossi, V. Influence of current density and temperature in the zinc electroplating process at sulfate-based acid solution - study on process efficiency and coating morphology. *Scientia Plena* **17**, 1–11 (2021).
121. Hermanne, A. *et al.* Reference cross sections for charged-particle monitor reactions. *Nuclear Data Sheets* **148**, 338–382 (2018).
122. Tárkányi, F. *et al.* Excitation functions of deuteron induced nuclear reactions on natural zinc up to 50 MeV. *Nuclear Instruments and Methods in Physics Research Section B: Beam Interactions with Materials and Atoms* **217**, 531–550 (2004).
123. Khandaker, M. U., Haba, H., Murakami, M. & Otuka, N. Production cross-sections of long-lived radionuclides in deuteron-induced reactions on natural zinc up to 23MeV. *Nuclear Instruments and Methods in Physics Research Section B: Beam Interactions with Materials and Atoms* **346**, 8–16 (2015).
124. Amjed, N., Tárkányi, F., Ditrói, F., Takács, S. & Yuki, H. Activation cross-sections of deuteron induced reaction of natural Ni up to 40MeV. *Applied Radiation and Isotopes* **82**, 87–99 (2013).
125. Hermanne, A., Takacs, S., Adam-Rebeles, R., Tárkányi, F. & Takács, M. P. New measurements and evaluation of database for deuteron induced reaction on Ni up to 50 MeV. *Nuclear Instruments and Methods in Physics Research Section B: Beam Interactions with Materials and Atoms* **299**, 8–23 (2013).
126. Assessment, U. E. N. C. for E. Description of input and examples for PHREEQC version 3: a computer program for speciation, batch-reaction, one-dimensional transport, and inverse geochemical calculations. https://hero.epa.gov/hero/index.cfm/reference/details/reference_id/7676153 (2009).

127. Reichle, R. A., McCurdy, K. G. & Hepler, L. G. Zinc Hydroxide: Solubility Product and Hydroxy-complex Stability Constants from 12.5–75 °C. *Can. J. Chem.* **53**, 3841–3845 (1975).
128. Merck | France. https://www.sigmaaldrich.com/FR/fr.
129. Gadolinium Isotopes - Gd Isotopes - Stable Gadolinium Isotopes Supplier. http://www.tracesciences.com/gd.htm.
130. Uher, C. Thermal Conductivity of Metals. in *Thermal Conductivity: Theory, Properties, and Applications* (ed. Tritt, T. M.) 21–91 (Springer US, 2004). doi:10.1007/0-387-26017-X_2.
131. Comparaison PEEK/PEK/PTFE. *Greene Tweed* https://fr.gtweed.com/materials/peek-vs-pek-vs-ptfe/.
132. French Home - Goodfellow. https://www.goodfellow.com/fr/fr.
133. Akhtar, K., Khan, S. A., Khan, S. B. & Asiri, A. M. Scanning Electron Microscopy: Principle and Applications in Nanomaterials Characterization. in *Handbook of Materials Characterization* (ed. Sharma, S. K.) 113–145 (Springer International Publishing, 2018). doi:10.1007/978-3-319-92955-2_4.
134. Dusevich, V. M., Purk, J. H. & Eick, J. D. Choosing the Right Accelerating Voltage for SEM (An Introduction for Beginners). *Microscopy Today* **18**, 48–52 (2010).
135. Olesik, J. W. Elemental Analysis Using ICP-OES and ICP/MS. *Anal. Chem.* **63**, 12A-21A (1991).
136. SCP SCIENCE. https://www.scpscience.com/fr.
137. iCAP 6000 Series ICP Emission Spectrometer. 8.
138. Jeon, S.-H., Choi, W.-I., Song, G.-D., Son, Y.-H. & Hur, D. H. Influence of Surface Roughness and Agitation on the Morphology of Magnetite Films Electrodeposited on Carbon Steel Substrates. *Coatings* **6**, 62 (2016).
139. Amiriafshar, M., Rafieazad, M., Duan, X. & Nasiri, A. Fabrication and coating adhesion study of superhydrophobic stainless steel surfaces: The effect of substrate surface roughness. *Surfaces and Interfaces* **20**, 100526 (2020).
140. Kong, A., Gong, B.-K., Wang, G. & Cui, H.-W. INFLUENCE OF SURFACE ROUGHNESS OF SUBSTRATE ON THE PROPERTIES OF Ni–Co–Fe ELECTRODEPOSITION COATING ON COPPER. *Surf. Rev. Lett.* **25**, 1850120 (2018).
141. Castro-Rodríguez, R., Oliva, A. I., Sosa, V., Caballero-Briones, F. & Peña, J. L. Effect of indium tin oxide substrate roughness on the morphology, structural and optical properties of CdS thin films. *Applied Surface Science* **161**, 340–346 (2000).
142. Milošev, I. & Kosec, T. Study of Cu–18Ni–20Zn Nickel Silver and other Cu-based alloys in artificial sweat and physiological solution. *Electrochimica Acta* **52**, 6799–6810 (2007).
143. Ćirović, N., Spasojević, P., Ribić-Zelenović, L., Mašković, P. & Spasojević, M. Synthesis, structure and properties of nickel-iron-tungsten alloy electrodeposits - part I: Effect of synthesis parameters on chemical composition, microstructure and morphology. *Science of Sintering* **47**, 347–365 (2015).
144. Jović, V. D., Jović, B. M. & Pavlović, M. G. Electrodeposition of Ni, Co and Ni–Co alloy powders. *Electrochimica Acta* **51**, 5468–5477 (2006).
145. Nikolić, N. D. & Popov, K. I. Hydrogen Co-deposition Effects on the Structure of Electrodeposited Copper. in *Electrodeposition: Theory and Practice* (ed. Djokic, S. S.) 1–70 (Springer, 2010). doi:10.1007/978-1-4419-5589-0_1.
146. Low, C. T. J., Wills, R. G. A. & Walsh, F. C. Electrodeposition of composite coatings containing nanoparticles in a metal deposit. *Surface and Coatings Technology* **201**, 371–383 (2006).

147. Guglielmi, N. Kinetics of the Deposition of Inert Particles from Electrolytic Baths. *J. Electrochem. Soc.* **119**, 1009 (1972).
148. Sabzi, M., Dezfuli, S. M. & Mirsaeedghazi, S. M. The effect of pulse-reverse electroplating bath temperature on the wear/corrosion response of Ni-Co/tungsten carbide nanocomposite coating during layer deposition. *Ceramics International* **44**, 19492–19504 (2018).
149. Turner, M., Thompson, G. E. & Brook, P. A. The anodic behaviour of nickel in sulphuric acid solutions. *Corrosion Science* **13**, 985–991 (1973).
150. Kim, S. K. & Yoo, H. J. Formation of bilayer Ni–SiC composite coatings by electrodeposition. *Surface and Coatings Technology* **108–109**, 564–569 (1998).
151. Tóth, B. G. *et al.* Influence of Cu deposition potential on the giant magnetoresistance and surface roughness of electrodeposited Ni–Co/Cu multilayers. *Electrochimica Acta* **91**, 122–129 (2013).
152. Gunko, Yu. L., Kozyrin, V. A., Kozina, O. L., Ananieva, E. Yu. & Mikhalenko, M. G. Cathodic Reduction of Zinc Oxide in Alkaline Electrolyte. *Russ J Electrochem* **58**, 60–73 (2022).
153. Influência da densidade de corrente e da temperatura no processo de eletrodeposição de zinco em solução ácida à base de sulfato: estudo da eficiência do processo e da morfologia do revestimento | Scientia Plena. https://scientiaplena.org.br/sp/article/view/6278.
154. Wang, K., Xiao, Y., Pei, P., Liu, X. & Wang, Y. A Phase-Field Model of Dendrite Growth of Electrodeposited Zinc. *J. Electrochem. Soc.* **166**, D389–D394 (2019).
155. Alias, N. & Mohamad, A. A. Morphology study of electrodeposited zinc from zinc sulfate solutions as anode for zinc-air and zinc-carbon batteries. *Journal of King Saud University - Engineering Sciences* **27**, 43–48 (2015).
156. Nakano, H. Effects of plating factors on morphology and appearance of electrogalvanized steel sheets. *Transactions of Nonferrous Metals Society of China* **19**, 835–841 (2009).
157. Xu, Z., Fan, Q., Li, Y., Wang, J. & Lund, P. D. Review of zinc dendrite formation in zinc bromine redox flow battery. *Renewable and Sustainable Energy Reviews* **127**, 109838 (2020).
158. Wang, R. Y., Kirk, D. W. & Zhang, G. X. Characterization and Growth Mechanism of Filamentous Zinc Electrodeposits. *ECS Trans.* **2**, 19 (2007).
159. Mahmoodi, F. Compression Mechanics of Powders and Granular Materials Probed by Force Distributions and a Micromechanically Based Compaction Equation. (2012).
160. Johansson, B., Wikberg, M., Ek, R. & Alderborn, G. Compression behaviour and compactability of microcrystalline cellulose pellets in relationship to their pore structure and mechanical properties. *International Journal of Pharmaceutics* **117**, 57–73 (1995).
161. Hewitt, R. L., Wallace, W. & de Malherbe, M. C. Plastic Deformation in Metal Powder Compaction. *Powder Metallurgy* **17**, 1–12 (1974).
162. Eriksson, M. & Alderborn, G. The Effect of Particle Fragmentation and Deformation on the Interparticulate Bond Formation Process During Powder Compaction. *Pharm Res* **12**, 1031–1039 (1995).
163. A330, 30 Ton, Arbor Hydraulic Press | Enerpac. https://www.enerpac.com/en-us/30-ton-presses/arbor-press/A330.
164. Perry, D. L. *Handbook of inorganic compounds*. (CRC press, 2016).
165. Epp, J. 4 - X-ray diffraction (XRD) techniques for materials characterization. in *Materials Characterization Using Nondestructive Evaluation (NDE) Methods* (eds. Hübschen, G., Altpeter, I., Tschuncky, R. & Herrmann, H.-G.) 81–124 (Woodhead Publishing, 2016). doi:10.1016/B978-0-08-100040-3.00004-3.

166. Ruoho, M., Valset, K., Finstad, T. & Tittonen, I. Measurement of thin film thermal conductivity using the laser flash method. *Nanotechnology* **26**, 195706 (2015).
167. Fujii, K. Precision density measurements of solid materials by hydrostatic weighing. *Meas. Sci. Technol.* **17**, 2551–2559 (2006).
168. CAPACITÉS filiale de valorisation de la recherche de Nantes Université. *CAPACITÉS* https://capacites.fr/a-propos/.
169. Kylyshkanov, M. K. *et al.* Research on obtaining gadolinium oxide from waste technologies for processing of uranium-gadolinium containing materials. *J. Phys.: Conf. Ser.* **2155**, 012026 (2022).
170. Qiu Tingting *et al.* Solubility of rare earth fluorides in nitric acid. *Nuclear Techniques* **38**, 6 (2015).
171. Patnaik, P. *Handbook of inorganic chemicals*. (McGraw-Hill, 2003).
172. Gorejová, R. *et al.* Corrosion Behavior of Zn, Fe and Fe-Zn Powder Materials Prepared via Uniaxial Compression. *Materials* **14**, 4983 (2021).
173. Cieszykowska, I. *et al.* Manufacturing and characterization of molybdenum pellets used as targets for 99mTc production in cyclotron. *Applied Radiation and Isotopes* **124**, 124–131 (2017).
174. Nelson, B. J. B. *et al.* Taking cyclotron 68Ga production to the next level: Expeditious solid target production of 68Ga for preparation of radiotracers. *Nuclear Medicine and Biology* **80–81**, 24–31 (2020).
175. Zweit, J., Downey, S. & Sharma, H. L. Production of no-carrier-added zirconium-89 for positron emission tomography. *International Journal of Radiation Applications and Instrumentation. Part A. Applied Radiation and Isotopes* **42**, 199–201 (1991).
176. Molybdenum properties. https://www.imoa.info/molybdenum/molybdenum-properties.php.
177. Yang, Z. *et al.* Why thermal conductivity of CaO is lower than that of CaS: a study from the perspective of phonon splitting of optical mode. *Nanotechnology* **32**, 025709 (2020).
178. Szelagowski, H., Arvanitidis, I. & Seetharaman, S. Effective Thermal Conductivity of Porous Strontium Oxide and Strontium Carbonate Samples. *Journal of Applied Physics* **85**, 193–198 (1999).
179. Kaneko, H., Saito, Y., Umeda, M. & Nagai, K. . Thermal decomposition of gadolinium(III) oxalate. *Nippon Kagaku Kaishi* **1977**, 792–797 (1977).
180. Manigandan, R. *et al.* Structural, optical and magnetic properties of gadolinium sesquioxide nanobars synthesized via thermal decomposition of gadolinium oxalate. *Materials Research Bulletin* **48**, 4210–4215 (2013).
181. Iso, I. & OIML, B. Guide to the Expression of Uncertainty in Measurement. *Geneva, Switzerland* **122**, 16–17 (1995).
182. Blessing, G. *et al.* Internal irradiation system for excitation function measurement via the stacked-foil technique. *Applied Radiation and Isotopes* **46**, 955–960 (1995).
183. Ridikas, D. IAEA activities in support of nuclear physics research and applications. *J. Phys.: Conf. Ser.* **1643**, 012206 (2020).
184. Alharbi, A. A. *et al. Medical Radioisotopes Production: A Comprehensive Cross-Section Study for the Production of Mo and Tc Radioisotopes Via Proton Induced Nuclear Reactions on natMo*. *Radioisotopes - Applications in Bio-Medical Science* (IntechOpen, 2011). doi:10.5772/20598.
185. Ziegler, J. F., Ziegler, M. D. & Biersack, J. P. SRIM – The stopping and range of ions in matter (2010). *Nuclear Instruments and Methods in Physics Research Section B: Beam Interactions with Materials and Atoms* **268**, 1818–1823 (2010).
186. JFZ IBM-Web page 001. http://www.srim.org/SRIM/SRIMINTRO.htm.

187. Lee, I. Y., Deleplanque, M. A. & Vetter, K. Developments in large gamma-ray detector arrays. *Rep. Prog. Phys.* **66**, 1095–1144 (2003).
188. Debertin, K. & Helmer, R. G. *Gamma- and X-ray spectrometry with semiconductor detectors*. (North-Holland, 1988).
189. Détecteurs 锗 超 大 功 率 探 测 器 . https://www.canberra.com/fr/produits/detectors/germanium-detectors.html.
190. Knoll, G. F. *Radiation Detection and Measurement*. (John Wiley & Sons, 2010).
191. Nigron, E., Guertin, A., Haddad, F. & Sounalet, T. Is 70Zn(d,x)67Cu the Best Way to Produce 67Cu for Medical Applications? *Frontiers in Medicine* **8**, (2021).
192. Logiciels de Spectrométrie Gamma LVIS. *HTDS* https://www.htds.fr/nucleaire-radioprotection/logiciels-de-spectrometrie/logiciels-de-spectrometrie-gamma-lvis/.
193. FitzPeaks Gamma Analysis and Calibration Software. http://www.jimfitz.co.uk/fitzpeak.htm.
194. Koskelo, M. J., Aarnio, P. A. & Routti, J. T. SAMPO80: An accurate gamma spectrum analysis method for minicomputers. *Nuclear Instruments and Methods in Physics Research* **190**, 89–99 (1981).
195. Perfection V600 Photo | Scanner grand public | Scanners | Produits | Epson France. https://www.epson.fr/fr_FR/produits/scanners/consumer/perfection-v600-photo/p/3597.
196. GIMP. *GIMP* https://www.gimp.org/.
197. Rochman, D. *et al.* The TENDL library: Hope, reality and future. *EPJ Web Conf.* **146**, 02006 (2017).
198. Q-value Calculator (QCalc). https://www.nndc.bnl.gov/qcalc/.
199. Vermeulen, C. *et al.* Cross sections of proton-induced reactions on natGd with special emphasis on the production possibilities of 152Tb and 155Tb. *Nuclear Instruments and Methods in Physics Research Section B: Beam Interactions with Materials and Atoms* **275**, 24–32 (2012).
200. Welcome to Python.org. *Python.org* https://www.python.org/.
201. PyInstaller Manual — PyInstaller 4.10 documentation. https://pyinstaller.org/en/stable/.
202. Sitarz, M. Research on production of new medical radioisotopes with cyclotron. (2019).
203. outils-Radionuclide Yield Calculator. *Arronax Nantes* https://www.arronax-nantes.fr/outil-telechargement/outils-radionuclide-yield-calculator/.
204. Sitarz, M., Nigron, E., Guertin, A., Haddad, F. & Matulewicz, T. New Cross-Sections for natMo(α,x) Reactions and Medical 97Ru Production Estimations with Radionuclide Yield Calculator. *Instruments* **3**, 7 (2019).
205. İzgü, K. F. *et al. european pharmacopoeia 3rd edition*. (null, 1997).
206. Energy Dispersive X-ray Microanalysis An Introduction. 64.
207. Gagnon, K., Avila-Rodriguez, M. A., Wilson, J. & McQuarrie, S. A. Experimental deuteron cross section measurements using single natural titanium foils from 3 to 9MeV with special reference to the production of 47V and 51Ti. *Nuclear Instruments and Methods in Physics Research Section B: Beam Interactions with Materials and Atoms* **268**, 1392–1398 (2010).
208. Khandaker, M. U., Haba, H., Kanaya, J., Otuka, N. & Kassim, H. A. Activation Cross-sections of Deuteron-induced Nuclear Reactions on Natural Titanium. *Nuclear Data Sheets* **119**, 252–254 (2014).
209. Takács, S., Király, B., Tárkányi, F. & Hermanne, A. Evaluated activation cross sections of longer-lived radionuclides produced by deuteron induced reactions on natural titanium. *Nuclear Instruments and Methods in Physics Research Section B: Beam Interactions with Materials and Atoms* **262**, 7–12 (2007).
210. Castro, R. M. *et al.* Developing 152Eu into a standard for detector efficiency calibration. *Applied Radiation and Isotopes* **60**, 283–287 (2004).

211. Yoshizawa, Y., Iwata, Y. & Iinuma, Y. Precision measurements of gamma-ray intensities. II. 152Eu, 154Eu and 192Ir. *Nuclear Instruments and Methods* **174**, 133–139 (1980).
212. Nigron, E. Isotopes radioactifs produits par voies non conventionnelles. (Université de Nantes - Faculté des Sciences et Techniques, 2019).

# Résumé de thèse


**Introduction**

Le terbium est considéré comme le "couteau suisse" en médecine nucléaire car plusieurs radionucléides de la famille de terbium, tels que $^{149}$Tb, $^{152}$Tb, $^{155}$Tb et $^{161}$Tb, peuvent avoir de grandes perspectives d'application en médecine nucléaire. Le $^{149}$Tb, avec une demi-vie relativement courte ($t_{1/2}$ = 4,1 h) et émettant une faible énergie alpha ($E_\alpha$ = 3.97 MeV), a été proposé comme candidat pour une thérapie alpha[1]. Le $^{152}$Tb, en tant qu'émetteur $\beta^+$, il peut être utilisé en imagerie TEP en raison de deux énergies $\beta^+$ de 2620 keV (6 %) et 2970 keV (8 %)[2]. Le $^{155}$Tb peut être utilisé pour l'imagerie SPECT et la thérapie Auger car il s'agit d'un émetteur $\gamma$ et Auger[3]. En outre, le radionucléide $^{161}$Tb utilisé pour la thérapie, en tant qu'émetteur $\beta^-$ à faible énergie avec une demi-vie relativement courte (6,95 j), a été étudié comme une alternative au $^{177}$Lu en raison de son comportement chimique et de ses caractéristiques de désintégration similaires[4]. Cependant, à l'exception du $^{161}$Tb, la production des autres radionucléides se fait principalement par réaction de spallation à très haute énergie (plus de 400 MeV) suivi d'une séparation des masses en ligne. L'utilisation de cette séparation est coûteuse et nécessite des équipements correspondants, seulement seules très peu d'installations peuvent le faire (par exemple, CERN-MEDICIS[5] et TRIUMF[6]). Une autre façon d'augmenter leur disponibilité est d'utiliser des cibles de Gd hautement enrichies avec des cyclotrons à faible énergie (10-70 MeV) par des réactions avec des particules légères (proton ou deutéron). Les réactions sont les suivants : $^{152}$Gd(p,4n) $^{149}$Tb, $^{152}$Gd(p,n)$^{152}$Tb, $^{155}$Gd(p,n)$^{155}$Tb et $^{155}$Gd(d, 2n)$^{155}$Tb. Le niveau d'enrichissement en $^{152}$Gd n'est que de 34% alors que celui en $^{155}$Gd peut atteindre 92%[7]. Ainsi, dans ce travail, nous avons choisi d'étudier à partir de gadolinium enrichi en 155 comme matière première sous forme d'oxyde, $^{155}Gd_2O_3$ pour produire du $^{155}$Tb par la voie réaction nucléaire de $^{155}$Gd(d, 2n)$^{155}$Tb. Le deutéron a été choisi pour mesurer la section efficace grâce à son meilleur rendement de production ce qui facilitera la preuve de concept malgré la présence d'impureté de $^{156}$Tb. Deux types de cibles ont été développés dans ce travail, les cibles minces fabriquées par la méthode de co-électrodéposition ont été utilisées pour mesurer les sections efficaces et estimer le rendement de production ; et les cibles épaisses fabriquées par la méthode de pastillage ont été utilisées pour produire en masse du $^{155}$Tb.

**Méthodologie et expérimentaux**

La méthode de co-électrodéposition a été développée dans ce travail pour fournir des cibles minces de Gd avec une épaisseur de dizaines de micromètres. Cette méthode consiste à déposer un dépôt autre que Gd et de piéger des particules de Gd dans celui-ci. Il n'est pas possible de déposer Gd en milieux aqueux du fait de son potentiel de réduction de $Gd^{3+}$/Gd très négative (-2,3 V/NHE[8]). Les particules en question sont $Gd_2O_3$; elles sont insolubles et mélangées uniformément dans l'électrolyte, et sous un certain potentiel appliqué, elles peuvent être mécaniquement transportées et physiquement intégrées dans une couche de métal déposée en croissance. Le nickel et le zinc ont été choisis comme métaux déposés sur un substrat en Au. À l'aide de poudre naturelle de $Gd_2O_3$, plusieurs paramètres influant sur la performance expérimentale ont été étudiés afin de déterminer les conditions expérimentales optimales, tels que le potentiel appliqué, la quantité de charge en $Gd_2O_3$, la vitesse d'agitation, la température de l'électrolyte et la rugosité du substrat. La morphologie et la composition des cibles ont été étudiées par microscope électronique à balayage (MEB) couplé à la spectroscopie de rayons X

à dispersion d'énergie (EDX) et par plasma à couplage inductif - spectroscopie d'émission atomique (ICP-AES).

Après avoir vérifié l'homogénéité et l'adhérence de la cible, ces cibles minces ont été utilisées pour mesurer les sections efficaces des réactions nucléaires de $^{nat}$Gd(d,x)Tb et $^{*}$Gd(d,x)Tb, où « $^{nat}$Gd » indique gadolinium naturel et « *Gd » indique gadolinium enrichi en 92.8% de $^{155}$Gd (fourni par TraceScience). La technique des « stacked foils » est utilisée pour mesurer les sections efficaces de différentes réactions nucléaires à énergies différentes en utilisant un seul tir. Des feuilles de nickel et de titane ont été choisies comme moniteurs qui permettent de mesurer le flux de faisceau, et des feuilles d'aluminium ont été choisies comme dégradeurs qui permettent de changer l'énergie de deutéron en valeur plus faible dans le « stack ». L'activités des radionucléides produits sont mesurés par un détecteur au germanium de haute pureté, HPGe, le nombre de noyau de Gd dans la cible a été mesuré par ICP-AES, et la surface de dépôt a été estimée en comptant le nombre de pixels à l'aide d'un logiciel GIMP. Pour vérifier la fiabilité de la cible faite par co-électrodéposition, des expériences de preuve de concept ont d'abord été réalisées en utilisant des cibles de gadolinium naturel. Ces cibles ont été irradiées au cyclotron ARRONAX avec un faisceau de deutérons allant de l'énergie de 8 MeV à 30 MeV pendant 30 min avec une intensité de 50 nA, et les résultats ont été comparés avec les données existantes. Ensuite, les cibles enrichies ont été irradiées à une intensité de 50 nA pendant 30 min pour mesurer les sections efficaces de $^{*}$Gd(d,x)Tb dans la plage d'énergie de 8 MeV à 30 MeV. Les sections efficaces obtenues permettent de choisir une fenêtre énergétique adaptée pour la production, et d'estimer le rendement de production et la pureté de $^{155}$Tb.

Après avoir estimé le rendement de production et choisi une fenêtre énergétique, la fabrication de cibles épaisses est étudiée pour une production en série de $^{155}$Tb. La méthode de pastillage a été développée pour des cibles de gadolinium plus épaisses (plus de 100 µm). Une presse hydraulique a été utilisée pour comprimer la poudre contenant Gd enrichi afin de produire des cibles compactes et uniformes. Le $Gd_2O_3$, le $GdCl_3$ et le $GdF_3$ ont d'abord été considérés comme des poudres candidates pour le pastillage. Parmi les trois, seul sous forme de $Gd_2O_3$ est enrichie et disponible commercialement, cette poudre est utilisée pour le pastillage. La pression de compression et le temps de granulation ont été étudiés pour trouver la condition optimale de pastillage. La qualité de pastille a été caractérisée par MEB et diffractométrie de rayons X (DRX). Des tests avec de la poudre naturelle ont d'abord été réalisés pour étudier et caractériser les propriétés physique et morphologique de la pastille. La conductivité thermique de la pastille a été mesurée sous température différente (24 °C, 100 °C, 200 °C, 300 °C, et 400 °C). En utilisant l'équation de transfert de chaleur, la température de la pastille sous irradiation a été estimée en supposant un système de refroidissement dans les deux côtés de la pastille.

Une pastille de $Gd_2O_3$ enrichi en $^{155}$Gd a été irradiée comme un premier test pour obtenir le rendement expérimental de la production en masse à ARRONAX. L'intensité de faisceau était 368 ± 26 nA, l'énergie d'incident était 15.1 ± 0.1 MeV et la durée d'irradiation était 1 h.

**Résultat**

Pour les cibles minces, plusieurs cibles d'une épaisseur comprise entre 10 et 20 µm ont été fabriquées avec succès par la méthode de co-déposition. Pour les cibles Ni-$Gd_2O_3$, les expériences ont montré que plusieurs paramètres influencent la qualité de dépôt. Un potentiel électrique trop faible, une vitesse d'agitation trop élevée et un support trop rugueux rendront la surface du dépôt non uniforme (soit des dendrites se forment, soit la distribution de $Gd_2O_3$ n'est

pas uniforme). Cependant, un potentiel trop élevé, une charge de $Gd_2O_3$ trop faible, une vitesse d'agitation trop faible et une température trop basse entraîneront une moindre piégeage de $Gd_2O_3$ dans le dépôt de Ni. Par conséquent, la condition optimale était à -1,20 V/NHE, avec autant que possible de la poudre de $Gd_2O_3$, à une vitesse de balayage de 300 trs/min, à 30°C et déposée sur un substrat d'or lisse. Dans cette condition, des cibles d'une épaisseur de 10 à 20 μm ont été obtenues pour une durée de dépôt de 60 min. La teneur en Gd de la cible était de 3,0 ± 0,4 mg selon les résultats du ICP-AES. Les images au MEB ont montré que les particules de $Gd_2O_3$ se répartissaient uniformément sur la surface. Des expériences ont également montré que la présence de $Gd_2O_3$ était aussi bien sur la surface qu'à l'intérieur du dépôt mais la distribution longitudinale sur l'épaisseur n'était pas uniforme, avec plus de particules de $Gd_2O_3$ à la surface qu'à l'intérieur. Cependant, comparé avec la taille de faisceau (1,0-1,5 cm), cette répartition inhomogène est négligeable. Pour les cibles Zn-$Gd_2O_3$, même constat que celle de Ni-$Gd_2O_3$, un potentiel trop faible ou une vitesse d'agitation trop élevée conduisent à l'inhomogénéité de la surface du dépôt, et le chargement plus important en $Gd_2O_3$ favorise l'incorporation de Gd dans le dépôt. La qualité du dépôt était meilleure avec un potentiel de -1,52 V/NHE, une vitesse d'agitation de 800 tr/min. Cependant, comparés aux cibles de Ni-$Gd_2O_3$, les cibles Zn-$Gd_2O_3$ ont un problème d'adhérence au bord à cause de la formation de dendrites. La cible Zn-$Gd_2O_3$ est donc fragile et n'est donc pas choisie pour la suite d'expériences. De ce fait, les autres paramètres, comme la température de l'électrolyte et la rugosité du substrat, n'ont pas été étudiés. La surface de la cible de Ni-$Gd_2O_3$ est plus homogène que celle de Zn-$Gd_2O_3$ et a une bonne adhérence, la qualité de la cible de Ni-$Gd_2O_3$ prime donc devant celle de Zn-$Gd_2O_3$. De plus, l'élément Ni du dépôt donnera, en plus que la feuille de Ni, une information supplémentaire sur la détermination du flux de faisceau dans la cible. Par conséquent, la cible Ni-$Gd_2O_3$ a finalement été choisie comme cible mince utilisée pour la mesure de la section efficace. La réutilisation des charges de $Gd_2O_3$ a également été étudiée dans ce travail, 1,0 g de poudre a été ajouté pour obtenir 10 dépôts, comparé à 10 fois 0,1 g de poudre pour obtenir 10 dépôts, la réutilisation de 1,0 g de poudre peut emprisonner plus de Gd dans le dépôt.

Huit cibles composites Ni-$^{nat}Gd_2O_3$ ont été irradiées au cyclotron ARRONAX avec un faisceau de deutéron allant de 8 MeV à 30 MeV pour une durée de tir de 30 min ou 60 min. Le radionucléide d'intérêt $^{155}$Tb et d'autres impuretés, $^{153}$Tb, $^{154}$Tb, $^{156}$Tb et $^{160}$Tb, ont été détectés et leurs fonctions d'excitation ont été étudiées. Les valeurs mesurées de la voie de production de $^{nat}$Gd(d,x)Tb ont été mesurées et comparées aux données existantes. Les valeurs mesurées sont cohérentes avec les données de Duchemin et al.[9] et aussi comparables avec d'autres données[10,11]. La cohérence des valeurs mesurées a démontré la fiabilité des cibles composites de Ni-$Gd_2O_3$. Ensuite, les sections efficaces de $^{*}$Gd(d,x)Tb ont été mesurées grâce aux 10 cibles composites enrichies Ni-$^{155}Gd_2O_3$ fabriquées. Les radionucléides $^{155}$Tb et $^{156}$Tb ont été détectés dans ces 10 cibles à toutes énergies. La section efficace maximale de $^{*}$Gd(d,x)$^{155}$Tb est de 797,9 ± 77,8 mb à 14,2 ± 0,3 MeV alors que celle de $^{*}$Gd(d,x)$^{156}$Tb est de 83,1 ± 8,1 mb à la même énergie. Théoriquement, la coproduction de $^{153}$Tb ou $^{154}$Tb est possible lorsque l'énergie est plus grande que celle de 13,16 MeV, alors que ces deux radionucléides n'ont été détectés que lorsque l'énergie de la cible était supérieure à 19,4 ± 0,3 MeV. Cela peut être dû au fait que la quantité de ces deux radionucléides produites n'est pas suffisante pour être détectée par le détecteur. Grâce à l'étude des fonctions d'excitation, le « thick target yield » a

été calculé dans la fenêtre d'énergie pour la production en masse de $^{155}$Tb entre 4 MeV et 14 MeV. Les rendements de production de $^{155}$Tb et $^{156}$Tb ont été estimés par le logiciel RYC (développé par GIP ARRONAX) en utilisant les fonctions d'excitation de $^{155}$Tb et $^{156}$Tb. Le rendement de cible épaisse (thick target yield) dans la fenêtre d'énergie choisie est de 6,9 MBq/μAh. La pureté de $^{155}$Tb passe de 60% à 89% lorsque l'énergie passe de 9 MeV à 15 MeV, et la pureté est maintenue à 89 % lorsque l'énergie se situe entre 14 et 16 MeV.

Pour les cibles plus épaisses obtenues après pastillage, l'étude montre que la pression s'est avérée avoir un effet sur l'intégrité de la cible. Après multitude tests, la pression optimale sur la cible a été fixée à 600 bars. La durée de pastillage n'a pas montré d'effets évidents sur la qualité de la cible, la durée de pastillage a donc été fixée à 60 s. 3 pastilles ont été obtenues, $GdCl_3$, $GdF_3$ et $Gd_2O_3$, mais les deux premières ont été abandonnées car pour la pastille $GdCl_3$ elle était très hygroscopique et facilement cassable après une température élevée et pour celle de $GdF_3$, elle était très difficile à dissoudre pour traiter chimiquement pour récupérer l'élément d'intérêt $^{155}$Tb. De plus, que ce soit pour $GdCl_3$, $GdF_3$, il était difficile d'obtenir des échantillons de haute pureté. En effet, ces deux poudres ont été fabriquées à partir de $Gd_2O_3$, des impuretés se sont incrustés après plusieurs réactions chimiques jusqu'à l'obtention de $GdCl_3$, $GdF_3$. La poudre $Gd_2O_3$ naturelle a été compressée sous la condition optimale, la densité moyenne des granulés obtenus est de 5,08 g/cm$^3$. Cette densité n'est que de 72% de la densité théorique, ce qui indique la présence de vides dans la cible. Les images au MEB confirmaient la présence de vides dans les pastilles et des fissures et trous ont été trouvés sur la surface. Ces images au MEB étaient semblables pour toutes les pastilles, même si les épaisseurs étaient différentes. Toutefois, ces non-uniformités imparfaites sont négligeables par rapport à la taille de faisceaux (1.0-1.5 cm). La température de la pastille pendant le tir a été estimée, avec le système de refroidissement, et cette valeur se situait entre 258°C et 267°C quand l'intensité de faisceau est 1 μA, l'énergie d'incident est 14 MeV et la durée d'irradiation de 1 h. La pastille a été chauffé jusqu'à 600°C, et les résultats au MEB ont montré que la surface ne changeait pas à haute température, ce qui indique la bonne résistance thermique de la pastille.

L'étude de la cible naturelle de $Gd_2O_3$ a démontré une bonne qualité de la cible épaisse en utilisant la méthode de pastillage, une pastille $Gd_2O_3$ enrichie a donc été fabriqué en appliquant les même paramètres que celles qui a été utilisées pour fabriquer les pastilles de $Gd_2O_3$ naturelle. La poudre enrichie est utilisée en récupérant ce qu'il en reste après la co-électrodéposition. Cette pastille, avec une masse de 0.63 g et une épaisseur de 0.39 mm, a été emballée de deux feuilles d'aluminium de 10 μm d'épaisseur et encapsulée dans une capsule en acier inoxydable. L'ensemble de capsule et de pastille a été irradié par un faisceau de deutéron d'une énergie incidente de 15,1 ± 0,1 MeV et d'une énergie de sortie de 8,6 ± 0,2 MeV pendant 1 h. L'intensité du faisceau était de 368 ± 26 nA. Le rendement de $^{155}$Tb était de 10,2 ± 0,7 MBq/μAh alors que celui de $^{156}$Tb de 1,3 ± 0,1 MBq/μAh. Ces résultats sont cohérents avec les résultats déterminés à partir des fonctions d'excitation, qui étaient de 10,1 MBq/μAh pour $^{155}$Tb et de 1,2 MBq/μAh pour $^{156}$Tb. Le radionucléide $^{154}$Tb a aussi détecté dans la pastille 7 jours après EOB à cause d'énergie d'incident élevée, mais il a disparu 14 jours après EOB grâce à la désintégration. La pureté de $^{155}$Tb était de 89% 14 jours après EOB, ce résultat est en accord avec la pureté estimée à partir des fonctions d'excitation. Comparativement à d'autres voies de production, notamment celle de la réaction induite par le proton, qui a un rendement de production d'environ 3

MBq/μAh et une pureté d'environ 93% (96 h après EOB), la réaction induite par le deutéron triple le rendement de production en gardant une pureté proche.

La dissolution de la pastille et le recyclage de poudre de $Gd_2O_3$ ont aussi été étudiés à partir de $Gd_2O_3$ naturel. Cette expérience a montré que 100 mL de 2 mol/L de HCl pouvait dissoudre 1 g de $Gd_2O_3$ en 60 min avec une vitesse d'agitation de 350 trs/min et une température de la solution de 90°C. Pour récupérer $Gd_2O_3$, 100 mL de 1 mol/L d'acide oxalique a été ajouté à la solution pour obtenir la précipitation de $Gd_2(C_2O_4)_3 \cdot 10H_2O$. La précipitation a ensuite été chauffée jusqu'à 800°C pour être transférée en $Gd_2O_3$. L'analyse DRX a indiqué que la structure cristalline de la poudre obtenue était bien celle de $Gd_2O_3$. Enfin, le taux de récupération a atteint 84 %.

**Conclusion**

Ce travail impliquait diverses étapes de la production de radionucléides, notamment la fabrication et l'encapsulation de cibles solides, la mesure de section efficace, l'estimation des rendements de production et la production en masse, la dissolution des cibles et le recyclage des cibles. Les sections efficaces mesurées à partir de l'élément enrichi en $^{155}$Gd sont les premières valeurs expérimentales, ces valeurs peuvent s'appliquer non seulement à estimer les rendements de production, mais aussi à valider des modèles physiques de réactions nucléaires et améliorer des codes de simulation. En conclusion, ce travail fournit non seulement une alternative pour augmenter la disponibilité de Tb, mais fournit également des idées pour la fabrication des autres cibles.

**Référence**


1. Beyer, G.-J. *et al.* Targeted alpha therapy in vivo: direct evidence for single cancer cell kill using 149Tb-rituximab. *Eur. J. Nucl. Med. Mol. Imaging* **31**, 547–554 (2004).
2. Cleeren F. Theranostics studies using 152/149Tb-labeled anti-CXCR4 probes in tumor mice. *CERN Document Server* https://cds.cern.ch/record/2753398 (2021).
3. Cavaier, R. F., Haddad, F., Sounalet, T., Stora, T. & Zahi, I. Terbium radionuclides for theranostics applications: a focus on MEDICIS-PROMED. *Phys. Procedia* **90**, 157–163 (2017).
4. Lehenberger, S. *et al.* The low-energy β− and electron emitter 161Tb as an alternative to 177Lu for targeted radionuclide therapy. *Nucl. Med. Biol.* **38**, 917–924 (2011).
5. Duchemin, C. *et al.* CERN-MEDICIS: A UNIQUE FACILITY FOR THE PRODUCTION OF NONCONVENTIONAL RADIONUCLIDES FOR THE MEDICAL RESEARCH. in *11th International Particle Accelerator Conference* (2020). doi:10.18429/JACoW-IPAC2020-THVIR13.
6. Fiaccabrino, D. E., Kunz, P. & Radchenko, V. Potential for production of medical radionuclides with on-line isotope separation at the ISAC facility at TRIUMF and particular discussion of the examples of 165Er and 155Tb. *Nucl. Med. Biol.* **94–95**, 81–91 (2021).
7. Gadolinium Isotopes - Gd Isotopes - Stable Gadolinium Isotopes Supplier. http://www.tracesciences.com/gd.htm.
8. Patnaik, P. *Handbook of inorganic chemicals*. (McGraw-Hill, 2003).
9. Duchemin, C., Guertin, A., Haddad, F., Michel, N. & Métivier, V. Deuteron induced Tb-155 production, a theranostic isotope for SPECT imaging and auger therapy. *Appl. Radiat. Isot.* **118**, 281–289 (2016).
10. Szelecsényi, F., Kovács, Z., Nagatsu, K., Zhang, M.-R. & Suzuki, K. Investigation of deuteron-induced reactions on natGd up to 30 MeV: possibility of production of medically relevant 155Tb and 161Tb radioisotopes. *J. Radioanal. Nucl. Chem.* **307**, 1877–1881 (2016).

11. Tárkányi, F. *et al.* Activation cross-sections of deuteron induced reactions on natGd up to 50MeV. *Appl. Radiat. Isot.* **83**, 25–35 (2014).

DOCTORAT MATIERE BRETAGNE MOLECULES LOIRE ET MATERIAUX

Nantes Université

**Titre :** Développement d'une cible enrichie de gadolinium pour la mesure de la section efficace et la production future de terbium pour la médecine nucléaire

**Mots clés :** production de terbium, mesure de section efficaces, rendement de production, irradiation aves des deutérons, théranostique, cyclotron

**Résumé :** Les radionucléides du terbium ont attiré beaucoup d'attention pour leurs applications potentielles en médecine nucléaire. Cependant, leurs applications ont limitées par leur pénurie. Ce travail propose d'utiliser des cibles de gadolinium enrichies pour produire du terbium dans des cyclotrons biomédicaux. Le radionucléide $^{155}$Tb est pris comme cas d'étude via la réaction $^{155}$Gd(d,2n)$^{155}$Tb.
Pour estimer le rendement de production, des cibles minces contenant du Gd ont été développées pour la mesure des sections efficaces. La méthode de co-électrodéposition a été choisie pour fabriquer des cibles composées Ni-$Gd_2O_3$. Plusieurs paramètres ont été étudiés pour augmenter la masse de Gd dans la cible.
Les sections efficaces de la réaction $^{155}$Gd(d,2n)Tb ont été mesurées au cyclotron du GIP ARRONAX dans une gamme d'énergie de 8 MeV à 30 MeV. Le rendement est estimé à partir de ces nouveaux résultats.
Pour la production de masse, des cibles épaisses ont été développées via la méthode de pastillage. La condition expérimentale optimale et les propriétés sous cette condition ont été étudiées. Une cible de $Gd_2O_3$ enrichie a été irradiée avec une énergie incidente de 15 MeV. Le rendement est de 10 MBq/µAh et la pureté est de 89 %.
La coproduction d'autres isotopes de Tb, et le recyclage de Gd sont également présentés dans cette thèse.

**Title :** Development of Enriched Gadolinium Target for Cross Section Measurement and Future Production of Terbium for Nuclear Medicine

**Keywords :** terbium production, cross section measurement, production yield, deuteron irradiation, theranostics radioisotope, cyclotron-produced radionuclide

**Abstract :** Radionuclides of terbium have attracted much attention for their potential applications in nuclear medicine. However, the short supply of terbium isotopes has limited their applications. This work proposes to use enriched gadolinium targets to produce terbium radioisotopes in biomedical cyclotrons via light-particle-induced reactions. The Auger and gamma emitter $^{155}$Tb is taken as a study case using the reaction $^{155}$Gd(d,2n)$^{155}$Tb.
To estimate the production yield, thin Gd-containing targets have been firstly developped to measure the cross sections. To this end, the co-electrodeposition method has been chosen to manufacture Ni-$Gd_2O_3$ composite targets. Several process parameters that have an impact on deposit quality are stutied to increase the Gd content (up to 3 mg in the deposit). The cross section measurement of $^{nat}$Gd(d,2n)Tb, as a proof-of-conception experiment, has been carried out at GIP ARRONAX cyclotron facility using natural Ni-$Gd_2O_3$ targets. The production yield is estimated using these results.
Thick targets have also been developped via pelletizing method for mass production. The optimal experimental conditions and pellet properties under these conditions have been investigated. An enriched $^{155}Gd_2O_3$ target was irradiated with an incident energy of 15 MeV. The production yield of $^{155}$Tb was found to be 10 MBq/µAh and the purity was 89%, which are consistent with the estimation.
The coproduction of other Tb isotopes and the recycle of Gd are also involved in this thesis.